



HAL
open science

Experimental and numerical study of model gravity currents in coastal environment : bottom gravity currents

Dhafar Ibrahim Ahmed

► **To cite this version:**

Dhafar Ibrahim Ahmed. Experimental and numerical study of model gravity currents in coastal environment : bottom gravity currents. Other. Université de Bretagne occidentale - Brest, 2017. English. NNT : 2017BRES0060 . tel-01810835

HAL Id: tel-01810835

<https://theses.hal.science/tel-01810835>

Submitted on 8 Jun 2018

HAL is a multi-disciplinary open access archive for the deposit and dissemination of scientific research documents, whether they are published or not. The documents may come from teaching and research institutions in France or abroad, or from public or private research centers.

L'archive ouverte pluridisciplinaire **HAL**, est destinée au dépôt et à la diffusion de documents scientifiques de niveau recherche, publiés ou non, émanant des établissements d'enseignement et de recherche français ou étrangers, des laboratoires publics ou privés.

THÈSE / UNIVERSITÉ DE BRETAGNE OCCIDENTALE

sous le sceau de l'Université Bretagne Loire

pour obtenir le titre de

DOCTEUR DE L'UNIVERSITÉ DE BRETAGNE OCCIDENTALE

Mention : Sciences pour l'Ingénieur

Discipline : Génie côtier

Spécialité : L'Environnement ; les modèles de qualité de l'eau

École Doctorale des Sciences de la Mer

Présentée par

Dhafar Ibrahim AHMED

Préparée au sein de la FRE CNRS 3744 IRDL

Institut de Recherche Dupuy de Lôme

**Etude Expérimentale et
Numérique de Courants
Gravitaires Modèles en
Environnement Côtier:
Courant gravitaire dense**

Thèse soutenue le (01/09/2017)

Devant le jury composé de :

Mr Lalaonirina RAKATOMANANA

Professeur, Université de Rennes 1, *président*

Mr Innocent MUTABAZI

Professeur, Université du Havre, *rapporteur*

Mr Ahmed OULD EL MOCTAR

Maître de Conférences HDR, Université de Nantes, *rapporteur*

Mme Cécile LEMAITRE

Maître de Conférences HDR, Université de Lorraine, *examineur*

Mr Didier BERNARD

Maître de Conférences HDR, Université des Antilles, *examineur*

Mr Bernard POTTIER,

Professeur, UBO, *examineur*

Mr Noureddine LATRACHE

Maître de Conférences, UBO, *Co-encadrant de thèse*

Mr Blaise NSOM

Professeur UBO, *Directeur de thèse*

Mr Fulgence RAZAFIMAHERY

Maître de Conférences, Université de Rennes 1, *invité*

University of Western Brittany
Doctoral School of Marine Sciences

DISSERTATION

Experimental and Numerical Study of Model Gravity Currents in Coastal
Environment: Bottom Gravity Currents

Submitted by
Dhafar Ibrahim Ahmed

In partial fulfillment of the requirements
For the degree of Doctor of Philosophy
In
Coastal Engineering
Speciality: Environment; water quality models

Supervised by
Prof. Dr. Blaise Nsom
Dr. Nouredine Latrache

01. September. 2017

ABSTRACT

This manuscript presents the results of a thorough experimental and numerical investigation on model dense gravity currents. The gravity currents prepared are salt/tap water solutions at assigned concentrations. They are released in the form of a jet into a calm lighter ambient liquid (fresh tap water in this case) over a flat, smooth, and rigid bottom in order to simulate the discharge of a denser fluid in the coastal environment. The release of pollutants into rivers, oil spillage on the sea environment and desalination plants outflow are example of man-made gravity currents that frequently cause negative environmental impacts. The aim of this investigation is to contribute to a better understanding of the propagation dynamics and the mixing process of dense gravity currents. The Laboratory experiments proceeded with a fixed initial gravity current concentration in one experimental set-up. The gravity currents are injected using a rectangular injection channel into a rectangular basin containing the ambient lighter liquid. The injection studied is said in unsteady state volume, as the Reynolds number lies in the range 1111 - 3889. The experiments provided the evolution of the boundary interface of the jet, and it is used to validate the numerical model.

The numerical model depends on the Reynolds-Averaged Navier Stokes equations (RANS). The $k-\varepsilon$ (K-epsilon) and the Diffusion-Convective Equation (DCE) of the saline water volume fraction were used to model the mixing and the propagation of the gravity current jet. On the other hand, comparison of the mean flow ($z/z_{0.5} = u/u_{max}$) with previous two-dimensional numerical simulations and experimental measurements have shown similarities. The numerical simulations of the hydrodynamic fields indicate that the velocity maximum at $0.18z_{0.5}$, where $z_{0.5}$ is the height at which the mean velocity u is the half of the maximum velocity u_{max} . The excess-density shows a radial symmetry close to the inlet and asymmetry far from the inlet. As well, calculation of the gradient of the Richardson number Ri_g as a function of the height of different longitudinal positions can give the zone of turbulent mixing. The comparison of the numerical with the experimental front positions presents an excellent agreement for Reynolds and Richardson's numbers varying in the ranges $2222 < R < 3889$ and $0.003 < Ri < 0.01$ respectively. The local gradient Richardson number Ri_g shows that the maximum of the turbulent mixing occurs at $z \approx z_{0.5}$ in the first stage of the gravity current, i.e. close to the inlet and it collapses far from the inlet. Consequently, calculation of the relative volume of the gravity current jet and entrainment as the threshold in the space or in the time permitted to evaluate the degree of the mixing. By analyzing the turbulent mixing in a 3D configuration, the volume of the turbulent mixing increases with the x -coordinate close to the inlet jet and decreases far from the inlet. The entrainment depends both on the front position and on the values of the iso-density threshold. The entrainment is found independent on Reynolds numbers between 2222 and 3889.

Keywords: Bottom Gravity Current, Buoyant jet, Entrainment, Experiments, Mixing, Numerical simulations, RANS model.

RESUME

Nous présentons une étude expérimentale et numérique systématique de jets gravitaires dans un liquide ambiant moins dense et statique au-dessus d'une plaque lisse et rigide pour représenter le déversement d'un fluide lourd en environnement côtier. Le but de ce travail de recherche est de contribuer à une meilleure compréhension de la dynamique de propagation et de la miscibilité de jets gravitaires au-dessous d'un liquide ambiant. Des expériences ont été réalisées en laboratoire à l'aide d'une plateforme expérimentale constituée d'un bassin parallélépipédique contenant de l'eau douce et d'un canal d'injection de section rectangulaire de jets gravitaires de concentration constante initiale fixée.

Les calculs mathématiques et numériques sont basés sur les modèles RANS (Reynolds-Averaged Navier Stokes equations), $k-\varepsilon$ (K-epsilon) et DCE (Diffusion-Convective Equation) de la fraction volumique de l'eau salée pour décrire la propagation et le mélange du jet gravitaire. L'évolution du front du jet obtenue expérimentalement est utilisée pour valider le modèle numérique. Par ailleurs, la comparaison des résultats obtenus sur l'écoulement moyen ($z/z_{0.5} = u/u_{max}$) avec ceux des études 2D expérimentales et numériques antérieures ont montré des similarités. La simulation numérique des champs hydrodynamiques montre que la vitesse maximale est atteinte à la position $0.18 z_{0.5}$, où $z_{0.5}$ est la hauteur d'eau pour laquelle la vitesse moyenne u est égale à la moitié de la vitesse maximale u_{max} . La densité excédentaire présente une symétrie radiale proche de l'injection et une dissymétrie loin de l'injection.

De même, le calcul du gradient du nombre de Richardson Ri_g en fonction de la hauteur d'eau pour différentes positions longitudinales peut indiquer la zone où se produit le mélange turbulent. La comparaison des résultats expérimentaux et numériques des positions du front présente une bonne concordance pour les gammes respectives suivantes des nombres de Reynolds et de Richardson $2222 < R < 3889$ et $0.003 < Ri < 0.01$. Le gradient local du nombre de Richardson Ri_g montre que le maximum du mélange turbulent se produit en $z \approx z_{0.5}$ dans la première phase de propagation du courant gravitaire, donc proche de l'injection, et s'effondre loin de l'injection. Par conséquent, le calcul avec le volume relatif du jet gravitaire et de l'entraînement comme seuil dans l'espace ou dans le temps permet d'évaluer le degré de mélange. L'analyse du mélange turbulent 3D montre que le volume du mélange turbulent croît avec la coordonnée longitudinale proche de l'injection et décroît loin de l'injection. L'entraînement dépend de la position du front et des valeurs du seuil de l'iso-densité. L'entraînement ne dépend pas du nombre de Reynolds pour des valeurs comprises entre 2222 et 3889.

Mots clés: Courant gravitaire dense, Jet flottant, Entraînement, Expériences, Mélange, Simulations Numériques, Modèle RANS.

DEDICATION

In memory of my father “Ibrahim Ahmed Abdan” with love and eternal appreciation.

[Friday.17.08.2017]

AKNOWLEDGEMENT

This dissertation is the result as four years of research, I would like to express my heartfelt gratitude to my supervisor Prof. Dr. Blaise NSOM and my co-supervisor Dr. Nouredine LATRACHE for their invaluable suggestions, assistance and encouragement during last four years

I also thank the members of my doctoral dissertation committee. Pr. Dr. Lalaonirina RAKATOMANANA (Université de Rennes 1), Pr. Dr. Innocent MUTABAZI (Université du Havre), Pr. Dr. Bernard POTTIER, (Université de Bretagne Occidentale), Dr. HDR, Ahmed OULD EL MOCTAR (Université de Nantes), Dr. HDR, Cécile LEMAITRE (Université de Lorraine), Dr. HDR Didier BERNARD (Université des Antilles, Guadeloupe), and Dr. Fulgence RAZAFIMAHERY (Université de Rennes 1). I would like to extend my gratitude to Prof. Dr. Mohamed BENBOUZID director of Institut de Recherche Dupuy de Lôme (Université de Bretagne Occidentale).

I would like to thank the technician S. DEGOUZON for assisting me by computer resources, Papa NIANG for his numerical simulation help, and S. PIAT for experimental help. Thank you my colleagues and friends (especially; Tony EL-TAWIL, Kamal NOUNOU, DJameleddine BOUGRINE, Abdelkadir LEBSIR, and Zakarya OUBRAHIM) of the Institut de Recherche Dupuy de Lôme-FRE CNRS 3744 IRDL at university of Brest, IUT of Brest.

This work described was funded by the Iraqi Government through an Iraqi Ministry of Higher Education and Scientific Research is represented by Wassit University studentships in partnership with a French Ministry of Higher Education and Research is represented by Campus France and is not subject to copyright. Doctoral School of Marine Sciences (EDSM) also provided a travel grant towards one international conference expenses as award for best presentation of my poster in days of the EDSM 2015.

Forever, I thank my parents, without whom I would not be who I am now. Finally, and most importantly, I would like to thank my wife Nidhal. Her standing beside me throughout my career and writing this work. I do not forget my children Ibrahim, Mohammed, and Razan, who are just about the best kids could hope for: happy, loving, and fun to be with.



CONTENTS

ABSTRACT	I
AKNOWLEDGEMENT	IV
CONTENTS	V
LIST OF FIGURES	VIII
LIST OF TABLES	X
ACRONYMS	XI
LIST OF SYMBOLS	XII
CHAPTER 1 : INTRODUCTION	1
1.1 GRAVITY CURRENTS	1
1.2 STATEMENT OF THE PROBLEM	3
1.3 METHODOLOGY	4
1.4 OUTLINE OF DISSERTATION.....	5
1.5 ORIGINAL CONTRIBUTIONS	5
CHAPTER 2 : LITERATURE REVIEW	7
2.1 CLASSIFICATION OF GRAVITY CURRENTS.....	7
2.1.1 Density ratio of current to ambient fluids.....	9
2.1.2 Density difference of current and ambient fluids	9
2.1.3 Continuous release with finite volume	10
2.1.4 Geometrical limitations	10
2.2 BOTTOM GRAVITY CURRENTS STRUCTURE.....	11
2.2.1 Distribution of bottom gravity current concentration.....	12
2.2.2 Distribution of the velocity in a bottom gravity current.....	13
2.3 DISPERSION OF DISCHARGES OF BUOYANT GRAVITY CURRENT JET	14
2.3.1 The flow conditions	15
2.3.2 Buoyant jet length scales	16
2.3.3 Gravity currents on a flat bottom in calm ambient waters	18
2.3.4 Physical properties of heavy gravity currents.....	18
2.4 ENTRAINMENT AND MIXING GRAVITY CURRENTS	20
2.4.1 Entrainment	20
2.4.1.1 Analysis of entrainment.....	21
2.4.1.2 Total entrainment.....	23
2.4.1.3 Entrainment of dense jets	23
2.4.1.4 The dependency and velocity of entrainment.....	25
2.4.2 Turbulent mixing	27
2.4.2.1 Fractional area/volume ratio of the dense current	28
2.4.2.2 Potential energy	28
2.5 NUMERICAL MODELING OF GRAVITY CURRENTS.....	30
2.5.1 Gravity current model into static ambient water	31
2.5.2 Gravity current model with dynamic ambient water	32

2.5.3 Numerical methods.....	33
CHAPTER 3 : EXPERIMENTAL STUDY	36
3.1 INTRODUCTION	36
3.2 APPARATUS AND EXPERIMENTAL PROCEDURE.....	36
3.2.1 Experimental setup	36
3.2.2 Measurement techniques	37
3.2.3 Experimental procedures	38
3.3 EXPERIMENTAL PARAMETERS.....	39
3.4 IMAGE ANALYSIS TECHNIQUE	40
3.4.1 ImageJ software.....	40
3.4.2 Image processing	41
3.5 THE CONFIGURATION OF GRAVITY CURRENTS	50
3.5.1 Experimental front position.....	50
3.5.2 Propagation Phase Transitions	51
3.5.3 The lobe-cleft instabilities	54
3.6 SUMMARY	54
CHAPTER 4 : 3D NUMERICAL MODEL AND COMPUTATIONAL DETAILS	56
4.1 INTRODUCTION	56
4.2 NAVIER-STOKES EQUATIONS	56
4.3 THREE-DIMENSIONAL NUMERICAL MODELING.....	57
4.3.1 The numerical model.....	57
4.3.2 Initial and boundary conditions	60
4.3.2.1 Initial conditions.....	60
4.3.2.2 Boundary conditions.....	61
4.4 NUMERICAL METHOD DESCRIPTION	63
4.4.1 OpenFOAM characterization	64
4.4.2 File structure of OpenFOAM cases	65
4.4.2.1 A constant directory.....	65
4.4.2.2 A system directory.....	67
4.4.2.3 The time “0” directories	68
4.5 IMAGE PROCESSING ANALYZE.....	69
4.6 THE CONFIGURATION OF GRAVITY CURRENTS	71
4.6.1 Numerical front position.....	71
4.6.2 Propagation Phase Transitions	71
4.6.3 The lobe-cleft instabilities	71
CHAPTER 5 : RESULTS	74
5.1 INTRODUCTION	74
5.2 FRONT POSITION OF THE JET: EXPERIMENTAL AND NUMERICAL RESULTS	74
5.3 VELOCITY AND DENSITY PROFILES	80
5.4 TURBULENT MIXING.....	84

5.5	ENTRAINMENT RATES	86
5.6	SUMMARY	92
CHAPTER 6 : CONCLUSIONS AND FUTURE WORKS		93
6.1	CONCLUSIONS	93
6.2	FUTURE WORKS	95
APPENDIX A : NEWTONIAN GRAVITY CURRENT EQUATIONS		97
A.1	EQUATIONS FOR HORIZONTAL CHANNEL	97
A.2	EQUATIONS OF SLOPING BOTTOM	101
A.2.1	Conclusion	103
A.2.2	Verification	104
A.2.3	Remark about a horizontal channel	105
A.3	EXACT SOLUTION TO NEWTONIAN GRAVITY CURRENT BENEATH A STATIC WATER LAYER IN HORIZONTAL BASIN	107
APPENDIX B : NON-NEWTONIAN GRAVITY CURRENT EQUATIONS		110
B.1	EQUATION FOR HORIZONTAL CHANNEL	110
B.1.1	Calculating the pressure	111
B.1.2	Equation of conservation of momentum	112
B.2	EQUATIONS OF MOTION IN AN INCLINED BOTTOM	115
BIBLIOGRAPHY		119

LIST OF FIGURES

Figure 1.1: Examples of gravity currents in the environment: (a) Treatment wastewaters are rejected in the St. Lawrence River (Montréal). (b) A plume of acidic aluminum-rich water in the Manning River (Australia). (c) and (d) Sand storms are examples of buoyancy driven gravity currents in the atmosphere of specific interest is how ground friction affects speed of propagation and mixing in gravity currents in Iraq, 2015. (e) Gravity currents, in the form of pyroclastic flows, propagate down the flanks of the volcano in Mayon, Philippines, 1984. And (f) avalanche from Hunza Peak, Karimabad, in Pakistan.....	2
Figure 2.1: Schemes as example of possible density flow patterns for a gravity current discharge into the water bodies ρ_1 intruding in the ambient fluid with uniform density ρ_2 , and $\rho_{2a} < \rho_1 < \rho_{2b}$: a) underflow gravity current, b) overflow gravity current, and c) interflow gravity current (Morris & Fan 1998, and Cesare <i>et al.</i> 2006). In this study: $\rho_1 = \rho_{saline}$ and $\rho_2 = \rho_{water}$	8
Figure 2.2: Structure Scheme of a bottom gravity current (Chowdhury & Testik 2014).	11
Figure 2.3: The mean concentration profiles found in previous literature; a) Smooth profile, b) Stepped profile, and c) Lutocline profile [Jacobson, & Testik (2014), and Kneller& Buckee (2000)]......	12
Figure 2.4: The mean velocity profile of a constant-flux release two-dimensional gravity current, the x- and y-axis values are normalized (Kneller & Buckee 2000 and Jacobson, & Testik 2013)......	13
Figure 2.5: Schematic of flow a) a vertical positively downward discharge of the denser (than ambient water) fluids, b) a vertical negatively upward discharge of lighter fluids, c) the angled upward negatively discharge of denser fluids and d) a horizontal positively discharge of denser fluids (Papakonstantis & Christodoulou 2010 and Chowdhury & Testik 2014)......	15
Figure 2.6: The experimental measurements and proposed fits of the dependency of entrainment on Richardson number [Johnson & Hogg (2013) compared their results with those of Christodoulou (1986), Parker <i>et al.</i> (1987) and Ross <i>et al.</i> (2006)].....	26
Figure 3.1: Experimental setup of the horizontal miscible jet.	37
Figure 3.2: Definition sketch of the basin used to perform 3D injection experiment: (a) top view; and (b) side view.....	38
Figure 3.3: Overview of ImageJ software.	40
Figure 3.4: The steps of profile result realization for $R=2778$: (a) the source of images series without motion (<i>img1</i>) (b) the first image (<i>img2</i>) at $t=0$, (c) the Difference result of images series; Difference: $img1 = img1 - img2$, (d) the image after applying the adjust brightness/contrast at $t=2s$, (e) the binary image at $t=2s$, and (f) the skeletonized image at $t=2s$	42
Figure 3.5: Experimental frames captured by difference (row 1), made binary (row 2), and skeletonize (row 3) processes of two dimensional gravity currents performed with initial density $\rho_s = 1040 \text{ kg/m}^3$ and $\rho_{water} = 1000 \text{ kg/m}^3$ for $R=1111$, and frames acquired at (a) $t= 2s$, (b) $t=4s$, (c) $t=6s$, (d) $t=8s$, (e) $t=10s$, and (f) $t=12s$	44
Figure 3.6: Experimental frames captured by difference (row 1), made binary (row 2), and skeletonize (row 3) processes of two dimensional gravity currents performed with initial density $\rho_s = 1040 \text{ kg/m}^3$ and $\rho_{water} = 1000 \text{ kg/m}^3$ for $R=1667$, and frames acquired at (a) $t= 2s$, (b) $t=4s$, (c) $t=6s$, (d) $t=8s$, (e) $t=10s$, and (f) $t=12s$	45
Figure 3.7: Experimental frames captured by difference (row 1), made binary (row 2), and skeletonize (row 3) processes of two dimensional gravity currents performed with initial density $\rho_s = 1040 \text{ kg/m}^3$ and $\rho_{water} = 1000 \text{ kg/m}^3$ for $R=2222$, and frames acquired at (a) $t= 2s$, (b) $t=4s$, (c) $t=6s$, (d) $t=8s$, (e) $t=10s$, and (f) $t=12s$	46
Figure 3.8: Experimental frames captured by difference (row 1), made binary (row 2), and skeletonize (row 3) processes of two dimensional gravity currents performed with initial density	

$\rho_s = 1040 \text{ kg/m}^3$ and $\rho_{water} = 1000 \text{ kg/m}^3$ for $R=2778$, and frames acquired at (a) $t=2\text{s}$, (b) $t=4\text{s}$, (c) $t=6\text{s}$, (d) $t=8\text{s}$, (e) $t=10\text{s}$, and (f) $t=12\text{s}$	47
Figure 3.9: Experimental frames captured by difference (row 1), made binary (row 2), and skeletonize (row 3) processes of two dimensional gravity currents performed with initial density $\rho_s = 1040 \text{ kg/m}^3$ and $\rho_{water} = 1000 \text{ kg/m}^3$ for $R=3333$, and frames acquired at (a) $t=2\text{s}$, (b) $t=4\text{s}$, (c) $t=6\text{s}$, (d) $t=8\text{s}$, (e) $t=10\text{s}$, and (f) $t=12\text{s}$	48
Figure 3.10: Experimental frames captured by difference (row 1), made binary (row 2), and skeletonize processes (row 3) of two dimensional gravity currents performed with initial density $\rho_s = 1040 \text{ kg/m}^3$ and $\rho_{water} = 1000 \text{ kg/m}^3$ for $R=3889$, and frames acquired at (a) $t=2\text{s}$, (b) $t=4\text{s}$, (c) $t=6\text{s}$, (d) $t=8\text{s}$, (e) $t=10\text{s}$, and (f) $t=12\text{s}$	49
Figure 3.11: Original Frames capturing of two-dimensional gravity currents performed with initial density $\rho_s = 1040 \text{ kg/m}^3$ and $\rho_{water} = 1000 \text{ kg/m}^3$ for $R=2778$, and frames acquired at (a) $t=2\text{s}$, (b) $t=4\text{s}$, (c) $t=6\text{s}$, (d) $t=8\text{s}$, (e) $t=10\text{s}$, (f) $t=12\text{s}$	50
Figure 3.12: Dimensional characteristics of salt gravity currents front position versus time for the x and y axes.	51
Figure 3.13: Experimental outer positions of the mixing gravity current at $x_f(y, t)$: a) $R=2222$; b) $R=2778$; c) $R=3333$; d) $R=3889$	53
Figure 3.14: Snapshots with 2D lobes and clefts structures at the front of the intruding gravity current development over a smooth bottom for: (a) $R=1111$, (b) $R=1667$, (c) $R=2222$, (d) $R=2778$, (e) $R=3333$, and (f) $R=3889$ at $t=2, 4, 6, 8, 10$, and 12s respectively.	55
Figure 4.1: The configuration of an injection by a square channel and into fresh water basin.	63
Figure 4.2: Overview of OpenFOAM structure.	64
Figure 4.3: Scheme of the general configuration of OpenFOAM.	65
Figure 4.4: The meshes 3D view.	67
Figure 4.5: Scheme of the boundary conditions of the basin in the numerical model.	69
Figure 4.6: Iso-volume fraction evolution of the saline gravity current jet (x, y) with $\alpha=3\%$ for Run6 ($R=3889$): a) $t=0\text{s}$, b) $t=2\text{s}$, c) $t=4\text{s}$, d) $t=6\text{s}$, e) $t=8\text{s}$, f) $t=10\text{s}$, and g) $t=12\text{s}$	69
Figure 4.7: Numerical frames captured by difference (row 1), made binary (row 2), and skeletonize (row 3) processes of two dimensional gravity currents performed with initial density $\rho_s = 1040 \text{ kg/m}^3$ and $\rho_{water} = 1000 \text{ kg/m}^3$ for $R=3889$, and frames acquired at (a) $t=2\text{s}$, (b) $t=4\text{s}$, (c) $t=6\text{s}$, (d) $t=8\text{s}$, (e) $t=10\text{s}$, and (f) $t=12\text{s}$	70
Figure 4.8: Numerical outer positions of the mixing gravity current at $x_f(y, t)$: a) $R=2222$; b) $R=2778$; c) $R=3333$; d) $R=3889$	72
Figure 4.9: Evolution of spreading with time for: a) $R=1111$, b) $R=1667$, c) $R=2222$, d) $R=2778$, e) $R=3333$, and f) $R=3889$	73
Figure 5.1: Evolution of the experimental (left side) and numerical (right side) mixing gravity current jet from the top view (x, y) for $R=3889$. Experimental (left side) profiles are the treated images of light intensity recorded by the camera $I(x, y)$ and numerical (right side) profiles are the variation of the density.	75
Figure 5.2: Evolution of the numerical density of the mixing gravity current jet from the side view (x, z) for $R=3889$: a) $t=1\text{s}$; b) $t=5\text{s}$; c) $t=11\text{s}$	76
Figure 5.3: a) Evolution of the light intensity of mixing gravity current obtained by the contrast difference using the Rhodamine B as function of x direction, b) Evolution of numerical density of jet as function of x direction at $y=l/2$; $z=0.005\text{m}$; $t=5\text{s}$ for $R = 2778$, and x_f is the front position at $y=l/2$	77
Figure 5.4: Experimental and numerical positions of the mixing gravity current x_f as a function of time for: a) $R=1111$; b) $R=1667$; c) $R=2222$; d) $R=2778$; e) $R=3333$; and f) $R=3889$	78
Figure 5.5: Experimental and numerical continuous of the mixing gravity current $x_f(y, t)$: a) $R=2222$; b) $R=2778$; c) $R=3333$; and d) $R=3889$	79
Figure 5.6: Mean horizontal velocity profile $u(x, z)$ at $y=l/2$	80

Figure 5.7: Dimensionless mean horizontal velocity profile versus the vertical coordinate z/z_0 at $y = l/2$.	81
Figure 5.8: Dimensionless mean excess-density profiles in the (x, z) plane at $y = l/2$.	82
Figure 5.9: Dimensionless mean excess-density profiles.	82
Figure 5.10: Dimensionless mean excess-density profiles in the (y, z) plane at: a) $x/d=20$ and b) $x/d=50$.	83
Figure 5.11: Profiles of the excess-density and velocity in y -coordinate at: a) $x/d=20$, $x/d=50$.	84
Figure 5.12: Gradient Richardson number profiles indicating the increase in stable stratification with downstream distance for $x/d > x_{max}/d$ where $x_{max}/d=50$ for $R=3889$ (run 6).	85
Figure 5.13: Position of Gradient Richardson number Ri_g at 0.25 in the (y, z) plane for different position from the inlet x/d . a, b, c, d, e, f, g, h, i and k represent the position from the inlet respectively for 8, 15, 20, 25, 30, 35, 40, 45, 55 and 60.	86
Figure 5.14: Iso-density evolution of the gravity current jet with $\alpha=3\%$ for Run6 ($R=3889$): a) $t=1s$, b) $t=5s$; c) $t=11s$.	87
Figure 5.15: Evolution of the volume fraction of salt water with time with $\alpha=3\%$ for Run6 ($R=3889$): a) 1s; b) 4s; c) 8s; d) 10s; and e) 12s.	88
Figure 5.16: The fractional volume V/V_0 of total volume to the initial injection volume of the fluid current plotted as a function of the front position run3.	89
Figure 5.17: Fraction volume V/V_0 of total volume to the initial injection volume of the fluid current plotted as a function of the front position for: a) run4, b) run5, and c) run6.	90
Figure 5.18: Fraction volume V/V_0 of total volume to the initial injection volume of the fluid current for different concentrations threshold plotted as a function of position front: a) 3%, b) 20%, c) 35%, d) 45%, e) 55%, and f) 65%.	91
Figure A.1: A plot of the gravity current flow and co-ordinate system.	97
Figure A.2: Two transversal cross section view element	99
Figure A.3: A plot of the inclined gravity current flow.	101
Figure A.4: A plot of the inclined gravity current flow and co-ordinate system.	102
Figure A.5: A plot of the inclined frontal gravity current head flow and co-ordinate system.	103
Figure A.6: A plot of pressure field the inclined gravity current in the ambient fluid.	104

LIST OF TABLES

Table 3.1: Inlet experimental control parameters conditions ($x/d=0$) with $Sc=667$ and $g'_0 = 0.39 \text{ m/s}^2$.	40
Table 3.2: Scaling laws for two dimensions gravity currents: $x = f(t)$, and $y = f(t)$.	52
Table 4.1: The values of the empirical constants in the high Reynolds number of $k - \varepsilon$ model.	59
Table 4.2: Inlet conditions ($x/d = 0$) with $Sc=667$ and $g'_0 = 0.39 \text{ m/s}^2$.	61
Table 4.3: Boundary conditions.	63
Table 4.4: Positions of physical properties of OpenFOAM.	66
Table 4.5: Main keywords used in fvSchemes.	68

ACRONYMS

CFD	Computational Fluid Dynamics
CFM2015	22ème Congrès Français de Mécanique
DNS	Direct Numerical Simulation
FLUVISU2015	16 ^{ème} colloque français sur la Visualisation et le Traitement d'Images en Mécanique des Fluides
ICCOE 2016	The 2016 3rd International Conference on Coastal and Ocean Engineering
ic-rmm2-2015	2 nd International Conference on Rheology and Modelling of Materials
IJET	International Journal of Engineering and Technology
JWARP	Journal of Water Resource and Protection
LES	Large Eddy Simulation
LS-PIV	Large Scale-Particle Image Velocimetry
MTT1956	Morton-Taylor-Turner
ODE	Ordinary Differential Equation
PDE	Partial Differential Equation
PIV	Particle Image Velocimetry
PSFVIP10	10 th Pacific Symposium on Flow Visualization and Image Processing Conference
RANS	Reynolds-Averaged Navier-Stokes
VOF	Volume of Fluid

LIST OF SYMBOLS

Symbol	Definition	Units
σ	surface tension coefficient	N/m
ρ	density of gravity current jet	kg/m^3
ν	molecular kinematic viscosity	m^2/s
μ	viscosity	m^2/s
θ	slop angle of the basin bottom	$^\circ$
ε	dissipation rate of turbulent kinetic energy	m^2/s^3
α	threshold concentrations	-
$\Delta\rho$	excess-density of the mixing	kg/m^3
w_o	initial vertical velocity component	m/s
u_o	initial dense fluid injection velocity (or U_0)	m/s
t	time	s
k	turbulent kinetic energy	m^2/s^2
g	magnitude of gravity acceleration	m/s^2
d	initial depth of the dense fluid channel jet	m
V	volume of gravity current at defined threshold concentration α	m^3
Sc	Schmidt number	-
Ri	bulk Richardson number (or Ri_b)	-
R	initial Reynolds number (or Re_0)	-
Q_o	initial dense flow rate	m^3/s
L	length of experimental basin (l_x)	m
H	depth of ambient fluid (l_z) or (H_0)	m
Fr	initial Froude number (or Fr_0)	-
$C's$	empirical constants (C_{ab})	-

z	vertical spatial coordinate	m
y	lateral spatial coordinate	m
x	streamwise spatial coordinate	m
w	width of experimental basin (l_y)	m
u	mean horizontal velocity	m/s
P	pressure	N/m^2
h	inlet depth of the gravity current jet ($d = l_0$)	m
Δu	difference between mean velocities of both denser and return currents	m/s
\emptyset	fractional height	-
ϑ_f	momentum diffusivity	m^2/s
v_0	initial lateral velocity component	m/s
ρ_{water}	density of fresh water	kg/m^3
ρ_s	density of salt water	kg/m^3
ν_t	turbulent kinematic viscosity	m^2/s
μ_{water}	water viscosity	m^2/s
μ_t	effective dynamic turbulence viscosity	m^2/s
μ_s	saline fluid turbulence viscosity	m^2/s
μ_{eff}	effective viscosity	m^2/s
θ_0	discharge angle to the horizontal	$^\circ$
ε_0	initial dissipation rate	m^2/s^3
Z_f	final terminal height of rise (refers to upper jet boundary)	m
$Z_{0.5}$	height of half the maximum streamwise velocity	m
Z^*	vertical distance of the source-bottom separation from the nozzle	m
x_f	streamwise front position of the gravity current (or X_f)	m
u_{max}	maximum mean horizontal velocity	m/s

t_j	duration (time) of the wall jet phase	s
t_*	certain time	s
k_0	initial turbulent kinetic energy	m^2/s^2
g'_i	impingement visual acceleration of gravity	m/s^2
X_j	radial extent/length of the wall-jet	m
X_{im}	distance from the source and impinges at an angle θ to the horizontal	m
V_0	volume of saline water injected	m^3
U_i	initial dense fluid injection velocity	m/s
S_{ij}	interface point	m
Sc_t	turbulence Schmidt number	-
Ri_g	gradient Richardson number	-
Q_i	impingement dense flow rate	m^3/s
P_{atm}	atmospheric pressure	N/m^2
N^2	buoyancy frequency	s^{-2}
M_i	impingement momentum flux	m^4/s^2
M_0	initial momentum flux (mass flux)	m^4/s^2
L_Q	source length scale	m
L_M	momentum jet length scale	m
D_m	mass molecular (diffusivity) of the injected saline fluid	m^2/s
$C_{\sigma\varepsilon}$	dissipation rate empirical constant	-
$C_{\sigma k}$	turbulent kinetic energy empirical constant	-
C_μ	turbulent viscosity empirical constant	-
B_i	impingement buoyancy flux	m^4/s^3
B_0	initial buoyancy flux	m^4/s^3
Γ_w	solid wall boundary condition	-

Γ_{out}	outlet boundary condition	-
Γ_{in}	inlet boundary condition	-
h_i	impingement depth	m
h^*	non-constant depth	m
$\Delta\rho_{max}$	maximum mean excess density	kg/m^3
g'_0	initial visual acceleration of gravity at the injection source	m/s^2
N	frequency of the buoyancy oscillation (Brunt–Väisälä frequency)	$1/s$
U	characteristic velocity	m/s
E_T	entrainment of the tail	-
\bar{w}_E	entrainment velocity into the tail (or w_e)	m/s
$\Delta\psi$	growing in transport of the density current over the length of the tail	m^2/s
l	length of the tail section	m
E_H	entrainment in the head	-
E	total entrainment quantitatively of ambient fluid into gravity current	-
A_{total}	total area of dense fluid	m^2
A_0	total area that has entered the domain	m^2
z_{max}	maximum rise of the plume height	m
w_{ei}	bulk entrainment at high Richardson number	-
Q_{ei}	bulk entrainment discharge	m^3/s
E_a, E_b, E_p	total, background, and potential energies	$kg \cdot m^2/m^2$

Chapter 1: Introduction

1.1 Gravity currents

The subject of this dissertation is Experimental and Numerical study of Model Gravity currents in Coastal Environment “Bottom Gravity Currents”. Gravity currents, sometimes called density currents or buoyancy currents, are flows generated by a density gradient between two fluids and occur in both natural and industrial flows. The density differences can be due to the variations in salinity, temperature, or concentration of suspended particulates (Benjamin 1968, and Simpson 1997). The flow of a gravity current is predominantly horizontal. It can occur as either a top or bottom boundary current, or as an intrusion at some intermediate level. The spreading of one fluid into another fluid of a lower density, due to the horizontal density difference, is significant for many geophysical and industrial applications. Natural examples include sea breezes, avalanches (Allen 1982), estuaries (where fresh water meets salt water), surges from volcanoes, thunderstorm outflows, and sand storms (Bagnold 1941). Man-made examples include the accidental release into the atmosphere of dense gasses, early stages of an oil spillage (Kubat et al. 1998), etc. They can be either toxic or poisonous. Fig. 1.1 shows some examples of cases cited earlier.

In his theoretical work, Von Kàrmàn (1940) proposed a perfect-fluid model for steadily gravity currents propagation as a first calculation. Also, he used an inviscid analysis to predict the front speed and interface shape of a gravity current flowing under an infinite ambient fluid. Von Kàrmàn’s (1940) work was updated by Benjamin (1968). In Simpson’s (1997) book a comprehensive description of gravity current flows in both environmental and laboratory fields can be found. Huppert (2006), and Ungarish (2009) give excellent reviews on the conceptual foundations used to understand and evaluate the evolution of gravity currents. Bottom and free-surface gravity currents are produced by a multitude of municipal, agricultural, domestic, and industrial fluid buoyant jet discharge operations. These currents are a vital source of environmental concerns in that they present a typically adverse effect on the water quality, underwater flora and fauna, and the benthic environment. For example, bottom gravity currents generated by the buoyant sediment-laden jet disposal in coastal dredging and disposal operations can significantly affect the surrounding aquatic environment (Nichols & Thompson 1978, and Hales 1996). Because of the density difference between fluids produced by dissolved substances (i.e. salt), the current is conservative since the total mass of the dissolved substance is conserved. Variations in density in such currents are only due to entrainment of ambient fluid (Nogueira 2013c).

The turbidity currents, which are sediment-laden underflows driven by a density difference between the ambient fluid and saline density currents, are examples of gravity currents. The driving buoyancy forces are simply due to the presence of suspended particles getting a turbidity current. The lower current, which is formed inside an intrusive turbidity gravity current at some neutrally buoyant intermediate depth, depends upon the volume fraction of both fluids. Furthermore, particle settling can lead to complete buoyancy reversal, the initiation of a buoyant plume, and the subsequent creation of a surface gravity current in which the few remaining particles play no role in the dynamics of the flow (Montgomery & Moodie 1999).



Figure 1.1 : Examples of gravity currents in the environment: (a) Treatment wastewaters are rejected in the St. Lawrence River (Montréal). (b) A plume of acidic aluminum-rich water in the Manning River (Australia). (c) and (d) Sand storms are examples of buoyancy driven gravity currents in the atmosphere of specific interest is how ground friction affects speed of propagation and mixing in gravity currents in Iraq, 2015. (e) Gravity currents, in the form of pyroclastic flows, propagate down the flanks of the volcano in Mayon, Philippines, 1984. And (f) avalanche from Hunza Peak, Karimabad, in Pakistan.

1.2 Statement of the problem

Various municipal, agricultural, domestic, and industrial liquid discharge into lakes, estuaries, reservoirs, rivers, seas, and oceans. Most waste water, heated water from power plants, brine slurry from desalination plants, and dredged mud slurry are routinely released both intentionally and accidentally. In many of these operations, the discharges occur through a submerged round outfall into the receiving waters. The gravity currents were investigated in a 2D configuration experimentally and numerically in several previous works (e.g. Turner 1973, Simpson & Britter 1979, Huppert & Simpson 1980, Rottman & Simpson 1983, Hallworth *et al.* 1993 & 1996, Winter *et al.* 1995, Hacker *et al.* 1996, Shin *et al.* 2004, Lowe *et al.* 2005, Ungarish 2007, and 2009, Nogueira *et al.* 2013a, Fragoso 2013, among others). There are only few studies devoted to the 3D mixing gravity current (Özgökmen *et al.* 2004a, Chang *et al.* 2005, Ilicak 2014, and Ottolenghi *et al.* 2016a, b & 2017).

The primary motivation behind this work in my dissertation is a study of both 2D and 3D dense bottom gravity currents propagation on a smooth bed, experimentally and numerically respectively. Also, it provides fundamental knowledge for the flow characteristics of the environmental impacts associated with the dense gravity current phenomenon. To our best knowledge, studies focusing on the mixing of the gravity flow in 3D jet configurations for the weak turbulent regime are very few. Notably, in all these studies cited previously, four key issues were not addressed: i) the dynamics of a 3D gravity current jet, ii) the hydrodynamic and density distributions of a 3D gravity current jet, iii) the turbulent mixing in a 3D gravity current jet for the weak turbulent regime, and iv) the entrainment of a 3D mixing gravity current jet.

These four issues contribute to the internal structuration of the spatiotemporal evolution of a 3D density current in a miscible ambient fluid. Fulfilling that gap constitutes the motivation of the present work. In this dissertation, RANS with $k-\varepsilon$ and diffusion-convection equations were used to model the 3D propagation and mixing of a saline gravity current into the ambient fresh water over a smooth horizontal bottom. The dynamics of the gravity current obtained by that numerical model and experimental studies present a good agreement. The Reynolds number R and the Richardson number Ri vary in the intervals [2222, 3889] and [0.003, 0.01] respectively. The mean flow profiles of the velocity and density obtained by the numerical simulations are used to calculate the gradient Richardson number Ri_g with the distance from the inlet. The spatial evolution of Ri_g can give the turbulent mixing zone following the criterion value of Turner (1973). The entrainment estimates the characterization of the mixing process at different values of the iso-density threshold with the front position.

1.3 Methodology

In our example of gravity currents, such as the spreading of a dense gravity current jet, the flow over the smooth bottom of the calm ambient fluid is turbulent. Small scale mixing processes between the ambient fluid and the dense fluid, due to turbulence, are important to the dynamics of the flow. As a result of the complication of the flow in a gravity current, it is difficult to understand the flow development. There are several approaches which can be used to solve this problem. The first approach is the state of the art, in order to develop a comprehensive look of the bottom gravity currents moving forward with front velocity. The resulting gravity current propagation calculation were deduced from experimental studies. The gravity current head was neglected because is very small and very difficult for Newtonian gravity currents to handle. Furthermore, investigations of the horizontal injection gravity currents propagation were presented in the state of the art.

The second approach for studying problems involving gravity currents, which complements the bibliography work, is the use of experiments. These can be small scale jet gravity currents experiments in the laboratory. The experiments or measurements of jet flows, include all the details of the flow and can be used to obtain values for experimental parameters in the numerical model, as well as checking if the model gives reasonable predictions. Experiments are the only means to provide a full study of the weak turbulent high Reynolds number flows.

The third approach which is numerical, aims at characterizing the mixing of fresh and saline waters by applying the Reynolds-Averaged Navier-Stokes equations (RANS), K-epsilon ($k-\epsilon$) and the Diffusion-Convective equation (DCE) of the volume fraction. It also compares the mean flow profiles by RANS with measurement results, and calculates the Richardson number Ri_g as a factor representing the turbulent mixing zone. Consequently, this third approach examines the effects of volume ratio with time, as well as the quantity and the concentrations of mixed fluid produced leading to entrainment as a function of threshold with time were investigated. The use of simple scaling arguments for the bulk motion of the fluid gives some insight into the physical processes involved in the jet flow.

The two-dimensional gravity currents experiments play a valuable role with the three-dimensional gravity currents numerical model, and often give a good agreement in the x-axis and y-axis. Mixing is generally included through some form of parameterization, but it is currently limited to moderate Reynolds numbers by the computational requirements.

1.4 Outline of dissertation

The dissertation is organized in six chapters and two appendices. In this chapter, an introduction to gravity currents was provided, where the main motivation and objectives of this work were presented. Chapter 2 provides a review of the previous literature and the main contributions to date on bottom gravity currents. Specific topics are covered by this dissertation, and important experimental, theoretical, and numerical results are described. In Chapter 3, the use and applicability of laboratory experiments to saline gravity current jet flow over a rigid, and smooth horizontal bottom into the lighter fluid is discussed. The different experimental apparatus, techniques, and image processing used in this work are described in detail, as well as comparison between results of experiments.

In Chapter 4, a numerical model for the flow of the saline gravity current jet into the ambient fresh water in a basin and axisymmetric gravity currents is developed. The Reynolds-Averaged Navier-Stokes (RANS) and the diffusion-convection equation of the volume fraction of the saline water are used to model the mixing and the propagation of the saline gravity current. Chapter 5 presents the main results arising from the experimental measurements and numerical computations of the numerical model, then validated by comparing the predictions with the experimental results. In Chapter 6, the main conclusions of the present research are drawn and suggestions and recommendations for future works are given.

Two appendices are included at the end of the dissertation, complementing the information presented in Chapters 3, 4, and 5. Appendix A representing the development of Huppert's theory: solution of Newtonian gravity current equations, whereas Appendix B includes the equations relating to the solution of non-Newtonian gravity current (Rheology). Two solutions give additional details of the equations relating to the bottom gravity current beneath a static water layer at rest in the horizontal and inclined basin.

1.5 Original contributions

A number of contributions emerged during these four years of research, either by papers published (or submitted) in peer-reviewed journals or by papers published in conference proceedings, these are listed below:

- Dhafar, I. A., Latrache, N., and Nsom, B. (2015a). Applied the Large-Scale Particle Image Velocimetry Technique for Measurement the Velocity of Gravity Currents in the Laboratory. DOI: 10.4236/jwarp.2015.78048, Journal of Water Resource and Protection 07(08):597-604.

- Dhafar, I. A., Latrache, N., and Nsom, B. (2015b). Image processing applied to characterize the denser gravity current propagates over rigid surface into the lighter fluid. 10th Pacific Symposium on Flow Visualization and Image Processing Conference, Naples, Italy, 15-18 June.
- Dhafar, I. A., Latrache, N., Niang, P., and Nsom, B. (2015c). Etalement d'un jet horizontal miscible de flottabilité positive. 22ème Congrès Français de Mécanique, Lyon, France, 24 au 28 Août.
- Dhafar, I. A., Nsom, B. and Latrache, N., (2015d). Effect of slope change on the dynamics of pseudoplastic mass movements beneath a static volume of water, ic-rmm2-2 nd International Conference on Rheology and Modelling of Materials, Miskolc-Lillafüred, Hungary, 5-9, October.
- A prize of Doctoral School of Marine Sciences (EDSM) worth 1300 € by my presentation of the poster entitled: Experimental and Numerical Study of Model Gravity Currents in Coastal Environment. The days of the Doctoral School of Marine Sciences (EDSM) were held on 5 and 6 November 2015e.
- Dhafar, I. A., Latrache, N., and Nsom, B. (2015f). Mesure de vitesse par PIV à grande échelle d'un écoulement de courant gravitaire d'un liquide léger à la surface libre d'un liquide dense. 16ème congrès français du Club FLUVISU (« Visualisation et Traitements d'images en Mécaniques des Fluides pour l'Industrie »), associé au 14ème colloque international francophone du Club CMOI (« Contrôles et Mesures Optiques pour l'Industrie»). Lannion, France, Du 16 au 20 novembre.
- Dhafar, I. A., Latrache, N., and Nsom, B. (2016). Experimental Study of the Effect of the Spreading Buoyant Gravity Current on the Coastal Environment. The 2016 3rd International Conference on Coastal and Ocean Engineering (ICCOE 2016), Tokyo, Japan, 8-9, April.
- Dhafar, I. A., Latrache, N., and Nsom, B. (2017a). Experimental Study of the Effect of the Spreading Buoyant Gravity Current on the Coastal Environment. DOI: 10.7763/IJET.2017.V9.957. International Journal of Engineering and Technology, 09(02):129-132.
- Dhafar, I. A., Latrache, N., and Nsom, B. (2017b). Mixing of Saline gravity Current Jet into Fresh Water in the Weakly Turbulent Regime (under review).

Chapter 2: Literature Review

Many studies investigated gravity currents using both laboratory experiments and numerical simulations. The aim of this chapter is to provide a review of some literature centered on gravity currents that are relevant to this dissertation, and specifically related to the dense gravity current phenomenon. As discussed in Chapter 1, various municipal, agricultural, domestic, and industrial liquid discharge in the sea or ocean incredibly cause adverse environmental impacts via the formation of gravity currents. In section 2.1, the classification of gravity currents, then, the structure of the bottom gravity currents in section 2.2 are summarized. Section 2.3 presents the dispersion characteristics of buoyant gravity current jet discharges. Entrainment and mixing gravity currents are described in section 2.4, while the section 2.5 includes the numerical modeling. The discussion is mostly focused on the process of interest of this investigation “bottom gravity currents”. However, many of the concepts, results, and conclusions of studies concentrate on a gravity current flow composed of a different medium are advantageous in this analysis.

2.1 Classification of gravity currents

A gravity current is a flow of a fluid with density ρ_1 within an ambient fluid of different density, ρ_2 . The density gradient between fluids in such currents is primarily horizontal. The flows generated by vertical density gradients as a plumes are not within the scope of the present study. According to the different density types of the current and the ambient fluid, gravity currents can be classified as bottom currents (Fig. 2.1), when the current is denser than the ambient fluid, $\rho_1 > \rho_2$; top currents, if the density of the current is lower than the ambient fluid, $\rho_1 < \rho_2$; or intermediate currents, when the current has intermediate density value when compared to the stratified ambient fluid, $\rho_{2a} < \rho_1 < \rho_{2b}$. The total depth of the two fluids is H , and non-constant depth h^* moves forward with front velocity U_f into the surrounding fluid with the lower density ρ_2 . Moreover, gravity currents can be categorized as *compositional* or *particle-driven* gravity currents. In the case of compositional gravity currents, the driving force appears in dissolved solute like salt in the sea or difference of temperature. While for particle-driven gravity currents, the driving force is represented by the suspension of sediments. In a compositional gravity current, the current is conservative since the total mass of the dissolved substance is conserved. Variations in density in such currents are only due to entrainment of the ρ_1 , ρ_2 ambient fluid.

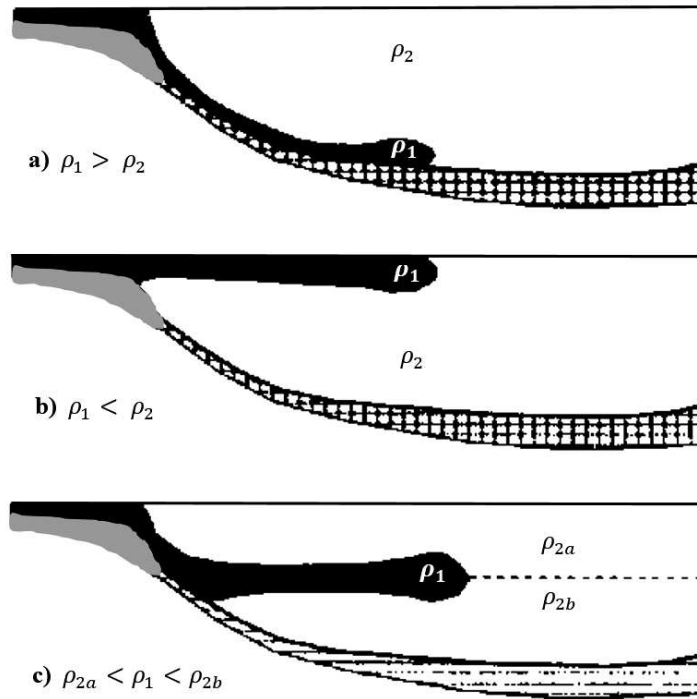


Figure 2.1: Schemes as example of possible density flow patterns for a gravity current discharge into the water bodies ρ_1 intruding in the ambient fluid with uniform density ρ_2 , and $\rho_{2a} < \rho_1 < \rho_{2b}$: a) underflow gravity current, b) overflow gravity current, and c) interflow gravity current (Morris & Fan 1998, and Cesare *et al.* 2006). In this study: $\rho_1 = \rho_{saline}$ and $\rho_2 = \rho_{water}$.

Gravity currents, of a high Reynolds number flow rate, are unsteady, turbulent, and tend to entrain ambient fluid. For instance, when gravity currents can entrain particles from the bed and deposit suspended material, changing the total amount of particles in the flow. The results of such entrainment, and the resulting dilution of the original intruding fluid, can be quite important. For example, many industrial pollutants are discharged into the atmosphere or hydrosphere with a contrasting density to their ambient surroundings. The dilution with distance of any resulting gravity currents by entrainment has important implications for toxicity levels and the degree and extent of contamination (Hallworth *et al.* 1993 & 1995). In the following, a summary for relevant bottom gravity current classifications related to this dissertation, will be presented. The dynamics of gravity current jets are developed following different phases: the first phase is the balance between the radial momentum flux and the rate of change of the inertial force and is characterized by a constant speed front (Chen, 1980). While the second phase (inertia regime) is characterized by the equilibrium between inertia and buoyancy forces, and the third phase (viscous regime) by the equilibrium between viscous and buoyancy forces (Hoult, 1972, Huppert & Simpson 1980, and Huppert 1982). The internal flow structure of density currents is a key issue for understanding the spatiotemporal evolution of the mixing or entrainment of the ambient fluid into the head of the current during its propagation.

2.1.1 Density ratio of current to ambient fluids

Benjamin (1968), Rottman & Simpson (1983), Haertel *et al.* (2000), Marino *et al.* (2005), and Ungarish & Zemach (2005) discussed the term of Boussinesq flows, which correspond to a small density difference between fluids. The density difference is mostly driving a high flow of the initial density jumping across the interface. The differences in the structure and shape of a gravity current depend on the ratio of initial density between the dense and the light fluids. When the two fluids densities are comparable (approximately equal), the progress of the gravity current helps understanding the presence of the ambient fluid, which imposes a significant resistive force on the intruding current. However, Birman *et al.* (2005), Etienne *et al.* (2005), Lowe *et al.* (2005), Ungarish (2007), and Bonometti *et al.* (2008) focused of the cases in which the current density is much higher than the ambient one. In the case of a dam break flow in which water spreads in the air, the current is not affected by any resistance from the surrounding ambient. Typically, the density difference is small enough for the Boussinesq approximation to be valid. The Boussinesq approximation is applied to problems where the fluid varies in temperature from one place to another, driving a flow of fluid and heat transfer. The Boussinesq gravity current acquires shape with a head, and a body as shown in (§2.2-Fig.2.2), while the thickness of a non-Boussinesq current decreases monotonically while approaching the ambient fluid, reaching a minimal value at the front of the current. Also, the current acquires a final height at which the flow is reversed, and returns to the bottom where it spreads as a gravity current. The brines produced from the desolation process are usually discharge into coastal waters as an example of denser current injection into lighter ambient.

2.1.2 Density difference of current and ambient fluids

The difference in density between the gravity current and ambient fluids is due to temperature, concentration, or compositional (different fluids completely) variations, or as an outcome of particles suspended. Bonnecaze *et al.* (1993), Hallworth & Huppert (1998), Gladstone *et al.* (1998), and Necker *et al.* (2002) characterized the case of a particle-laden current. Fresh water (lighter fluid) exits from a river into the ocean (dense liquid), it flows along the surface, partially due to the difference in salinity between fresh and saline water as shown in Fig. 2.1b. The turbid mixture spreading on the seafloor represents an example where the excess density in the current comes about from the suspension of sediments as shown in Fig. 2.1a. In a non-mixing case, the density of a particle-laden current continues to develop in space and time as a result of the continuous deposition of particles and possible re-entrainment back into the flow (if the current is energetic enough).

2.1.3 Continuous release with finite volume

Simpson (1972), Huppert & Simpson (1980), Bonnetcaze *et al.* (1995), Hacker *et al.* (1996), Gladstone *et al.* (1998), Shin *et al.* (2004), and Cantero *et al.* (2007a) described the gravity current as a finite release. Following their description, a fixed volume of fluid is suddenly discharged into an ambient environment of a different density. Whereas Garcia & Parker (1993), Hogg *et al.* (2005), Sequeiros *et al.* (2009), and Shringarpure *et al.* (2012) described a continuous release. Based on the source configuration, there are two major types of gravity currents: constant-volume (or fixed-buoyancy) and continuous-flux (or continuous-buoyancy). Constant-volume gravity currents are generated in the laboratory through the use of a lock-exchange tank (Chowdhury & Testik 2014). As a rule, the current release is produced from a large tank with a time-dependent flux q as $q = q_s t^s$, where q_s is a positive constant, t is the time of positions, and s is an exponent either positive (waxing release), negative (waning release) or null (fixed, limited volume release). The limited release is observed when the sides of a container suddenly collapses releasing the embodied fluid instantaneously, while a continuous release can be the consequence of a small rupture along one of the edges of a large container or a pipeline leading to a continuous discharge of material. The fluid spreading due to a constant source of buoyancy on the surface or the bottom of a calm ambient was investigated experimentally and theoretically. Britter (1979), Chen (1980), Didden & Maxworthy (1982), Huppert (1982), and Lister & Kerr (1989) provided the estimation equations of the axisymmetric gravity current radius as a function of time, and source flow parameters (see §§2.3.1).

2.1.4 Geometrical limitations

In general, the gravity currents are studied in one of two geometric constraints, in particular the planar and the axisymmetric setups. These configurations are widely searched due to their simplicity on the contrary of my dissertation case. Experimental and numerical studies provide an easily construct and a more flexible challenge for modeling aims (Shallow Water equations and Box Model). The planar release case, a flat rectangular gate at first separates a rectangular reservoir of fluid from an ambient with lower density. As well, at the start of the axisymmetric three-dimensional release case, the current is confined inside a hollow circular cylinder at the center of a large tank containing the ambient fluid (Huppert 1982, and Cantero *et al.* 2007b). Huppert & Simpson (1980), and Cantero *et al.* (2007a) was investigated the small angle of expansion typically $10\text{-}15^\circ$ by an expanding inside the tank.

The gate would be partially lifted up, and the restricted fluid would be continuously fed to maintain the desired volumetric discharge rate as a continuous release. The setup of the planar case used of as a two-dimensional releasing since the current is confined to move in a specified direction. While for the set-up of the circular discharge case, the current would spread radially outwards (in all directions) but remains axisymmetric because of the fundamental circular nature of the release.

2.2 Bottom gravity currents structure

Bottom gravity currents are formed by a head region at the front, which is usually deeper than the following tail. It advances into the ambient fluid and it is followed by the body or sometimes a tail (Kneller & Buckee, 2000). Although some mixing usually occurs at the head, the clear distinction between the gravity current and the ambient fluid typically remains. During propagation, the mass and momentum balance in the head differs significantly from in the body (Middleton 1993). The head must displace the stationary ambient water resulting in a greater thickness than the trailing body. As shown in Fig.2.2, a cross-section of 2D gravity current along a horizontal bottom surface, generated by a constant buoyancy flux ‘constant-volume release’ (see §§ 2.1.3) at the left end could be considered. It propagates with a distinct dividing line making a body, a head or/and a front.

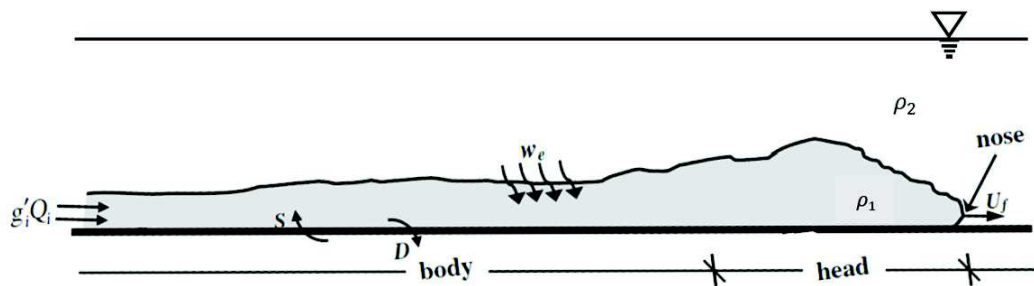


Figure 2.2: Structure Scheme of a bottom gravity current (Chowdhury & Testik 2014).

Generally, the front part of this current, which is deeper/thicker than the body, is known as the head of the gravity current (Britter & Simpson 1978). The symbols: S represents the particle erosion from the bottom, D particle deposition from the gravity current, U_f velocity of the front, w_e entrainment velocity into the current, ρ_1 density of the current, and ρ_2 density of the ambient water (Chowdhury & Testik 2014). The frontal zone of a propagating saline gravity current had been investigated in a number of previous studies (e.g. Simpson 1969, Fleischmann *et al.* 1994, Härtel *et al.* 2000a & b, La Rocca *et al.* 2008, and Ottolenghi *et al.* 2016a, b & 2017). The following sections focus on the structure of the bottom gravity currents propagation over a horizontal bed.

2.2.1 Distribution of bottom gravity current concentration

For a Newtonian fluid, the experimental measurements of concentration profiles revealed the existence of two main types. For constant-flux release-inertial gravity currents: the smooth profile and the stepped profile are shown in Fig. 2.3a and b respectively (Chowdhury & Testik 2014). In one of the earlier studies on gravity currents, Ellison & Turner (1959) studied concentration profiles in constant flux gravity currents as shown in Fig.2.3a. They observed a decline concentration gradient near the bottom boundary that fell off rapidly near the height of the velocity maximum. Garcia (1993 & 1994) found a layer of nearly constant density extending up to the velocity maximum then decreasing dramatically in the vertical direction as shown in Fig.2.3b. While, for a non-Newtonian fluid, Van Kessel & Kranenburg (1996) observed a lutocline profile for high concentration fluid of mud gravity currents which they attributed to the Bingham rheology of the liquid mud as shown in Fig2.3c. It is similar to the stepped profile presented in Fig.2.3b.

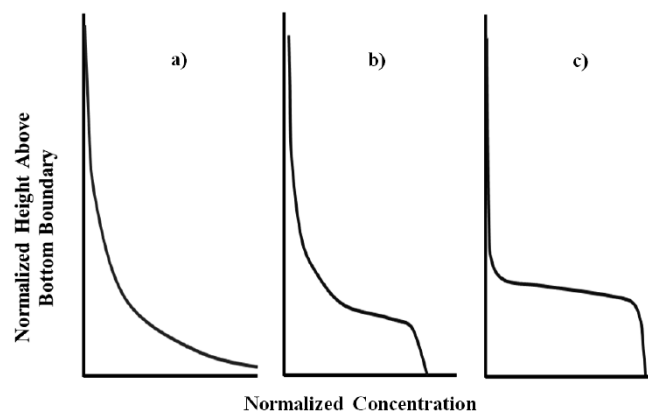


Figure 2.3: The mean concentration profiles found in previous literature; a) Smooth profile, b) Stepped profile, and c) Lutocline profile [Jacobson & Testik (2014) and Kneller & Buckee (2000)].

Three-Dimensional unsteady flow characterizes the gravity current head. Two types of turbulence structures of instability which govern the mixing processes are the Kelvin-Helmholtz instability on the one hand and lobes and clefts on the other hand (Simpson 1969, 1972, 1997, Allen 1971, Britter & Simpson 1978, Chowdhury *et al.* 2009, and Peng & Lee 2010). Kelvin-Helmholtz billow (wave) are generated in the interfacial region, at the rear of the current head, and roll up as the current advances. They remain quasi-steady in the current body, disappearing away due to continuous mixing with the surrounding fluid. Lobes and clefts produced by a convective instability formed at the first region of the head, are caused by the incorporation of less dense fluid by the current head during its propagation which is a direct result of the no-slip boundary condition at the bottom boundary such as a rigid surface.

2.2.2 Distribution of the velocity in a bottom gravity current

The general form of the mean velocity profile in a typical inertial gravity current flow consists of a thinner inner region (near-basin wall) and a thicker outer region, both regions are separated by the maximum velocity as shown in Fig.2.4. The inner region has a positive velocity gradient and behaves similarly to a conventional turbulent boundary layer. The outer area has a negative velocity gradient that acts as a shear layer. The vertical position of the velocity maximum is controlled by the ratio of drag forces at the upper interface and the lower boundary (Middleton 1993 and Chowdhury & Testik 2014).

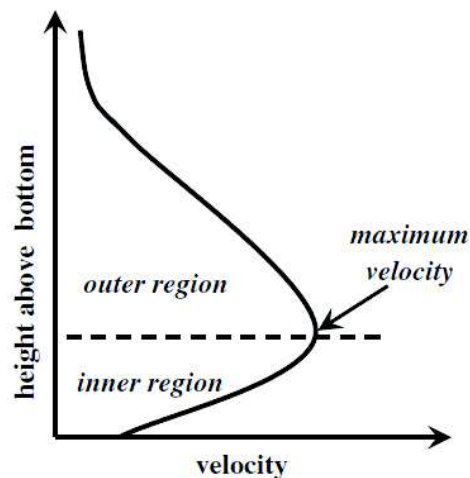


Figure 2.4: The mean velocity profile of a constant-flux release two-dimensional gravity current, the x- and y-axis values are normalized (Kneller & Buckee 2000, and Jacobson & Testik 2013).

Prandtl theory (1952), concerns the transient phase (see §2.4.2) following the release of dense fluid in a low surrounding fluid with lower density. Neglecting hydrostatic forces and applying the hypothesis, which formed a roll at the rear of the head of the current, does not fall backwards. He obtained the ratio of the propagation velocity to the flow velocity by the evaluation of the dynamic pressures against the front. Prandtl's theory can be only applied to the "transient phase" during which the confluence between the two fluids occurs after opening the injection orifice partly. The roll formed at the rear of the head of the currents fell behind and entrained with the lower layer, developing a turbulent motion at the front. After this stage of development, a state of stationary propagation takes place. Then the turbulent motion is confined to the head of the current, and the ratio of the propagation velocity to the flow velocity must be 1 (Benjamin 1968).

2.3 Dispersion of discharges of buoyant gravity current jet

Buoyancy forces are the engine for gravity current propagation. These forces are in turn counterbalanced by inertia as well as resistance due to Reynolds stress and viscous drag, both acting at the upper and lower boundaries of the current. When the propagation velocity decreases, viscous stresses become significant and counterbalance buoyancy as well (Nogueira 2013c). The developed gravity currents is typically an unsteady phenomenon, i.e., the current kinematics and the internal density distribution are time varying. Many buoyant jet discharge configurations can be found. Only the four following ones, which concern our study, are presented. Firstly, the vertical positively downward discharges of denser fluids (Fig. 2.5a). Secondly, the vertical negatively upward discharges of lighter fluids (Fig. 2.5b). Thirdly, the inclined negatively upward discharges of dense fluids at an angle, θ_0 to the horizontal (i.e., the angle between the discharge axis of the outlet and the horizontal, $\theta_0 = 0$ to 90°) (Fig. 2.5c). And fourthly, the discharge at an angle of a positively buoyant jet with similar source and ambient conditions (Fig.2.5d).

For the downward or upward discharges (with $\theta_0 = 90^\circ$), the descending (Fig. 2.5a) and rising (Fig. 2.5b) entrain ambient water of buoyant jets, expand in the water column, and eventually impinge on either the bottom or free-surface boundary. In the angled discharge configurations (Fig. 2.5c), the negatively buoyant jet of the dense fluids first rises to its high elevation over the port of discharge and then retreats in the water column to impinge on the lower boundary. A positively buoyant jet is caused from the impingement at an angle (Fig. 2.5d). The flow spreads initially as a short-lived wall jet before becoming a gravity current, when the impingement redirects the flow of the discharge as a radial outflow.

The flow spreads in x-axis, y- axis, and z-axis near the impingement point as a gravity current, i.e. a dense layer propagates horizontally on the bottom. The downward flow, after the location of the ultimate height, accelerates since the buoyancy now effects in the flow direction (Chen 1980, Moursi *et al.* 1995, Kotsovinos 2000, Lawrence & Maclatchy 2001, Papakonstantis & Christodoulou 2010 and Chowdhury & Testik 2014). In laboratory experiments, gravity currents are studied by releasing a dense fluid into a lighter fluid by the lock-exchange technique or using a continuous source with a constant inflow rate such as a jet (Nogueira *et al.* 2014, Lombardi *et al.* 2015, Cenedese and Adduce 2008, and Ottolenghi *et al.* 2017). In 2D-flow theory, box models or shallow-water theory can describe the dynamics of the front and the height of the gravity currents (Hoult 1972, Huppert & Simpson 1980, and Huppert 1982).

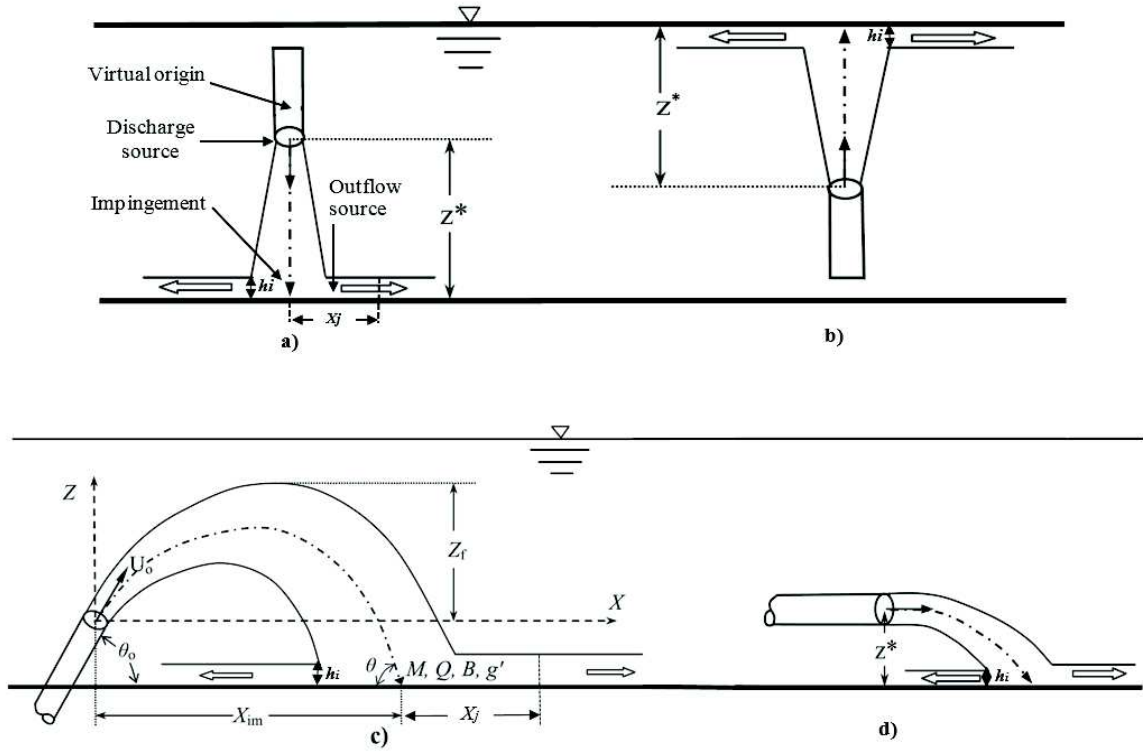


Figure 2.5: Schematic of flow a) a vertical positively downward discharge of the denser (than ambient water) fluids, b) a vertical negatively upward discharge of lighter fluids, c) the angled upward negatively discharge of denser fluids and d) a horizontal positively discharge of denser fluids (Papakonstantis & Christodoulou 2010 and Chowdhury & Testik 2014).

2.3.1 The flow conditions

The flow conditions (e.g., flow rate, buoyancy flux, and momentum flux) at the outflow source (see Fig. 2.5a) serve as the parameters of origin for the gravity current. These parameters effect significantly the current dynamics (Papakonstantis & Christodoulou 2010 and Chowdhury & Testik 2014).

For the injection (discharge) in Fig.2.5 (presented above), a fluid with a density of ρ_1 was injected at a velocity U_0 from an injection source with a radius d_0 , into an ambient water at a depth of H with a density of ρ_2 . The main parameters at the injection source are the initial specific volume flux, Q_0 [$Q_0 = \pi U_0 d_0^2 / 4$]; the initial specific momentum flux, M_0 [$M_0 = U_0 Q_0$]; the initial specific buoyancy flux, B_0 [$B_0 = g'_0 Q_0$]; and the density metric Froude number, Fr_0 [$Fr_0 = U_0 / \sqrt{g'_0 d_0}$], where $g'_0 = g(\rho_1 - \rho_2) / \rho_2$ is the reduced acceleration of gravity at the injection source (Fischer *et al.* 1979).

According to (Papakonstantis & Christodoulou 2010), the spreading is an unsteady problem since the gravity current develops with time and the outer boundaries changes, i.e. for a certain position x , while $y = y(t)$, the radial distance R can be expressed by:

$$R(t) = (x^2 + y(t)^2)^{1/2} \quad (x=\text{constant}) \quad (2.1)$$

Four regimes are shown in the growing period of the gravity current, which may not be present, depending on the flow conditions. Using the force balance method and considering the first leading and resistance forces, according to Chen (1980) and Kotsovinos (2000), the following regimes of radial spreading are expected, as time t from initiation of spreading increases:

- I. For small times, assuming the radial momentum is dominant and neglecting other variables, dimensional analysis, leads to (Chen 1980):

$$C_1 = R(t)/(M^{1/4}t^{1/2}) \quad (2.2)$$

where C_1 represents a constant of the experiment.

- II. For a slightly longer period of times, the balancing between the radial momentum flux and the inertial force changes rate (Kotsovinos, 2000):

$$C_2 = R(t)/[(M/Q)t] \quad (2.3)$$

where C_2 represents a constant of the experiment. Ansong *et al.* (2008), studied the regime of constant velocity, which is controllable by both momentum and buoyancy.

- III. After that, the balancing between buoyancy and inertia forces gives (Chen and List, 1976):

$$C_3 = R(t)/(B^{1/4}t^{3/4}) \quad (2.4)$$

where C_3 represents a constant of the experiment. Eq. (2.4) shows the spreading when buoyancy is higher than the radial momentum, and the inertia is more important than the viscous drag. The relation $R \sim t^{3/4}$ was found to characterize initially the radial spreading studied by Chen and List (1976) and Britter (1979) and was also confirmed by Kotsovinos (2000) and Ansong *et al.* (2008).

- IV. Finally, the equilibrium between buoyancy and viscous drag force implies:

$$C_4 = R(t)/[(g'Q_0^3/\nu)^{1/8}t^{1/2}] \quad (2.5)$$

where C_4 represents a constant of the experiment and ν is the kinematic viscosity of the fluid. Eq. (2.5) predicts the manner of the gravity current spreading, when the viscous drag producing from boundary or interfacial shear is higher than the inertia (Huppert 1982).

2.3.2 Buoyant jet length scales

Three relevant length scales determine buoyant jet behavior in Fig. 2.5. In Fig.2.5a and b; the source length scale:

$$L_Q = Q_0 M_0^{1/2}, \quad (2.6)$$

the momentum jet length scale:

$$L_M = M_0^{3/4} / B_0^{1/2}, \quad (2.7)$$

and the source-bottom separation distance:

$$z^* = h_d + z_0 \quad (2.8)$$

where, h_d is the vertical distance from the discharge source to the impingement point, and z_0 is the vertical distance from the discharge source to the virtual origin. Determining whether a buoyant jet discharge shows either a plume-like or jet-like behavior at the impingement location is important as it may dictate the conduct of the radial outflow. For example, if the discharge occurs in very shallow waters, the buoyant jet may impinge the bottom as an energetic jet, with the outflow spreading as a wall jet for an extended period and distance. Similarly, a shorter wall jet may be expected for the plume-like impingement (Chowdhury & Testik 2014).

The dynamics of the angled and horizontal discharge configurations (Fig. 2.5c, and d) are more complex than the other two as the impingement occurs at a radial distance X_{im} from the discharge source ($X_{im} = 0$ in Fig. 2.5a, b). In Fig. 2.5 (c and d), the jet elevates and its momentum decreases due to the negative buoyancy. Then at the steady state is acquiring a latest head of elevation z_f . After the reflection of the flow, the jet reflects back on the bottom at a horizontal distance X_{im} from the source point and impinges at an angle θ to the horizontal (Papakonstantis & Christodoulou 2010).

Consequently, the flow spreads in all directions near the impingement point as a gravity current, i.e. a dense layer propagates horizontally on the bottom. Also, in most cases, especially through $0^\circ < \theta < 90^\circ$, since the impingement does not occur at 90° (i.e., $\theta \neq 90^\circ$), the outer boundary shape is non-axisymmetric. However, for axisymmetric outer boundary, only one Q_i value governs the spreading of the gravity current in all directions (Q_i —volume flow rate at the outflow source, see Fig. 2.5).

For asymmetric outer boundary, Q_i values may differ in every direction, resulting in different radial positions in each direction at a particular time, t . Unlike the vertical discharge configurations (Fig. 2a, and b), a substantial deficit exists in the basic understanding of the dynamics of negatively buoyant jets in the angled discharge configuration, mainly due to lack of experimental data (Bleninger & Jirka 2007). Jirka (2008), and Shao & Law (2010) found that X_{im} depends upon the values of L_M and the discharge angle of θ_0 .

If flow measurements are unavailable and theoretical models are available, the local flow parameters at the outflow source (U, M, B, Q , and g' counterparts of U_0, M_0, B_0, Q_0 , and g'_0 respectively at the outflow source) can be estimated according to (Chowdhury & Testik 2014). As for the discharge configuration of Fig. 2.5a, which presents a plume-like impingement on a smooth bottom, the radial extent/length of the wall-jet, X_j , was found to depend on the length-scale, z^* . For example, (Kaye & Hunt 2007) found that $X_j = 0.66z^*$ for a saline discharge. Once X_j is known, the duration of the wall jet phase, t_j and for a sloping bottom topography, the slope angle, along with z^* and L_M , influences the extent, X_j and the dynamics of the wall jet phase (Ross 2000).

2.3.3 Gravity currents on a flat bottom in calm ambient waters

According to (Chowdhury & Testik 2014), the post-impingement bottom outflow is reflected by a buoyancy flux, $B_i = g'_i Q_i$, at the discharge source. First (for $X < X_i$) experiences present a short-lived wall jet phase. Then, the jet (for $X_j < X < X_f$) conducts as a fully developed gravity current [X radial distance from the impingement point to the measurement position, X_f radial position of the gravity current front at a particular time, t]. Papakonstantis & Christodoulou (2010) debated the case of buoyant jets in a positively state, a comparable linkage cannot be made in principle. However, the parameters at the bottom surface may depend on the source location, i.e. the head z^* (Fig. 2.5a). In the case of negatively buoyant jets, the buoyancy dominates the flow after its reversal, and the flow impinging on the bottom resembles a plume. Therefore, it is expected that the spreading is described by Eq. (2.4) or (2.5). In the case of the positively buoyant jet, the same may occur if the flow at the bottom level is buoyancy driven (Papakonstantis & Christodoulou 2010).

2.3.4 Physical properties of heavy gravity currents

Sang (2011) described the physical properties of gravity currents, and presented several dimensionless parameters frequently used to provide important quantitative information on the turbid density flows.

I. Density stratification

The densities of gravity currents can be defined as a function of temperature and sediment concentration. Therefore, the density structure of ambient fluid can have a significant effect on density current dynamics. Density currents occurs mostly due to a density difference between density current (ρ_1) and ambient water (ρ_2). Also, the densimetric gravitational acceleration

results from the difference in specific weight between the density flows and ambient water ($g\Delta\rho$ where $\Delta\rho = \rho_1 - \rho_2$). The specific weight difference (also called buoyancy) per unit mass ($g\Delta\rho/\rho_1$) can be viewed as a reduced gravitational acceleration (g'). Turner (1973) considered the gravity currents propagating in a stratified ambient fluid, the gravity currents will fluctuate in pure harmonic with-angular frequency as:

$$N = \left(-\frac{g}{\rho} \frac{\partial \rho}{\partial z}\right)^{1/2} \quad (2.9)$$

This equation defines the Brunt-Väisälä frequency also called the buoyancy frequency.

II. Richardson Number

The Richardson number is defined as the ratio of the square of the buoyancy frequency (N) to the square of velocity gradient represented (Richardson 1920). It writes:

$$Ri = N^2 / \left[\left(\frac{\partial u}{\partial z} \right)^2 + \left(\frac{\partial v}{\partial z} \right)^2 \right] = -\frac{g}{\rho} \frac{\partial \rho}{\partial z} / \left[\left(\frac{\partial u}{\partial z} \right)^2 + \left(\frac{\partial v}{\partial z} \right)^2 \right] \quad (2.10)$$

The gradient Richardson number Ri_g can be used to determine the dynamic instability of the flow. The laboratory results showed that flow becomes unstable due to the dynamic instability when $Ri < R_c$, where R_c is a stability threshold value and $Ri \approx 0.25$ (Taylor 1931, Miles 1961, and Geyer & Smith 1987).

Besides, the overall Richardson number Ri_0 (or bulk Richardson number, Ri_b) is defined as the ratio of buoyancy to kinetic energy of inflows. A large overall Richardson number Ri_0 means that the buoyancy becomes dominant, resulting in less mixing across the interface between turbidity currents and ambient fluid. It can be predicted using the scales of length L (generally vertical length scale, i.e. water depth and velocity U).

$$Ri_0 = \frac{g'L}{U^2} \quad (2.11)$$

III. Densimetric Froude Number

The densimetric Froude number is similar to the Froude number. Where the densimetric Froude number is the inverse square root of Ri_0 .

$$Fr_0 = \frac{U}{\sqrt{g'L}} \quad (2.12)$$

The ratio also clarifies the relation between the gravitational forces resisting the mixing to the inertial forces of the flow. Laboratory experiments have shown that the potential effect of the saline water boundary form increases with the densimetric Froude number.

2.4 Entrainment and mixing gravity currents

In general, the entrainment of ambient fluid into a gravity current propagation has important effects. Dense gravity currents characteristics have applications in geophysics and in coastal engineering. They are specially characterized by the amount of ambient entrained into the gravity current during its evolution. For example, the horizontal spreading of dense fluid in a relatively buoyant ambient, due to gravity, occurs in oceans naturally or from anthropogenic causes. Also, if a polluted industrial effluent is pumped into a river or the seas, it is essential to identify when the entrainment of the ambient fluid has diluted this deadly flow to a safe level (Simpson 1997).

The mixing of buoyant fluid released into the surrounding fluid is of essential concern for a significant number of industrial and environmental turbulent flows. Also, the evaluation of mixing occurring between a denser current and the ambient fluid is an important issue, since it affects the buoyancy forces of the motion driving (Ottolenghi *et al.* 2016a, b, and 2017). Therefore, it can have an effect on the dynamics of the gravity current propagation through the reduction of the density difference that drives the flow (Johnson & Hogg 2013). Entrainment and mixing in the case of unsteady gravity currents flow have been studied less extensively, in both experimental and numerical cases (Özgökmen & Chassignet 2001, Chang *et al.* 2005, Özgökmen & Fischer 2008, Özgökmen *et al.* 2009, and Adduce *et al.* 2012).

2.4.1 Entrainment

Morton *et al.* (1956) has provided an effective way of modelling dense vertical plumes and jets. They formulated their modelling using the volume, momentum and buoyancy fluxes (Q , M and F respectively) as variables. Afterwards, Ellison & Turner (1959) drew attention to the entrainment as a specific phenomenon. They fixed the important role of the entrainment on the gravity currents motion, a request justified by its measurable impact on the natural flows. Also, Ellison & Turner (1959) performed a laboratory experiments of continuously fed dense gravity current over smooth bottom, with varying slope (horizontal and inclined bottom), inside a pool of mixed dense and ambient fluid, and the currents were fixed at a length of $R \sim 1000$. According to (Huppert & Simpson 1980), they observed in their experiments that the initial stages of the motion transit from the inertia regime to a viscous regime as a small scale. They observed that the entrainment occurred in transition regime. It becomes significant, preventing the monitoring of the entrain regime. While, Özgökmen, & Chassignet (2002) studied the natural flows in large scale. After that, they studied the beginning of viscous effects which occurs much later. The entraining is described by a flow regime dominating the dense current.

According to Ross (2000), many works related on buoyant, dense plumes, and jets, depend more or less on the work of Morton *et al.* (1956), and Cenedese & Adduce (2010). They proposed a new parameterization for entrainment in overflows that takes into account the dependence of the entrainment on both the Fr and Re . Accordingly, obtaining accurate knowledge of the gravity current dynamics evolution requires a deeper understanding of the entrainment. Also, Johnson & Hogg (2013) fixed the entrainment effect on the current dynamics. Subsequently, this influence becomes ultimately important at long times, for the case of gravity currents propagating on horizontal surfaces. Furthermore, the absence of entrainment effect cannot monitor the gravity currents. Experimentally, the propagation of gravity currents without the flow influence becomes controlled by viscous forces (Huppert & Simpson 1980). The accuracy of the entrainment depends on the accuracy of the measured of the density structure itself. Also, this accuracy depends upon specifying the quantified self of the mixing between dense and lighter fluids. After that, several experimental studies concentrated on entrainment into the head at the current front becomes significant, when a gravity current is instead led by progressing flow front.

2.4.1.1 Analysis of entrainment

In literature, studies dealing with theoretical and experimental investigation on entrainment in gravity currents have been brought out in laboratory and in nature. Morton *et al.* (1956) proposed an effective way of modelling dense vertical plumes and jets. They formulated their model using the volume, momentum and buoyancy fluxes (Q , M and B respectively) as variables. Notably, they found that the entrainment rate of ambient fluid into a propagation flow results from turbulent motion and is proportional to the difference in velocity between the current and surrounding flow.

By dimensional arguments, with Turner's model (1986) of the entrainment phenomenon makes the same assumption. For gravity currents, most entrainment analyses have been conducted by using constant-flux gravity currents where the fresh ambient fluid is steadily supplied to the system in order to account for the ambient lost through entrainment (Fernando 1991, Breidenthal 1992, Princevac *et al.* 2005 among others). The flow is considered in steady state. These analyses generally assume the Morton-Taylor-Turner (MTT 1956) entrainment hypothesis, that writes:

$$E = \frac{w_e}{U} \quad (2.13)$$

where E represents the entrainment coefficient, w_e corresponding to Fernando (1991), Breidenthal (1992), and Princevac *et al.* (2005), is an inflow velocity or entrainment velocity as shown as previously in Fig.2.2, also called the entrainment velocity, and U is the characteristic velocity (Morton *et al.*, 1956, and Turner 1986). Depending on Eq. (2.13) the entrainment of the tail is given by Morton *et al.* (1956), and expressed as:

$$E_T = \frac{\bar{w}_E}{U_T} \quad (2.14)$$

where \bar{w}_E represents the entrainment velocity into the tail of the gravity current, and can be estimated by:

$$\bar{w}_E = \frac{\Delta\psi}{l} \quad (2.15)$$

$\Delta\psi$ describes the growth in the transport of the density current over the length of the tail section (l). Similarly, the entrainment in the head is measured according to the definition of (Ellison & Turner 1959, and Turner 1986), and can be written as:

$$E_H = \frac{dH}{dX} \quad (2.16)$$

The right-side of Eq. (2.16) represents the rate of change in the head thickness H versus the distance X down the slope. Turner's definition (1986) of the tail entrainment:

$$E_T \approx \Delta h / \Delta X \quad (2.17)$$

where h is the thickness of the tail, it is comparable to Eq. (2.14), since $E_T = \Delta\psi(U_T l) \approx \Delta h / \Delta X$.

In large scale of experiments, Özgökmen & Chassignet (2002) assumed:

$$\Delta\psi(U_T l) = \Delta h, \quad (2.18)$$

and $l = \Delta X$.

Equation (2.18) helps investigating the influence of the density difference and the slope on the dynamics of the bottom gravity currents in a nonrotating and homogenous environment. Furthermore, in the case of steady gravity currents Turner (1986) and Parker (1987) discussed Eq. (2.18), based on experiments data, and when the entrainment is parameterized as a function of the Froude number.

2.4.1.2 Total entrainment

Özgökmen & Chassignet (2002) stated that the previous two Eqs. (2.14) and (2.16) represent the definitions of entrainment and they are valid only as long as the tail and the head stay separate. When the head grows and develops downstream, there are no merges between the tail and head. Following this idea, Meleshko & Van Heijst (1995) defined an unambiguous metric for obtaining a better understanding of the total entrainment quantitatively of ambient fluid into the gravity currents, written as:

$$E \equiv \frac{A_{total} - A_0}{A_0} \quad (2.19)$$

where

$$A_0 = \int_0^h \int_0^t u(x_0, z, t) dz dt = \int_0^t \psi(x_0, h, t) dt \quad (2.20)$$

Herein, the total volume per unit depth (area) of dense fluid has entered the domain across x_0 with thickness h in the straight distance. In the absence of entrainment, the total area that has entered the domain A_0 is equal the total area of dense fluid within the domain A_{total} . This leads to an absence of any mixing and the entrainment coefficient is $E = 0$. Furthermore, if the total area of the dense fluid inside the domain would be larger than the area that has indeed entered across the boundary, $A_{total} > A_0$, then $E > 0$. For example, $E = 1$ for 50% dilution of the gravity current or, in other words, the expansion of the area of dense fluid is doubled. Although, Hallworth *et al.* (1993 & 1996) and Hacker *et al.* (1996) studied the entrainment rate depending on a specified value of E , as dimensionless entrainment ratio, in order to quantify the experimental results.

2.4.1.3 Entrainment of dense jets

Morton *et al.* (1956), built the classical approach to turbulent entrainment based on macroscopic conservation equations for mass fluxes, buoyancy, and momentum, with the assumption that turbulent jets are self-similar with respect to dimensionless downstream distance from the source. Also, they described how a buoyant plume propagation from a point source can be modeled by the next equations (Eqs. 2.21-2.26) for the horizontally integrated buoyancy, volume and momentum fluxes in the plume. The constant of proportionality, α is known as the entrainment coefficient. In this model, the volume flux is defined by:

$$Q = \pi b^2 U \quad (2.21)$$

Its x-variation is a result of this entrainment and it is governed by the following linear function of U (average velocity in the plume):

$$\frac{dQ}{dx} = 2\pi\alpha bU, \quad (2.22)$$

where the constant of proportionality, α is known as the entrainment coefficient and is equal to 1.85, b is the plume radius. The momentum flux is expressed as:

$$M = \pi b^2 U^2, \quad (2.23)$$

the momentum flux is governed by the momentum that writes:

$$\frac{dM}{dx} = \pi b^2 g'. \quad (2.24)$$

Therefore, the buoyancy is conserved with the following expression:

$$B = \pi b^2 g' U \quad (2.25)$$

This model predicts the shape and density of the plume as a function of the height and it concords well with both laboratory experiments and field observations. Turner (1966) injected a salt water vertically upwards in a basin of static water. Dimensional arguments allow the maximum elevation height (jet length) as being proportional to $M_0^{3/4}/F_0^{1/2}$. Also, Britter (1979) detected the apparent difference between theoretical and experimental values of proportionality constants C_3 in Eq. 2.4. These values were correctly associated with the entrainment of ambient fluid in a positively buoyant jet. Subsequently, the entrainment occurred as a significant result of the supercritical flow at the outflow source from the impingement of vertical downward discharges.

Initially, an excess of momentum compared to the unmixed plume due to the forced plume was described by Morton *et al.* (1956), and it was completed by Morton (1959). As a result of the dense forced plume with the initial momentum directed upwards, the buoyancy will act against on the flow. The maximum rise height for a plume with initial buoyancy and momentum fluxes B_0 and M_0 , and with no initial volume flux is:

$$z_{max} = 4.21\alpha^{1/2} \frac{M_0^{3/4}}{B_0^{1/2}} \int_0^1 \frac{s^3}{(1-s^5)^{1/2}} ds \quad (2.26)$$

For the sources have a finite small volume flux, the previous constant of proportionality in the experiments was found to be 1.85 according to (Turner 1966). The model of plume propagation provides a description of the upward part of the flow and predicts the height at which the flow will reverse. But it does not predict the motion in the downwards part of the flow, nor does it take into account the flows interaction between the upward and downward.

According to Ross (2000), the integral in the above Eq. (2.22) can be found equal 0.46 and the constant proportionality as 1.73. Also, assuming an entrainment coefficient of 0.1, the maximum evolution height z_{max} for plume can be calculated depending on the prediction of Morton (1959) as a comparison with the experimental background.

2.4.1.4 The dependency and velocity of entrainment

Cenedese & Adduce (2008), Adduce *et al.* (2012), Nogueira *et al.* (2014), and Ottolenghi *et al.* (2016a & b) considered the flow of a dense gravity current with a mixing occurring with the ambient lighter fluid. They notably stated that along its path, the gravity current entrains fresh water and increases its volume. The entrainment velocity can be modelled as a fresh water discharge per unit area crossing the interface between the two fluids, which causes an increase in volume of the gravity current. Also, Johnson & Hogg (2013) considered the rate of entrainment of ambient fluid into current due to turbulent mixing as introduced by Morton *et al.* (1959). They calculated the difference in velocity between the gravity current and the stationary ambient $|u|$. Morton *et al.* (1959), Turner (1986), and Johnson & Hogg (2013) defined the entrainment velocity as: $w_e = E|u|$. Ellison & Turner (1959) stated that the entrainment coefficient E is mostly a function of the bulk Richardson number $Ri = g'h/u^2$, in high Reynolds and high Péclet numbers configurations respectively. Boussinesq approximation, where $E(Ri)$ tends to a constant, almost equal to 0.075, for $Ri \ll 1$, and vanishing at high Richardson numbers. After that, Ottolenghi *et al.* (2016a) defined the bulk entrainment velocity w_{ei} within the interface S_i separating the two fluids with different density as:

$$w_{ei} = \frac{Q_{ei}}{S_i} \quad (2.27)$$

where the interface is scaled by $S_i = dx_{fi}$ in the x - z plane, and a bulk entrainment discharge can be calculated at each time by:

$$Q_{ei} = \frac{\Delta V_i}{\Delta t_i} \quad (2.28)$$

where ΔV_i represents the increasing in volume at a given time t_i (Δt_i increasing time steps). The experimental measurements of Johnson & Hogg (2013) are in good concordance with the theoretical results of Ellison & Turner (1959) and can be viewed as the vanishing act of entrainment approximately as $E \sim 1/Ri$ at high Richardson number as shown in Fig. 2.6. Johnson & Hogg (2013) considered the variation between different experiments of (Fernando 1991). Also, they gathered theoretical considerations of the turbulent kinetic energy balance in a gravity current studied by Sherman *et al.* (1978) for the two following configurations:

$E \sim 1/Ri$ when $Ri \gg 1$, and $E \sim \text{constant}$ when $Ri \ll 1$. In this aim, they chose a model equation of entrainment velocity. They assumed a dependency relation of the entrainment coefficient on the Richardson number that captures the observed behavior of $E(Ri)$, in both low and high Richardson number regimes. Therefore, the entrainment velocity equation was written as:

$$w_e = E|u| = \frac{E_0}{1+\psi Ri} |u| \quad (2.29)$$

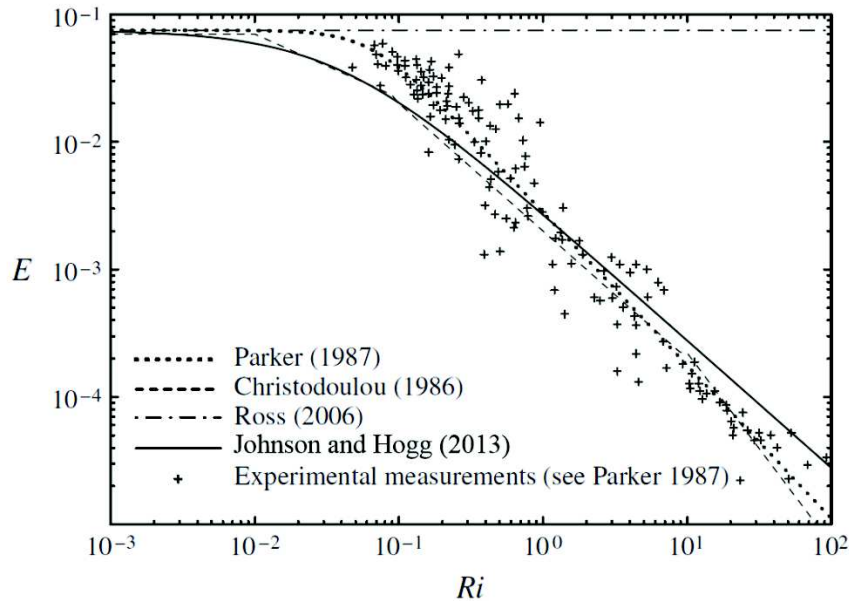


Figure 2.6: The experimental measurements and proposed fits of the dependency of entrainment on Richardson number [Johnson & Hogg (2013) compared their results with those of Christodoulou (1986), Parker *et al.* (1987), and Ross *et al.* (2006)].

They notably found the following values of the constants appearing in Eq. (2.29): $E_0 = 0.075$ and $\psi \approx 27$, which are suitable for the experimental measurements of entrainment presented in Fig. (2.6). Also, this Eq. (2.29) was simplified dependency captures the reduction of entrainment with growing Richardson number. Hallworth *et al.* (1993 & 1996) observed the dilution in the vicinity of the head, after passing the slumping point (because the entrainment is negligible in the slumping phase). They could not provide a physical clarification of the relation between this transition and entrainment within the head. As a result, the cavity transmits backwards from the front of the head, reflects off the back wall, and catches up with the head (Rottman & Simpson 1983, Bonnezaze *et al.* 1993, and Fragozo *et al.* 2013).

2.4.2 Turbulent mixing

The dense mixing occurs within the boundary between the current and the ambient fluid which indicates that no acute density transition exists (Middleton 1993). Fernando (1991), Breidenthal, (1992), and Princevac *et al.* (2005) studied different mixing mechanisms concerns of the entrainment velocity (w_e), applied across a density interface. Such phenomenon is complex and difficult to study. The turbulent mixing between the gravity current and the ambient fluid is determined by the use of the gradient Richardson number Ri_g , which is the ratio of the stabilizing current stratification to the destabilizing velocity shear (Ellison & Turner 1959, Turner, 1973 and 1986). The turbulence eventually collapses for $Ri_g > 0.25$ (Turner 1973). The turbulence is characterized by the presence of buoyancy forces, and the term “stratified turbulence”, as discussed by Fernando (2000), is used when the mixing can only takes place in the horizontal plane. Furthermore, the so-called “pancake” mixing, demonstrated in laboratory experiments, occurs for a stratified flow with $Ri_g > 0.7$.

Chang *et al.* (2005) used vertical shear (diffusivity) related to Ri_g and Turner’s work (Ellison & Turner 1959, Turner 1986, and Hallberg 2000) as two entrainment parameterizations to model the mixing. Their results present an agreement with two entrainment parameterizations, resulting from ocean circulation and nonhydrostatic models. However, Britter and Simpson (Britter & Simpson 1978 and Simpson & Britter 1979) studied the steady-state transport and mixing of fluids via the head of the gravity current, by using a gravity current released into a tank with a streaming ambient over a horizontal surface. For example: Simpson & Britter (1979) quantified the bulk mixing rates for a steady-state current. To this aim, they used either from an apparatus in which the head is brought to rest by an opposite flow and a moving floor, they used a modified lock exchange flow. Unfortunately, they could not determine the density structure produced. Later, using a technique involving a chemical reaction by Hallworth *et al.* (1993) observed the mixing only after the transition to the self-similar phase, while, (Hacker *et al.* 1996, Jacobson & Testik 2013, and Nogueira *et al.* 2013a, 2014) observed the mixing during the slumping phase. They measured the density structure and estimated the mixing by the entrainment based on the analysis of iso-density levels.

The entrainment depends strongly on the choice of the density threshold used to define the interface through the dense current and the ambient fluid. Hacker *et al.* (1996) used a large interval of threshold values from 5% to 100%. While in the experiments of Fragoso *et al.* (2013), small values of density were not detected and the values of the threshold used varied from 50% to 92%. In all the experiments reported (Hallworth *et al.* 1996, Hacker *et al.* 1996;

Nogueira *et al.* 2013, and Fragoso *et al.* 2013), the determination of density distribution of the gravity currents was limited to the 2D configuration with many present difficulties related to the experimental methods (calibration curve, coloured pH indicator, etc.), and the results were often presented without accuracy.

2.4.2.1 Fractional area/volume ratio of the dense current

The ratio of the field of the current A to the initial area of the discharge fluid A_0 changes with time depending on the iso-density level selection. These changes are determined by the propagation internal structure. Hacker (1996) and Jacobson & Testik (2014) used the ratio A/A_0 with dimensionless front location of the gravity current as indicator of the entrainment in lock-release gravity currents. To this aim, Hacker (1996) used a new experimental technique to investigate the density structure of mixed gravity current in the lock-release case. This experimental technique is produced across the limit of the concentration range, and studied the effect of the aspect ratio of the release on the subsequent evolution of the propagation flow. Fragoso *et al.* (2013) and Ottolenghi *et al.* (2016a & b) followed the method proposed by Hacker (1996). Their contribution consisted in evaluating entrainment and mixing for the unsteady gravity currents case. They notably focused on the effect of the aspect ratio between the initial water depth and the lock length, and the driving motion of the initial excess density. Ottolenghi *et al.* (2016) suggested that the existence of ambient fluid entrainment for the total time of the experiments and the choice of the iso-density thresholds values $> 40\%$ leads to opposite results: the slope of the curves is negative, therefore the volume of the fluid starts decreasing at high density. Fragoso *et al.* (2013) discussed the fractional area of the current and found sudden changes in mixing in the vicinity of the slumping point by a suitable choice of threshold value. The different thresholds are used by Ottolenghi *et al.* (2016) to determine the edge of the current: 2%, 5%, 20%, 40%, 60%, 80%, and 100% for A_k/A_0 with dimensionless front location of the gravity current comparable to Hacker's (1996). While, the thresholds used by Fragoso *et al.* (2013) were: 50%, 80%, and 92% for A/A_0 with t/t_s .

2.4.2.2 Potential energy

Winters *et al.* (1995) studied the effect of the critical value of the density threshold that is used to determine the interface between the two layers. This method is useful for the evaluation of irreversible mixing inside a lock-release gravity current by the energy budget. This process is not dependent on the distinction between the dense current volume and the ambient fluid volume.

For the reason mentioned above, Patterson *et al.* (2006), and Frago *et al.* (2013) did not need to specify any interface between the dense and light fluids. This methodical approach was successfully applied to investigate the dynamics of lock-release gravity currents propagation over horizontal surfaces. Ottolenghi *et al.* (2016a & b) used depending the energy budget method to get the distinction between the adiabatic processes for horizontal and inclined boundaries cases. This can modify the initial potential energy E_p of the flow without exchanges between the mass or heat, and the adiabatic ones. The definition of the potential energy E_p of the flow is given by:

$$E_p(t) = g \int_V \langle \rho(x, y, t) \rangle y dV \quad (2.30)$$

where V represents the entire volume of the fluid (dense and ambient fluids), x and y are respectively the streamwise and vertical directions, $\langle \rho \rangle$ represents the spanwise averaged density field. The definition of the background potential energy E_b is defined as:

$$E_b(t) = g \int_V \langle \tilde{\rho}(x, y, t) \rangle y dV \quad (2.31)$$

where $\langle \tilde{\rho} \rangle$ represents the spanwise averaged density field adiabatically compatible with the minimum state of the potential energy. Consequently, E_b can be estimated from the fluid particles redistribution in a perfectly stable horizontally stratified configuration. According to the definition of Winters *et al.* (1995), $\langle \rho \rangle$ and $\langle \tilde{\rho} \rangle$ are used to calculate the quantities of E_p and E_b . This relation was adopted in each of the Patterson *et al.* (2006), and Frago *et al.* (2013) studies. As a result, the difference between E_p and E_b can be a useful approximation for obtaining the available potential energy E_a :

$$E_a(t) = E_p(t) - E_b(t) \quad (2.32)$$

From $\langle \rho(x, y, t) \rangle$ to $\langle \tilde{\rho}(x, y, t) \rangle$ and within an adiabatic transition, the available potential energy E_a was released without changing in the probability density function of the density. Also, the potential energy E_p can be modified by adiabatic processes during a redistribution of ρ without changing the background energy. Furthermore, the state of the background potential energy E_b can be changeable in order to obtain the direct measure of the energy expended in the fluid mixing due to dilution (Winters *et al.* 1995). Frago *et al.* (2013) relying upon the density threshold method together with an integral method of (Winters *et al.* 1995) rearranged the potential energy to investigate the evolution of a continuous density field. Then, Ottolenghi *et al.* (2016a, b, & 2017) characterized the potential energy budget with dimensionless front location of gravity current for different cases. Finally, Gerber *et al.* (2011) drew the profiles of excess density difference and buoyancy production of turbulent kinetic energy, and detected only local maximum at the interface with the ambient fluid.

2.5 Numerical modeling of gravity currents

The investigation of the gravity currents field is typically very difficult, due to unexpected characteristic and complication occurrences. Numerical models are valuable tools for investigating the gravity currents impact, and such models are used in the studies of water quality. In order to achieve a higher clarification, laboratory experiments have been widely used to explore the gravity currents dynamics. Therefore, numerical models are not able to faithfully reproduce the experimental studies but are dependent on the available amount of computational resources. In order to reduce the duration of the calculations, numerous simplifying assumptions must be taken in the numerical model. Furthermore, the equations governing the gravity current model usually contain the mass and momentum conservation equations, as well as possible addition of one or more scalar transport equations. The scalar transport equations are chosen depending on the situation of the modeled turbulence, and the density variances caused by the variations in temperature or changes in fluid mixture composition.

According to Chowdhury & Testik (2014), the quantitative gravity currents models are the most widely used: the force-balance, box and depth-averaged modeling for currents generated in controlled laboratory setups. The force-balance modeling provides the choice and definition of the parameters necessary for front position temporal evolutions and gravity currents height. In the box modeling, the gravity current is represented in a series of boxes; either rectangular for 2D flows or cylindrical for radial currents instantaneously with uniform properties. Solutions of the box modeling for compositional gravity currents is obtained by using mass conservation and front or dynamic conditions of the head. In depth-averaged modeling, the negligible effect of vertical variations assumption in the characteristics of the current represents the best solution of Navier-Stokes equations. The equations of fluid mass and momentum conservation are solved simultaneously for compositional gravity currents.

Two-dimensional (2D) gravity currents have been widely examined by both laboratory experiments and numerical simulations on the contrary of three-dimensional (3D) gravity currents. Both numerical configurations depend on the theoretical formulation. In the following, different gravity current propagation model types are reviewed, considering the gravity currents propagation as a constant-flux release: theoretically, within the static ambient water in (§§2.5.1); dynamically, gravity currents are affected by hydrodynamics of ambient water in (§§2.5.2); and several numerical methods are described in (§§2.5.3).

2.5.1 Gravity current model into static ambient water

Britter (1979) was the first to use shallow water model as a force-balance modeling approach to investigate the parameterization of the radial axisymmetric spreading of compositional gravity currents in the inertial regime from the impingement point of downward discharges over a horizontal bottom (see § 2.3, and Fig. 2.5a: a vertical positively buoyant jet) over a horizontal bottom. Chowdhury & Testik (2014) indicated that the shallow water models are applicable for the layer of gravity current (single-layer models) and for the improvement accuracy, of both the ambient fluid layer and the underlying current layer (double-layer models).

Moreover, Huppert & Simpson (1980) were the first to propose that the parameterization can be obtained from the box modeling for constant volume gravity currents. The equation of sediment mass conservation is used as an additional equation in the box model to specify particle deposition from a particle-laden bottom gravity currents. Referring to (Eq. 2.4 in §§ 2.3.1), the resulting term of $R(t)$ from the force-balance and box models is similar to the force balance term in Eq. (2.4) with analytical term for the proportionality constant C_3 .

Bonnecaze *et al.* (1995) extended and solved the shallow water model (force-balance modeling) numerically, and Dade & Huppert (1995b) extended the box modelling of compositional gravity current to examine carefully the particle-laden gravity currents. The force-balance modelling is not compatible with particle-laden gravity currents depending on the development of theoretical considerations. Also, Bonnecaze *et al.* (1995) validated the force-balance and box models relying on the observations of experiments for the axisymmetric gravity currents. These axisymmetric gravity currents were generated by subcritical inlet source conditions over a horizontal bottom. The prediction based on the horizontal and vertical variations of gravity currents dynamics is impossible; for this reason the two models resolve the interior dynamics of the motion. The expression in Eq. (2.5), applied to each of the force-balance models depending on Huppert's [lubrication] theory (Huppert 1982), and the box model (Ungarish 2009) investigated the propagation of viscous compositional gravity currents over a horizontal bed for Newtonian fluid as a radial spread of the constant flux release axisymmetric. Didden & Maxworthy (1982) agreed with Huppert's (1982) experimental results, which showed proportionality constant ($C_4 = 0.63$ discussed in §§ 2.3.1) as a consequence of the similarity solution of the lubrication theory model. Depth-averaged modeling follow the lubrication theory model: the inertia force is neglected from the equation of momentum conservation for the viscous gravity currents.

As for inertial gravity currents: the viscous force is neglected from the equation of momentum conservation, when the depth-averaged modeling is following the shallow water models. The horizontal variations are formed during the depth-averaged modeling, but this model cannot predict the vertical variations.

Consequently, the modeling of the interior dynamics can use complex numerical models such as Navier-Stokes equations in the Reynolds-averaged numerical solver. These equations, considered as governing equations, are used to model the vertical variations within the mean flow structure of inertial gravity currents. Several studies for each of: Hallworth *et al.* (2001, & 2003), Patterson *et al.* (2006), and Ungarish (2007) were performed to investigate the experimental and numerical axisymmetric gravity currents in a rotating system using both shallow water equations and complete Navier-Stokes equations. La Rocca *et al.* (2008) studied the propagation of the bottom gravity currents on both smooth and rough surfaces using experimental, numerical, and mathematical models. These models are based on shallow water theory together with the single-layer approximation.

2.5.2 Gravity current model with dynamic ambient water

The ambient water flow affects the dynamics of two dimensional bottom gravity currents. Hogg *et al.* (2005) studied the effects of both co-and counter- flowing uniform ambient fresh water flows. Hogg's (2005) experimental setup was similar to the two dimensional narrow rectangular channel employed by Hallworth *et al.* (1998) and the bottom gravity currents were generated by impingement of buoyant jet discharges at the channel bottom in the middle of the channel. The generated gravity currents followed a two-dimensional propagation and they were flowing with either both co- or along counter- flowing the ambient fresh water flow relying upon the position of the impingement point. Before that, Simpson & Britter (1980) used the moving belt setup in order to generate the saline fluid into a co-moving ambient fluid and stopping the advance of the dense fluid.

Hogg *et al.* (2005) formulated a model combining both multi-layered shallow-water model and depth-averaged model. Such model calculates the heights, densities, and velocities of the movable layer and the ambient fluid as functions of space and time. As well, this model depends on previous models of shallow salt wedges in estuaries developed by (Schijf & Schönfeld 1953, and Sorgard 1991) and of particle-driven gravity currents developed by (Bonnecaze *et al.* 1993) using ambient fresh water entrainment within a gravity current and the opposite when the gravity current fluid entrainment within ambient fresh water.

This multi-layered shallow-water model consists of: i) a bottom layer of a dense gravity current, ii) a top layer of an ambient fresh water, and iii) a layer of the bottom and top layers mixture. The above mentioned studies found that the shallow-water and box models not agreement expectations for experimental results except close to the point of impingement. Consequently, Slim & Huppert (2008) reanalyzed the Hogg's (2005) shallow-water model, and they succeeded in solving the one-layer shallow water model analytically (consisted of a compositional gravity currents similarity solution and a particle-laden gravity currents asymptotic solution).

A theoretical framework of varying degrees of complexity was employed to model the gravity currents motion. Rottman & Simpson (1983) used the depth-averaged modeling for the shallowness of the flow, and Klemp *et al.* (1994) used the full equations of the motion for obtaining the numerical simulations. Eames *et al.* (2005) acquired a similarity solution for the equation of the non-linear advection to examine carefully how a laminar co-flowing ambient flow is affected by the Newtonian viscous gravity current spreading. Huppert & Simpson (1980), Dade & Huppert (1995a), and Harris *et al.* (2001) studied the bulk characteristics by exploiting the basic or box models without including any solving of the internal dynamics of the motion. Few studies has been proceeded to research the dynamics of gravity current advected by ambient flow. Kranenburg (1993) established a relation of the front velocity of the bottom gravity current with the counter-flowing ambient flow and Liu & Moncrieff (1996) studied the bottom gravity currents propagation by an elastic equation solution of the motion but did not utilize experimental results to validate their theoretical formulations.

2.5.3 Numerical methods

The dynamics and mixing of the gravity currents can be modeled using the Navier-Stokes equations with the Boussinesq approximation. The resolution of this model is made using DNS (direct numerical simulations) or LES (large eddy simulations). Numerical models can give unlimited information in the three-dimensional and time coordinates, but they need many computing resources. In the last two decades, there were several studies of the gravity currents using high-resolution numerical models, which use the three-dimensional Boussinesq form for solving the Navier-Stokes equations. According to Härtel *et al.* (1997, 1999, & 2000a, b), Cantero *et al.* (2007, 2008), Ooi *et al.* (2007, 2009), Tokyay *et al.* (2011, 2012), Dai (2013, 2015), and Ottolenghi (2016a, b) different settings employed either large eddy simulations (LES) or direct numerical simulations (DNS) to study lock-exchange gravity currents. However, they are very complex and require high computing resources.

These models supply significant details for the description of the gravity current's dynamics as Computational Fluid Dynamics (CFD) and have reached better and more reliable understanding of their dynamics results. DNS needs significant amounts of computer power in the case of the initial two-dimensional simulations. Examples include Härtel *et al.* (1997, 1999, & 2000b), which suffered from some of the same problems as other two-dimensional models. In fact, they could not capture all the three-dimensional features of the flow. To reduce the computational resources, the numerical models can use different assumptions to solve the system equations.

Direct numerical simulations (DNS) and large eddy simulations (LES) in the turbulent flows are costly compared to the models based on the Reynolds Averaged Navier-Stokes (RANS) equations usually used in CFD codes, but still expensive because of the complexity of the eddy viscosity. Reynolds Averaged Navier-Stokes (RANS) equations models can be employed without assumptions to investigate the mean flow, and are often functional to simulate the turbulent flows with less computational resources comparing to DNS or LES. The governing equations of three-dimensional models include Reynolds Averaged Navier-Stokes (RANS) equations, mass conservation equations, free surface equations, the equation of state relating density to temperature and sediments, and a conservation equation for each scalar variable. To simplify the governing equations, the models use the Boussinesq, and hydrostatic assumptions and the water is assumed to be incompressible. The standard ($k - \varepsilon$) model is most commonly used with (RANS), which has been in usage since the 1970s.

Hossain and Rodi (1977), using a RANS model with Reynolds stress and mass transport equations, showed that the entrainment in such model is reduced as a result of the collapse of turbulence due to a stable stratification. Brørs and Eidsvik (1992) studied the turbidity current flows using a RANS multiphase mixture model. They used transport equations instead of the Boussinesq and flux-gradient hypotheses for the individual Reynolds stresses and fluxes. They argued that ($k - \varepsilon$) turbulence model underestimated the turbulent mass transport at the height of velocity maximum. They showed that their model gave higher predictions. Huang *et al.* (2005) used a RANS multiphase mixture model with the Boussinesq and flux-gradient hypotheses to investigate turbidity currents with deforming bottom boundary. For model validation, they compared model results with some of the two-dimensional flume experiments of Garcia (1993) for both saline and sediment-laden flows. A satisfactory concordance was shown for velocity profile, similarity profiles of velocity and sediment concentration between the model and Garcia's (1990) experimental results.

Gerber *et al.* (2011) investigated a two-dimensional, unsteady gravity saline using Reynolds-averaged Navier-Stokes model (2DV-URANS). The Reynolds-averaged equations of the flow state a mixture continuity, a mixture momentum based on the Boussinesq approximation and a conservation of salt mass fraction (Rodi 1980). To compute the mixture density, the equation of state proposed by Lide (1997) was used, while closure for the Reynolds stress tensor was obtained using the Boussinesq hypothesis (Pope 2001). An agreement was found between the modeled and the measured (using PIV facilities)^{1, 2} normalized mean profiles.

According to Sangdo An *et al.* (2012) an approximated study of the gravity current propagation dynamics is investigated using the FLOW-3D computational dynamic code. The performance of the numerical model uses two different turbulence closure schemes namely the renormalization group [(RNG) $k - \varepsilon$] schemes in a Reynolds-averaged Navier-Stokes framework (RANS) and the large-eddy simulation (LES) technique. They studied the Intrusive Gravity Currents (IGC) and Particle-Driven Gravity Currents (PDGC) using the three dimensional non-hydrostatic FLOW-3D CFD code. Also, Özgökmen & Chassignet (2002) used nonhydrostatic, high- horizontal and vertical resolution and two-dimensional simulations of gravity currents to conduct their research in large scale model. They notably showed the primary characteristics of this simulation is of the Kelvin-Helmholtz billows instability in nonrotating laboratory gravity currents. These instabilities have a predominantly two-dimensional structure. The hydrostatic assumption neglects vertical acceleration and non-hydrostatic pressure gradients so that it can be employed for a reservoir in which horizontal length scales are larger than vertical scales (Hodges 2009). The three-dimensional model has been successfully applied to water quality simulations, providing physical understanding on a full seasonal limnological process in a reservoir.

¹ Dhafar, I. A., Latrache, N., and Nsom, B. (2015a). Applied the Large-Scale Particle Image Velocimetry Technique for Measurement the Velocity of Gravity Currents in the Laboratory. DOI: 10.4236/jwarp.2015.78048, Journal of Water Resource and Protection 07(08):597-604.

² Dhafar, I. A., Latrache, N., and Nsom, B. (2015f). Mesure de vitesse par PIV à grande échelle d'un écoulement de courant gravitaire d'un liquide léger à la surface libre d'un liquide dense. 16ème congrès français du Club FLUVISU (« Visualisation et Traitements d'images en Mécaniques des Fluides pour l'Industrie »), associé au 14ème colloque international francophone du Club CMOI (« Contrôles et Mesures Optiques pour l'Industrie»). Lannion, France, Du 16 au 20 novembre.

Chapter 3: Experimental Study

3.1 Introduction

In this chapter, we present the experimental study of the two-dimensional propagation of saline gravity currents into calm fresh water contained in a basin covered with a smooth bottom. The experimental investigation of the outer boundaries of gravity currents and their front positions from the injection point such as those which occur in the environment are a traditional topic in the laboratory. In this study, we determined the relation of the space versus time ($x \sim At^B$ and $y \sim Ct^D$) under the influence of initial or local parameters of the jet flow. Part of the results and analysis presented in this chapter appeared in Dhafar *et al.* (2015b)³. Several reasons are presented for studying the dense gravity currents: Firstly, laboratory experiments are carried out in a more controlled environment than larger scale field experiments. This means that more data of higher quality can be collected. Secondly, the effect of each aspect of the flow can be carefully studied for a full understanding. Thirdly, experiments can easily be repeated, either with the same parameters or for a wide range of parameters.

3.2 Apparatus and experimental procedure

3.2.1 Experimental setup

The experiments were performed at the Institut de Recherche Dupuy de Lôme (IRDLD) Laboratory of Brest University (UBO). The experimental setup as shown in Fig. 3.1 consists of a rectangular basin containing a static ambient fresh water of $11 \times 10^{-3} m^3$ at $H = 5 \times 10^{-2} m$. The dimensions of the basin are the following: $L = 55 \times 10^{-2} m$ length, $w = 4 \times 10^{-2} m$ width, and $H = 5 \times 10^{-2} m$ depth. The walls of the basin are made of 5mm transparent glass allowing the visualization of the gravity current development. A tank with a capacity of $60 \times 10^{-3} m^3$ was used to prepare the salt fluid. The denser fluid is pumped to another tank with a capacity of $20 \times 10^{-3} m^3$, where it was colored with Rhodamine B dye. The colored salt water was injected into the basin via a transparent plastic square channel at the horizontal bottom surface made of a smooth white plastic. The injection tube is a square channel with a length of $d = 5 \times 10^{-3} m$, and it is kept horizontal for the duration of all the experiments.

³ Dhafar, I. A., Latrache, N., and Nsom, B. (2015b). Image processing applied to characterize the denser gravity current propagates over rigid surface into the lighter fluid. 10th Pacific Symposium on Flow Visualization and Image Processing Conference, Naples, Italy, 15-18 June.

The fractional height is $\phi = h/H = 0.1$ defined as the ratio of the initial salt water height ($d = h$) to the total height H of the fresh water in the basin as shown in Fig.3.2. For all the experiments performed, the smooth bottom of the basin is considered as the reference level used to measure the initial depth of both fluids and the gravity current head. When the injection orifice opens instantly, the two fluids with different densities come in contact and a non-equilibrium condition occurs.

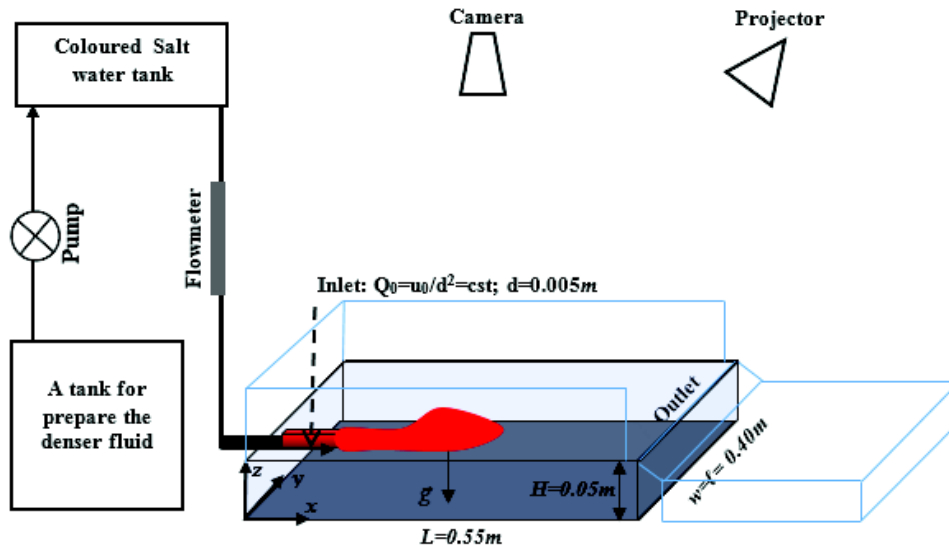


Figure 3.1: Experimental setup of the horizontal miscible jet.

3.2.2 Measurement techniques

In this study, compositional of dense gravity currents were performed using a solution of tap water and soluble sodium chloride (NaCl). This solution is the denser fluid (salt water) with an excess density $\Delta\rho = 40 \text{ kg/m}^3$ (equivalent to an effective density $\rho_s = 1040\text{kg/m}^3 \pm 1$). The tap water is the surrounding ambient fluid with a density of $\rho_{\text{water}} = 1000\text{kg/m}^3$. The density of salt water $\rho_{s,\text{measured}}$ was measured in the tank using a “WTW Conductivity meter”. The relative difference of the salt water densities was very low $[(|\rho_s - \rho_{s,\text{measured}}|/\rho_s < 0.2\%)]$. The flow rate Q_0 of the gravity current released from the colored salt water tank into the basin was controlled by a flowmeter “TechFluid 2300”. A light source made of 50 Hz-500w projector lamp was placed in front of the basin. The experiments were undertaken in a dark room to avoid other disturbing light sources (Fig.3.1). A small red soluble dye quantity of Rhodamine B was used as a tracer in order to visualize the instantaneous state of the dense gravity current (salt water) released from the “coloured salt water tank”. Rhodamine B was introduced as an agent for video-photographic analysis purposes, and the dye did not affect the density and viscosity of the salt water.

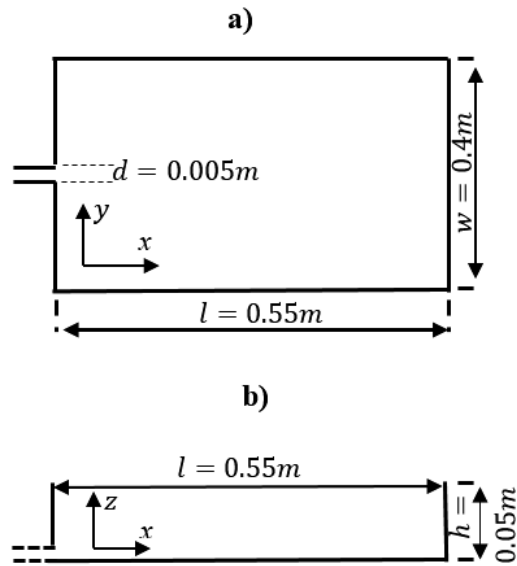


Figure 3.2: Definition sketch of the basin used to perform 3D injection experiment: (a) top view; and (b) side view.

A video sequence with a frequency of 38 frames per second was considered for each experiment. An observation system consisting of one camera (type: Photron Fastcam) taking 190 images per second with a resolution of (1024x1024 Pixels) was used as well. The camera was placed 1m above the water surface of the basin. The pictures observed by the camera were captured at a frequency of 38 Hz owing to a system of image processing consisting of a PC equipped with a Pentium IV processor (2.6 GHz) of a 1024 Mb random-access memory.

3.2.3 Experimental procedures

This work presents six experiments, in which every flow rate was tested three times to check the reproducibility of the experiment. The initial values of each flow rate Q_0 were chosen from $(2.00 \pm 0.03) \times 10^{-6} m^3/s$ to $(3.00 \pm 0.05) \times 10^{-5} m^3/s$, with an increment of $2.78 \times 10^{-6} m^3/s$. The reduced gravity g'_0 and viscosity ν were fixed at $0.39 m/s^2$, and $10^{-6} m^2/s$ respectively. The dense gravity current was represented by a salt water with a density equal to $\rho_s = 1040 kg/m^3$ prepared in a tank of the denser fluid and pumped towards the colored salt water tank. The colored salt gravity currents were accelerated by the gravity towards the flowmeter. Then, it was injected via the flowmeter along the bottom of the basin by a square channel into a static lighter fluid represented by a fresh water with density equal $\rho_{water} = 1000 kg/m^3$ as shown in Fig.3.1. The room temperature ranged from 19 to 24 °C measured during experiments. The fluid plane as shown in Fig.3.2 is divided into two sections; a first section where the length of the injection zone is represented by d , and a second section where the length is represented by H .

3.3 Experimental parameters

The experiments were performed to estimate the shape and investigate the outer boundaries of gravity currents. The horizontal propagation of the denser fluid region is due to the initial momentum flux:

$$M_0 = Q_0 \cdot u_0 \quad (3.1)$$

where u_0 indicates the velocity of the initial salt water injection, Q_0 is the initial flow rate;

$$Q_0 = u_0 \cdot d^2 \quad (3.2)$$

and d denotes the side of the injection channel. The flow of the denser fluid into the bottom deep lighter fluid formed an immersed bulk due to the buoyancy flux:

$$B_0 = g'_0 \cdot Q_0 \quad (3.3)$$

where g'_0 , is the initial reduced acceleration of the gravity at the injection source, it defined as:

$$g'_0 = \frac{\rho_s - \rho_{water}}{\rho_{water}} \cdot g \quad (3.4)$$

and g is the acceleration of gravity. The fluid densities $\rho_{water} = 1000 \text{ kg/m}^3$ and $\rho_s = 1040 \text{ kg/m}^3$ are chosen in order to obtain the initially reduced gravity current $g'_0 = 0.39 \text{ m/s}^2$. Consequently, the initial (at the injection orifice) parameters Q_0 , M_0 , B_0 , and g'_0 can be derived for the flow analysis. The experimental parameters are presented in the non-dimensional form by adopting the following dimensionally independent scales (Hacker *et al.* 1996, Marino *et al.* 2005, Ungarish & Zemach 2005, and Papakonstantis & Christodoulou 2010):

- the Reynolds number based on the initial quantities is given by:

$$R = u_0 \frac{d}{\nu} \quad (3.5)$$

where ν is the kinematic viscosity of the salt fluid,

- the initial Richardson number is a ratio of buoyancy to the flow shear:

$$Ri = g (\rho_s - \rho_{water}) d / (\rho_{water} u_0^2) \quad (3.6)$$

- the initial Froude number is estimated by:

$$Fr = 1 / \sqrt{Ri} \quad (3.7)$$

- the Schmidt number:

$$Sc = \nu/D_m \quad (3.8)$$

$Sc=667$ is defined as the ratio of the kinematic viscosity $\nu = 10^{-6} m^2/s$ to the molecular diffusivity $D_m = 1.5 \times 10^{-9} m^2/s$ for the salt water. The values of the experimental control parameters are summarized in table 3.1.

Table 3.1: Inlet experimental control parameters conditions ($x/d=0$) with $Sc=667$ and $g'_0 = 0.39 m/s^2$

Variable	Exp.1	Exp.2	Exp.3	Exp.4	Exp.5	Exp.6
$Q_0(m^3/s)$	5.56×10^{-6}	8.33×10^{-6}	1.11×10^{-5}	1.39×10^{-5}	1.67×10^{-5}	1.94×10^{-5}
R	1111	1667	2222	2778	3333	3889
Fr	5.1	7.7	10.2	12.8	15.3	17.9
$u_0(m/s)$	0.22	0.33	0.44	0.55	0.66	0.77
$B_0(m^4/s^3)$	2.1×10^{-6}	3.1×10^{-6}	4.2×10^{-6}	5.2×10^{-6}	6.3×10^{-6}	7.3×10^{-6}
$M_0(m^4/s^2)$	1.23×10^{-6}	2.77×10^{-6}	4.9×10^{-6}	7.7×10^{-6}	1.11×10^{-5}	1.51×10^{-5}

3.4 Image analysis technique

3.4.1 ImageJ software

An image analysis technique was applied to assess the two-dimensional planar top view of the gravity current flow. Using the ImageJ image processing software allowed the video images to be captured directly from the camera during the experiments. Using the captured video tapes allowed the analysis of the experiments results as shown in Fig. 3.2. ImageJ is written in Java, which allows it to run on Linux, Mac OS X or Windows, in both 32-bit and 64-bit modes. ImageJ and its Java source code are freely available in the public domain, where no license is required. ImageJ can calculate area and pixel value statistics of user-defined selections. It can measure distances and angles. It can create density histograms and line profile plots. It supports standard image processing functions such as contrast manipulation, sharpening, smoothing, edge detection and median filtering. ImageJ can be zoomed up to 32:1 and down to 1:32. All analysis and processing functions are available at any magnification factor.

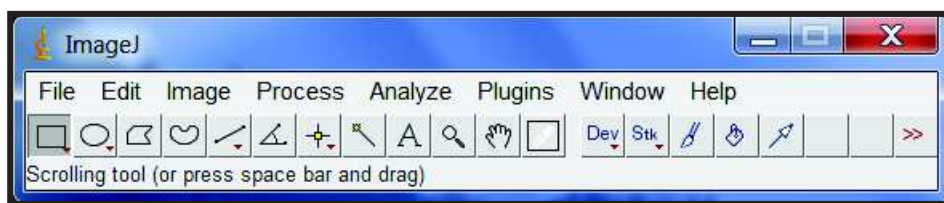


Figure 3.3: Overview of ImageJ software.

The program supports any number of windows (images) simultaneously, limited only by the computing available memory. ImageJ supports 8-bit, 16-bit and 32-bit (real) grayscale images and 8-bit and 32-bit color images. 8-bit images are represented using unsigned integers in the range 0 to 255. 16-bit images use unsigned integers (0 to 65,535) and 32-bit grayscale images use floating-point numbers.

3.4.2 Image processing

In Fig. 3.4, each frame of the movie acquired by the camera is a rectangular matrix (522×766 pixels) of integers representing the gray level “intensity level” of the corresponding pixel and ranging from 0 (black) to 255 (white). A ruler was dependent along both the length and width scales of the basin in order to obtain the conversion factor pixel/mm. The gray level of the interface between the two fluids was chosen as the threshold value.

Firstly, all frames were converted to grayscale. Subsequently, individual video frames are captured and stored in computer memory (use the submenu to save the active image in Tiff) as single instantaneous snap-shots of the flow sampled with an exposure of $n/38$ second “ n represented the increments of images”. The recorded images are analyzed in order to extract the position of the gravity current boundaries.

By opening a series of images in a chosen folder as a stack, images may have different dimensions and can be of any format supported by ImageJ as shown in Fig.3.4-a [the source image(*img1*)]. Afterwards, the frame where chosen before the dense gravity current released as the base image as shown in Fig.3.4-b [the destination image(*img2*)]. Instantaneously, the first injection introduced at the bottom of the basin of the video sequence of all the tests is considered as the time zero. The Process menu lists all commands related to image processing. Then, going to the submenu, image Calculator was used for *img1* and *img2* as shown in Fig.3.4-a, and b. The results shown in Fig.3.4-c were obtained using $img1 = |img1 - img2|$ in the Difference option of the ImageJ software.

Using the Image menu, the Adjust submenu contains commands that adjust the brightness/contrast, the threshold levels and the image size in order to produce clear image series as shown in Fig.3.4-d. By returning to the Process menu: the FFT submenu supports frequency domain display, editing and processing; using a Bandpass Filter in order to remove high frequencies (blurring the image) and low frequencies (similar to subtracting a blurred image). After using the FFT, the Binary submenu creates binary images (black and white) in the Process menu as well.

Assume that saline gravity currents injected are black and the background is white and represents the static fresh water as shown in Fig.3.4-e. Furthermore, in the Process menu, the Find Edge submenu was used as shown in Fig. 3.4-f (using the Sobel edge detector) in order to highlight sharp changes in intensity in the active image or selection. The final image is produced by combining the two derivatives using the square root of the sum of the squares.

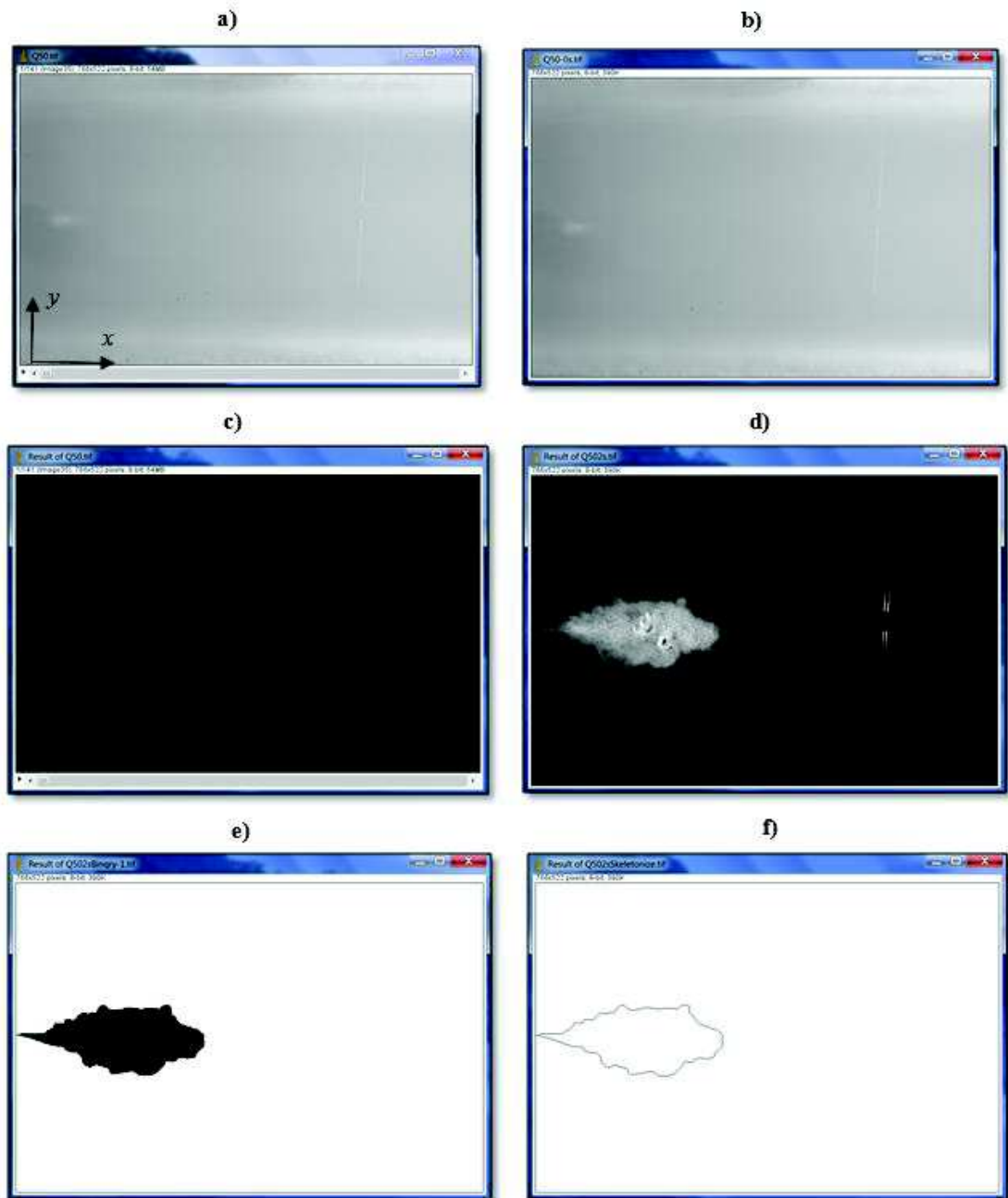


Figure 3.4: The steps of profile result realization for $R=2778$: (a) the source of images series without motion (*img1*) (b) the first image (*img2*) at $t=0$, (c) the Difference result of images series; Difference: $img1 = |img1 - img2|$, (d) the image after applying the adjust brightness/contrast at $t=2s$, (e) the binary image at $t=2s$, and (f) the skeletonized image at $t=2s$.

Finally, the Analyze menu contains commands related to statistical measurements on the image data, profile, histogram plotting and plugins related to image analysis. The Tools submenu provides access to various image analysis plugins. Then in Tools by using the Save XY Coordinate command, the system provides a text file where the XY coordinates and pixel value of all non-background pixels in the active image are written. Such data file helps drawing the final shape of the gravity current outer boundaries during its propagation. A comparison between the different flows rates presents different figures of image processing analyses as shown in figures 3.5-3.10.

A controlled quantity of red dye Rhodamine B was used to obtain the instantaneous images sequences of the saline gravity currents injection into the static fresh water. The procedure depended on each pixel in the image relating to the amount of dye uniformly distributed in the colored salt water tank and the intensity corresponding to images as shown in Fig. 3.11 (see Exp.4). This procedure is a simple way to assess the time-evolution within the gravity current, allowing the investigation of gravity current dynamics and mixing processes. Assuming that the diffusivity of the salt and dye are equal, the concentration of dye is proportional to the concentration of salt. The change in color and net attenuation can be used to make quantitative as well as qualitative measurements.

The experimental basin was placed in a dark room where the source of light could be controlled. The illumination is provided by the means of a light projector. The upper part of the basin is uncovered and the bottom part is covered with a smooth white plastic. During the experiments, no erosion of the bottom material was observed. Hence the heavier fluid flows under the lighter one, producing the gravity current. The experiment stops when the current's front reaches the end of the sidewall of the basin.

The estimation of the gravity current is based on a relation between the reflected light intensity and the concentration of dye present in the injection flow. As the light passes through the dye, the wavelengths of the complementary color are absorbed preferentially. The light intensity between the two video images gives a measure of the absorbed light amount, and hence the amount of dye in the various parts of the flow.

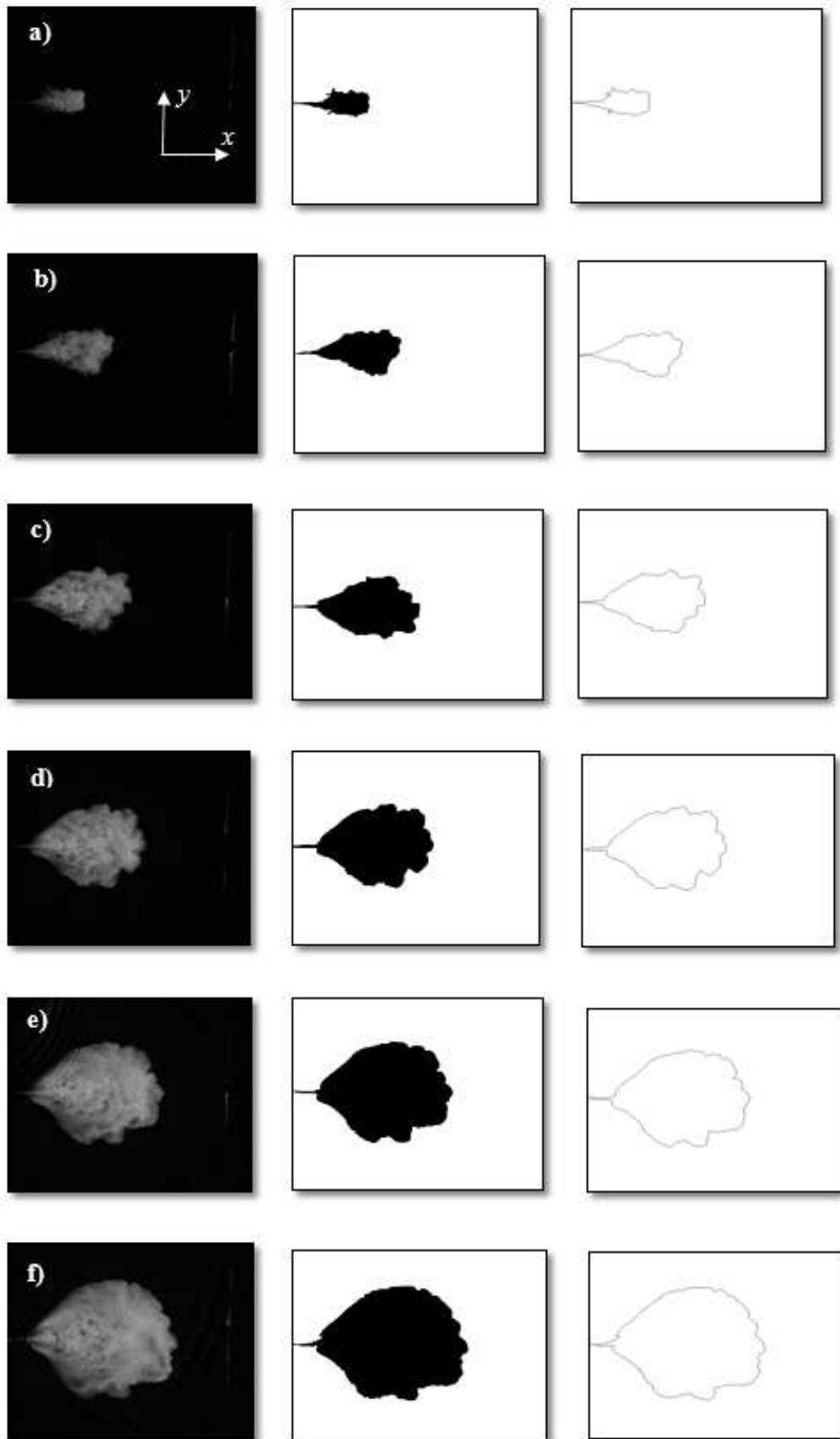


Figure 3.5: Experimental frames capturing by difference (row 1), make binary (row 2), and skeletonize (row 3) processes of two dimensional gravity currents performed with initial density $\rho_s = 1040kg/m^3$ and $\rho_{water} = 1000kg/m^3$ for $R=1111$, and frames acquired at (a) $t= 2s$, (b) $t=4s$, (c) $t=6s$, (d) $t=8s$, (e) $t=10s$, and (f) $t=12s$.

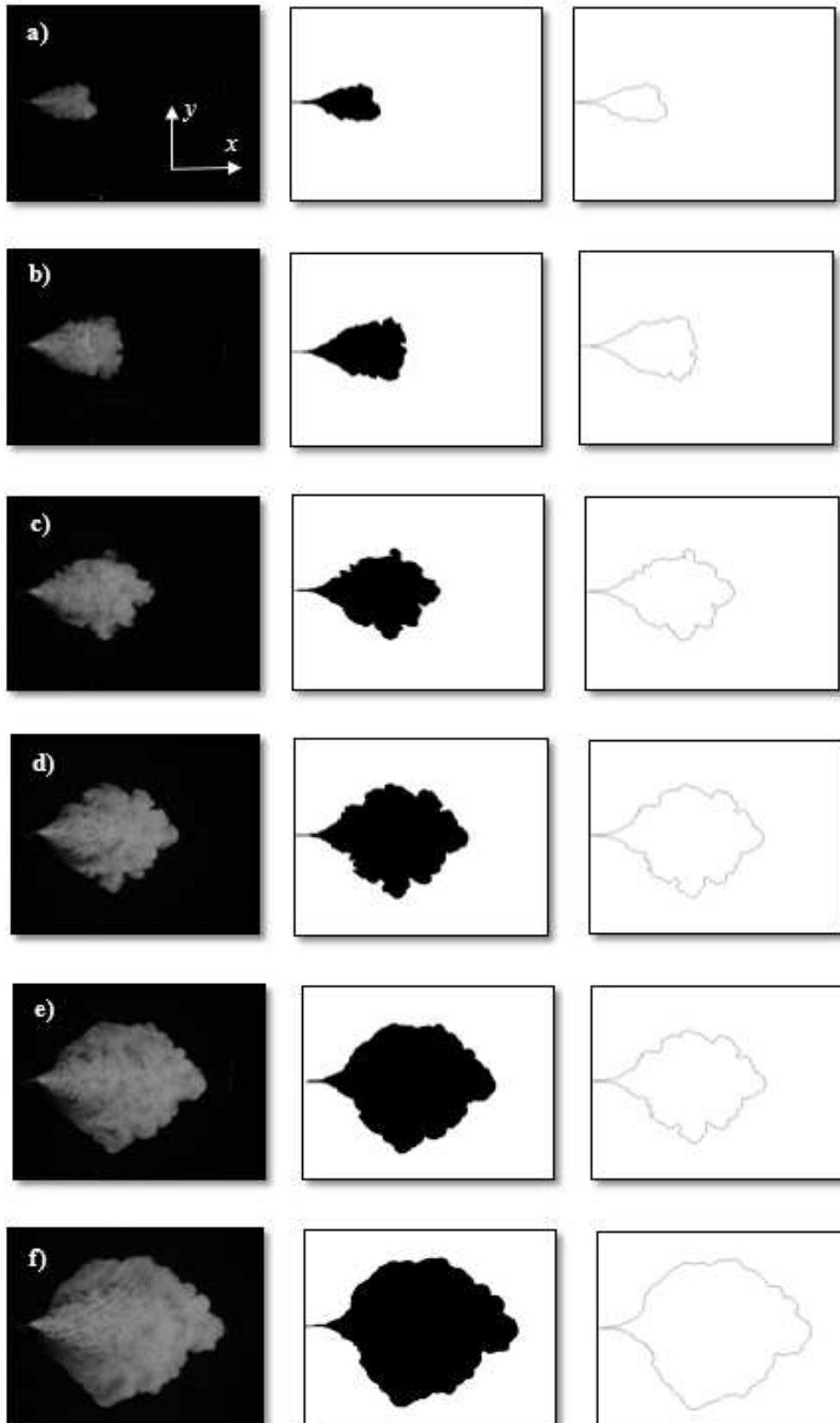


Figure 3.6: Experimental frames capturing by difference (row 1), make binary (row 2), and skeletonize (row 3) processes of two dimensional gravity currents performed with initial density $\rho_s = 1040 \text{ kg/m}^3$ and $\rho_{water} = 1000 \text{ kg/m}^3$ for $R=1667$, and frames acquired at (a) $t=2\text{s}$, (b) $t=4\text{s}$, (c) $t=6\text{s}$, (d) $t=8\text{s}$, (e) $t=10\text{s}$, and (f) $t=12\text{s}$.

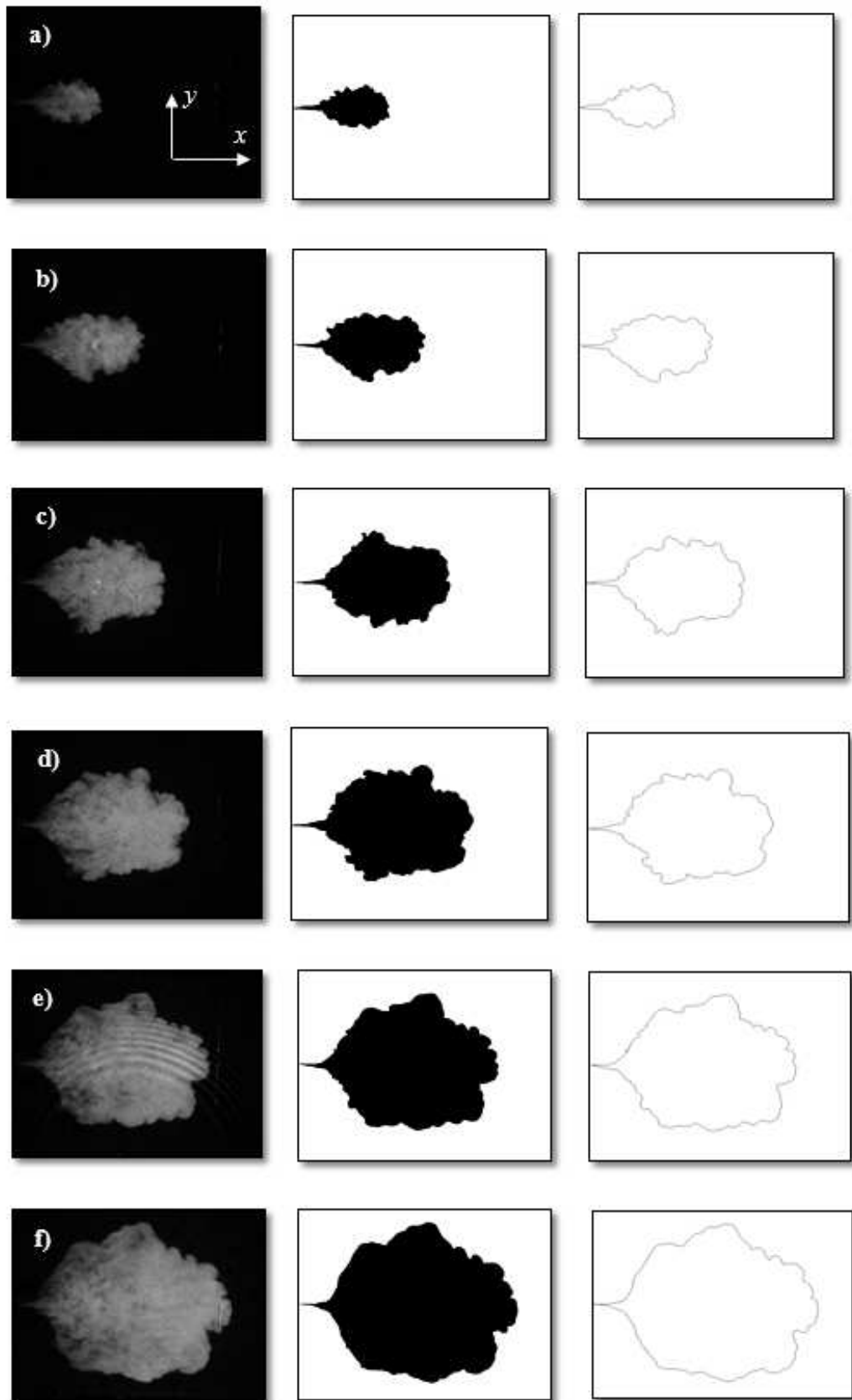


Figure 3.7: Experimental frames capturing by difference (row 1), make binary (row 2), and skeletonize (row 3) processes of two dimensional gravity currents performed with initial density $\rho_s = 1040 \text{ kg/m}^3$ and $\rho_{water} = 1000 \text{ kg/m}^3$ for $R=2222$, and frames acquired at (a) $t=2\text{s}$, (b) $t=4\text{s}$, (c) $t=6\text{s}$, (d) $t=8\text{s}$, (e) $t=10\text{s}$, and (f) $t=12\text{s}$.

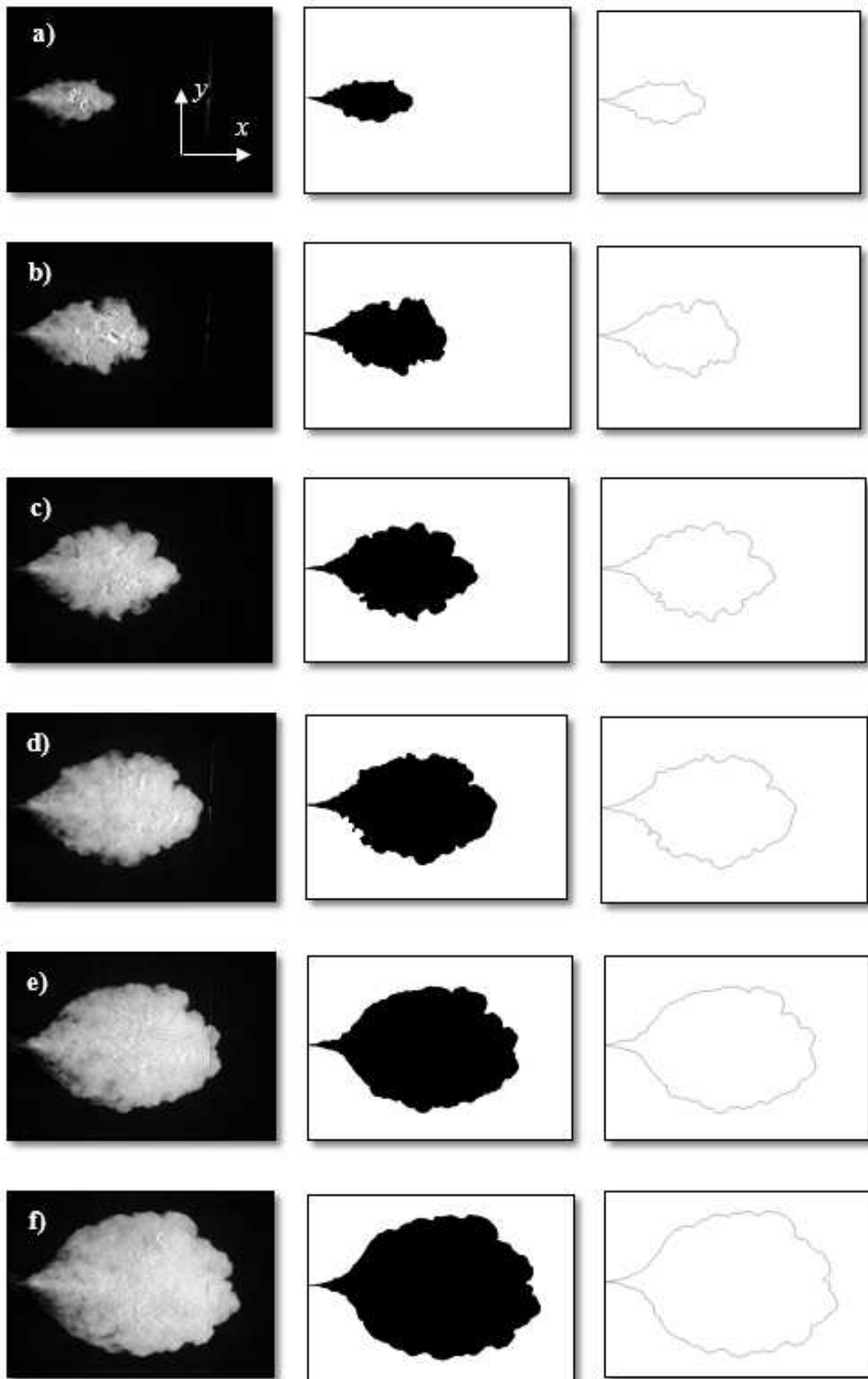


Figure 3.8: Experimental frames capturing by difference (row 1), make binary (row 2), and skeletonize (row 3) processes of two dimensional gravity currents performed with initial density $\rho_s = 1040 \text{ kg/m}^3$ and $\rho_{water} = 1000 \text{ kg/m}^3$ for $R=2778$, and frames acquired at (a) $t= 2\text{s}$, (b) $t=4\text{s}$, (c) $t=6\text{s}$, (d) $t=8\text{s}$, (e) $t=10\text{s}$, and (f) $t=12\text{s}$.

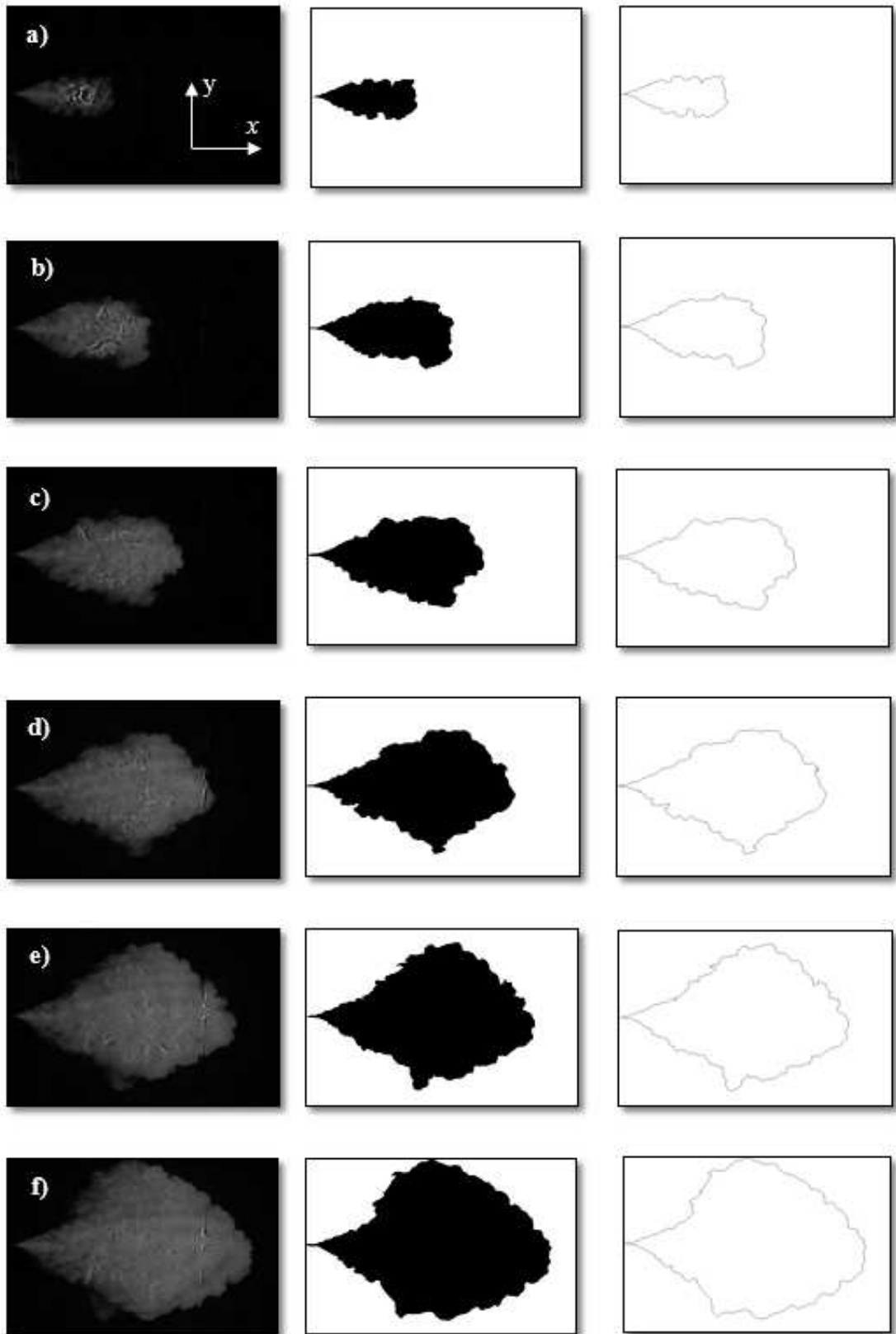


Figure 3.9 : Experimental frames capturing by difference (row 1), make binary (row 2), and skeletonize (row 3) processes of two dimensional gravity currents performed with initial density $\rho_s = 1040 \text{ kg/m}^3$ and $\rho_{water} = 1000 \text{ kg/m}^3$ for $R=3333$, and frames acquired at (a) $t= 2\text{s}$, (b) $t=4\text{s}$, (c) $t=6\text{s}$, (d) $t=8\text{s}$, (e) $t=10\text{s}$, and (f) $t=12\text{s}$.

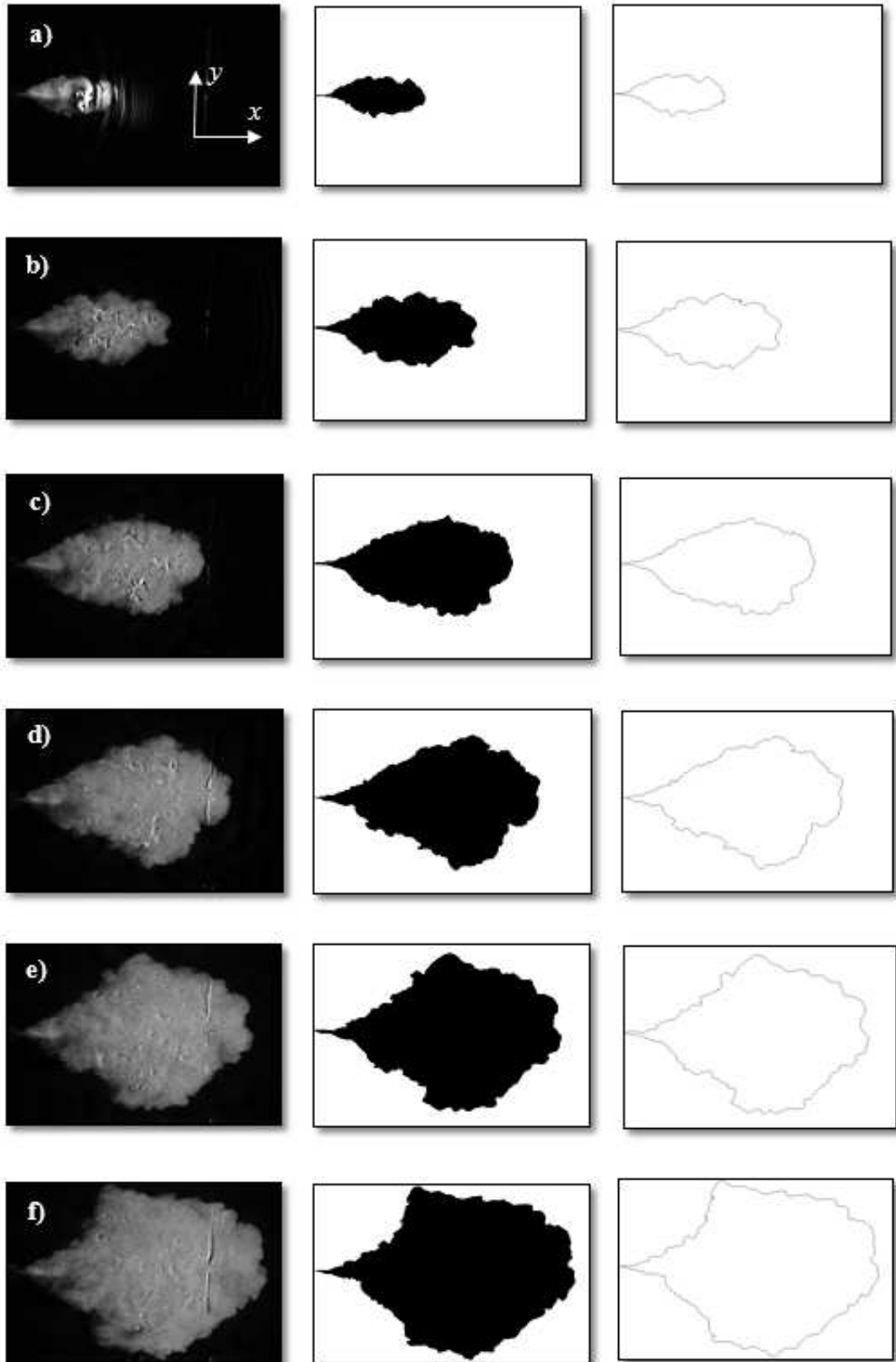


Figure 3.10: Experimental frames capturing by difference (row 1), make binary (row 2), and skeletonize processes (row 3) of two dimensional gravity currents performed with initial density $\rho_s = 1040kg/m^3$ and $\rho_{water} = 1000kg/m^3$ for $R=3889$, and frames acquired at (a) $t=2s$, (b) $t=4s$, (c) $t=6s$, (d) $t=8s$, (e) $t=10s$, and (f) $t=12s$.

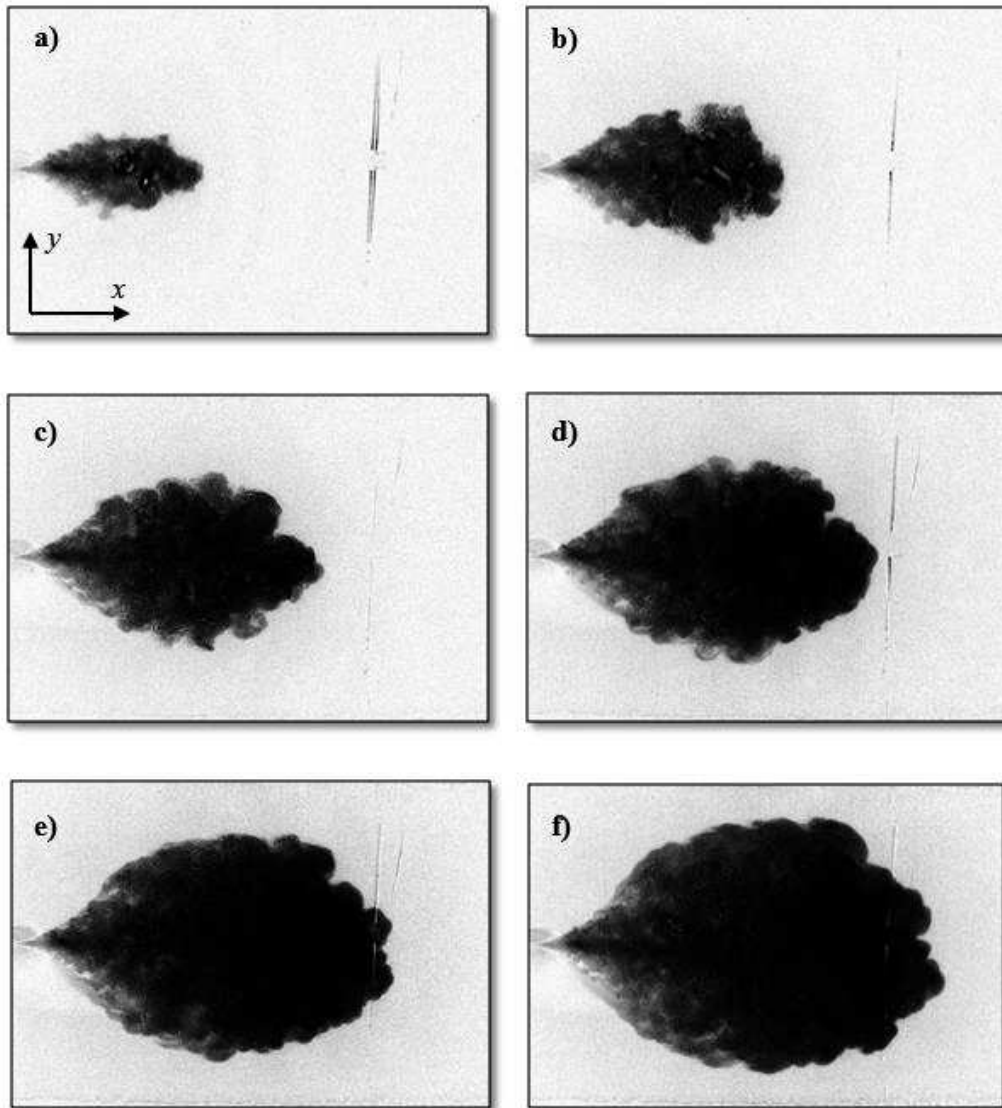


Figure 3.11: Original Frames capturing of two-dimensional gravity currents performed with initial density $\rho_s = 1040\text{kg/m}^3$ and $\rho_{water}=1000\text{ kg/m}^3$ for $R=2778$, and frames acquired at (a) $t= 2\text{s}$, (b) $t=4\text{s}$, (c) $t=6\text{s}$, (d) $t=8\text{s}$, (e) $t=10\text{s}$, (f) $t=12\text{s}$.

3.5 The configuration of gravity currents

3.5.1 Experimental front position

The instantaneous front position $x_f(t)$ was estimated through the instantaneous injection salt gravity current by taking the x -position of the foremost point of the outer boundary current. Also, the width of the gravity current increased with time in the y -direction. The two dimensional profiles of the gravity current showed that the flow is non-axisymmetric. This technique works well for flows without depth variations, where an approximately uniform light source can be placed in front of the experiment and where there are no free surface disturbances (see e.g. Cenedese & Dalziel, 1998).

The techniques of image processing are suitable for characterizing the gravity current flow. Fig. 3.12a-b shows the variation in time of the front position at both x and y directions of the visual outer boundaries, and shows that the gravity current increases with the initial density ρ_s of the injected current. For a certain time (t_i), the gravity current with an initial density covering a long distance is represented by front positions x_f for every flow rate. As expected, that the rapid expansion and change of the outer boundary shape depends on the releasing characteristic of the salt water, which presents a possibility of important current dynamics.

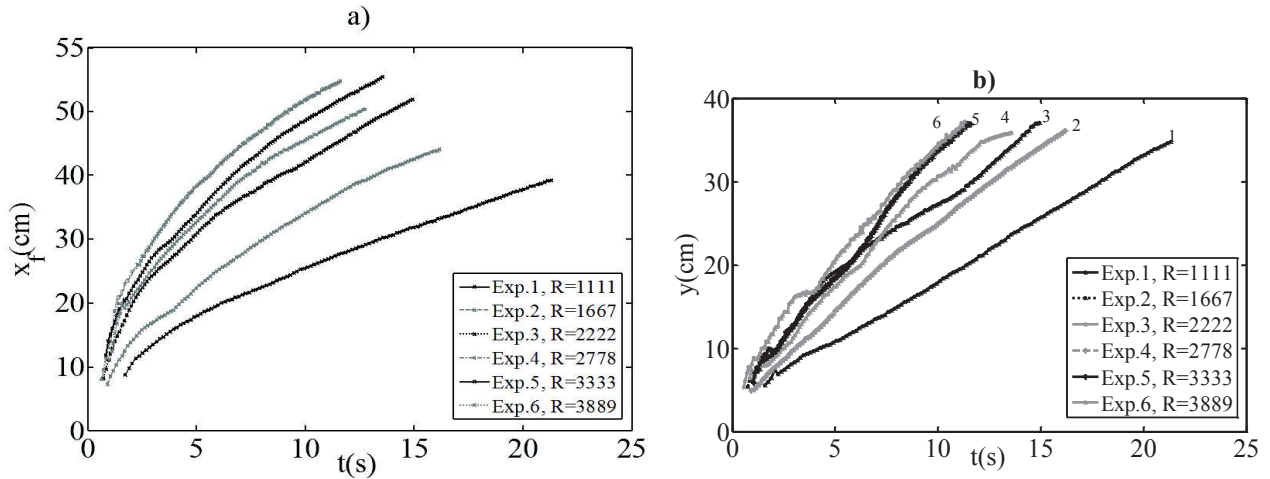


Figure 3.12: Dimensional characteristics of salt gravity currents front position versus time for the x and y axes.

All the experiments shown in this section are performed with d and H kept constant. The values of the experimental parameters are shown in Table 3.1. Once a horizontal injection is introduced into the ambient fluid, the motion is non-axisymmetric, and this adds further complexity to the model. Subsequently, the denser fluid collapses, flowing under the lighter one, and forming therefore the gravity current. The front position x_f is determined by a power law, varying in time and in horizontal bottom coordinate x - y according to Fig.3.12a.

3.5.2 Propagation Phase Transitions

For an initially salt gravity current flow injected over the horizontal bottom of fresh water, the gravity current initial motion is non-axisymmetric. Using the scaling law applied to a power fitting for measurements of the exponents B and D (for $x = At^B$, $y = Ct^D$). All the experiments gave a functional form of the internal details in a two-dimensional configuration with x and y varying with the time t . Table 3.2 shows the variation of distance with time, following the approximated laws: $x \sim t^{0.45}$, and $y \sim t^{0.65}$. It was found that B and D did not vary noticeably for all experiments, their values being around $B = 0.45 \pm 0.04$ and $D = 0.65 \pm 0.06$.

Table 3.2: Scaling laws for two dimensions gravity currents: $x = f(t)$, and $y = f(t)$.

Variable	Exp.1	Exp.2	Exp.3	Exp.4	Exp.5	Exp.6
$Q_o(m^3/s)$	5.56×10^{-6}	8.33×10^{-6}	1.11×10^{-5}	1.39×10^{-5}	1.67×10^{-5}	1.94×10^{-5}
$x_f(m)$	$108.5t^{0.49}$	$128.8t^{0.47}$	$144.5t^{0.46}$	$163.4t^{0.45}$	$181.2t^{0.43}$	$204.4t^{0.42}$
$y(m)$	$46t^{0.71}$	$54.7t^{0.69}$	$56.3t^{0.67}$	$66.4t^{0.64}$	$76.3t^{0.62}$	$84.3t^{0.59}$
$t(s)$	$0.16 < t(s) < 20.64$	$0.13 < t(s) < 15.9$	$0.1 < t(s) < 14.7$	$0.1 < t(s) < 14.5$	$0.1 < t(s) < 13.3$	$0.08 < t(s) < 10.9$

Fig 3.13 shows the outer boundary when the front position and the time are normalized by the geometric and experimental parameters introduced earlier. Generally, two distinct phases were observed during the development of the gravity current: i) The equilibrium between the inertia and the gravity forces, characterized by a linear relation between the front position and the time after the injection started. ii) The equilibrium between the viscous and the gravity forces in which the current moves under the balance between buoyancy and viscous forces, while the front position is a nonlinear function of time. Consequently, the propagation of a gravity current can be viewed as an evaluative phenomenon since the gravity current grows with time.

In the inertia-buoyancy phase, the gravity current propagates starts experiencing an increasing viscous force. The viscous force may become comparable to the inertia force after a period of time. After that, the effect of viscosity becomes more and more pronounced, and the propagation of the gravity current may transition into the viscous-buoyancy phase. Furthermore, the propagation is mainly dominated by the driving buoyancy force and the retarding viscous force, with negligible effects due to the inertia force. All the measurements performed start about one second after the starting of the gravity current injection because it was difficult to measure the profiles of the gravity current during its initial stage of development. Huppert and Simpson (1980) studied the transition in their dense gravity current experiments and provided an expression for the transition time based on their experimental data. Different integral and shallow water models accurately predict the volume motion for such cases. Huppert (1982) derived the transition time expressions for two-dimensional and radial gravity currents from order-of-magnitude relationships.

Although by using the same experimental 2D procedure as Huppert (1982) and Rottman & Simpson (1983) it can be predicted that dense gravity currents develop not in three phases during their evolution, but only in the second and third phases (see §2.1).

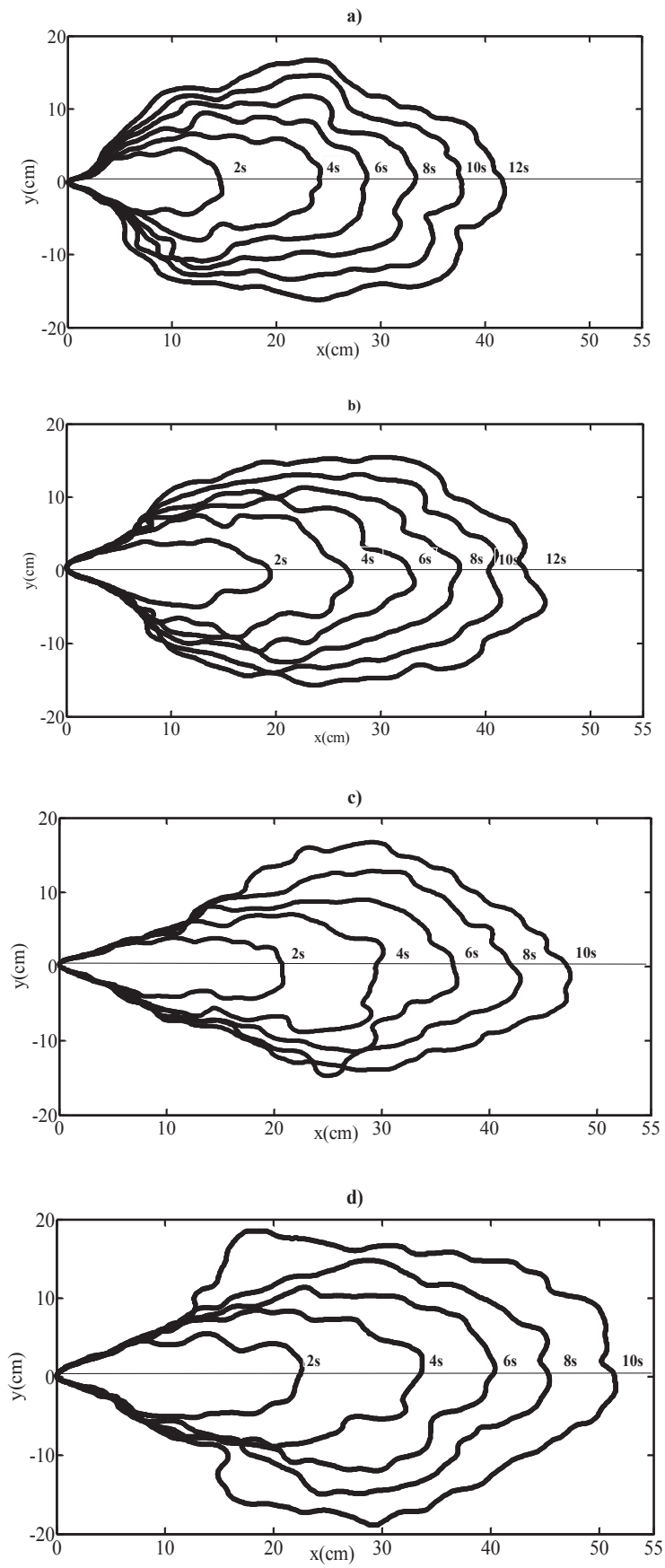


Figure 3.13: Experimental outer positions of the mixing gravity current at $x_f(y, t)$: a) $R=2222$; b) $R=2778$; c) $R=3333$; d) $R=3889$.

Bonnecaze *et al.* (1993) derived critical Reynolds number criterion for the transition based on the transition time expression of Huppert and Simpson (1980). Indeed, the first phase seems not to occur in the gravity current's evolution, because of the nonexistence of the resistance due to the bottom shear stress of the smooth bottom used. A second factor is the decreasing of the gravity current buoyancy due to the entrainment of the ambient fluid at the bottom level. This may cause an earlier end of the first phase as shown in Fig.3.14. Amy *et al.* (2005) widened the work of Hallworth & Huppert (1998) and explored the presence of abrupt transitions in homogeneous gravity currents. They notably confirmed the presence of abrupt transitions to dynamic changes in the propagation phases. The slumping phase "first phase" transitions directly to the viscous-buoyancy phase that is similar to the work presented in this study.

3.5.3 The lobe-cleft instabilities

In this study, the small density inversions occur at the outer edges boundaries of the intrusion as saline gravity current is raised and the ambient fresh water is pushed below it. These inversions are distinct from the larger-scale billows caused by the shear instability on the outer edges boundaries of the intrusion as shown in Fig.3.14. This mode of instability which occurs only when the gravity current is propagating along a no-slip boundary, is a convective instability known as lobes and clefts (Simpson 1972). A top-view of the gravity current planform, using the shadowgraph technique visualizes the flow in Fig.3.14. The evolution of a snapshots lobe-cleft pattern was found and measured as a function of time as shown in Table 3.2 and also in Fig.3.13.

3.6 Summary

This chapter begins with a brief description of the experiments brought out for modelling bottom gravity currents jet flows, focusing on the use of salt water to create saline gravity currents. These laboratory experiments are used to validate the numerical simulation model. The experimental apparatus used in the experiments of this study is described, and the image processing techniques applied are discussed. The experimental data collected come firstly from visual method (e.g. visual technique measurements, red dye Rhodamine B) and from conductivity and salinity probe measurements. This method provides a large amount of information, enabling techniques of the bottom gravity current propagation and dilution of a denser current jet flow through a static lighter ambient fluid. Such as the studied in this dissertation, to be measured in detail. Further details of different experiments are given in the follow.

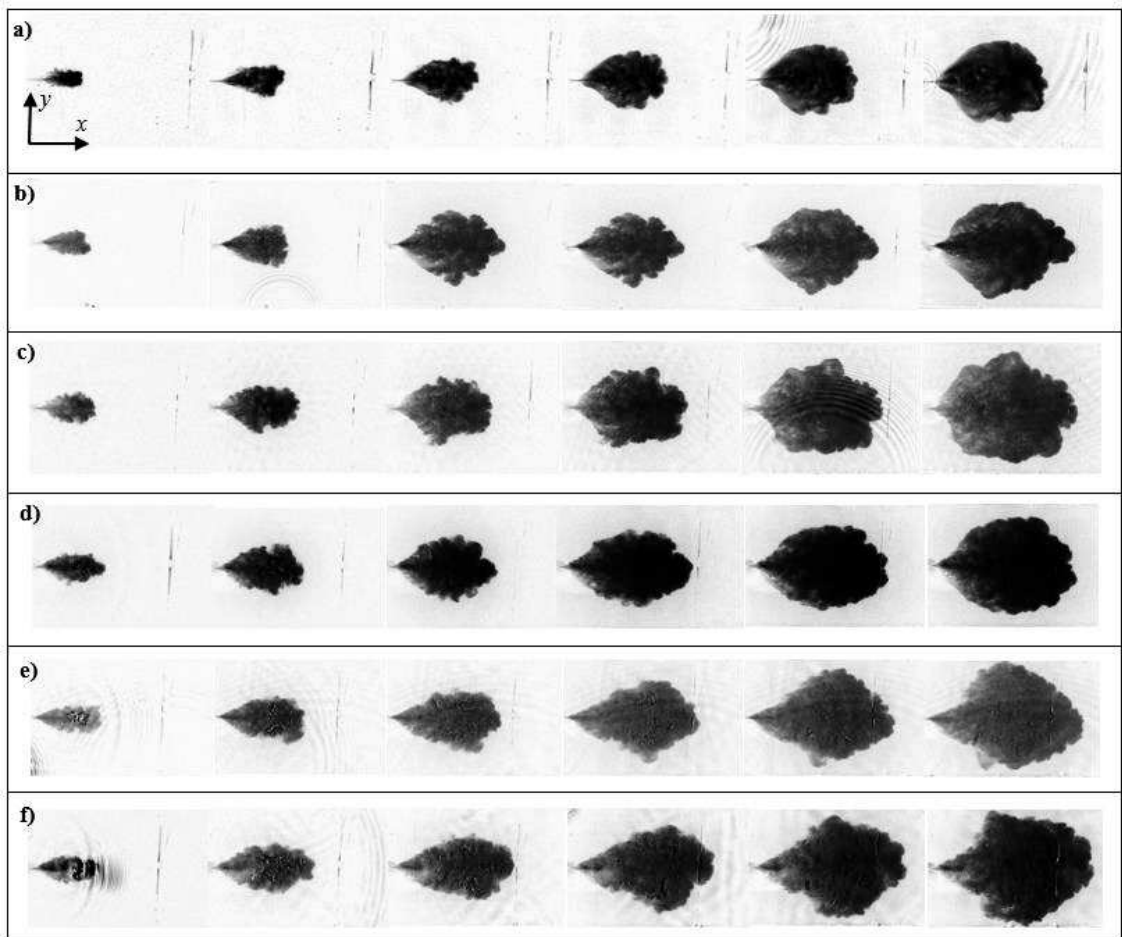


Figure 3.14: Snapshots with 2D lobes and clefts structures at the front of the intruding gravity current development over a smooth bottom for: (a) $R=1111$, (b) $R=1667$, (c) $R=2222$, (d) $R=2778$, (e) $R=3333$, and (f) $R=3889$ at $t=2, 4, 6, 8, 10,$ and 12 s respectively.

Chapter 4: 3D Numerical Model and Computational Details

4.1 Introduction

Many situations where an accidental or intentional release of dense fluid such as industrial or agricultural effluents into river or ocean can pollute the environment. The ambient liquid can slow down or speed up the propagation of a dense gravity current, leading to significant differences in the injection dose and exposure time at a given location and altering the area affected by the release. In this Chapter, numerical simulations are using RANS (Reynolds Averaged Navier Stokes) with $k-\varepsilon$ and diffusion-convection equations. Part of the numerical model presented in this chapter appeared in Dhafar *et al.* (2015c)⁴. A turbulent model of the 3D propagation and mixing of a saline gravity current into ambient fresh water over a smooth horizontal bottom, incompressible fluid, two-fluids, no-slip boundary condition, and unsteady formulation.

4.2 Navier-Stokes Equations

Navier-Stokes equations are a set of partial differential equations of space and time that describe the motion of fluids with flow velocity and pressure as unknown functions. The fluid can be a liquid or a gas. The general Navier-Stokes equations can be written as:

$$\rho\left(\frac{\partial u}{\partial t} + u\nabla u\right) = -\nabla p + \nabla \cdot T + f \quad (4.1)$$

where: ρ =density, u =velocity, p =pressure, T =stress tensor, and f =sum of external forces.

In general, Eq. (4.1) representing the momentum equation is equivalent to Newton's second law of motion. The left hand side of the equation is the product of density and acceleration; the right hand side is the sum of forces per volume acting on a fluid particle, an infinitesimal fluid volume. It is completed by Eq. (4.2) representing the continuity equation which ensures conservation of mass for an incompressible fluid.

$$\frac{\partial \rho}{\partial t} + \nabla \cdot (\rho u) = 0 \quad (4.2)$$

⁴ Dhafar, I. A., Latrache, N., Niang, P., and Nsom, B. (2015). Etallement d'un jet horizontal miscible de flottabilité positive. 22ème Congrès Français de Mécanique, Lyon, France, 24 au 28 Août.

All the variables above are functions of time t and space (x , y , and z). The velocity vector \mathbf{u} is sometimes split into its components u , v , and w . In the following sub-sections, each of the terms in the equations is explained.

4.3 Three-dimensional numerical modeling

Since there is no known analytical solution of the momentum and continuity equations except for some model simplified cases, they must be solved numerically. The model simultaneously solves the governing equations of the three-dimensional motion of fluids, the conservation of mass, and the transport of numerical variables. RANS (Reynolds-average Navier-Stokes), the volume of fluid (VOF) model using a single set of momentum equation, and $k - \varepsilon$ are used to describe the flow field in this work. The absence of surface tension and the presence of molecular diffusion can affect the miscible gravity currents formed by the salt and fresh water. A finite-volume scheme has been widely applied in the various engineering branches of fluid mechanics due to its high accuracy. However, the application of the CFD model to the research for turbulent gravity currents in a basin is a relatively new approach in a three-dimensional configurations.

4.3.1 The numerical model

Certain assumptions were made to simplify the complexity of a saline gravity current flow dynamics. The governing equation describing its dynamics in an ambient fluid are derived from principles of mass, momentum, and energy conservation. A volume-fraction transport equation is used to characterize the mixing of the ambient fluid with the saline fluid. In order to provide predictions of the saline gravity current flow within the basin containing fresh water adjacent to the wall, the form of model given below must be enlarged in three ways. These are:

- i. Viscous diffusion of k and ε must be included.
- ii. The terms containing the C 's in equations (4.10) and (4.11) will become dependent upon the turbulence Reynolds number, defined by: C_μ , $C_{\sigma k}$, $C_{\sigma \varepsilon}$, C_1 , and C_2 .
- iii. Further terms must be added to account for the fact that the dissipation processes are not isotropic.

The equations have been solved using the Finite Volume method, with the application of the VOF method. In general, the volume-of-fluid method (VOF) is a method for keeping track of two different fluids in two-phase flow simulations. The method tracks the volume of each fluid in each cell. For each time iteration, the interface between the two fluids is reconstructed from the volume data.

As well, the advection-diffusion equation for the volume fraction of salt water c is solved. The Reynolds Averaged mass and momentum conservation equations for the incompressible saline mixture can be expressed as:

$$\frac{\partial \bar{u}_j}{\partial x_j} = 0 \quad (4.3)$$

$$\frac{\partial \rho \bar{u}_i}{\partial t} + \frac{\partial \rho \bar{u}_i \bar{u}_j}{\partial x_j} = -\frac{\partial \bar{p}}{\partial x_i} + \frac{\partial}{\partial x_j} \left(\mu \frac{\partial \bar{u}_i}{\partial x_j} - \rho \overline{u'_i u'_j} \right) - \rho g \delta_{i3} \quad (4.4)$$

$$-\rho \overline{u'_i u'_j} = \mu_t \left(\frac{\partial \bar{u}_i}{\partial x_j} + \frac{\partial \bar{u}_j}{\partial x_i} \right) - \frac{2}{3} \rho k \delta_{ij} \quad (4.5)$$

where \bar{u}_i denotes the Reynolds-averaged velocity in the x_i directions (also referred to as x, y, z); \bar{p} is the Reynolds-averaged pressure; μ and ρ are respectively the viscosity and the density of the saline mixture fluid.

The gravitational acceleration acting along x_3 or z direction is g ; $\overline{u'_i u'_j}$ is the Reynolds-stress tensor obtained by using the Boussinesq hypothesis (Eq. 4.5) and δ_{ij} Kroneker delta; k is half the trace of the Reynolds-stress tensor, referred to as turbulent kinetic energy can be expressed by:

$$k = \frac{1}{2} \overline{u'_i u'_i} \quad (4.6)$$

The turbulent viscosity can be written as:

$$\mu_t = C_\mu \rho \frac{k^2}{\varepsilon} \quad (4.7)$$

where C_μ is one of the constants of the $k - \varepsilon$ model (see table 4.1); and ε is the turbulent energy dissipation rate.

The Navier-Stokes equations are solved as usual with the interpolated fluid properties. No boundary conditions need to be applied at the interface (Ashley *et. al.* 2003). The equations (4.3) to (4.5) represent the governing equations for the turbulence regime. The equations (4.3) and (4.5) above are called the Reynolds-Averaged Navier-Stokes (RANS), and the details of these equations are detailed in section 4.2.

Consider the heavier fluid to be below the interface, and the lighter fluid above the interface. A volume-fraction transport equation is used to characterize the mixing of fresh water with the injected saline gravity current. The Reynolds-Averaged mass and momentum conservation equations have been solved, with density ρ and viscosity μ determined in each cell by the volume fraction of salt to the fresh water present. Thus, if the volume fraction of salt water is c , and the density of salt water is $\rho_s = 1040 \text{ kg/m}^3$ and the density of fresh water $\rho_{water} = 1000 \text{ kg/m}^3$. The density and viscosity are linearly interpolated between the two fluids, respectively as:

$$\rho = c\rho_s + (1 - c)\rho_{water} \quad (4.8)$$

$$\mu = c\mu_s + (1 - c)\mu_{water} \quad (4.9)$$

The volume fraction value in a cell is in the range $[0, 1]$ and defines how much of the cell is filled with heavier fluid. The remaining part of the cell is filled with light fluid. The volume-fraction c equal 1 for saline gravity current fluid, c equal 0 for ambient fresh water, and for mixture $0 < c < 1$.

The standard turbulence model employed in our simulations for computation of the turbulence viscosity ν_t is the realizable $k - \varepsilon$ model, based on the Reynolds-Averaged Navier-Stokes (RANS) equations. This model was chosen over the standard $k - \varepsilon$ model because it is more accurate at predicting the spreading rate of saline bottom gravity current injection into ambient fresh water. The equations for k and ε are given in Eqs. (4.10) and (4.11) respectively:

$$\frac{\partial k}{\partial t} + \bar{u}_j \frac{\partial k}{\partial x_j} = \frac{\partial}{\partial x_j} \left[\left(\nu + \frac{\nu_t}{C_{\sigma k}} \right) \frac{\partial k}{\partial x_j} \right] + \nu_t \left(\frac{\partial \bar{u}_i}{\partial x_j} + \frac{\partial \bar{u}_j}{\partial x_i} \right) \frac{\partial \bar{u}_i}{\partial x_j} \quad (4.10)$$

$$\frac{\partial \varepsilon}{\partial t} + \bar{u}_j \frac{\partial \varepsilon}{\partial x_j} = \frac{\partial}{\partial x_j} \left[\left(\nu + \frac{\nu_t}{C_{\sigma \varepsilon}} \right) \frac{\partial \varepsilon}{\partial x_j} \right] + \frac{\varepsilon}{k} \left[C_1 \nu_t \left(\frac{\partial \bar{u}_i}{\partial x_j} + \frac{\partial \bar{u}_j}{\partial x_i} \right) \frac{\partial \bar{u}_i}{\partial x_j} - C_2 \varepsilon \right] \quad (4.11)$$

The model contains five standard empirical constants which values are given in table 4.1 by (Launder & Spalding, 1974, Huang *et al.* 2005, Gerber *et al.* 2011, and Guillas *et al.* 2014). These values of constants were chosen for two reasons: i) they were obtained by data fitting for a wide range of flows (Launder & Spalding 1974); ii) they provided a good agreement with experimental data for the gravity currents studied (Huang *et al.* 2005, and Gerber *et al.* 2011). The kinematic turbulent viscosity can be defined as:

$$\nu_t = \frac{\mu_t}{\rho} \quad (4.12)$$

Table 4.1: The values of the empirical constants in the high Reynolds number of $k - \varepsilon$ model.

C_μ	$C_{\sigma k}$	$C_{\sigma \varepsilon}$	C_1	C_2
0.09	1.3	0.77	1.44	1.92

The terms containing $C_{\sigma k}$ and $C_{\sigma \varepsilon}$ in equations (4-10) and (4-11) represent the diffusion rates of k and ε respectively. These constants therefore possess the significance of turbulent Prandtl numbers for transport processes in equation, consequently, their values should lie close to unity accords with expectations. Equations (4.10 and 4.11) were solved using the Finite Volume method, with application of the VOF method. Density ρ and viscosity μ are determined in each cell by the volume fraction of the salt water c . The density variation in a cell is due to the densities difference between salt water and fresh water only, since the temperature is kept constant.

According to the state equation of density (Eq. 4.8), the mixture density and viscosity vary linearly with the volume fraction c , since ρ_s and ρ_{water} are kept constant in the numerical calculations. So, the advection-diffusion equation for the volume of the salt water fraction c was used to describe the mixture density and the viscosity in the flow (Eq. 4.13) as:

$$\frac{\partial c}{\partial t} + \frac{\partial \bar{u}_j c}{\partial x_j} = \frac{\partial}{\partial x_j} \left[\left(D_m + \frac{\mu_t}{\rho S c_t} \right) \frac{\partial c}{\partial x_j} \right] \quad (4.13)$$

where $[D_m + (\mu_t/\rho S c_t)]$ is the total diffusivity, $D_m = 1.5 \times 10^{-9} m^2/s$ is the molecular diffusion of the salt water, and $S c_t$ is the turbulent Schmidt number defined as the ratio of the turbulent viscosity to the turbulent diffusivity of the mixture fluid transported in the flow.

Three values of $S c_t = 0.5, 1$ and 2 were investigated in our numerical simulations. For $S c_t=0.5$, the numerical saline jet is over-diffusive where the numerical front is faster than the experimental front, while for $S c_t=2$, the numerical front is slower than the experimental front. For $S c_t=1$, the numerical simulations of the front position present a good agreement with the experimental data. A closer value of $S c_t=1.3$ was used in the numerical models of turbidity current (Huang *et al.* 2005) and of the saline density current (Gerber *et al.* 2011), where the numerical results present a good agreement with the experimental data.

4.3.2 Initial and boundary conditions

4.3.2.1 Initial conditions

Generally, it is difficult to put a reasonable initial guess for an unsteady-state simulation or suitable initial conditions for a dynamic one. If the velocity field is initialized by zero, the flow takes some time to become fully turbulent. The instantaneous velocities were measured at geometrical center of inlet injection, the inlet velocity \bar{u} is given as:

$$u_o = \frac{Q_o}{d^2}, v_o = 0, w_o = 0 \quad (4.14)$$

Therefore, we activate the $k-\varepsilon$ model at a certain time $t_* > 0$ after the startup. During the ‘laminar regime’ this means the initial phase ($t \leq t_*$) in the injection, a constant effective dynamic turbulent viscosity $\mu_{t_o} = \mathcal{O}(\mu_t)$ is prescribed. The values to be assigned to k and ε at $t = t_*$ are uniquely defined by the choice of μ_{t_o} and of the default mixing length in our case represented by d , and ($d = l_o$) where $l_o \in [l_{min}, l_{max}]$. Because, the numerical domain has dimensions $l_x = 0.55m, l_y = 0.4m$, and $l_z = 0.05m$. The threshold parameter l_{min} corresponds to the size of the smallest admissible eddies. We have:

$$k_o = \frac{(0.05u_o)^2}{2}, \quad \varepsilon_o = \frac{C_\mu^{3/4} \cdot k_o^{1/2}}{d} \quad \text{at } t \geq t_* \quad (4.15)$$

Table 4.2 presents the inlet conditions measured at the inlet ($x/d=0$). The initial values of k and ε can be estimated by means of a zero-equation (mixing length) turbulence model or computed using an extension of the inflow or wall boundary conditions (see below) into the interior of the computational domain. The inlet Reynolds number R and the turbulent viscosity ratio ν_t/ν indicated that the inflow was weakly turbulent, and the inflow is weakly turbulent, while the Richardson number Ri indicated that the inflow was supercritical.

Table 4.2: Inlet conditions ($x/d=0$) with $Sc=667$ and $g'_0 = 0.39 \text{ m/s}^2$.

Variable	Run1	Run2	Run3	Run4	Run5	Run6
$Q_o(\text{m}^3/\text{s})$	5.56×10^{-6}	8.33×10^{-6}	1.11×10^{-5}	1.39×10^{-5}	1.67×10^{-5}	1.94×10^{-5}
R	1111	1667	2222	2778	3333	3889
Fr	5.1	7.7	10.2	12.8	15.3	17.9
Ri	0.04	0.02	0.01	0.006	0.004	0.003
$k_o(\text{m}^2/\text{s}^2)$	62×10^{-6}	14×10^{-5}	25×10^{-5}	39×10^{-5}	56×10^{-5}	76×10^{-5}
$\varepsilon_o(\text{m}^2/\text{s}^3)$	16×10^{-6}	54×10^{-6}	13×10^{-5}	25×10^{-5}	43×10^{-5}	68×10^{-5}
ν_t / ν	22	32	43	54	65	75

Fresh water was therefore entrained into the current body because the inertial forces dominated the stabilizing buoyancy forces (Gerber *et al.* 2011). The domain ($105 d$ to $110 d$, 0 to $80 d$, and $10 d$) placed far from the inlet represents the outlet of the overflow discharge. The Schmidt number Sc , defined as the ratio between the kinematic viscosity and the molecular diffusivity, was set to $Sc=667$ (the reference value for salt water).

4.3.2.2 Boundary conditions

The inlet boundary is used if the flow into (or out of) the domain is known. The normal component of the velocity is set to some prescribed value and the tangential component is set to zero. At the inflow boundary Γ_{in} , we prescribe all velocity components and the values of k and ε :

$$u = g, \quad k = C_{bc}|u|^2, \quad \varepsilon = \frac{C_\mu^{3/4} \cdot k_o^{1/2}}{d} \quad \text{on } \Gamma_{in} \quad (4.16)$$

where $C_{bc} \in [0.09, 1.92]$ is an empirical constant (see Table 4.1) and $|u| = \sqrt{u \cdot u}$ is the Euclidean norm of the velocity. The boundary condition for smooth surface is used to calculate the bottom and all the walls with flow interior.

When fluid is to flow freely across the boundary, the velocity gradient at the boundary is set to zero. Outlets should be placed far away from any obstacle such that the flow is allowed to develop and stabilize before reaching the boundary. If the flow is not fully developed at the boundary, the Neumann boundary conditions used for the velocity would be physically incorrect and lead to inaccurate results (Versteeg & Malalasekera 1995).

At the outlet Γ_{out} , the normal gradients of all variables are set equal to zero, which corresponds to the Neumann ('do-nothing') boundary condition:

$$n \cdot [\nabla u + \nabla u^T] = 0, \quad n \cdot \nabla k = 0, \quad n \cdot \nabla \varepsilon = 0, \quad \text{on } \Gamma_{\text{out}} \quad (4.17)$$

In the finite element framework, these homogeneous boundary conditions imply that the surface integrals resulting from integration by parts in the variational formulation vanish.

At an impermeable solid wall Γ_w , the normal component of the velocity is set equal to zero:

$$n \cdot u = 0 \quad \text{on } \Gamma_w \quad (4.18)$$

The no-slip boundary condition is used for walls in turbulent flow simulations. No-slip boundary conditions are applied at the basin walls and turbulent wall functions are employed near the wall. The flow field is initialized with the fluid at rest everywhere, this means the velocity is set to zero at the wall boundary. There is no flow across the wall boundary and the flow does not slip along the wall. Consequently, the symmetry boundary is used for symmetry axes or planes. Because of symmetry, the flow through the plane must be zero. The tangential velocity must be equal on each side of the symmetry plane, therefore the normal derivative of the tangential velocity must be zero.

Pressure boundaries should also be placed far away from any obstacles such that the flow is allowed to develop and stabilize before reaching the boundary. At the basin outlet, a zero-gradient or outflow condition is imposed. Because the simulation is incompressible, only the pressure gradient of the ambient surface equal to the atmospheric pressure, and therefore the outlet pressure is set to a reference value of zero. The boundary conditions are summarized in Table 4.3.

Table 4.3: Boundary conditions.

Variable	Inlet	Left	Right	Bottom	Atmosphere	FrontBack
u_o	fixedValue value u_o	fixedValue value 0	fixedValue value 0	fixedValue value 0	fixedValue value 0	fixedValue value 0
p_rgh	fixedFlux Pressure value 0	fixedFlux Pressure value 0	fixedFlux Pressure value 0	fixedFlux Pressure value 0	fixedFlux Pressure value 0	fixedFlux Pressure value 0
c	fixedValue 1	zeroGradient	zeroGradient	zeroGradient	zeroGradient	zeroGradient
k	zeroGradient	kqRWall Function Value k_0	kqRWall Function Value k_0	kqRWall Function Value k_0	zeroGradient	kqRWall Function Value k_0
ε	zeroGradient	epsilonWall Function Value ε_0	epsilonWall Function Value ε_0	epsilonWall Function Value ε_0	zeroGradient	epsilonWall Function Value ε_0
ν_t	Calculated Value 0	nutkWall Function Value 0	nutkWall Function Value 0	nutkWall Function Value 0	Calculated Value 0	nutkWall Function Value 0

A spatial injection distribution of the scalar is imposed at $t=0$ with a discontinuity in correspondence of the plane $x=d$ (or h): in our case the initial length same the depth of the saline gravity current h . This depth represents the injection channel as a square side section Fig.4.1. The salinity values are fixed to obtain the initial density value of ρ_s on the injection plane of h , whereas the density is equal to ρ_{water} elsewhere in the basin.

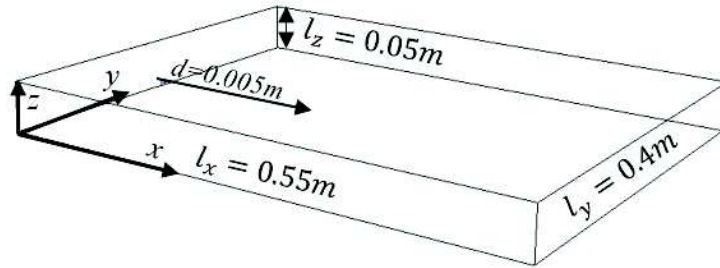


Figure 4.1: The configuration of an injection by a square channel and into fresh water basin.

4.4 Numerical method description

The simulation of the three-dimensional spreading of the saline gravity current injection by OpenFOAM is the most popular open-source of Computational fluid dynamics (CFD) program in the world today. CFD codes are structured around the numerical algorithms that can tackle fluid flow problems. OpenFOAM (Open Field Operation and Manipulation) is first and foremost a C++ library, used primarily to create executables, known as applications.

In 1993, it was developed by Imperial College London as a computer code using the finite volume method. The code in C++ provides an alternative and more simple simulation software. Since December 2004, it can be downloaded from the site of OpenFOAM (www.openfoam.org) freely. OpenFOAM represents one of the several existing mathematical models such as CFX, and FLUENT among others, for predicting numerically the flow field and concentration distribution.

4.4.1 OpenFOAM characterization

The OpenFOAM distribution contains numerous solvers and utilities covering a wide range of problems. One of the power points of OpenFOAM is that new solvers and utilities can be created by its users with some pre-requisite knowledge of the underlying method, physics and programming techniques involved. OpenFOAM is supplied with pre- and post-processing environments. The interface to the pre- and post-processing are themselves OpenFOAM utilities, thereby ensuring consistent data handling across all environments. The overall structure of OpenFOAM is shown in Fig.4.2.

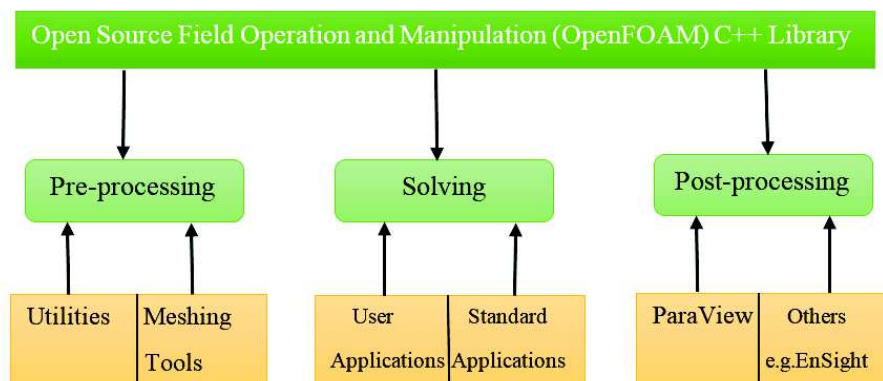


Figure 4.2: Overview of OpenFOAM structure.

For solving numerical equations, several commercial CFD packages include a graphical user interface (GUI) for a user friendly setup of simulations to input problem parameters and to examine the results like OpenFoam. The applications fall into two categories: solvers, that are each designed to solve a specific problem in continuum mechanics; and utilities, that are designed to perform tasks that involve data manipulation. There are many advantages to OpenFOAM: It solves the partial differential equations by the finite volume method and takes by default into account 3D geometries. It is free software with no licensing fee. It support automatic parallelization of applications written using OpenFOAM with a wide range of applications, and models ready to use. As each software, OpenFOAM has disadvantages: The absence of an integrated graphical user interface. The Programmer's guide does not provide sufficient details. It operates with C++ and Linux.

4.4.2 File structure of OpenFOAM cases

The block Mesh process makes the geometry meshes within pre-processing tool of open-source code OpenFoam 2.30, also can be imported and converted mesh by using OpenFOAM converter. This software contains several solvers for all types of flow. In my study, the two liquid mixing foam was used (Simple Foam and turbulent (turbo Foam)). The results come from OpenFOAM analysis by the Para view process and can be exported to other post-processing softwares. The basic directory structure for an OpenFOAM case that contains the minimum set of files required to run an application is shown in Fig. 4.3 and described as follows:

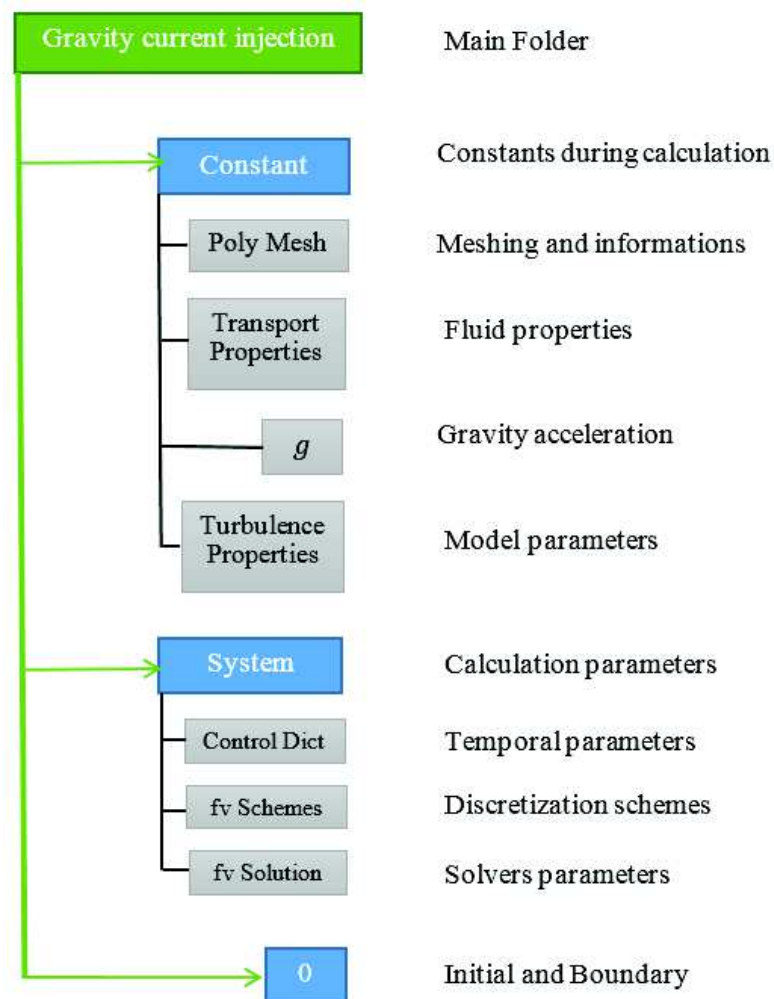


Figure 4.3: Scheme of the general configuration of OpenFOAM.

4.4.2.1 A constant directory

The package contains a full description and the information needed to construct the mesh case and the gravity acceleration in a subdirectory polyMesh and files specifying physical properties for the application concerned, e.g. transport properties. There are four files (Poly mesh, g, transport properties, turbulence properties).

In continuum mechanics, properties are represented in some chosen units, e.g. mass in kilograms(kg), volume in cubic metres(m^3), the pressure in Pascals ($kg.m^{-1}.S^{-2}$). Algebraic operations must be performed on these properties using consistent units of measurement; in particular, addition, subtraction, and equality are only physically meaningful for properties of the same dimensional units. As a safeguard against implementing a meaningless operation, OpenFOAM attaches dimensions to field data and physical properties and performs dimension checking on any tensor operation. For example, the value x of viscosity ϑ such that $\vartheta = x m^2 s^{-1}$, we obtain the statement in the following manner $\vartheta [0 2 - 1 0 0 0]$. These units should be written respecting this order in table 4.4.

The transport properties file can give the properties of the two fluids (fresh and salt water). The transport properties file defines transport model for both Newtonian phases and gives information on the viscosity and density of two phases.

Table 4.4: Positions of physical properties of OpenFOAM.

Positions	1	2	3	4	5	6	7
Variables	Mass	Lenght	Time	Temperature	Quantity	Current	Luminousi Intensity
SI unit	Kilogram (kg)	Meter (m)	Second (s)	Kelvin (K)	Mole (mol)	Ampere (A)	Candela (cd)

The file g defines the value of g and the direction of gravity acceleration. Also, notice in this folder a file dynamic Mesh Dict that indicates if the meshing is static or dynamic. In our case, Meshing is programmed to be static fv Mesh which means static. OpenFOAM always operates in a 3D Cartesian coordinate and all geometries are generated in 3D. The simulation was conducted for a total of (0.5) seconds with time step, based on the smallest grid spacing (1 mm) and the maximum velocity value found for each time step. In Fig.4.4 shows the structure of the mesh for the domain basin filled with fresh water completely. The grids were equidistant and structured. Several meshes were compared to select those giving and the best results without numerical diffusion. The final runs were made on a $275 \times 80 \times 50$ grid following x , y and z coordinates, respectively. The constant directory contains a Poly Mesh subdirectory that has a block Mesh Dict file; this file allows creating the mesh and generating it. The block Mesh file can define the conversion of dimensions in the meter.

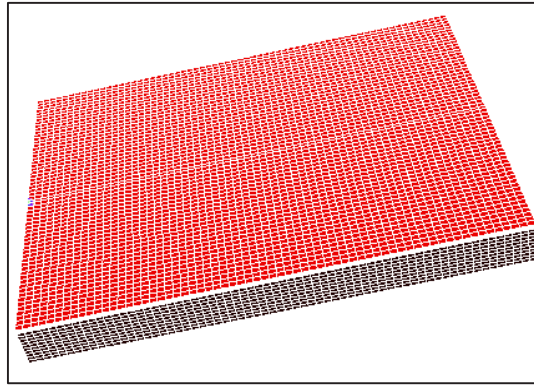


Figure 4.4: The meshes 3D view.

For example, since the dimensions are expressed in mm, in block Mesh file, we can put convert to Meters “0.001” to convert it to meters. Also, we can define vertices to create blocks in 3D. Indeed, the OpenFOAM always uses three-dimensional mesh, even for two-dimensional simulations such as 3-D blocks and mesh can be defined as vertices. Also, we can define border areas or stick two blocks that are not connected but share the same physical area associated with the patch / boundary.

4.4.2.2 A system directory

A system directory is consists of 3 files. The first file is represented by controlDict where run control parameters are set including start/end time, time step and parameters for data output. In the second file, fvSchemes, where discretisation schemes used in the solution may be selected at run-time. In the third file, called fvSolution, where the equation solvers, tolerances, and other algorithm controls are set for the run. These 3 files were used to set parameters associated with the solution procedure itself. The fvSchemes sub-dictionary in the system directory sets the numerical schemes for terms, such as derivatives in equations that appear in applications being run. This section describes how to specify the schemes in the fvSchemes sub-dictionary. The terms that must typically be assigned a numerical scheme in fvSchemes range from derivatives, e.g. gradient ∇ , and interpolations of values from one set of points to another.

The aim of OpenFOAM is to offer an unrestricted choice to the user. For example, while linear interpolation is effective in many cases, OpenFOAM offers complete freedom to choose from a wide selection of interpolation schemes for all interpolation terms. The derivative terms further exemplify this freedom of choice. The user first has a choice of discretisation practice where standard Gaussian finite volume integration is a common choice. Gaussian integration is based on summing values on cell faces, which must be interpolated from cell centres.

The user again has a completely free choice of interpolation scheme, with certain schemes being specifically designed for particular derivative terms, especially the convection divergence $\nabla \cdot$ terms. The set of terms, for which numerical schemes must be specified, are subdivided within the fvSchemes sub-dictionary into the categories listed in table 4.5.

Table 4.5: Main keywords used in fvSchemes.

Keyword	Category of mathematical terms
interpolationSchemes	Point-to-point interpolations of values
SnGradSchemes	Component of gradient normal to a cell face
GradSchemes	Gradient ∇
DivSchemes	Divergence $\nabla \cdot$
LaplacianSchemes	Laplacian ∇^2
TimeScheme	First and second time derivatives $\partial/\partial t, \partial^2/\partial^2 t$
fluxRequired	Fields which require the generation of a flux

Each keyword in table 4.5 is the name of a sub-dictionary which contains terms of a particular type, e.g.gradSchemes contains all the gradient derivative terms such as grad (p) (which represents ∇p). The sub-directory “fv Solution”: represent the equation solvers, tolerances and algorithms are controlled from the fv Solution sub-dictionary in the system directory. Fv Solution contains a set of sub dictionaries that are specific to the solver being run. The sub-directory Control Dict: to control the step of time that is important in the resolution of problem. We can use a fixed step time to achieve temporal accuracy and numerical stability when running the solver.

4.4.2.3 The time “0” directories

These directories is containing individual files of data for particular fields. The data can be either both initial values and boundary conditions that the user must specify to define the problem or results written to file by OpenFOAM. Note that the OpenFOAM fields must always be initialised, even when the solution does not strictly require it, as in steady-state problems. It is sufficient to say now that since we usually start our simulations at time $t = 0$, the initial conditions are usually stored in a directory named 0 or 0.000000e+00, depending on the name format specified. There are three parameters; we will impose some conditions if the case of laminar regime model resolved which are: velocity field U , pressure field p_rgh , and presence of salt water phase α . In the case where the turbulent regime model is processed, also taking into consideration the turbulence the k, ϑ_t , and ϵ . Fig.4.5 shows the different boundary conditions in our simulation and all the conditions represented in table 4.3.

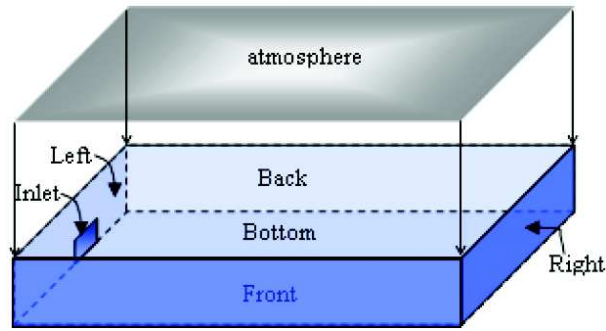


Figure 4.5: Scheme of the boundary conditions of the basin in the numerical model.

OpenFOAM needs to read a range of data structures such as strings, scalars, vectors, tensors, lists and fields. The input/output (I/O) format of files is designed to be extremely flexible to enable the user to modify the I/O in OpenFOAM applications as easily as possible. The I/O follows a simple set of rules that make the files extremely easy to understand, in contrast to many software packages whose file format may not only be difficult to understand intuitively but also not be published anywhere.

4.5 Image processing analyze

Fig. 4.6 shows the saline gravity currents development for Run6 ($R=3889$). While, Fig. 4.7 shows the ImageJ software steps that were applied to obtain the profile of 2D gravity current on both the numerical and experimental runs and the details was explained in the chapter 3 in §3.4.2.

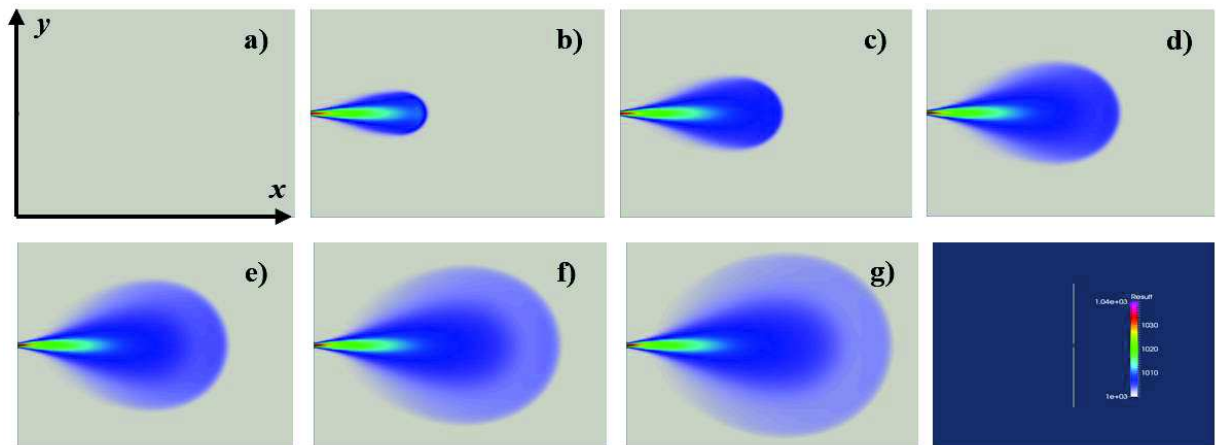


Figure 4.6: Iso-volume fraction evolution of the saline gravity current jet (x, y) with $\alpha=3\%$ for Run6 ($R=3889$): a) $t=0s$, b) $t=2s$, c) $t=4s$, d) $t=6s$, e) $t=8s$, f) $t=10s$, and g) $t=12s$.

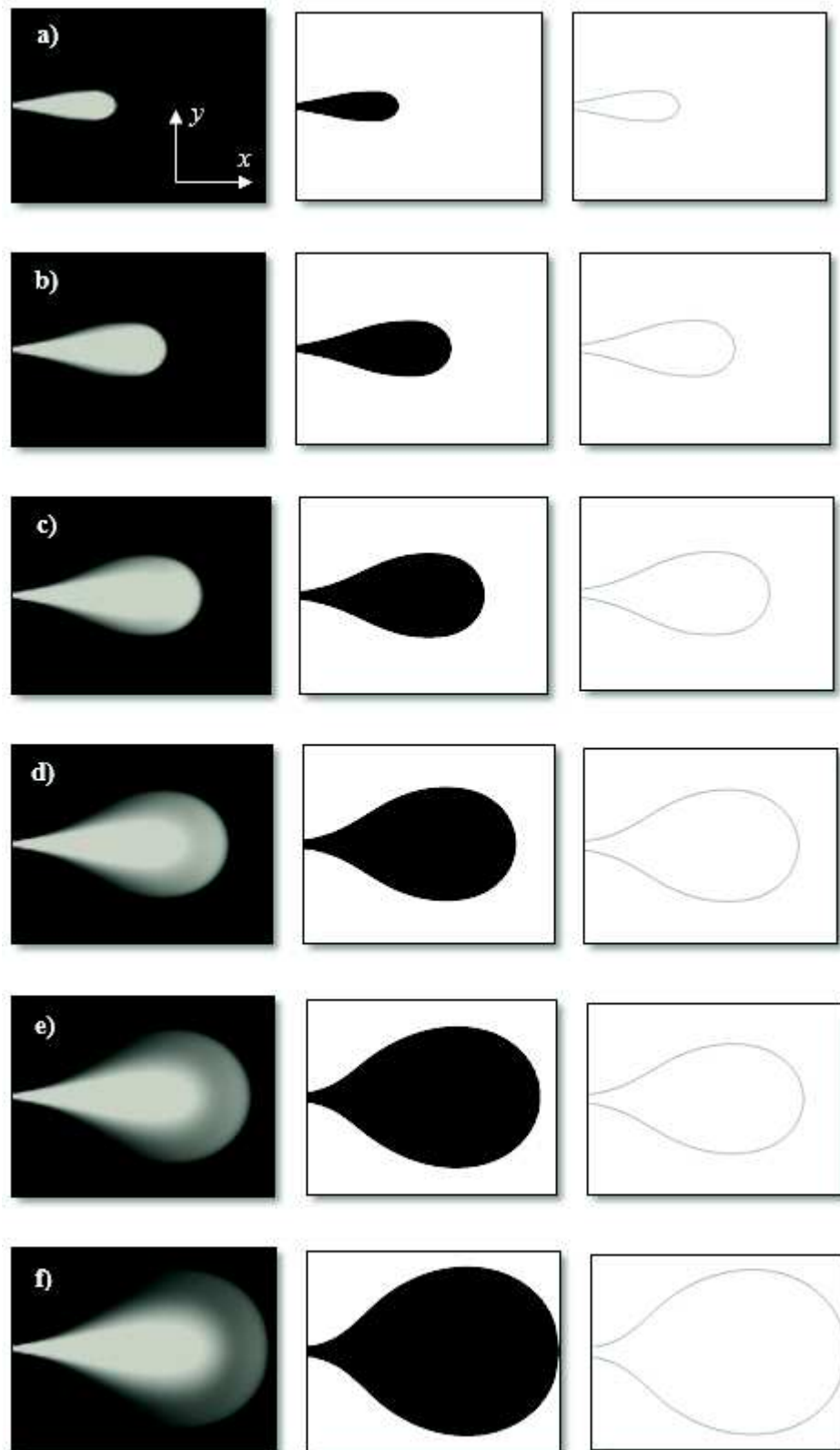


Figure 4.7: Numerical frames captured by difference (row 1), made binary (row 2), and skeletonize (row 3) processes of two dimensional gravity currents performed with initial density $\rho_s = 1040 \text{ kg/m}^3$ and $\rho_{\text{water}} = 1000 \text{ kg/m}^3$ for $R=3889$, and frames acquired at (a) $t=2\text{s}$, (b) $t=4\text{s}$, (c) $t=6\text{s}$, (d) $t=8\text{s}$, (e) $t=10\text{s}$, and (f) $t=12\text{s}$.

4.6 The configuration of gravity currents

4.6.1 Numerical front position

The front position of the gravity current is shown in Fig.4.8. Because of the axisymmetric spreading in numerical simulation, the position of the front is taken as the location where the head (height) current thickness drops to minimum value with respect to the fractional height \bar{z} . Our last four runs results from the six numerical runs for Reynolds number ($2222 \leq R \leq 3889$) simulations are in good agreement with their experimental in terms of outer boundaries in spite of the difference in the axisymmetric numerical and non- axisymmetric experimental on account of the rule of instability in the experiments.

4.6.2 Propagation Phase Transitions

The numerical results are compared with experimental measurements of two dimensional gravity currents front positions. These results are subject to change of scaling law by applying the power fitting in the same procedure followed experimentally. After some time, depending on the salinity properties of the current fluid jet, the viscous drag force may become comparable to the inertia buoyancy force. The effect of viscous drag becomes more and more clearly dominant after further propagation, the gravity current injection may undergo a transition to the viscous-buoyancy propagation with negligible effects due to the inertia force. The difference between experimental (set of exp1-6) and numerical (set of run1-6) is explained (§5.2).

4.6.3 The lobe-cleft instabilities

We concluded that lobes and clefts are formed due to hydrostatic instability exclusively in gravity currents propagation over a non-slip boundary. This type of the instability occurs visibly in the experiments but in our numerical simulation it was not is observed. The disappearance is occurred due to the average quantities were used in the RANS model could not detect the entire space scales like the lobe-cleft structures of the front. Furthermore, the change was appeared in the frontal dynamics as a result of used the $k - \epsilon$ model with the Reynolds-Averaged Navier-Stokes (RANS) equations as shown as in Figs. 4.9. In the morphological analysis of lobes and clefts (LC). Simpson (1982) described the clefts as v-shaped initial distances in the front positions that propagate and integrate along the front. Also, their lobes are described as a progression of localized bursts series along the front that appear as notable noses with bulges or buttresses which continuously variable transmission shape. Simpson (1972) found through the propagation of the gravity current, along a non-slip boundary is not imparts the shear stress effect on the current jet.

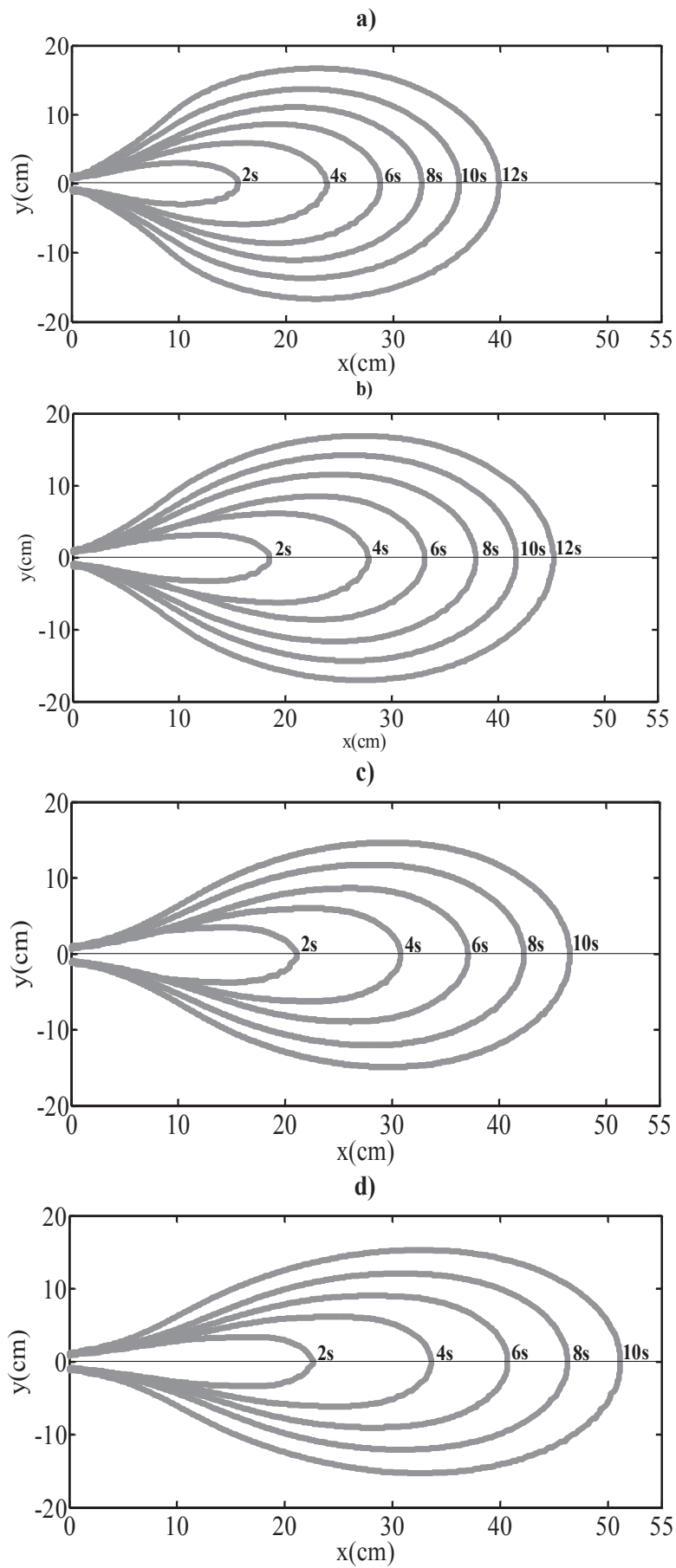


Figure 4.8: Numerical outer positions of the mixing gravity current at $x_f(y, t)$: a) $R=2222$; b) $R=2778$; c) $R=3333$; d) $R=3889$.

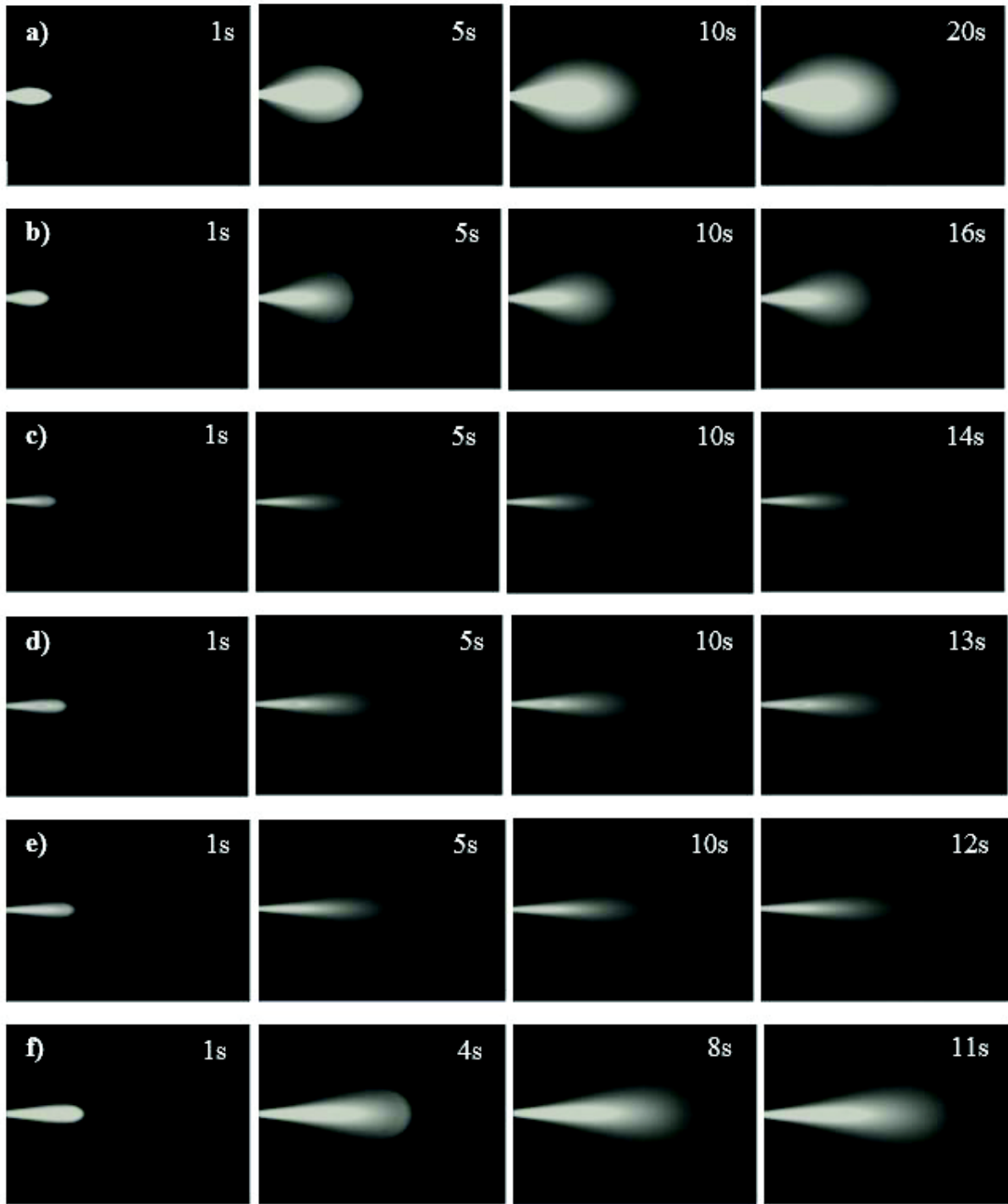


Figure 4.9: Evolution of spreading with time for: a) $R=1111$, b) $R=1667$, c) $R=2222$, d) $R=2778$, e) $R=3333$, and f) $R=3889$.

This a non-slip boundary is leads to absence in the overturning at the nose of the current. Subsequently, the hydrostatic instability does not generation with lobes and clefts. We observed the absence of lobes and clefts form in a numerical boundary stress. In our case, the domain of Reynolds number is not effect in the gravity current. This mean a bottom submerged nose front depending on the Reynolds values are not observed. Finally, they cannot be generated (LC) as a result of the predominant hydrostatic instability mechanism

Chapter 5: Results

5.1 Introduction

This chapter is devoted to the display of the numerical results and comparison with the experiments. The dense gravity currents are generated in the experimental setup described in chapter 3 to elucidate the propagation phases and their transitions, while the numerical simulations are described in chapter 4. Part of the results and comparison analysis presented in this chapter appear in Dhafar *et al.* (2017b)⁵. The propagation images (i.e. temporal evolution of front positions), and the propagation profiles for the denser fluid injection under the fresh water are presented in section 5.2. From the injection point, the coordinates of the outer visual boundaries of the gravity currents were determined at different flow rates and times. Using the velocity and the density profiles, the propagation phases observed in numerical results, and the mean flow structure of weakly turbulent regime gravity currents are identified in section 5.3. As the denser fluid propagates, it undergoes distinct propagation phases. In section 5.4 we studied numerically the turbulent mixing depending on the gradient Richardson number Ri_g profiles and the domain of the turbulent mixing between the current and the ambient fluid. Finally, in section 5.5, we investigate characteristics of the mixing that takes place between the saline bottom gravity currents and the fresh ambient fluid, the entrainment rates and the relationship between the entrainment and volume fractions.

5.2 Front position of the jet: experimental and numerical results

The shape of gravity currents for every flow Run depends on the volume of saline fluid that was released. The process consists in injecting a dense current with a constant velocity. This injection depends on initial flow, momentum, and buoyancy fluxes. Although, the current motion depends upon the initial depth (d) and the modified acceleration due to gravity (g'). Observation of the flow structures in a fully developed gravity current front were done by repeating experiments. However, these experiments served to emphasize the importance of including the effect of the ambient fluid on the gravity current. Figure 5.1 presents the evolution of the experimental (left side) and numerical (right side) gravity current jet from the top view (x, y) for $R=3889$.

⁵ Dhafar, I. A., Latrache, N., and Nsom, B. (2017b). Mixing of Saline gravity Current Jet into Fresh Water in the Weakly Turbulent Regime (under review).

In Fig.5.1, the images of the left-hand side represent the light intensity recorded by the camera where the mixing gravity current has a high intensity (white color) and the fresh water has a low intensity (black color). In Fig. 1, the sequences on the right-hand side represent the variation of the density of the mixing liquid $\rho(x, y)$ close to the bottom of the basin at $z=0.0005m$. The density of the mixing liquid varied from 1000 kg/m^3 (fresh water) to 1040 kg/m^3 (salt water). The lobe cleft instabilities was observed in the experiment (left-hand side of the Fig. 1) but it was not obtained by the RANS model in the numerical results. The average quantities used in the RANS model could not detect the entire space scales like the lobe-cleft structures of the front. The typical side view profiles of the numerical density $\rho(x, z)$ of the mixing between the gravity current and the ambient fresh water are shown in Fig. 5.2. The mixing gravity current have not any rise in it head, so the hydroplaning effects are not observed (Fig. 5.1).

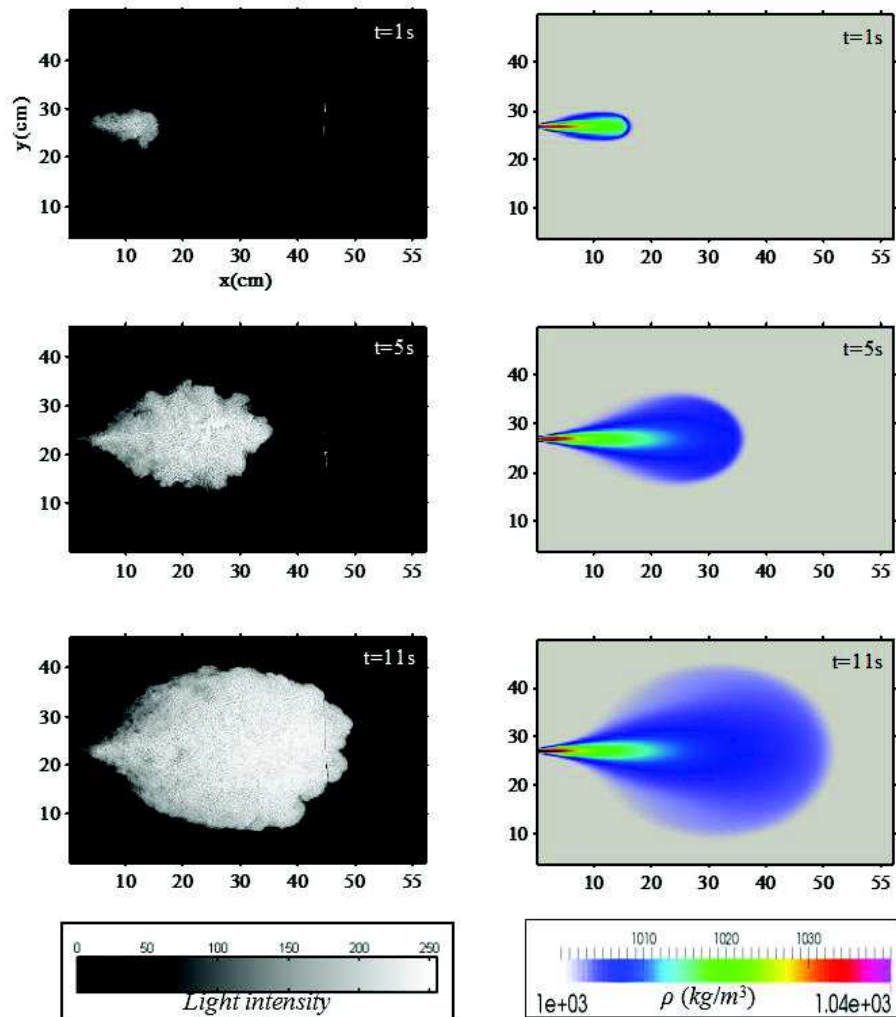


Figure 5.1: Evolution of the experimental (left side) and numerical (right side) mixing gravity current jet from the top view (x, y) for $R=3889$. Experimental (left side) profiles are the treated images of light intensity recorded by the camera $I(x, y)$ and numerical (right side) profiles are the variation of the density.

As described in the previous studies (Simpson & Britter 1979, Huppert & Simpson 1980, Rottman & Simpson 1983, Kneller *et al.* 1999, and Thomas *et al.* 2003), the density $\rho(x, z)$ of the mixing gravity current presents a frontal zone, named “head”, and is followed by a body zone (Fig.5.2). In our case, the head can be defined as the zone located at the front and has the maximum thickness h_f (Fig. 5.2-a). The maximum depth of the head h_f increases with the distance from the inlet. The head does not show any rise, so the hydroplaning effects are not observed (Fig. 5.2). Also, Fig. 5.2 shows that the numerical head development is the zone where higher density is spotted, which is in accordance with different previous studies (Hacker *et al.* 1996, Hallworth *et al.* 1996, Marino *et al.* 2005, and Nogueira *et al.* 2013a). This dimensionless evolution of the head of mixing gravity currents jet shows a head expansion and the disappearance of the density gradients throughout the gravity current development, which occurs through deterioration of the current jet velocity far off the jet source, and finally fades away in time by diffusion processes. Also, from Fig 5.2 can be adopted for the evolution of the current front position in x-z coordinates.

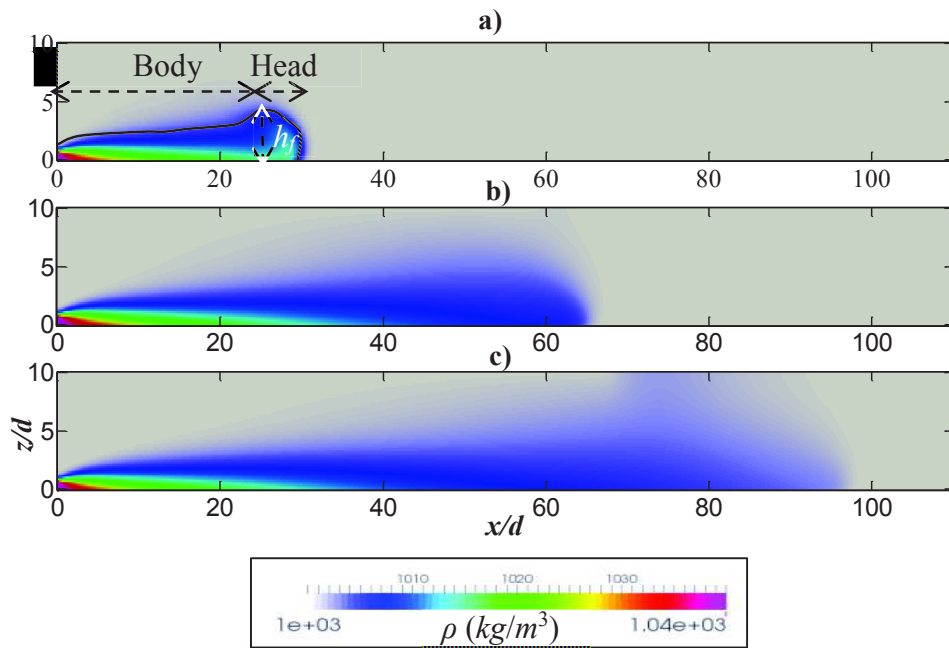


Figure 5.2: Evolution of the numerical density of the mixing gravity current jet from the side view (x, z) for $R=3889$: a) $t=1s$; b) $t=5s$; c) $t=11 s$.

From the profiles of Fig. 5.1, we plotted the spatial evolution of the light intensity as shown in Fig5.3-a, and the density as shown in Fig 5.3-b as function of the streamwise coordinate x . The profiles of intensity and density decrease in space from their maxima ($I_{max} \approx 255, \rho_s = 1040 \text{ kg/m}^3$) at $x = 0$ to their minima ($I_{min} \approx 178, \rho_{water} = 1000 \text{ kg/m}^3$) at x_f and remain constant at those minimum values for $x > x_f$.

The front position x_f is defined as the position where the profiles of intensity and density of mixing gravity currents decrease abruptly to the minima as shown in (Fig. 5.3a-b). The binarization technique based on the minimum thresholds of intensity and density makes it possible to automatically obtain the different front positions in the time and for all values of R (Fig. 5.4).

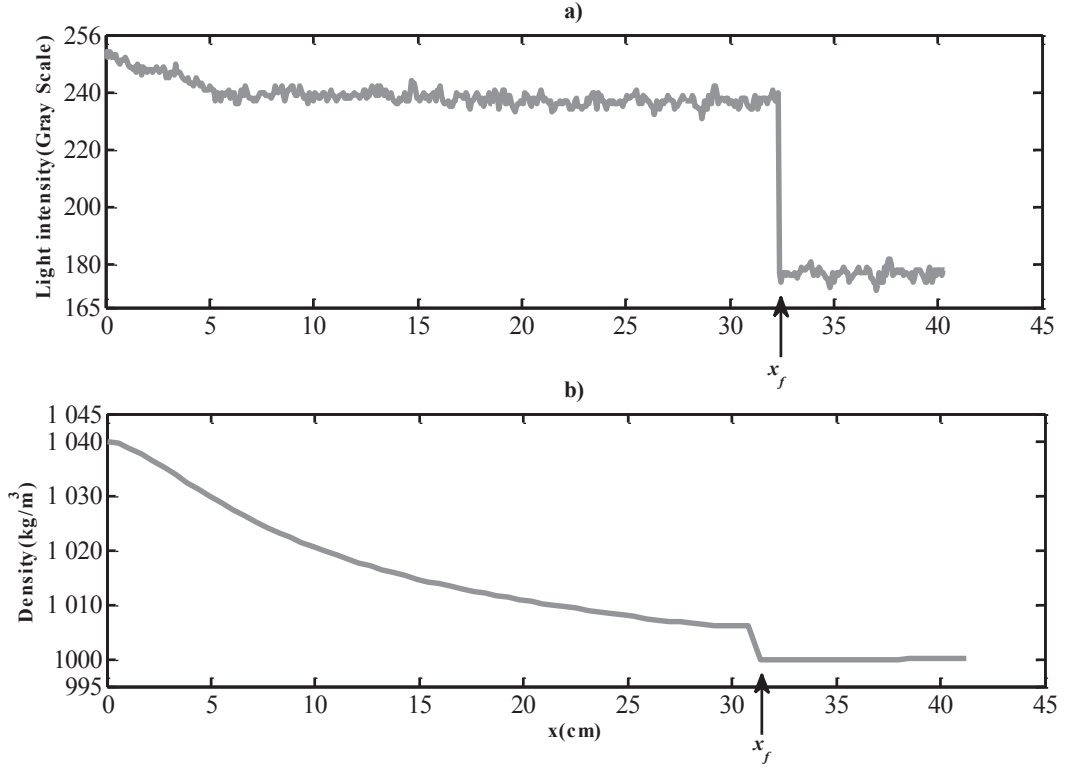


Figure 5.3: a) Evolution of the light intensity of mixing gravity current obtained by the contrast difference using the Rhodamine B as function of x direction, b) Evolution of numerical density of jet as function of x direction at $y=l/2$; $z=0.005m$; $t=5s$ for $R = 2778$, and x_f is the front position at $y=l/2$.

The quantitative comparison of experimental ($x_{f,exp}$) with numerical ($x_{f,num}$) front positions of mixing gravity current jet for different Reynolds numbers is shown in (Fig 5.4). For all the values of Reynolds number used in this study, the numerical simulations produced a good reproduction of the front position evolution over time. The difference between experimental and numerical front positions was estimated by the mean difference *Diff* of the relative difference in front positions, defined as:

$$Diff = mean \left| \frac{x_{f,exp} - x_{f,num}}{x_{f,exp}} \right| \quad (5.1)$$

The values of the mean difference are 6.1, 5.2, 2.8, 3.1, 3.1, and 2.8%, for (exp1; run1), (exp2; run2), (exp3; run3), (exp4; run4), (exp5; run5) and (exp6; run6) respectively.

The above estimation gives an overview of the accuracy as reasonable agreement between the experimental and the numerical positions of the outer fronts. In Fig. 5.4a-b the experimental and the numerical mean difference of front positions appears not satisfactory, unlike (Fig. 5.4c-f) where a good agreement is obtained for the front position for (exp3; run3), (exp4; run4), (exp5; run5) and (exp6; run6) particularly.

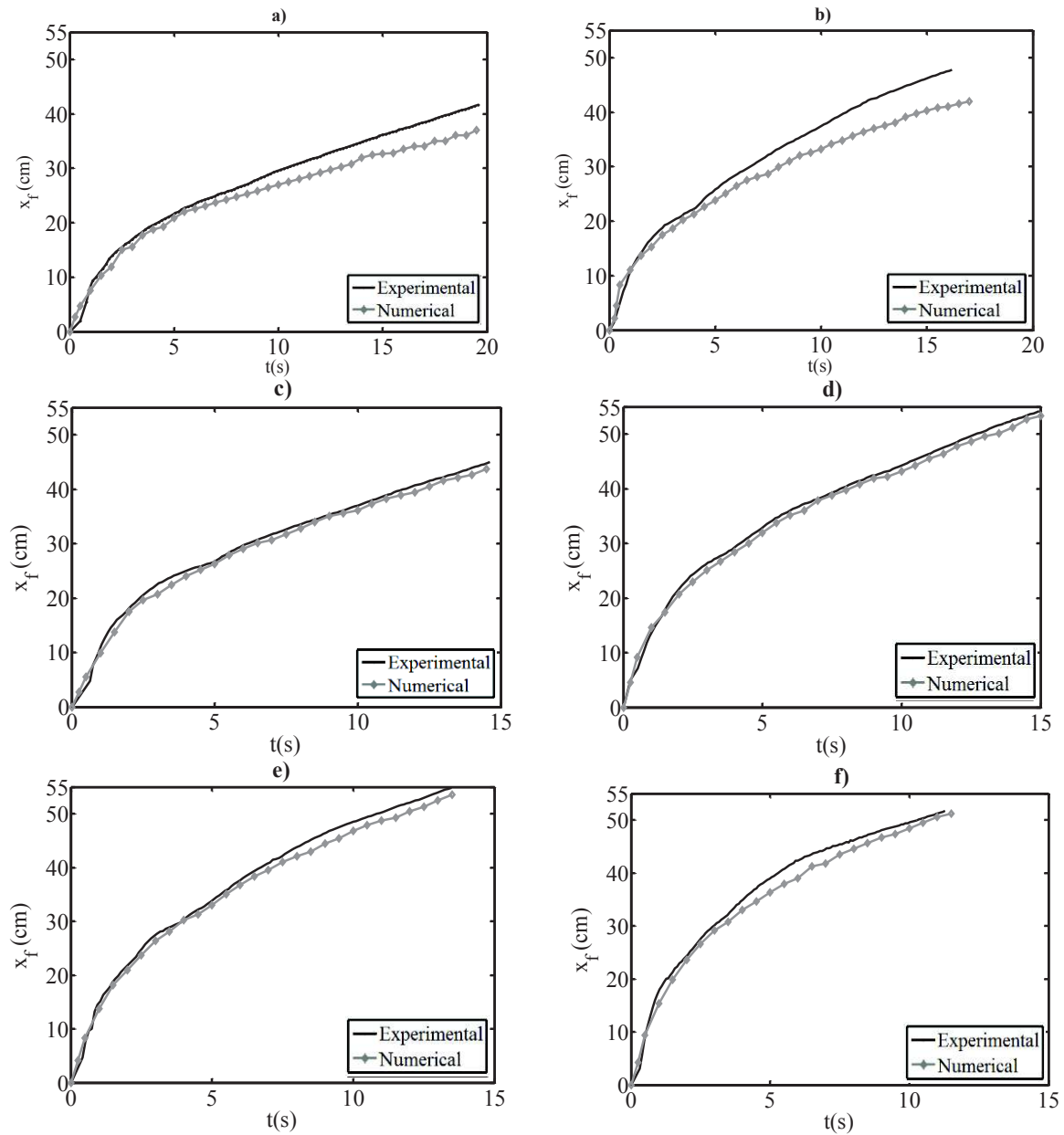


Figure 5.4: Experimental and numerical positions of the mixing gravity current x_f as a function of time for: a) $R=1111$; b) $R=1667$; c) $R=2222$; d) $R=2778$; e) $R=3333$; and f) $R=3889$.

A quantitative comparison between experimental and numerical continuous of a mixing gravity current jet for different Reynolds numbers are shown in (Fig 5.5).

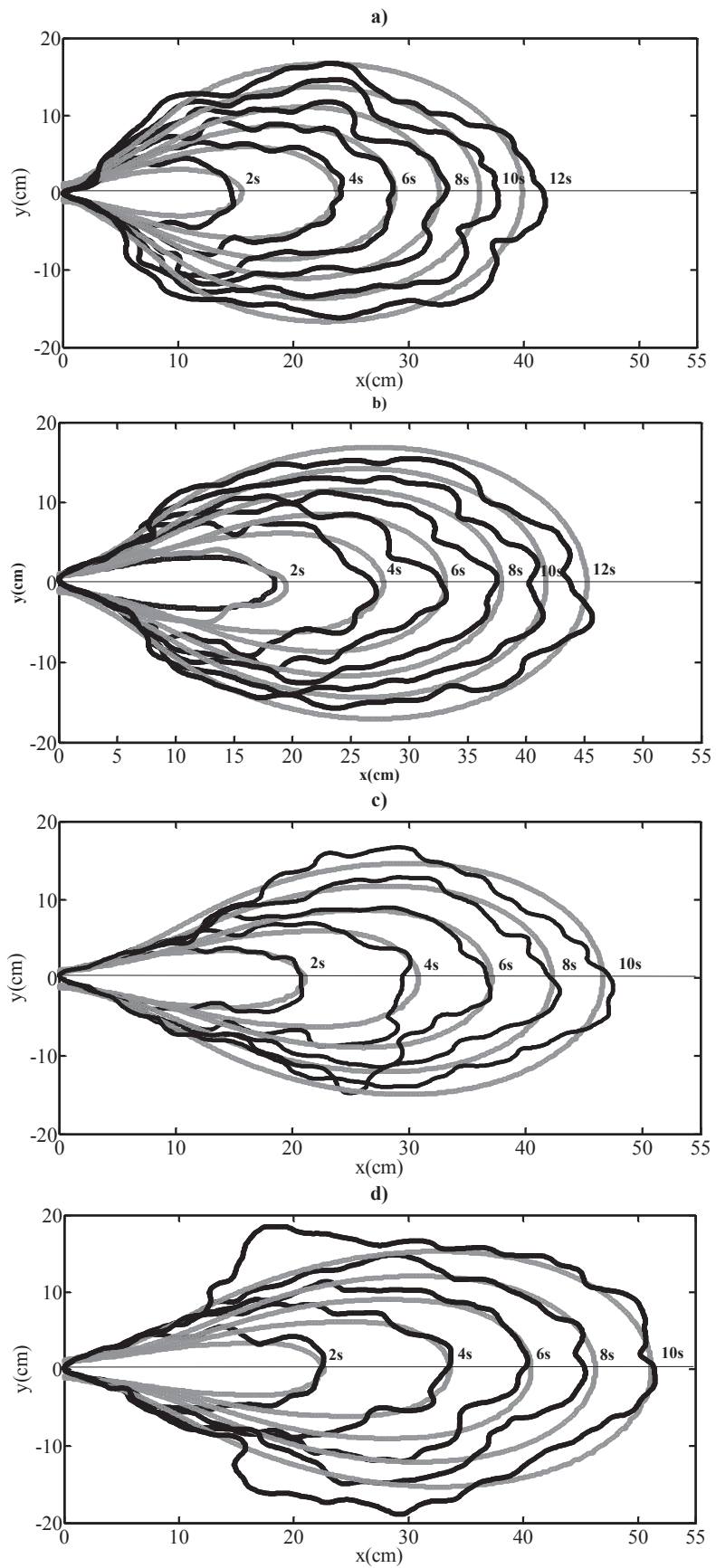


Figure 5.5: Experimental and numerical continuous of the mixing gravity current $x_f(y, t)$: a) $R=2222$; b) $R=2778$; c) $R=3333$; and d) $R=3889$.

The comparison shows a good agreement between experimental and numerical results. The absence of the lobe-cleft instability in the numerical simulations is revealed using the RANS model. The average quantities used in RANS model were not able to resolve the entire range of length scales present in the flow. Results similar to Fig.5.5 are shown in La Rocca *et al.* (2008 & 2012), where unconfined gravity currents are investigated by both laboratory experiments and shallow water simulations. The instabilities of the front gravity are also not captured in their numerical simulations (La Rocca *et al.* 2008 & 2012), but the lobe-cleft instability can be observed numerically by using the DNS method (Härtel *et al.* 2000, and Cantero *et al.* 2007) or LES method (Ottolenghi *et al.* 2016a, and 2016b).

5.3 Velocity and density profiles

The gravity jet current interacted with both the ambient fresh water and the bottom boundary of the basin. The basin bottom is solid, so a no-slip condition can be imposed, while the top is a free surface with zero gradient condition in our case. Consequently, the saline jet current could propagate asymmetrically in the vertical direction following two regions (inner and outer). The inner region is close to the solid boundary and resembles the turbulent boundary layer, while the outer region resembles a free shear flow (Turner 1973, Kneller *et al.* 1999, Erikson *et al.* 1988, and Gerber *et al.* 2011). Fig. 5.6 shows the simulated mean velocity profiles $\bar{u}(x, z)$ at $y = l/2$ and $t=11s$. The velocity presents a maximum close to the injection channel and it decreases strongly with the vertical (z) and the streamwise (x) coordinates.

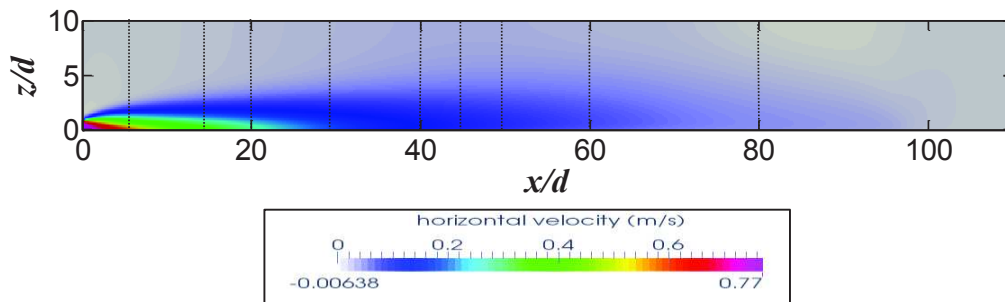


Figure 5.6: Mean horizontal velocity profile $u(x, z)$ at $y=l/2$.

We plotted in Fig. 5.7, the dimensionless mean horizontal velocity profiles with the dimensionless vertical coordinate $z/z_{0.5}$ at $x/d= 8, 15, 20, 30, 40, 45, 50, 60,$ and 80 . In these profiles, the velocity is normalized by its maximum \bar{u}_{max} , while the vertical position z is normalized by $z_{0.5}$, the height at which the mean velocity \bar{u} is equal to half the maximum mean velocity \bar{u}_{max} .

All simulated mean velocity profiles collapse for different positions (Fig. 5.7). Collapsed mean velocity profiles were also observed in the numerical and experimental works of Kassem and Imran (2001) and Gerber *et al.* (2011).

For $x/d \leq 50$ and $z/z_{0.5} > 3$, the velocity vanishes following the vertical axis. Such behavior can be explained by the absence of the return flow at $y = l/2$ in front of the inlet. For $x/d > 50$, the velocity vanishes at the free surface at $y = l/2$. The velocity profiles for all positions x/d presents a unique maximum value at $z/z_{0.5} \approx 0.18$. The height $z \approx 0.18z_{0.5}$ can be used to differentiate the inner and the outer regions of the flow with opposite velocity gradients. This value is in agreement with the wall-jet experiment of Eriksson *et al.* (1998), who found the maximum velocity to be at 0.17. This value is lower than that obtained by Gerber *et al.* (2011) in their experiment on saline density current and that laid between 0.37 and 0.4. Ahlman (2006) observed, for his compressible wall-jet simulations that the return flow velocity of the overlying ambient fluid increased the height of the velocity maximum. In our case, the absence of the return flow might explain why the height (0.18) of the maximum velocity is lower than that obtained by Gerber *et al.* (2011). To obtain lower values of the height (between 0.1 and 0.4), Buckee *et al.* (2009) minimized the return flow by using a perforated pipe in their experiment on dense gravity currents (density current).

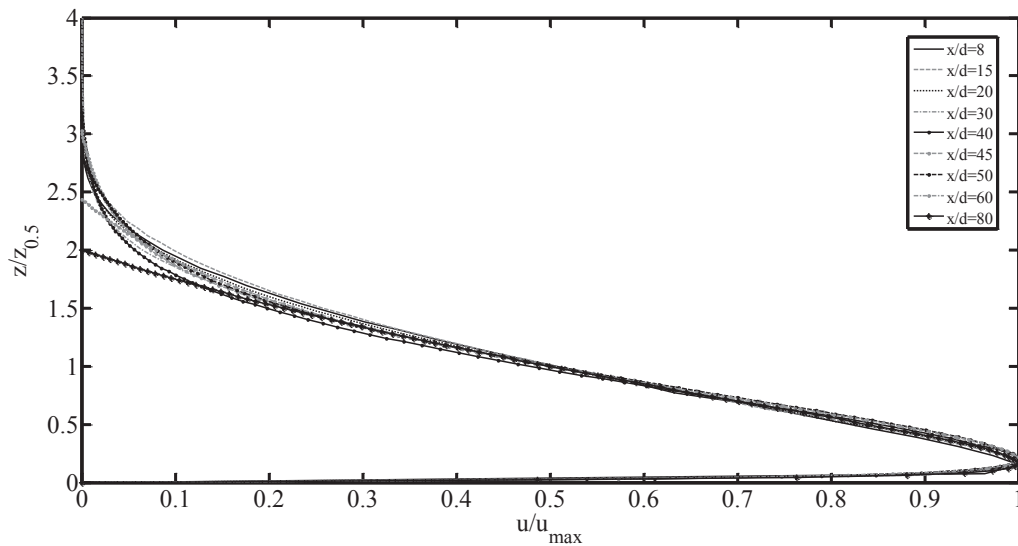


Figure 5.7: Dimensionless mean horizontal velocity profile versus the vertical coordinate $z/z_{0.5}$ at $y = l/2$.

Fig. 5.8 shows the simulated mean density profiles $\rho(x, z)$ at $y = l/2$. The density presents a maximum close to the injection channel and it decreases strongly versus the vertical (z) and the streamwise (x) coordinates.

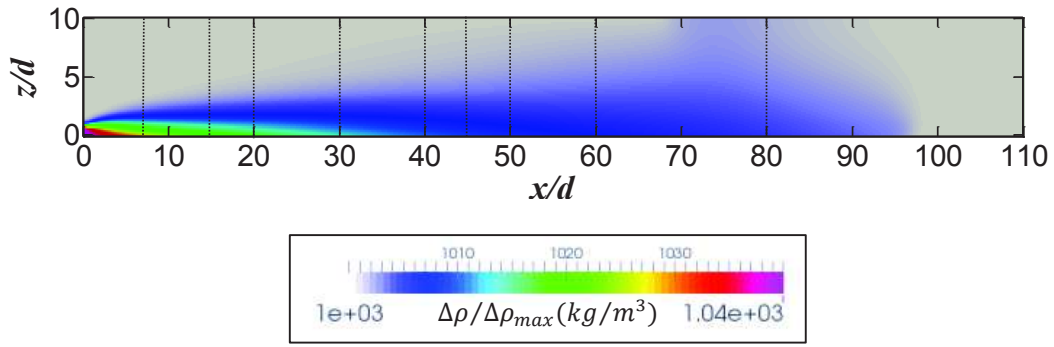


Figure 5.8: Dimensionless mean excess-density profiles in the (x, z) plane at $y = l/2$.

Fig. 5.9 shows the dimensionless mean excess density $\Delta\rho/\Delta\rho_{max}$ versus the dimensionless vertical coordinate $z/z_{0.5}$. For $x/d \leq 50$, the profiles of $\Delta\rho/\Delta\rho_{max}$ collapse versus $z/z_{0.5} < 3$ and versus $z/z_{0.5} > 3$, the profile $\Delta\rho/\Delta\rho_{max} = 0$ (zone without mixing). For $x/d > 50$, mixing occurs along the vertical direction and the profiles of the excess-density do not collapse for $x/d \leq 50$.

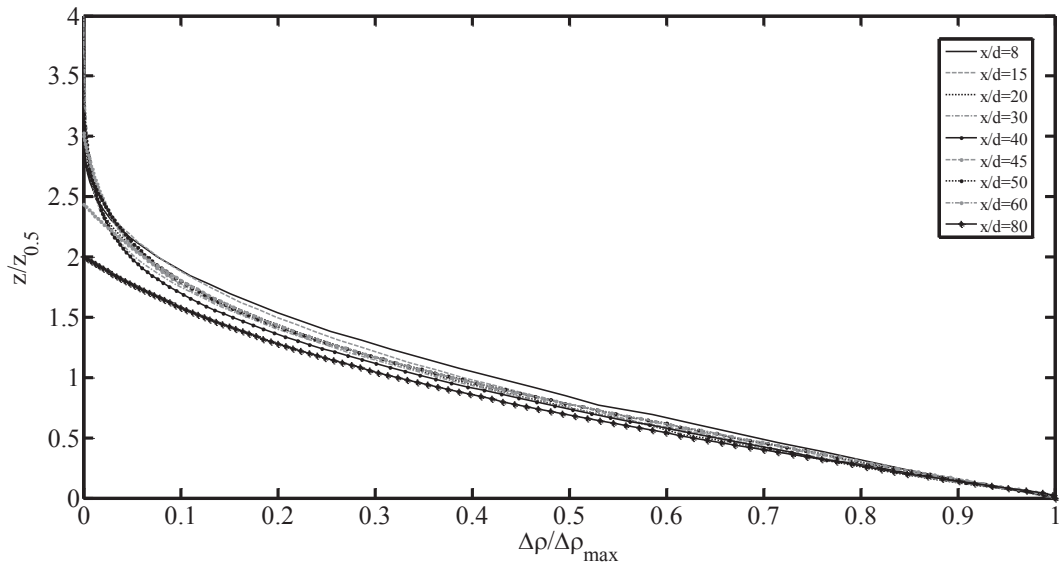


Figure 5.9: Dimensionless mean excess-density profiles.

Fig. 5.10 shows the mean density $\Delta\rho/\Delta\rho_{max}$ profiles at $x/d = 20$ and 50 in the (y, z) plane. The mean density shows a radial symmetry close to the inlet (Fig. 5.10-a) and asymmetry far from the inlet (Fig. 5.10-b). These profiles represented the increasing and occurring of mixing by the growth of the outer density scale $\Delta\rho_{max}$. Also for $x/d \leq 50$, all these profiles collapse and for $z/z_{0.5} > 3$, there is no mixing where the excess-density $\Delta\rho/\Delta\rho_{max} = 0$. For $x/d > 50$, the mixing occurs along the vertical axis and the profiles of the excess-density do not collapse as well as for $x/d \leq 50$.

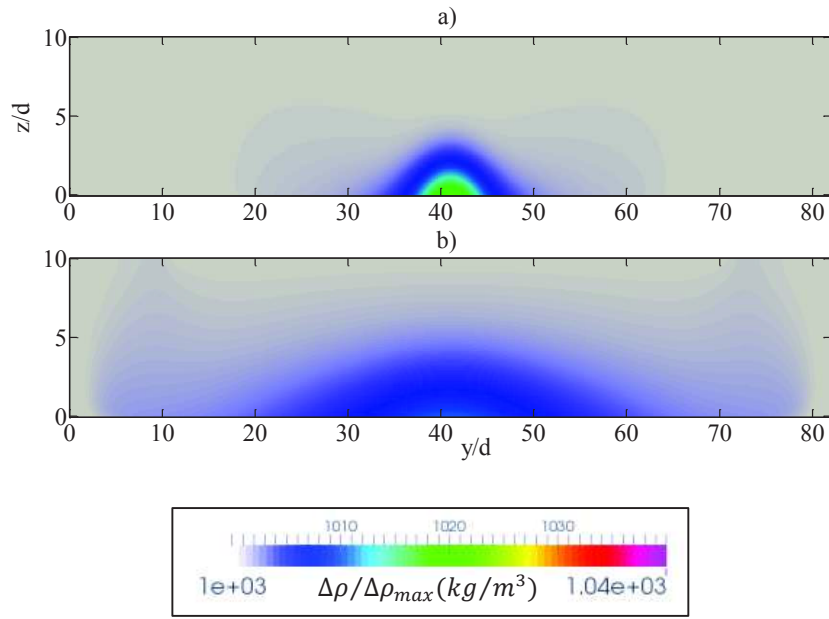


Figure 5.10: Dimensionless mean excess-density profiles in the (y, z) plane at: a) $x/d=20$ and b) $x/d=50$.

Fig. 5.11 shows the simulated mean density profiles $\rho(x, z)$ at $y=l/2$. The density presents a maximum close to the injection channel and it decreases strongly with the vertical (z) and the streamwise (x) coordinates.

In order to determine the dynamics of each fluid (mixing gravity current and ambient fresh water) in the y -coordinate, we plotted the density-excess and velocity profiles close to ($x/d=20$) and far from ($x/d=50$) the inlet and at the height z_{max} , which corresponds to the maximum velocity \bar{u}_{max} (Fig. 5.11). Close to the inlet ($x/d=20$, Fig. 5.11-a), the profiles show four zones: I) mixing zone ($\Delta\rho/\Delta\rho_{max} \neq 0$) where the gravity current moves streamwise ($\bar{u} \neq 0$) and horizontal ($\bar{v} \neq 0$) directions; II) mixing zone ($\Delta\rho/\Delta\rho_{max} \neq 0$) with motion only horizontal direction ($\bar{u} = 0$, $\bar{v} \neq 0$); III) zone without mixing ($\Delta\rho/\Delta\rho_{max} = 0$), where the fresh water moves in the horizontal direction ($\bar{u} = 0$, $\bar{v} \neq 0$), that can be explained by the presence of the viscous boundary layer (Philippe *et al.* 2005); IV) zone of fresh water without mixing. Far from the inlet ($x/d=50$, Fig. 5.11-b), the profiles show one mixing zone with motion.

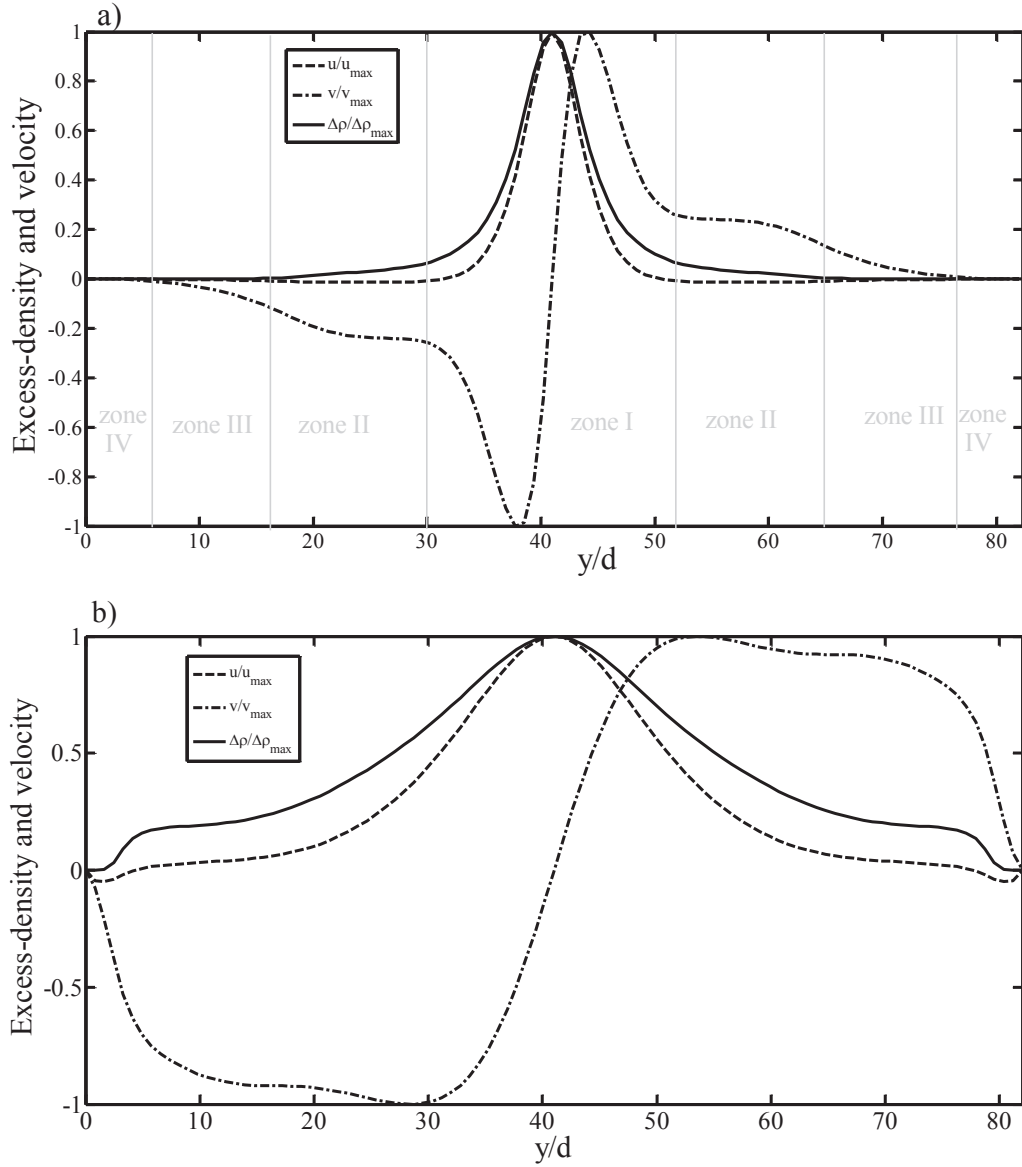


Figure 5.11: Profiles of the excess-density and velocity in y -coordinate at: a) $x/d=20$, $x/d=50$.

5.4 Turbulent Mixing

In order to characterize the turbulent mixing, we used the gradient Richardson number Ri_g (Turner 1973; Garcia 1993; Buckee *et al.* 2009; Gerber *et al.* 2011, Chang *et al.* 2005) defined as the ratio of the buoyancy frequency $N^2 = -\frac{g}{\rho_0} \cdot \frac{\partial \rho}{\partial z}$ to the vertical shear rate:

$$Ri_g \equiv N^2 / \left[\left(\frac{\partial u}{\partial z} \right)^2 + \left(\frac{\partial v}{\partial z} \right)^2 \right] \quad (5.2)$$

Turner (1973) showed that the turbulence mixing is low if the gradient Richardson number Ri_g exceeds 0.25. We plotted the Ri_g as function of $z/z_{0.5}$ for different axial positions: $x/d=8, 15, 20, 30, 60$ and 80 (Fig. 5.12).

Close to the inlet ($x_{max}/d < 50$), the gradient Richardson number Ri_g is a minimum at $z \approx z_{0.5}$ (Fig. 5.12), which means that maximum turbulent mixing occurs at height $z \approx z_{0.5}$, where the mean horizontal velocity u is equal to half the maximum mean velocity \bar{u}_{max} . In that position, the vertical shear dominates the stratification density. Far from the inlet ($50 < x/d < 80$), the turbulent mixing can occur close to the bottom boundary for $z/z_{0.5} < 0.2$, where $Ri_g < 0.25$.

For $0.25 < z/z_{0.5} < 2.8$, and $x/d < 50$, the gradient Richardson number Ri_g is lower than 0.25. It indicates that turbulent mixing is possible. Furthermore, we see that for $x/d > 50$, the gradient Richardson number Ri_g exceeds 0.25 and conclude that there is no turbulent mixing. In this case, mixing can occur only in the horizontal plane; a phenomenon known as “pancake” mixing that was demonstrated by Fernando (2000) in a laboratory experiment on stratified flow for $Ri_g > 0.7$.

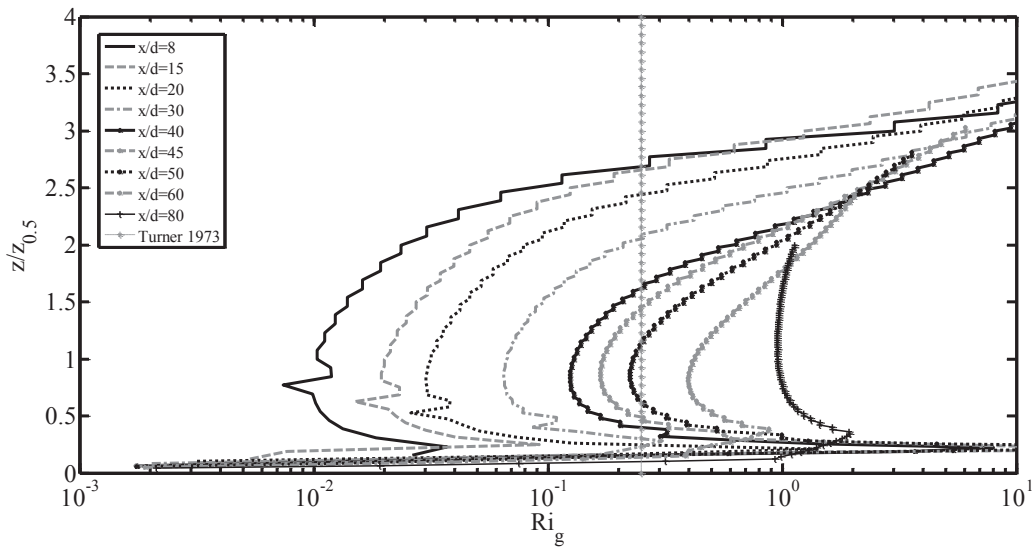


Figure 5.12: Gradient Richardson number profiles indicating the increase in stable stratification with downstream distance for $x/d > x_{max}/d$ where $x_{max}/d = 50$ for $R=3889$ (run 6).

To analyze the turbulent mixing in the 3D space, we plotted the contours of the gradient Richardson number at 0.25 (critical value determined by Turner, 1973) in the (y, z) plane at different x/d positions from the inlet (Fig. 5.13). For $x/d \leq 8$, the profile of Ri_g at 0.25 presents a radial symmetry with a semi-circular form. Therefore the turbulent mixing zone has a semi-circular form with radial symmetry and that is absent outside it. This can be explained by the absence of turbulent mixing in the outside of the semi-circular turbulent mixing zone. For $8 < x/d < 35$, the turbulent mixing zone becomes non-axisymmetric following the radial coordinate, increases in the $y-z$ and reaches its maximum at $x/d \approx 32$ (Fig. 5.13).

For $35 < x/d < 55$, the turbulent mixing zone decreases in the y - z (Fig. 5.13). For $x/d > 55$, the turbulent mixing zone decreases strongly and exists only close to the bottom of the basin (Fig. 5.13).

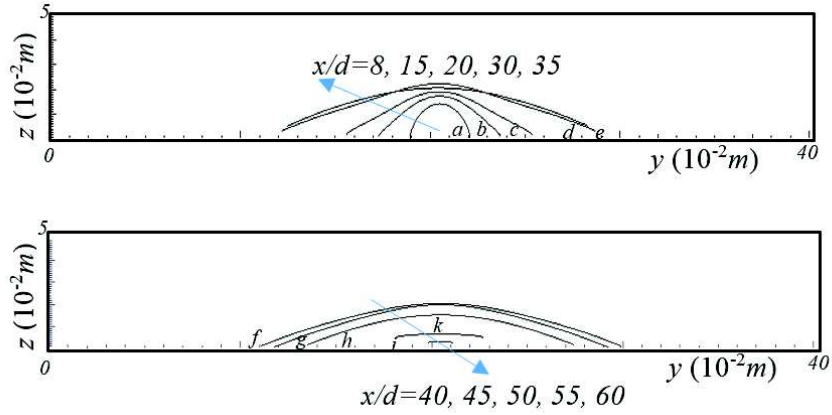


Figure 5.13: Position of Gradient Richardson number Rig at 0.25 in the (y,z) plane for different position from the inlet x/d . a, b, c, d, e, f, g, h, i and k represent the position from the inlet respectively for 8, 15, 20, 25, 30, 35, 40, 45, 55 and 60.

5.5 Entrainment Rates

Hacker *et al.* (1996) quantified mixing by examining the quantity and the concentrations of the mixed fluid in the lock-exchange gravity currents. They measured the ratio of the gravity current volume to the initial volume per unit width of the lock for different chosen concentration thresholds. Using the same idea, we calculated the volume fraction as V/V_0 , where V is the gravity current volume for different concentrations:

$$V \equiv \int_0^{y_f} \int_0^{x_f} \int_0^t h(x, y, t) dx dy dt, \quad (5.3)$$

$$h(x, y, t) = \int_0^{z^b} \delta(x, y, z, t) dz, \quad (5.4)$$

$$\text{where } \delta(x, y, z, t) = \begin{cases} 0, & \text{when } \Delta\rho(x, y, z, t)/\Delta\rho_{max} < \alpha, \\ 1, & \text{when } \Delta\rho(x, y, z, t)/\Delta\rho_{max} \geq \alpha. \end{cases}$$

and $\alpha = \{0.03, 0.05, 0.10, 0.15, 0.20, 0.25, 0.30, 0.35, 0.40, 0.45, 0.50, 0.55, 0.60, \text{ and } 0.65\}$.

Figures 5.14, and 5.15 show an example of the evolution of the iso-density gravity current corresponding to $\alpha = 3\%$ and $R = 3889$ (run6) that makes it possible to calculate V and the inlet volume, given by:

$$V_0 = Q_0 \cdot t \quad (5.5)$$

The ratio V/V_0 increases or decreases with time depending on the chosen threshold concentration. The ratio V/V_0 versus x_f/d can be viewed as a further indicator of the entrainment in the gravity current problem (Hacker *et al.* 1996, Frago *et al.* 2013, and Ottolenghi *et al.* 2016a & b).

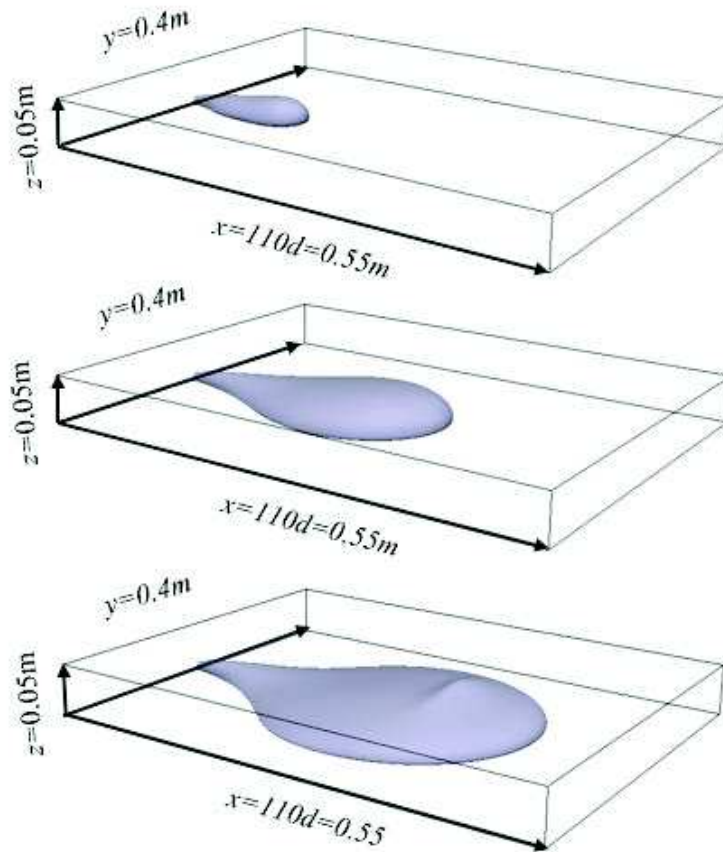


Figure 5.14: Iso-density evolution of the gravity current jet with $\alpha=3\%$ for Run6 ($R=3889$): a) $t=1s$, b) $t=5s$; c) $t=11s$.

As a result of the numerical calculations, the variation of the dense current fractional volume to the total basin volume as a function of time in the three directions can be seen in Fig. 5.15. Near the injection source, the head of the gravity current can have boundaries allowing the distinction between the saline and the fresh waters. On the other hand, far from the injection source, the gravity current is well established but it cannot be distinguished clearly the boundaries between two fluids due to the diffusivity and mixing, and the head of the gravity current represented by $\alpha_1(x, y, z, t)$. Therefore, the case of continuity of the gravity current head as shown as in Figs. 5.14-5.15 that the head of the gravity current front is almost similar in the lateral and axial directions. This evidence on the domain of the buoyancy because of the shortage of time. Also, it is related to the observation of the shape of the jet in the nearest zone of injection source.

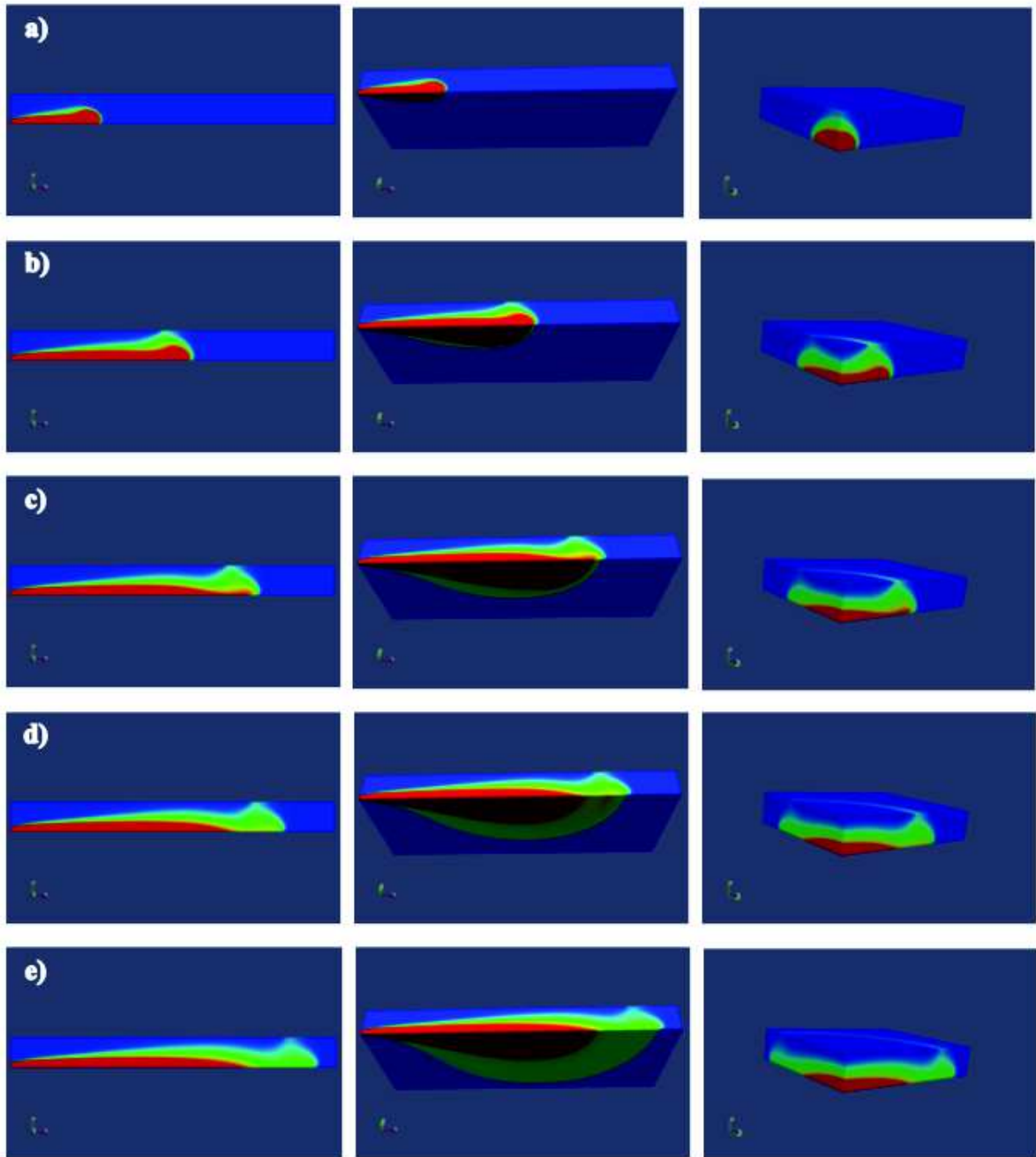


Figure 5.15: Evolution of the volume fraction of salt water with time with $\alpha=3\%$ for Run6 ($R=3889$): a) 1s; b) 4s; c) 8s; d) 10s; and e) 12s.

The non-dimensional volume fraction of the fluid current V/V_0 at different concentration thresholds is plotted versus the front position in Fig. 16 for $R=2778$ and in Fig. 17 for different values of R . For $\alpha \leq 0.15$, the volume of the jet current increases, then decreases, with the front position after reaching a maximum at x_m (Figs. 5.16, 5.17, & 5.18). The front position x_m corresponds to the maximum volume of the jet current. The position x_m decreases with α . The volume ratio is larger than unity throughout this range of concentration ($\alpha \leq 0.15$) and all values of initial Reynolds numbers (Figs. 5.16, 5.17, and 5.18).

This can be explained by the entrainment of the ambient fluid. For $\alpha \geq 0.20$, the volume ratio has a negative slope and decreases with the front position (Figs. 5.16, 5.17, & 5.18). The extent of mixing within the dense jet gravity current can be derived for different values of the initial Reynolds number R following the approach first adopted by Hacker *et al.* (1996). For $\alpha \leq 0.15$, mixing inside the jet gravity current is homogenous for $x/d < 15$, where the slope of V/V_0 shows no change with x/d . For $15 < x/d < x_m/d$, the slope changes with x/d , this can be explained by the non-homogeneity of the mixing inside the jet gravity current. For $\alpha = 0.10$ and $x > x_m$, the V/V_0 decreases and tends to be constant with x , we conclude that the dense jet current entrains light fluid only at the leading edge of the current, while the interior part is essentially unmixed. For $\alpha \geq 0.20$, the volume decreases with x/d , which indicates that the ambient fluid does not intrude into the core of the gravity current.

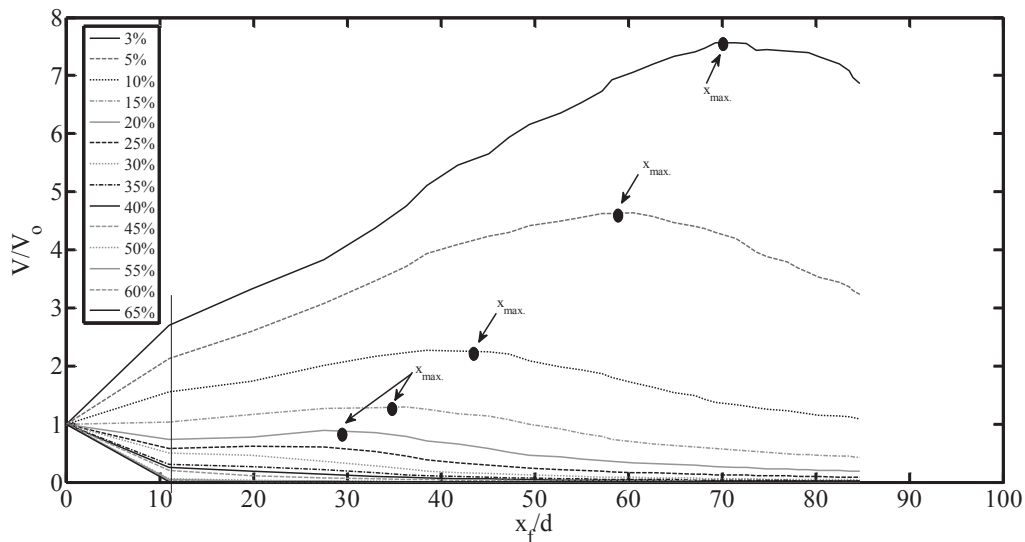


Figure 5.16: The fractional volume V/V_0 of total volume to the initial injection volume of the fluid current plotted as a function of the front position x/d .

The variation of volume fraction for different values of iso-density threshold (Figs. 5.16, 5.17, and 5.18) showed that the entrainment is affected by the choice of the iso-density threshold. This result confirms that obtained by Hacker *et al.* (1996). By fixing the threshold and varying the Reynolds number (Fig. 5.18), the volume fraction remains unchanged. So, we can conclude that the entrainment is not affected by the Reynolds number for R varying between 2222 and 3889. Previous investigations (Cenedese & Adduce 2008, Nogueira *et al.* 2014, and Ottolenghi *et al.* 2016a, 2016b, & 2017) found that there is a dependence of the entrainment on Reynolds number, but the R in the present simulations does not have an important variation ($2222 \leq R \leq 3889$).

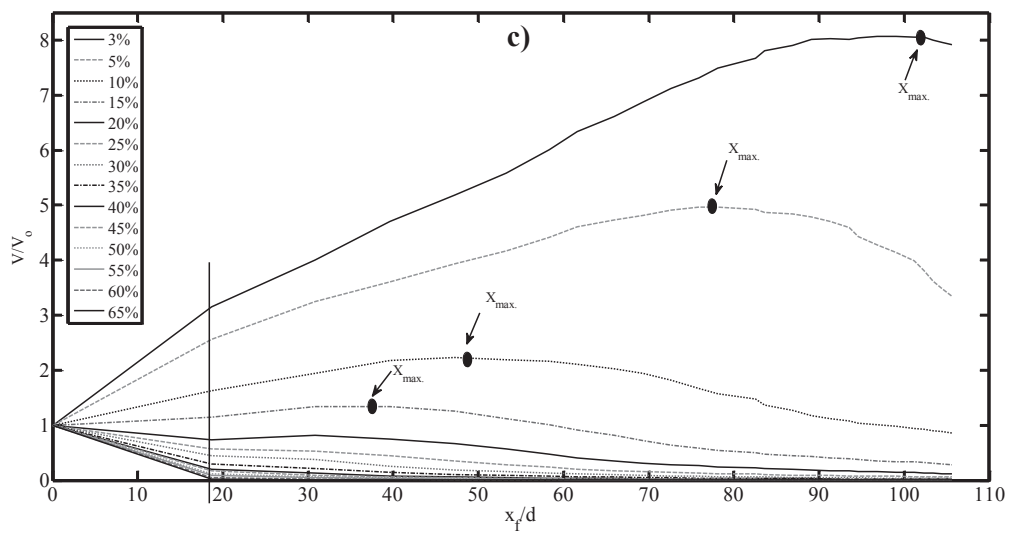
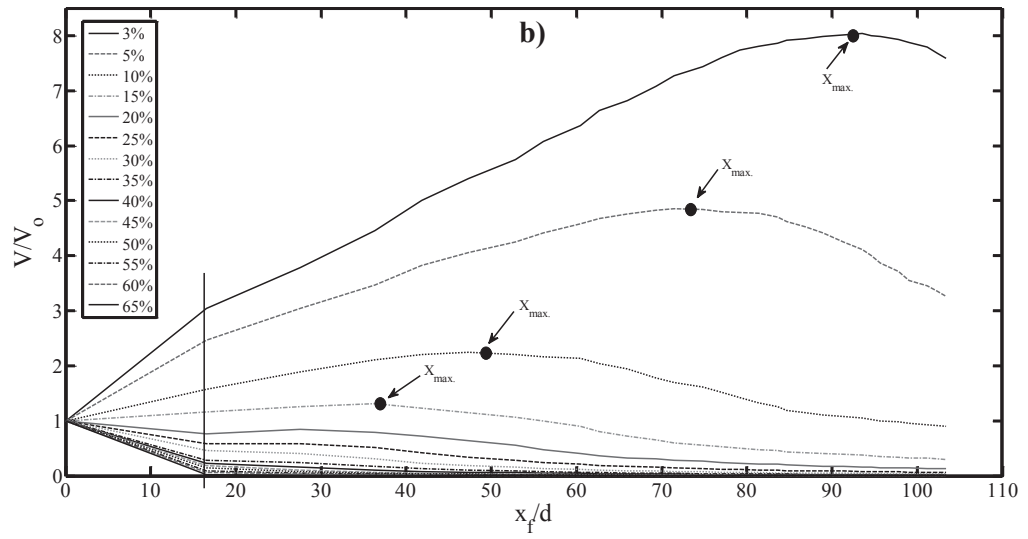
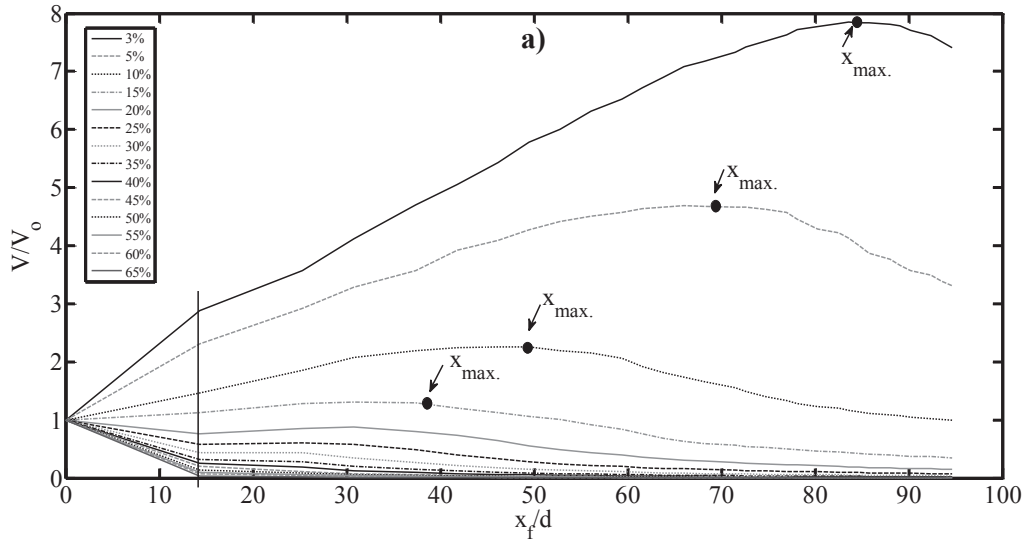


Figure 5.17: Fraction volume V/V_0 of total volume to the initial injection volume of the fluid current plotted as a function of the front position for: a) run4, b) run5, and c) run6.

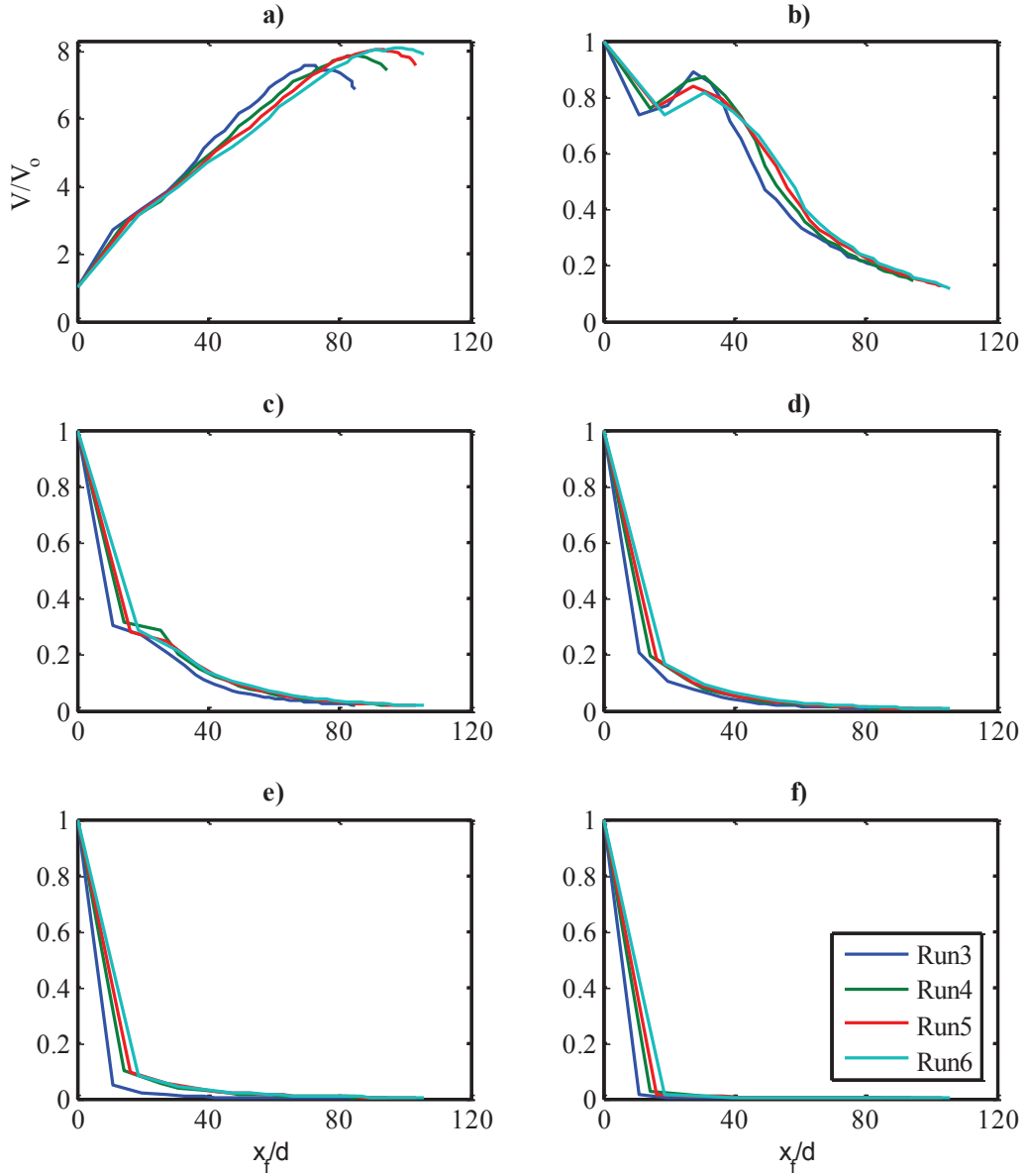


Figure 5.18: Fraction volume V/V_0 of total volume to the initial injection volume of the fluid current for different concentrations threshold plotted as a function of position front: a) 3%, b) 20%, c) 35%, d) 45%, e) 55%, and f) 65%.

To compare our result with that obtained in the previous investigations (Cenedese & Adduce 2008, Nogueira *et al.* 2014, and Ottolenghi *et al.* 2016a, 2016b, & 2017), we must use the bulk Reynolds and Froude numbers. Following Ottolenghi *et al.* (2016 a, and 2016b), bulk Reynolds R_b and Froude Fr_b numbers are defined as:

$$R_b = \frac{U H/2}{\nu} \quad (5.6)$$

$$Fr_b = \frac{U}{\sqrt{g'_m H/2}} \quad (5.7)$$

where U is a velocity scale defined as the ratio between a length scale L and a time scale T . L is chosen as $L = 0.55 \text{ m}$ and T is the time taken by the gravity current to travel a distance of 0.55 m . g'_m is the mean value of the reduced gravity between the initial and the final configuration of the gravity current. In this study, the velocity scale varied in the range $0.032 \text{ m/s} < U < 0.048 \text{ m/s}$, while the bulk Reynolds and Froude numbers varied in the ranges $800 < R_b < 1200$ and $0.3 < Fr_b < 0.5$, respectively. For $R_b \sim 1000$ and $3 < Fr_b < 6$ (closer values of R_b and larger values of Fr_b than those obtained in our study), Cenedese and Adduce (2008) showed that E does not present a clear variation and is almost constant in the mixing turbulent regime. For the studies of Ottolenghi *et al.* (2006a, 2016b, and 2017), E increases in larger ranges of R_b between (2000-16000) but with small values of Fr_b between (0.2-0.8). So, in the present study, we conclude that E is almost constant because R_b and Fr_b did not show large variations.

5.6 Summary

In this chapter of my dissertation, I investigated the mixing of a saline water current jet into the ambient fresh water at rest in a large basin. Reynolds-Averaged Navier-Stokes (RANS) and diffusion-convection equations of the saline water volume fraction are used to model the mixing and the propagation of the saline gravity current jet. The comparison of the numerical with the various experimental front positions presents a good agreement for Reynolds and Richardson numbers laying in the ranges $2222 \leq R \leq 3889$ and $0.003 < Ri < 0.01$ respectively.

The numerical simulations of the hydrodynamic fields show that the maximum velocity is located at $0.18z_{0.5}$, where $z_{0.5}$ is the height at which the mean velocity u is equal to the half of the maximum velocity u_{\max} . The excess-density shows a radial symmetry close to the inlet and asymmetry far from the inlet. The local gradient Richardson number Ri_g shows that the maximum of the turbulent mixing occurs at $z \approx z_{0.5}$ in the first stage of the gravity current close to the inlet and it collapses far from the inlet. By analyzing the turbulent mixing in a 3D configuration, the volume of the turbulent mixing increases with the x -coordinate close to the inlet jet and decreases far from the inlet. The entrainment depends both on the front position and on the values of the iso-density threshold. The entrainment is found independent of the Reynolds numbers between 2222-3889.

Chapter 6: Conclusions and Future Works

Section 6.1 highlights the main results of this dissertation, while Section 6.2 provides recommendations for future works.

6.1 Conclusions

In this dissertation, the results of a thorough experimental and numerical investigation was presented on Newtonian saline gravity current jet propagation into calm fresh water over a horizontal, rigid, and smooth bottom surface generated in a typical saline discharge as a jet into a coastal environment. The investigation was performed to determine the influence of the jet characteristics (e.g. the dynamics of a 3D gravity current jet, the hydrodynamic and density distributions of a 3D gravity current jet, the turbulent mixing in a 3D gravity current jet for the weak turbulent regime, and the entrainment of a 3D mixing gravity current jet) on the propagation dynamics of the saline gravity currents. According to literature reviewed in chapter two, there are very few experimental investigations on gravity currents jet and the experimental component of this research. Laboratory experiments were conducted with different initial flow rates and one concentration in the same experimental setup.

The experiments in the basin involved a typical denser fluid jet incoming into calm lighter ambient fluid submerged horizontally discharge configuration in the field and three-dimensional gravity currents were generated in these experiments. Immediately after the injection of the denser fluid into the basin, a gravity current of heavy fluid forms nearer the injector channel zone and the bottom surface. The propagation of the gravity currents evolves over time downstream; simultaneously, a current formed by ambient lighter fluid flows above the heavy current in the opposite direction, upstream. Through the development of the propagation, the saline gravity current mixes with the surrounding ambient fresh water and continuously entrains part (the entrainments occurring) of gravity current. Also, understanding the interactions between two fluids dynamically appears in the three dimensional representation.

In this study, the RANS model was used, while this model is known to be able to give good agreement with the experimental data of the dynamics at the front position, it presents difficulties to reproduce the instability at the same position. Therefore, the front instability for

the lock-exchange can be observed using the LES (Ottalenghi *et al.* 2016a, b, and 2017) or DNS (Illicak 2014) methods, but such method need high computer resources.

RANS with k- ϵ and diffusion-convection of the saline water volume fraction are used to study numerically the mixing in the weakly turbulent with Reynolds and Richardson numbers (R and Ri) lying between 1111-3889 and 0.001-0.03 respectively. The front positions obtained with numerical simulations and experiments present a good agreement with the regime studied ($2222 < R < 3889$).

For all positions from the inlet, the velocity profiles present a unique maximum value at $z/z_{0.5} \approx 0.18$. This value is close to the one observed in the 2D gravity current mixture (Buckee *et al.* 2009, and Gerber *et al.* 2011). The numerical simulations of the hydrodynamic fields show that the maximal mean velocity is located at $z \approx 0.18 z_{0.5}$, where $z_{0.5}$ is the height at which the mean velocity u is equal to half the maximal velocity \bar{u}_{max} . The excess-density shows a radial a symmetric close to the inlet and asymmetry far from the inlet. The local gradient Richardson number Ri_g shows that the maximum of the turbulent mixing occurs for $z \approx z_{0.5}$ in the first stage of the gravity current close to the inlet, while it collapses far from the inlet and the bottom surface. Also, the comparison between the density and velocity profiles in y-coordinates shows that close to the inlet, the mixing of gravity current jet propagates while the pure fresh water can move without mixing.

This can be explained by the presence of the viscous boundary layer zone of the fresh water without mixing (Philippe *et al.*, 2005). Far from the inlet, the presence of one mixing gravity current zone with motion, and by analyzing the turbulent mixing in the 3D space, the mixing turbulent zone increases close to the inlet and decreases far from the inlet. The turbulent mixing zone is characterized by the estimation of the gradient Richardson number Ri_g in the 3D coordinates. The entrainment at different values of the iso-density threshold shows that the mixing does not depend on the Reynolds number. The maximum of the turbulent mixing occurs at height $z \approx z_{0.5}$ where the mean horizontal velocity u is equal to half of the maximal mean velocity u_{max} .

The envelope of the mixing turbulent depends strongly to space from the inlet. Close to the inlet, the mixing turbulent zone presents a semi-circular form. The mixing turbulent zone increases and changes to a non-axisymmetric form. While, far from the inlet, the mixing turbulent zone decreases strongly and exists only close to the bottom of the basin. The entrainment of the mixing gravity current jet characterized by the determination of the non-

dimensional volume fraction of the fluid current V/V_0 depends strongly on the threshold chosen concentrations α and the front position x_f . While the entrainment is not affected by the Reynolds number for $2222 \leq R \leq 3889$. The entrainment at different values of the iso-density threshold shows that mixing does not depend on the Reynolds number for $2222 \leq R \leq 3889$. For this narrow range of R that corresponds to the weakly turbulent regime, we didn't observe the dependence of the entrainment E on the Reynolds number R . This result is in contrast from those obtained in the lock-release investigations where the entrainment E increases with R for a larger range ($2000 < R < 10000$) according to (Cenedese & Adduce 2008, Nogueira *et al.* 2014, and Ottolenghi *et al* 2016 a, 2016b, & 2017).

Derivations and evaluation of Navier Stokes equations mathematically as a theoretical study (presented in the two appendices A and B) for one and two dimensional. As well, for radially axisymmetric horizontal and inclined Newtonian and non-Newtonian gravity currents for: a) to investigate the gravity current height since the Newtonian gravity currents experiments presents difficulties getting it, and b) the non-Newtonian gravity current height, speed and impact of a pseudoplastic gravity current with the same rheological parameters.

6.2 Future works

It is expected that the theoretical, experimental, and numerical studies presented in this study will encourage numerous studies on the saline gravity currents generated in coastal discharges as well as other possible applications. Furthermore, this study has put forward some questions, particularly on the following areas:

- The obvious experiments of investigation part of this dissertation is to conduct a thorough laboratory study on the Newtonian gravity currents generated from horizontal injection (see Fig. 3.5 to Fig. 3.10 for example). The bottom slope is expected to influence the propagation dynamics significantly. It will be interesting to see all the locations where the phases of the propagation are occurring, how the front positions and the time vary in relation to the slope angle with either smooth or rough bottoms. The characteristics of the rough bottom materials such as the porosity and size play an important role in both dynamics and current kinematics. Also, must be taken into account the influence of the ambient water conditions with the slope of the bottom on the gravity currents propagation generating in a typical disc arches operation. It is necessary to see the effects of these ambient conditions in the experimental

investigations on the dynamics of the injection bottom propagation and such experiments may need a large experimental facility.

- The comparison between numerical and experimental results of the front's position shows a fairly good agreement for four runs in spite of the denser fluids initial head lower value. This fact can be due to the application of the RANS with $k-\varepsilon$ and diffusion-convection used for the numerical model, which seems to be suitable for lower initial depth of the gravity currents, when the development of this gravity current is influenced by the oscillations of the ambient fresh surface. The lower thickness of the denser gravity current layer, and such an ambient fresh surface oscillations should not be neglected in future studies as laminar current's dynamics and instability in the range of the Reynolds number for $10 < R < 1000$. Also, observation of mixing the dependency and velocity of entrainment, and potential energy occurring in the dense mixing within the boundary between the current and the ambient fluid. We aspire to using the direct numerical (DNS) for comparison with the (RANS with $k-\varepsilon$) and diffusion-convection model.
- Studying the effects of various slopes on the motion of Newtonian and non-Newtonian (Rheology) gravity current over a rigid surface generated by injecting a source experimentally and numerically. These external influences can play an important role in the gravity current development depending on the equations derivatives in the two appendices (Equations for Newtonian gravity current: A-77, and A-103, and for non-Newtonian gravity current: B-50, and B-84).

Appendix A

Newtonian gravity current equations

In the present appendix, we consider the derivation and the analytical solution to the 2D saline bottom gravity currents jet into fresh water in horizontal and in sloping channel. The case study of my dissertation “saline bottom gravity currents jet into fresh water” are subject to the no-slip condition at the smooth bottom boundary, while the fresh gravity currents jet over saline free-surface are subject to the free-slip condition at the free-surface boundary appear in the studies of Dhafar *et al.* (2016, and 2017b)^{6 7}.

A.1 Equations for horizontal channel

Consider a gravity current made of saline water introducing in a basin containing a static lighter liquid made of the fresh water. The lighter ambient liquid characteristics are: Density: $\rho_{water} = \rho - \Delta\rho$, Height= H , Pressure= P , and Viscosity= μ . While the denser gravity current characteristics are: Density: $\rho_s = \rho$, Height: $d = h(x, t)$, Viscosity: μ , Pressure: p , and Velocity: $\vec{v}(u, v = 0, w = 0)$.

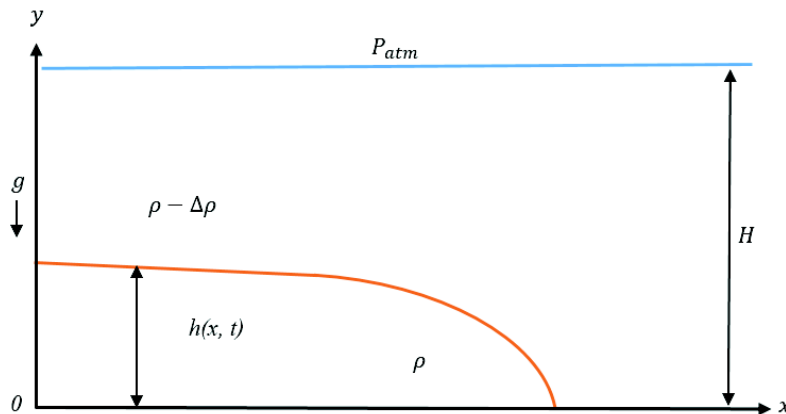


Figure A.1: A plot of the gravity current flow and co-ordinate system.

Gravity current flow is mono directional along the x-axis as shown in Fig.A.1 and is infinitely wide so it is planar in the (x, y) plane and therefore, the flow field (\vec{v}, p) does not depend on z . Its flow beneath the ambient liquid is described by the continuity equation together with Navier Stokes equation. The continuity equation expresses the mass conservation. It writes for an incompressible fluid case:

⁶ Dhafar, I. A., Latrache, N., and Nsom, B. (2016). Experimental Study of the Effect of the Spreading Buoyant Gravity Current on the Coastal Environment. The 2016 3rd International Conference on Coastal and Ocean Engineering (ICCOE 2016), Tokyo, Japan, 8-9, April.

⁷ Dhafar, I. A., Latrache, N., and Nsom, B. (2017a). Experimental Study of the Effect of the Spreading Buoyant Gravity Current on the Coastal Environment. DOI: 10.7763/IJET.2017.V9.957. International Journal of Engineering and Technology, 09(02):129-132.

$$\frac{\partial u}{\partial x} + \frac{\partial v}{\partial y} + \frac{\partial w}{\partial z} = 0 \quad (\text{A.1})$$

which leads to ($v = w = 0$), and; $\frac{\partial u}{\partial x} = 0$ (A.2)

but, as stated previously, u does not depend on the z , so: $u = u(y)$ (A.3)

The Navier Stokes equations describe the motion of fluid substances. These equations express the momentum conservation and they axis from applying Newton's second law to fluid motion, together with the assumption that the stress in the fluid is the sum of a diffusing viscous term (proportional to the gradient of velocity) and a pressure term.

$$\rho \frac{d\vec{v}}{dt} = -\vec{\nabla}p + \mu\overline{\Delta\vec{v}} + \rho\vec{F}_v \quad (\text{A.4})$$

Projecting vectorial equation (A.4) the Navier stokes equation on the (\overline{oy}) axis gives:

$$0 = -\frac{1}{\rho} \frac{\partial p}{\partial y} - g \quad (\text{A.5})$$

This differential equation can be integrated easily in the form:

$$p(y) = -\rho gy + A \quad (A = \text{constant of integration}) \quad (\text{A.6})$$

Equation (A.6) shows that $p(h)$ is described by the law of hydrostatic pressure (Pascal Law) in the gravity current. Now, in the ambient fluid the same hydrostatic pressure field takes the form:

$$P(y) = P_{atm} + (\rho - \Delta\rho)g \cdot (H - y) \quad (\text{A.7})$$

at the interface $y = h(x, t)$, it writes: $P_{atm} + (\rho - \Delta\rho)(H - h) = P(h)$ (A.8)

Equating that expression of $P(h)$ with that of $P(y)$ at the interface ($y=h$) given by Eq. (A.6) we get:

$$-\rho gh + A = P_{atm} + g(\rho - \Delta\rho)(H - h) \quad (\text{A.9})$$

The constant of integration A can be derived from Eq. (A.9) in the form:

$$A = P_{atm} + (\rho - \Delta\rho)Hg + g \cdot \Delta\rho \cdot h \quad (\text{A.10})$$

Introducing Eq. (A.10) in Eq. (A.6) gives the pressure field in the gravity current:

$$p(y) = P_{atm} + (\rho - \Delta\rho)g(H - h) + \rho g(h - y) \quad (\text{A.11})$$

Let us now project the Navier Stokes vectorial equation (A.4) on the (\overline{ox}) axis.

$$\frac{\partial p}{\partial x} = \mu\Delta u \quad (\text{A.12})$$

Taking account of (A.3), we get:

$$\frac{\partial p}{\partial x} = \mu \frac{\partial^2 u}{\partial y^2} \quad (\text{A.13})$$

While the pressure field is given by Eq. (A.11) so it can be derived that:

$$\frac{\partial p}{\partial x} = g\Delta\rho \cdot \frac{dh}{dx} \quad (\text{A.14})$$

If we note the differential gravity:

$$g\Delta\rho = g' \quad (\text{A.15})$$

The Eq. (A.13) becomes:

$$g' \frac{dh}{dx} = \mu \frac{d^2u}{dy^2} \quad (\text{A.16})$$

This ordinary differential equation can be solved easily by taking two successive quadratures:

$$\frac{du}{dy} = \frac{g'}{\mu} \cdot \frac{dh}{dx} y + k_1 \quad (\text{A.17})$$

$$\text{and, } u(y) = \frac{g'}{\mu} \frac{dh}{dx} \frac{y^2}{2} + k_1 y + k_2 \quad (\text{A.18})$$

where k_1 and k_2 are two constants of integration to be determined by the boundary conditions: the first boundary condition is the no slip condition at the basin bottom.

$$y = 0 \rightarrow u = 0 \quad (\text{A.19})$$

$$\text{which leads to: } k_2 = 0 \quad (\text{A.20})$$

The second boundary condition expresses the continuity of the shear stress at the free surface:

$$\frac{\partial u}{\partial y}(h, x, t) = 0 \quad \text{At } y=h \quad (\text{A.21})$$

which brings:

$$\frac{g'}{\mu} \frac{dh}{dx} h + k_1 = 0 \quad (\text{A.22})$$

$$\text{That is: } k_1 = -\frac{g'}{\mu} \cdot \frac{dh}{dx} \cdot h \quad (\text{A.23})$$

The velocity field is therefore obtained in the form:

$$u(y) = \frac{1}{2} \frac{g'}{\mu} \frac{dh}{dx} [y^2 - 2yh] \quad (\text{A.24})$$

The continuity equation that has been written in its local form (Eq. A.2) and that expresses the mass conservation can also be written in its global form. Consider two transversal sections s and s' at respective abscissa x and $x+dx$ as shown in Fig.A.2.

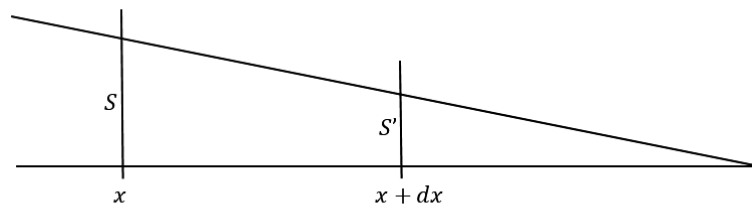


Figure A.2: Two transversal cross section view element

We must write that the variation of flow rate from station x to station $x+dx$ is due to the time variation of wet surface:

$$\frac{\partial S}{\partial t} + \frac{\partial Q}{\partial t} = 0 \quad (\text{A.25})$$

the section being rectangular and its width being l , we have: $s = l \cdot h$ (A.26)

and if we note q the unit flow rate, i.e. $q = \frac{Q}{b} = v \cdot h$ (A.27)

where v is the average velocity defined by:

$$v = \frac{\int_0^h u(y) dy}{h} \quad (\text{A.28})$$

∴ Equation (A.25) becomes:

$$\frac{\partial h}{\partial t} + \frac{\partial q}{\partial x} = 0 \quad (\text{A.29})$$

so:

$$\frac{\partial h}{\partial t} + \frac{\partial}{\partial x} \left[\frac{\int_0^h u(y) dy}{h} \cdot h \right] = 0 \quad (\text{A.30})$$

which gives:

$$\frac{\partial h}{\partial t} + \frac{\partial}{\partial x} \left[\int_0^h u(y) dy \right] = 0 \quad (\text{A.31})$$

Equation (A.31) is the global form of the continuity equation. Let us introduce the expression of the velocity field $u(y)$ obtained in Eq. (A.24) in the latter continuity equation (Eq. (A.31)) we get:

$$\frac{\partial h}{\partial t} + \frac{\partial}{\partial x} \left[\int_0^h \left(-\frac{1}{2} \frac{g'}{v} \frac{\partial h}{\partial x} y(2h-y) \right) dy \right] = 0 \quad (\text{A.32})$$

$$\frac{\partial h}{\partial t} - \frac{1}{2} \frac{g'}{v} \frac{\partial}{\partial x} \left[\int_0^h \left(\frac{\partial h}{\partial x} y(2h-y) \right) dy \right] = 0 \quad (\text{A.33})$$

$$\frac{\partial h}{\partial t} - \frac{1}{2} \frac{g'}{v} \frac{\partial}{\partial x} \left[\frac{\partial h}{\partial x} \left(\int_0^h (2hy - y^2) dy \right) \right] = 0 \quad (\text{A.34})$$

$$\frac{\partial h}{\partial t} - \frac{1}{2} \frac{g'}{v} \frac{\partial}{\partial x} \left[\frac{\partial h}{\partial x} \left(2h \cdot \frac{h^2}{2} - \frac{h^3}{3} \right) \right] = 0 \quad (\text{A.35})$$

$$\frac{\partial h}{\partial t} - \frac{1}{2} \frac{g'}{v} \frac{\partial}{\partial x} \left[\frac{\partial h}{\partial x} \left(h^3 - \frac{h^3}{3} \right) \right] = 0 \quad (\text{A.36})$$

$$\frac{\partial h}{\partial t} - \frac{1}{2} \frac{g'}{v} \frac{\partial}{\partial x} \left[\frac{\partial h}{\partial x} \cdot \frac{2h^3}{3} \right] = 0 \quad (\text{A.37})$$

$$\frac{\partial h}{\partial t} - \frac{g'}{3v} \frac{\partial}{\partial x} \left(h^3 \frac{\partial h}{\partial x} \right) = 0 \quad (\text{A.38})$$

This is the EDP dynamic equation governing (of gravity current) with unknown function $h(x, t)$.

Calculate $\frac{\partial}{\partial x} (h^4)$ to make more tractable the second term on the first member.

$$\frac{\partial}{\partial x} (h^4) = 4h^3 \frac{\partial h}{\partial x} \quad (\text{A.39})$$

$$h^3 \frac{\partial h}{\partial x} = \frac{1}{4} \frac{\partial}{\partial x} (h^4) \quad (\text{A.40})$$

is replaced in equation (equation is restored EDP):

$$\frac{\partial h}{\partial t} - \frac{g'}{12\nu} \frac{\partial}{\partial x} (h^4) = 0 \quad (\text{A.41})$$

A.2 Equations of Sloping Bottom

If the channel bottom is now inclined, with the gravity current the static ambient liquid, we can sketch the flow field as shown in Fig. A.3. Remark that the interface of the ambient liquid is horizontal, owing to the Pascal hydrostatic law and therefore the pressure field in the ambient liquid is given by:

$$P(Y) = P_{atm} + (\rho - \Delta\rho) \cdot g \cdot Y \quad (\text{A.42})$$

Remark secondly that the flows is entirely defined by the following three quantities; θ : Channel slope, H : down field height, and L : channel bottom length. While the gravity mono directional motion is still governed by the continuity and the Navier stokes equations (Eq. (A.2) and Eq. (A.4) :

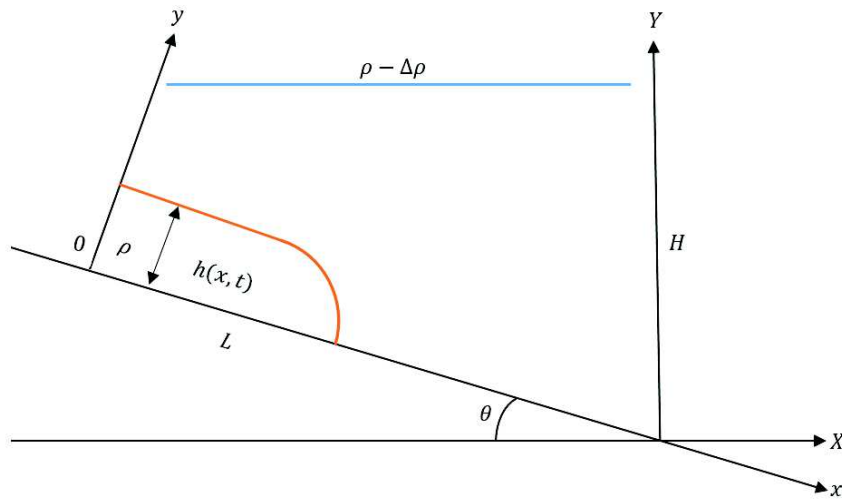


Figure A.3: A plot of the inclined gravity current flow.

The continuity equation (A.31) brings; $u = u(y)$. While, the Navier stokes equations can be projected respectively on the \overline{oy} axis as:

$$0 = -\frac{1}{\rho} \frac{\partial p}{\partial y} - g \cdot \cos\theta \quad (\text{A.43})$$

This differential equation can be solved as:

$$p(y) = -\rho g \cos\theta \cdot y + B \quad (\text{A.44})$$

where B is as constant of integration. Also here, we can see that a hydrostatic pressure field governs. While the same Pascal law writes, in the ambient liquid (see Eq. (A.42)):

$$P(Y) = P_{atm} + (\rho - \Delta\rho) g Y \quad (\text{A.45})$$

At the interface the $h = y$, the pressure in the gravity current is given by:

$$p(h) = -\rho g \cos \theta \cdot h + B \quad (\text{A.46})$$

While for the ambient fluid, we must first of all remark that: Only two lengths are needed to design the H_0 (downfield height) and L (length of channel bottom), and Using these three quantities H_0, L, θ , we can derive the following other axis. (See Fig.A.4).

The flow system is entirely defined by the three flowing parameters: D, L, θ . Indeed, we can calculate:

$$D = L \cdot \cos \theta \quad (\text{A.47})$$

$$\lambda = L \cdot \sin \theta \quad (\text{A.48})$$

$$\therefore \delta = H_0 - \lambda = H_0 - L \sin \theta \quad (\text{A.49})$$

$$\therefore O\hat{A}E = \theta \quad (\text{A.50})$$

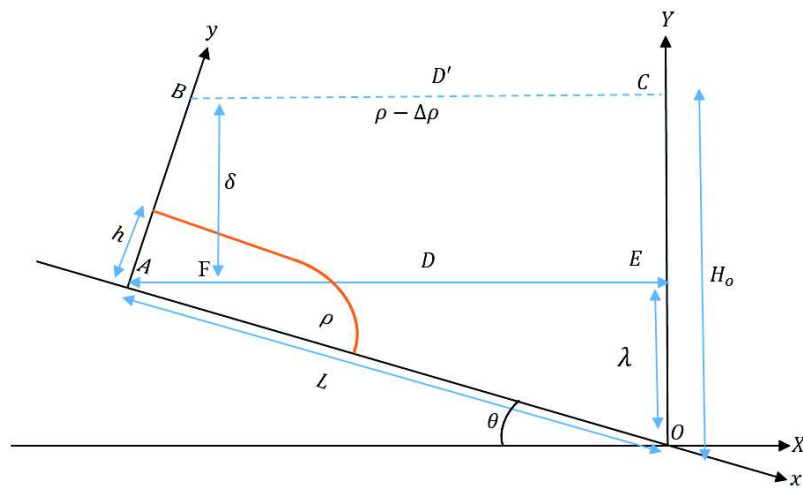


Figure A.4: A plot of the inclined gravity current flow and co-ordinate system.

$$\text{and so on: } E\hat{A}B = \frac{\pi}{2} - \theta \quad (\text{A.51})$$

$$\therefore \frac{\delta}{AF} = \tan(B\hat{A}F) \rightarrow \therefore AF = \frac{\delta}{\tan(B\hat{A}F)} = \frac{\delta}{\tan(\frac{\pi}{2} - \theta)} = \frac{\delta}{\cot \theta} \quad (\text{A.52})$$

$$\therefore D' = D - AF = L \cos \theta - \frac{\delta}{\cot \theta} \quad (\text{A.53})$$

$$\text{since it is: } \delta = AB \cos \theta \rightarrow \therefore AB = \frac{\delta}{\cos \theta} = \frac{H - L \sin \theta}{\cos \theta} \quad (\text{A.54})$$

What is the vertical height $H(x)$ at given abscissa x as shown in Fig. A.5.

$$OK = OI \cdot \sin \theta \quad (\text{A.55})$$

$$\text{at abscissa } x, \text{ the vertical height } H(x) \text{ is } IJ, \therefore IJ = CK = OC - OK, \quad (\text{A.56})$$

$$\text{and so: } H(x) = H_0 - x \cdot \sin \theta \quad (\text{A.57})$$

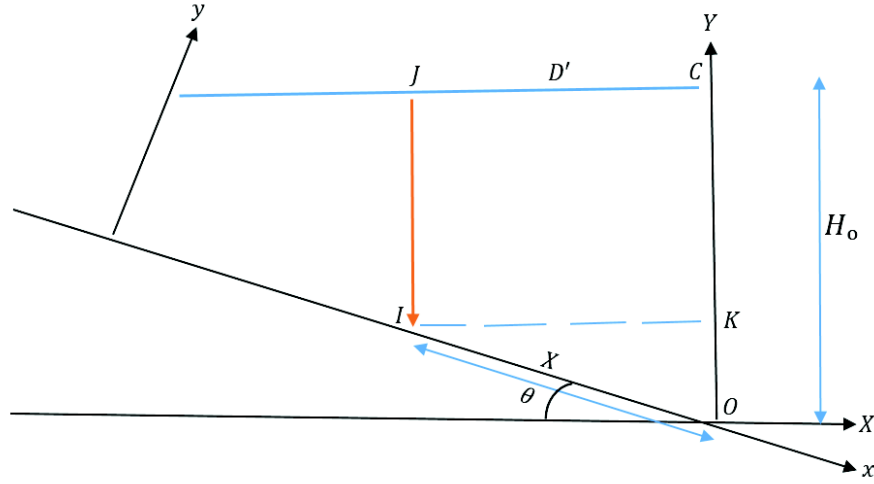


Figure A.5: A plot of the inclined frontal gravity current head flow and co-ordinate system.

A.2.1 Conclusion

Given a point at abscissa x inside the fluid domain and with coordinate y , what is its vertical depth Y as shown in Fig.A.6.

$$\because IJ = H(x), \quad (A.58)$$

given $IM=y$ we have:

$$\because IR = y \cdot \cos\theta \quad \rightarrow \quad \because JR = H(x) - IR \quad (A.59)$$

$$\text{and so: } Y = MQ = JR = [H_0 - x \cdot \sin\theta] - y \cdot \cos, \quad (A.60)$$

given a point with abscissa x , the total depth (river bottom) (see Eq. A.57) is:

$$H(x) = H_0 - x \cdot \sin\theta,$$

and for a point with abscissa x , inside the fluid domain (ambient fluid or gravity current) with coordinate y , its vertical depth is:

$$Y = H_0 - x \cdot \sin\theta - y \cdot \cos\theta \quad (A.61)$$

Can get the pressure field in the (ambient fluid or gravity current) by substitute Y in Eq. (A.42) is:

$$P(Y) = P_{atm} + (\rho - \Delta\rho) \cdot g \cdot (H_0 - x \cdot \sin\theta - y \cdot \cos\theta) \quad (A.62)$$

At the interface the depth of gravity current equal the depth y in the equations (A-59, 60, and 61) so the h from eq. (A-61) is: $p(\text{interface}) = p(y = h) = -\rho \cdot g \cdot \cos\theta + B$. Given by Eq. (A-46), and also the pressure at the interface equal the Eq. (A-62) written by:

$$\because P(\text{interface}) = P_{atm} + (\rho - \Delta\rho) \cdot g \cdot (H_0 - x \cdot \sin\theta - h \cdot \cos\theta) \quad (A.63)$$

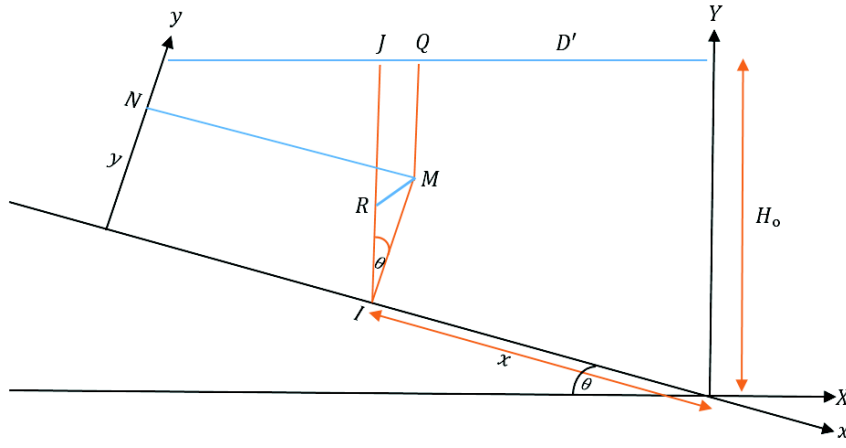


Figure A.6: A plot of pressure field the inclined gravity current in the ambient fluid.

Equating these two expression (Eq. (A.46) and Eq. (A-62) are brings:

$$-\rho \cdot g \cdot h \cdot \cos\theta + B = P_{atm} + (\rho - \Delta\rho) \cdot g \cdot (H_0 - x \cdot \sin\theta - h \cdot \cos\theta) \quad (\text{A.64})$$

$$\therefore B = \rho \cdot g \cdot h \cdot \cos\theta + P_{atm} + (\rho - \Delta\rho) \cdot g \cdot (H_0 - x \cdot \sin\theta) - \rho \cdot h \cdot \cos\theta + \Delta\rho \cdot h \cdot \cos\theta \quad (\text{A.65})$$

We introduce that expression of B in p(y) given by Eq. (A.44)

$$p(y) = -\rho \cdot g \cdot \cos\theta \cdot y + B$$

$$\therefore p(y) = -\rho \cdot g \cdot \cos\theta \cdot y + P_{atm} + (\rho - \Delta\rho) \cdot g \cdot (H_0 - x \cdot \sin\theta) + \Delta\rho \cdot h \cdot \cos\theta \quad (\text{A.65})$$

In that relation let us add and subtract the same quantity:

$$(\rho \cdot g \cdot h \cdot \cos\theta p(y) = P_{atm} - \rho \cdot g \cdot y \cdot \cos\theta + (\rho - \Delta\rho) \cdot g \cdot (H_0 - x \cdot \sin\theta) + \Delta\rho \cdot h \cdot \cos\theta + \rho \cdot g \cdot \cos\theta - \rho \cdot g \cdot h \cdot \cos\theta \quad (\text{A.66})$$

$$\therefore p(y) = P_{atm} + \rho \cdot g \cdot (h - y) \cdot \cos\theta + (\rho - \Delta\rho) \cdot g \cdot (H_0 - x \cdot \sin\theta - h \cdot \cos\theta) \quad (\text{A.67})$$

A.2.2 Verification

The above equation represents the pressure field, thereafter for the horizontal channel ($\theta=0$) in that expression, we recover Eq. (A.11) solution of the horizontal channel. The Navier Stokes vectorial equation is:

$$0 = -\vec{\nabla}p - \rho \vec{g} + \mu \Delta \vec{v} \quad (\text{A.68})$$

$$\overline{\partial x} \quad \left\{ 0 = -\frac{\partial p}{\partial x} - \rho \cdot g \cdot \sin\theta + \mu \left(\frac{\partial^2 u}{\partial x^2} + \frac{\partial^2 u}{\partial y^2} \right) \right\} \quad (\text{A.69})$$

$$\overline{\partial y} \quad \left\{ 0 = -\frac{\partial p}{\partial y} - \rho \cdot g \cdot \cos\theta \right\} \quad (\text{A.70})$$

The above equation represents the solved of Eq. (A.43), and, so:

$$\frac{\partial p}{\partial x} = -\rho \cdot g \cdot \sin\theta + \mu \frac{\partial^2 u}{\partial y^2} \quad (\text{A.71})$$

The same as mentioned above if ($\theta=0$), when the flow on a horizontal surface, we recover the equation (A.12): ($\frac{\partial p}{\partial x} = \mu \Delta u$): The Navier Stokes equation On the (\overline{ox}) axis gives:

$$0 = -\frac{\partial p}{\partial x} - \rho \cdot g \cdot \sin\theta + \mu \frac{d^2 u}{dy^2} \quad (\text{A.72})$$

$$\therefore \frac{\partial p}{\partial x} = -\rho \cdot g \cdot \sin\theta + \mu \frac{d^2 u}{dy^2} \quad (\text{A.73})$$

with,

$$p = P_{atm} + \rho \cdot g \cdot (h - y)\cos\theta + (\rho - \Delta\rho) \cdot g \cdot (H_0 - x\sin\theta - h\cos\theta) \quad (\text{A.74})$$

$$\frac{\partial p}{\partial x} = \rho \cdot g \cdot \cos\theta \cdot \frac{\partial h}{\partial x} + (\rho - \Delta\rho) \cdot g \cdot \left[-\sin\theta - \cos\theta \cdot \frac{\partial h}{\partial x} \right] \quad (\text{A.75})$$

$$\frac{\partial p}{\partial x} = \rho g \cos\theta \frac{\partial h}{\partial x} + g \left[-\rho \sin\theta - \rho \cos\theta \frac{\partial h}{\partial x} + \Delta\rho \sin\theta + \Delta\rho \cos\theta \frac{\partial h}{\partial x} \right] \quad (\text{A.76})$$

$$\therefore \frac{\partial p}{\partial x} = g \left[-\rho \sin\theta + \Delta\rho (\sin\theta + \cos\theta \frac{\partial h}{\partial x}) \right] \quad (\text{A.77})$$

A.2.3 Remark about a horizontal channel

For a horizontal channel, we have ($\theta = 0$) so the Eq. (A.77) reduces to:

$$\frac{\partial p}{\partial x} = g \cdot \Delta\rho \cdot \frac{\partial h}{\partial x} \quad (\text{A.78})$$

which is exactly the equation we obtained at (A-14). If we make the differential gravity:

$$g \cdot \Delta\rho = g' \quad (\text{A.79})$$

then, equation (A.73) becomes:

$$\mu \frac{d^2 u}{dy^2} = \rho \cdot g \cdot \sin\theta + \frac{\partial p}{\partial x} \quad (\text{A.80})$$

$$\mu \frac{d^2 u}{dy^2} = \rho \cdot g \sin\theta + \left\{ g \left[-\rho \sin\theta + \Delta\rho (\sin\theta + \cos\theta \cdot \frac{\partial h}{\partial x}) \right] \right\} \quad (\text{A.81})$$

$$\mu \frac{d^2 u}{dy^2} = \rho g \sin\theta - \rho g \sin\theta + g' (\sin\theta + \cos\theta \cdot \frac{\partial h}{\partial x}) \quad (\text{A.82})$$

$$\therefore \mu \frac{d^2 u}{dy^2} = g' (\sin\theta + \cos\theta \cdot \frac{\partial h}{\partial x}) \quad (\text{A.83})$$

This ordinary differential equation can be solved easily by taking two successive quadratures.

$$\frac{du}{dy} = \frac{g'}{\mu} \left(\sin\theta + \cos\theta \cdot \frac{dh}{dx} \right) y + c_1 \quad (\text{A.84})$$

and,

$$u(y) = \frac{g'}{\mu} \left(\sin\theta + \cos\theta \cdot \frac{dh}{dx} \right) \cdot \frac{y^2}{2} + c_1 y + c_2 \quad (\text{A.85})$$

where c_1 and c_2 are two constant of integration to be determined by the boundary condition. The first boundary condition is the no slip condition of the basin bottom:

$$\text{When } (y = 0) \rightarrow \therefore u = 0, \quad (\text{A.86})$$

which leads to:

$$c_2 = 0 \quad (\text{A.87})$$

The second boundary condition expresses the continuity of the shear stress at the interface:

$$\text{at } y = h \rightarrow \therefore \frac{\partial u}{\partial y}(h, x, t) = 0 \quad (\text{A.88})$$

$$\text{which brings: } \frac{g'}{\mu} \left[\sin\theta + \cos\theta \cdot \frac{dh}{dx} \right] \cdot h + c_1 = 0 \quad (\text{A.89})$$

$$c_1 = -\frac{g'}{\mu} \left[\sin\theta + \cos\theta \cdot \frac{dh}{dx} \right] \cdot h \quad (\text{A.90})$$

The velocity field is therefore obtained in the form:

$$u(y) = \frac{g'}{2\mu} \left(\sin\theta + \cos\theta \cdot \frac{dh}{dx} \right) \cdot y^2 + c_1 y \quad (\text{A.91})$$

$$u(y) = \frac{g'}{2\mu} \left(\sin\theta + \cos\theta \cdot \frac{dh}{dx} \right) y^2 - \frac{g'}{\mu} \left[\sin\theta + \cos\theta \cdot \frac{dh}{dx} \right] h \cdot y \quad (\text{A.92})$$

$$\text{which leads to: } u(y) = \frac{g'}{2\mu} \left[\sin\theta + \cos\theta \cdot \frac{dh}{dx} \right] \cdot [y^2 - 2yh] \quad (\text{A.93})$$

$$\text{Let us apply the equation of continuity (A-31): } \frac{\partial h}{\partial t} + \frac{\partial}{\partial x} \left[\int_0^h u(y) dy \right] = 0$$

If we replace $u(y)$ by the equation we just obtained:

$$\frac{\partial h}{\partial t} + \frac{\partial}{\partial x} \left\{ \int_0^h \frac{g'}{2\mu} \left[\sin\theta + \cos\theta \frac{\partial h}{\partial x} \right] (y^2 - 2yh) dy \right\} = 0 \quad (\text{A.94})$$

$$\frac{\partial h}{\partial t} + \frac{g'}{2\mu} \left\{ \frac{\partial}{\partial x} \int_0^h \sin\theta (y^2 - 2y) dy + \frac{\partial}{\partial x} \int_0^h \cos\theta \frac{\partial h}{\partial x} (y^2 - 2yh) dy \right\} = 0 \quad (\text{A.95})$$

$$\frac{\partial h}{\partial t} - \frac{g'}{2\mu} \left\{ \frac{\partial}{\partial x} \left[\sin\theta \int_0^h (2yh - y^2) dy \right] + \frac{\partial}{\partial x} \left[\cos\theta \int_0^h \frac{\partial h}{\partial x} (2yh - y^2) dy \right] \right\} \quad (\text{A.96})$$

$$\frac{\partial h}{\partial t} - \frac{g'}{2\mu} \left\{ \sin\theta \frac{\partial}{\partial x} \left[h^3 - \frac{h^3}{3} \right] + \cos\theta \frac{\partial h}{\partial x} \left[\frac{\partial h}{\partial x} \left(h^3 - \frac{h^3}{3} \right) \right] \right\} = 0 \quad (\text{A.97})$$

$$\frac{\partial h}{\partial t} - \frac{g'}{\mu} \left\{ \sin\theta \cdot \frac{\partial}{\partial x} \left[\frac{h^3}{3} \right] + \cos\theta \cdot \frac{\partial}{\partial x} \left[\frac{h^3}{3} \cdot \frac{\partial h}{\partial x} \right] \right\} = 0 \quad (\text{A.98})$$

$$\frac{\partial h}{\partial t} - \frac{g'}{3\mu} \left\{ \sin\theta (h^3) + \cos\theta \cdot \frac{\partial}{\partial x} \left(h^3 \cdot \frac{\partial h}{\partial x} \right) \right\} = 0 \quad (\text{A.99})$$

The DEP differential equation that governs the dynamics of the gravity currents with unknown function $h(x, t)$. Now calculate $\frac{\partial}{\partial x}(h^4)$ to make more tractable the second term in the first member:

$$\frac{\partial}{\partial x}(h^4) = 4h^3 \cdot \frac{\partial h}{\partial x} \quad (\text{A.100})$$

$$h^3 \cdot \frac{\partial h}{\partial x} = \frac{1}{4} \frac{\partial}{\partial x}(h^4) \quad (\text{A.101})$$

is replaced in the dynamic equation:

$$\frac{\partial h}{\partial t} - \frac{g'}{3\mu} \left\{ \sin\theta \cdot \frac{\partial}{\partial x}(h^3) + \frac{1}{4} \cos\theta \cdot \frac{\partial^2}{\partial x^2}(h^4) \right\} = 0 \quad (\text{A.102})$$

$$\therefore \frac{\partial h}{\partial t} - \frac{g'}{12\mu} \left\{ 4\sin\theta \cdot \frac{\partial}{\partial x}(h^3) + \cos\theta \cdot \frac{\partial^2}{\partial x^2}(h^4) \right\} = 0 \quad (\text{A.103})$$

A.3 Exact Solution to Newtonian gravity current beneath a static water layer in horizontal basin

The equation of motion that we established writes:

$$\frac{\partial h}{\partial t} - \frac{g'}{12\nu} \frac{\partial^2}{\partial x^2}(h^4) = 0 \quad (\text{A.104})$$

where: $g' = \frac{\Delta\rho}{\rho}$, $\nu = \frac{\mu}{\rho}$, and $\Delta\rho = \rho - \rho'$, ρ' being the density of the water. ρ : Density of the gravity current, and ν : kinematic viscosity of the gravity current. In our problem, the gravity current is released beneath the static water at conventional rate q ; at this point, Huppert (1982) makes the assumption that:

$$\int_0^{x_{N(t)}} h(x, t) dx = qt^\alpha$$

α being a constant whose value is determined by the flow configuration; $\alpha=0$ for the injection of a fixed volume of fluid, and $\alpha=1$ corresponding to constant inflow rate (this case). Such ad'hoc assumption is not satisfactory. In this work, we intend to build rigorously exact similarity solutions without such as assumption. The solution will be gives in terms of scaling laws. The form of the equation of motion.

$$\frac{\partial h}{\partial t} - \frac{g'}{12\nu} \frac{\partial^2}{\partial x^2}(h^4) = 0$$

Suggests to search solutions in the form of separated variables, i.e.:

$$h(x, t) = X(x) \cdot T(t) \quad (\text{A.105})$$

Substituting Eq. (A.105) into Eq. (A.104) we get:

$$[T(t) \cdot X(x)]_{,t} - \frac{g'}{2\nu} [T(t^4) \cdot X(x^4)]_{,xx} = 0 \quad (\text{A.106})$$

$$T'(t) \cdot X(x) - \frac{g'}{12\nu} T(t^4) \cdot X^4_{,xx} = 0 \quad (\text{A.107})$$

Let us divide the 2 members of Eq. (A.107) by $X(x) \cdot T(t^4)$ there comes:

$$\frac{T'(t)}{T^4(t)} - \frac{g'}{12\nu} \cdot \frac{1}{x} \cdot \frac{d^2}{dx^2}(X^4(x)) = 0 \quad (\text{A.108})$$

$\frac{T'(t)}{T^4(t)}$: $f(t)$ function of variable t only.

$\frac{g'}{12v} \cdot \frac{1}{x} \cdot \frac{d^2}{dx^2}(X^4(x))$: $g(x)$ function of variables x only. As the 2 variables are independent:

$$f(t) - g(x) = 0 \quad (\text{A.109})$$

Has as only solution:

$$\begin{cases} f(t) = C \\ g(x) = C \end{cases}, \quad C = C^{te}$$

The first equation of that system writes: $\frac{1}{T^4} \cdot \frac{dT}{dt} = C \rightarrow \therefore \frac{dT}{dt} = Cdt$. Taking one quadrature:

$$-\frac{T^4}{3} = C(t - t_0) \rightarrow \therefore T^{-3} = -3C(t - t_0)$$

$$\frac{1}{T^3} = -3C(t - t_0) \rightarrow \therefore T(t) = \frac{-1}{[3C(t - t_0)]^{1/3}}$$

The second equation of the system writes:

$$\frac{g'}{12v} \cdot \frac{1}{x} \cdot \frac{d^2(x^4)}{dx^2} = C$$

$$\frac{d^2}{dx^2}(x^4) = x \cdot \frac{12v}{g'} \cdot C$$

Put $x^4 = y$

$$\frac{d^2y}{dx^2} = \frac{12vC}{g'} y^{1/4} \quad (\text{A.110})$$

Ordinary differential equation is said to be autonomous. It means that variable x does not appear in it:

Let $F(y) = y'(x)$

$$y''(x) = \frac{dF}{dx} = \frac{dF}{dy} \cdot \frac{dy}{dx} = F'(y) \cdot F(y) \quad (\text{A.111})$$

The equation (A-111) becomes:

$$F'(y) \cdot F(y) = \frac{12vC}{g'} \cdot y^{1/4} \quad (\text{A.112})$$

$$\frac{dF}{dy} \cdot F(y) = \frac{12vC}{g'} \quad (\text{A.113})$$

$$F \cdot dF = \frac{12vC}{g'} \cdot y^{1/4} dy \quad (\text{A.114})$$

$$\frac{F^2}{2} = \frac{12vC}{g'} \cdot \frac{4}{5} \cdot y^{5/4} \quad (\text{A.115})$$

$$F(y) = \left(\frac{96}{5} \cdot \frac{vC}{g'} \cdot y^{5/4} \right)^{1/2} \quad (\text{A.116})$$

$$y'(x) = \sqrt{\frac{96}{5} \cdot \frac{vC}{g'}} y^{5/8} \quad (\text{A.117})$$

$$\frac{dy}{y^{5/8}} = \sqrt{\frac{96}{5} \cdot \frac{vC}{g'}} dx \quad (\text{A.118})$$

$$\frac{8}{3} y^{1/8} = \sqrt{\frac{96}{5} \cdot \frac{vC}{g'}} (x - x_0) \quad (\text{A.119})$$

$$y^{3/8} = 4 \sqrt{\frac{6}{5} \cdot \frac{vC}{g'}} \cdot \frac{3}{8} (x - x_0) \quad (\text{A.120})$$

$$y^{3/8} = \sqrt{\frac{54}{20} \cdot \frac{vC}{g'}} (x - x_0) \quad (\text{A.121})$$

$$y(x) = \left[\left(\frac{27}{10} \cdot \frac{vC}{g'} \right)^{1/2} \right]^{8/3} (x - x_0)^{8/3} \quad (\text{A.122})$$

$$y(x) = \left(\frac{27}{10} \cdot \frac{vC}{g'} \right)^{4/3} (x - x_0)^{8/3} \quad (\text{A.123})$$

$$\text{Or } y(x) = X^4(x) \quad (\text{A.124})$$

$$X^4(x) = \left(\frac{27}{10} \cdot \frac{vC}{g'} \right)^{4/3} (x - x_0)^{8/3} \quad (\text{A.125})$$

$$X(x) = \left(\frac{27}{10} \cdot \frac{vC}{g'} \right)^{1/3} (x - x_0)^{2/3} \quad (\text{A.126})$$

Finally:

$$h(x, t) = T(t) \cdot X(x) \quad (\text{A.127})$$

$$h(x, t) = \left(\frac{27}{10} \cdot \frac{vC}{g'} \right)^{1/3} \cdot \left(\frac{-1}{3C(t-t_0)} \right)^{1/3} \cdot (x - x_0)^{2/3} \quad (\text{A.128})$$

$$\therefore h(x, t) = \left(\frac{9}{10} \cdot \frac{v}{g'} \right)^{1/3} \frac{1}{(t-t_0)^{1/3}} \cdot (x - x_0)^{2/3} \quad (\text{A.129})$$

Appendix B

Non-Newtonian gravity current equations

The bottom gravity currents are dense fluids that can be non-Newtonian. Indeed, the introduction of additives in water can modify their rheological behaviour. In the present appendix, we consider the case where the dense gravity currents are shear-thinning in a horizontal and in the sloping configuration appear in Dhafar *et al.* (2016d)⁸.

A.4 Equation for horizontal channel

As shown in Fig. A.1, for a shear thinning fluid (gravity current) (example: polymer solution, mud, pollutants... etc). The rheological behavior is described by the following equation of state:

$$\underline{\sigma} = -p\underline{1} + k\underline{\dot{\epsilon}}^n \quad (\text{B.1})$$

where $\underline{1}$ is unit tension, p is the pressure field, $\underline{\sigma}$: stress tensor, $\underline{\dot{\epsilon}}$: is the rate of shear tensor, n : is the power law index, and k : is the consistency. The flow of such fluid is no more described by the Navier Stokes equations but by the general equation of conservation of momentum.

$$\rho\gamma_i = f_i + \sigma_{ij,j} \quad (\text{B.2})$$

where γ_i is the i_{th} component of the acceleration vector:

$$(1, 2, 3) = (x, y, z) \quad \vec{\gamma} \begin{cases} \gamma_1 \\ \gamma_2 \\ \gamma_3 \end{cases}$$

σ_{ij} is the component of i_{th} line and j_{th} column of the stress tensor:

$$\underline{\sigma} = \begin{pmatrix} \sigma_{11} & \sigma_{12} & \sigma_{13} \\ \sigma_{21} & \sigma_{22} & \sigma_{23} \\ \sigma_{31} & \sigma_{32} & \sigma_{33} \end{pmatrix} \quad (\text{B.3})$$

Recalling that the stress tensor is symmetric, i.e. $\sigma_{ij} = \sigma_{ji}$

$$\underline{\sigma} = \begin{pmatrix} \sigma_{11} & \sigma_{12} & \sigma_{13} \\ \sigma_{12} & \sigma_{22} & \sigma_{23} \\ \sigma_{13} & \sigma_{23} & \sigma_{33} \end{pmatrix} \quad (\text{B.4})$$

In fact when $i \neq j$, σ is noted τ , so:

⁸ Dhafar, I. A., Nsom, B. and Latrache, N., (2015d). Effect of slope change on the dynamics of pseudoplastic mass movements beneath a static volume of water, ic-rmm2- 2nd International Conference on Rheology and Modelling of Materials, Miskolc-Lillafüred, Hungary, 5-9, October.

$$\underline{\sigma} = \begin{pmatrix} \sigma_{11} & \tau_{12} & \tau_{13} \\ \tau_{12} & \sigma_{22} & \tau_{23} \\ \tau_{13} & \tau_{23} & \sigma_{33} \end{pmatrix} \quad (\text{B.5})$$

In the configuration of a 2D flows, the 3-cordinate does appear.

$$\underline{\sigma} = \begin{pmatrix} \sigma_{11} & \tau_{12} \\ \tau_{12} & \sigma_{22} \end{pmatrix} \quad (\text{B.6})$$

Using the equation of state, we see that: $\underline{\sigma} = -p\underline{1}\underline{1} + k\underline{\dot{\epsilon}}^n$

$$\text{With } \underline{\dot{\epsilon}} = \begin{pmatrix} \frac{\partial u}{\partial x} & \frac{1}{2}(\frac{\partial u}{\partial y} + \frac{\partial v}{\partial x}) \\ \frac{1}{2}(\frac{\partial u}{\partial y} + \frac{\partial v}{\partial x}) & \frac{\partial v}{\partial y} \end{pmatrix} \quad (\text{B.7})$$

For a 2D flows; but in this case: $\vec{v} \Big|_0^u$. Moreover, due to the continuity equation:

$$\frac{\partial u}{\partial x} + \frac{\partial v}{\partial y} + \frac{\partial w}{\partial z} = 0 \quad \text{With } v=w=0$$

So $\frac{\partial u}{\partial x} = 0$ but z does not play any role in our 2D flow. Finally $u = u(y)$

$$\therefore \vec{v} \Big|_0^u \begin{pmatrix} u(y) \\ 0 \\ 0 \end{pmatrix}$$

Finally the rate of shear is given by:

$$\underline{\dot{\epsilon}} = \begin{pmatrix} 0 & \frac{1}{2} \cdot \frac{\partial u}{\partial y} \\ \frac{1}{2} \cdot \frac{\partial u}{\partial y} + & 0 \end{pmatrix}, \quad (\text{B.8})$$

also, $\underline{1}\underline{1} = \begin{pmatrix} 1 & 0 \\ 0 & 1 \end{pmatrix}$, and unit tensor is: $\underline{\sigma} = -p\underline{1}\underline{1} + k\underline{\dot{\epsilon}}^n$

We can form the equation of state:

$$\underline{\sigma} = \begin{pmatrix} -p & 0 \\ 0 & p \end{pmatrix} + k \begin{pmatrix} 0 & \frac{1}{2^n} (\frac{\partial u}{\partial y})^n \\ \frac{1}{2^n} (\frac{\partial u}{\partial y})^n & 0 \end{pmatrix} \quad (\text{B.9})$$

$$\therefore \underline{\sigma} = \begin{pmatrix} -p & \frac{k}{2^n} (\frac{\partial u}{\partial y})^n \\ \frac{k}{2^n} (\frac{\partial u}{\partial y})^n & p \end{pmatrix} \quad (\text{B.10})$$

A.4.1 Calculating the pressure

Fluid constitutive law (rheology) occurs only for the dynamic, that is to say, when the fluid is moving. Statically, all the liquids obey the law of Pascal, whatever liquid behavior law studied. So we can fully resume the study of the Hydrostatic Newtonian fluid.

For the shear-thinning fluid (that is to say its viscosity decreases with increasing speed). Obeying the power law describing the pollutants, we find exactly the same equation for pressure, that is to say, as for the water;

$$p = p_{atm} + (\rho - \Delta\rho)g(H - h) + \rho g(h - z) \quad (\text{B.11})$$

That we have equation (B.11). So pass the hydrostatic to hydrodynamics that is for say for moving the gravity current.

A.4.2 Equation of conservation of momentum

$$\rho \gamma_i = f_i + \sigma_{ij,j} \quad (\text{B.12})$$

$$(i, j) \in (1, 2, 3) \quad (1 \rightarrow x, 2 \rightarrow y, 3 \rightarrow z)$$

Plane flow $\rightarrow z$ does not appear. Therefore only two equations following x and y,

$$\text{with } \vec{v} \Big|_0^{u(y)} \quad (\text{B.13})$$

•Projection $\parallel \vec{oz}$:

$$\rho \left[\frac{\partial u}{\partial t} + u \frac{\partial u}{\partial x} + v \frac{\partial u}{\partial y} \right] = f_x + (\sigma_{11,1} + \sigma_{12,2}) \quad (\text{B.14})$$

So $\frac{\partial u}{\partial t}$ is stationary, $u = u(y)$ is $\frac{\partial u}{\partial x}$, $v = 0$,

and $f_x = (\vec{f} = \rho \vec{g})$ only the weight.

$$\frac{\partial}{\partial x} (-p) + \frac{\partial}{\partial y} \left[k \frac{1}{2^n} \left(\frac{\partial u}{\partial y} \right)^n \right] = 0 \quad (\text{B.15})$$

with $\sigma_{11} = -p$

$$\sigma_{12} = k \cdot \frac{1}{2^n} \cdot \left(\frac{\partial u}{\partial y} \right)^n \quad (\text{B.16})$$

•Projection $\parallel \vec{oy}$:

$$\rho \left[\frac{\partial v}{\partial t} + u \frac{\partial v}{\partial x} + v \frac{\partial v}{\partial y} \right] = f_y + (\sigma_{21,1} + \sigma_{22,2}) \quad (\text{B.17})$$

As the $\frac{\partial v}{\partial t} = 0$, $\frac{\partial v}{\partial x} = 0$, $\frac{\partial v}{\partial y} = 0$ because $v = 0$ and $f_y = -\rho g$

$$\therefore \sigma_{21} = k \frac{1}{2^n} \left(\frac{\partial u}{\partial y} \right)^n, \text{ and } \sigma_{22} = -p \quad (\text{B.18})$$

$$0 = -\rho g + \frac{\partial}{\partial x} \left[k \frac{1}{2^n} \left(\frac{\partial u}{\partial y} \right)^n \right] + \frac{\partial}{\partial y} (-p) \quad (\text{B.19})$$

$\frac{\partial}{\partial x} = 0$ because $u = u(y)$. Resolution of the projection $\overline{\partial x}$ (Eq. B.17):

$$\frac{\partial}{\partial x}(p) - \frac{k}{2^n} \left[\frac{\partial}{\partial y} \left(\frac{\partial u}{\partial y} \right)^n \right] = 0 \quad (\text{B.20})$$

with the pressure given by eq. (B.11), i.e.

$$p = p_{atm} + (\rho - \Delta\rho)g(H - h) + \rho g(h - z)$$

$$p = p_{atm} + (\rho - \Delta\rho)gH - (\rho - \Delta\rho)h + \rho gh - \rho gz$$

$$\text{with } \frac{\partial}{\partial x} [p_{atm} + (\rho - \Delta\rho)gH - \rho gz] = 0$$

$$\therefore \frac{\partial p}{\partial x} = \frac{\partial}{\partial x} [-\rho gh + \Delta\rho gh + \rho gh] = \frac{\partial}{\partial x} [\Delta\rho \cdot gh] \quad (\text{B.21})$$

$$\frac{\partial p}{\partial x} = g\Delta\rho \cdot \frac{\partial h}{\partial x} \quad (\text{B.22})$$

So, Eq. (B.20) becomes:

$$g\Delta\rho \cdot \frac{\partial h}{\partial x} - \frac{k}{2^n} \left[\frac{\partial}{\partial y} \left(\frac{\partial u}{\partial y} \right)^n \right] = 0 \quad (\text{B.23})$$

Let $g \cdot \Delta\rho = g'$ denote the differential gravity:

$$g' \frac{dh}{dx} = \frac{k}{2^n} \left\{ \frac{d}{dy} \left[\left(\frac{du}{dy} \right)^n \right] \right\} \quad (\text{B.24})$$

Take one quadrature of that equation with respect to y :

$$g' \frac{2^n}{k} \cdot \frac{dh}{dx} = \frac{d}{dy} \left[\left(\frac{du}{dy} \right)^n \right] \quad (\text{B.25})$$

$$g' \frac{2^n}{k} \cdot \frac{dh}{dx} \cdot y + A = \left(\frac{du}{dy} \right)^n \quad (\text{B.26})$$

$$\frac{du}{dy} = \left[g' \frac{2^n}{k} \cdot \frac{dh}{dx} \cdot y + A \right]^{1/n} \quad (\text{B.27})$$

Taking a second quadrature with respect to y :

$$u(y) = \frac{1}{\frac{1}{n}+1} \times \frac{1}{g' \frac{2^n}{k} \cdot \frac{dh}{dx}} \times \left[g' \frac{2^n}{k} \cdot \frac{dh}{dx} \cdot y + A \right]^{\frac{1}{n}+1} + B \quad (\text{B.28})$$

where A and B are two constants of integration to be determined by the boundary conditions. The boundary conditions are applied to Eq. (B.28). Equation (B.28) can be rewritten in the form:

$$u(y) = \frac{n}{(n+1)} \cdot \frac{1}{\left(g' \frac{2^n}{k} \cdot \frac{dh}{dx} \right)} \times \left[g' \frac{2^n}{k} \cdot \frac{dh}{dx} y + A \right]^{1/n+1} + B$$

The first boundary condition is the no slip condition at the bottom of the basin:

$$y = 0 \quad \rightarrow \quad u = 0 \quad (B.29)$$

$$\text{which leads to: } \frac{nA^{\frac{1}{n}+1}}{(n+1) \cdot (g' \frac{2^n}{k} \cdot \frac{dh}{dx})} + B = 0 \quad (B.30)$$

The second boundary condition expresses the continuity of the shear stress at the free surface.

$$\frac{du}{dy}(h(x, t)) = 0 \quad \text{at} \quad y = h \quad (B.31)$$

The expression of $\frac{du}{dy}$ is given by Eq. (B-31) is write so in $y=h$:

$$[g' \cdot \frac{2^n}{k} \cdot \frac{dh}{dx} \cdot h + A]^{1/n} = 0 \quad (B.32)$$

$$\text{So, } g' \frac{2^n}{k} \cdot \frac{dh}{dx} \cdot h + A = 0 \quad (B.33)$$

$$\text{Then, } A = -g' \cdot \frac{2^n}{k} \cdot \frac{dh}{dx} \cdot h \quad (B.34)$$

Introducing that expression of A in Eq. (B.34):

$$B = -\frac{n}{(n+1) \cdot (g' \frac{2^n}{k} \cdot \frac{dh}{dx})} \cdot A^{\frac{1}{n}+1} \quad (B.35)$$

$$\therefore B = -\frac{n}{(n+1) \cdot (g' \frac{2^n}{k} \cdot \frac{dh}{dx})} \times [-g' \frac{2^n}{k} \cdot \frac{dh}{dx} \cdot h]^{1/n+1} \quad (B.36)$$

Substituting these expressions of A and B in Eq. (B.28), we obtain the velocity field in the form:

$$u(y) = \frac{n}{(n+1) \cdot (g' \frac{2^n}{k} \cdot \frac{dh}{dx})} \times [g' \frac{2^n}{k} \cdot \frac{dh}{dx} \cdot y - g' \frac{2^n}{k} \cdot \frac{dh}{dx} \cdot h]^{1/n+1} - \frac{n}{(n+1) \cdot (g' \frac{2^n}{k} \cdot \frac{dh}{dx})} \times [-g' \frac{2^n}{k} \cdot \frac{dh}{dx} \cdot h]^{1/n+1} \quad (B.37)$$

$$\therefore u(y) = \frac{n}{(n+1) \cdot (g' \frac{2^n}{k} \cdot \frac{dh}{dx})} \times \left\{ [g' \frac{2^n}{k} \cdot \frac{dh}{dx} (y - h)]^{\frac{1}{n}+1} - [-g' \frac{2^n}{k} \cdot \frac{dh}{dx} \cdot h]^{\frac{1}{n}+1} \right\} \quad (B.38)$$

Let us apply the continuity equation in its global form (mass conservation) ;(Eq. B.31):

$$\frac{\partial h}{\partial t} + \frac{\partial}{\partial x} \left[\int_0^h u(y) dy \right] = 0$$

To use it, let us calculate the derivative of the integral by Eq. (B.38) for $u(y)$.

$$\frac{\partial}{\partial x} \int_0^h u(y) dy = \frac{\partial}{\partial x} \left[\frac{n}{(n+1) \cdot (g' \frac{2^n}{k} \cdot \frac{dh}{dx})} \times \left\{ [g' \frac{2^n}{k} \cdot \frac{dh}{dx} (y - h)]^{\frac{1}{n}+1} - [-g' \frac{2^n}{k} \cdot \frac{dh}{dx} \cdot h]^{\frac{1}{n}+1} \right\} \right] dy \quad (B.39)$$

$$\frac{\partial}{\partial x} \int_0^h u(y) dy = \frac{n}{(n+1) \cdot (g' \frac{2^n}{k} \cdot \frac{dh}{dx})} \cdot \frac{\partial}{\partial x} \left\{ \int_0^h [g' \frac{2^n}{k} \cdot \frac{dh}{dx}]^{\frac{1}{n}+1} \times (y - h)^{\frac{1}{n}+1} dy - \int_0^h [-g' \frac{2^n}{k} \cdot \frac{dh}{dx} \cdot h]^{\frac{1}{n}+1} \cdot dy \right\} \quad (B.40)$$

$$\frac{\partial}{\partial x} \int_0^h u(y) dy = \frac{n}{(n+1) \cdot (g' \frac{2^n}{k} \cdot \frac{dh}{dx})} \times \frac{\partial}{\partial x} \left\{ [g' \frac{2^n}{k} \cdot \frac{dh}{dx}]^{\frac{1}{n}+1} \int_0^h (y - h)^{\frac{1}{n}+1} \cdot dy - \int_0^h (-1)^{\frac{1}{n}+1} h \cdot dy \right\} \quad (B.41)$$

$$\frac{\partial}{\partial x} \int_0^h u(y) dy = \frac{n}{n+1} \times \frac{\partial}{\partial x} \left\{ \left(g' \frac{2^n}{k} \cdot \frac{dh}{dx} \right)^{\frac{1}{n}} \times \frac{1}{\frac{1}{n}+2} \cdot [(y-h)^{\frac{1}{n}+2}]_0^h - (-1)^{\frac{1}{n}+1} h^{\frac{1}{n}+1} \cdot [y]_0^h \right\} \quad (\text{B.42})$$

$$\frac{\partial}{\partial x} \int_0^h u(y) dy = \frac{n}{n+1} \times \frac{\partial}{\partial x} \left\{ \left(g' \frac{2^n}{k} \cdot \frac{dh}{dx} \right)^{\frac{1}{n}} \times \frac{n}{2n+1} [-(-h)^{\frac{1}{n}+2}] - (-1)^{\frac{1}{n}+1} \cdot h^{\frac{1}{n}+1} \cdot h \right\} \quad (\text{B.43})$$

$$\frac{\partial}{\partial x} \int_0^h u(y) dy = \frac{n}{n+1} \times \frac{\partial}{\partial x} \left\{ \left(g' \frac{2^n}{k} \cdot \frac{dh}{dx} \right)^{\frac{1}{n}} \times \frac{n}{2n+1} [(-1) \cdot (-1)^{\frac{1}{n}} \cdot (-1)^2 \cdot h^{\frac{1}{n}+2}] - (-1)^{\frac{1}{n}} \cdot (-1) \cdot h^{\frac{1}{n}+2} \right\} \quad (\text{B.44})$$

$$\frac{\partial}{\partial x} \int_0^h u(y) dy = \frac{n}{n+1} \times \frac{\partial}{\partial x} \left\{ \left(g' \frac{2^n}{k} \cdot \frac{dh}{dx} \right)^{\frac{1}{n}} (-1)^{\frac{1}{n}} \times \frac{n}{2n+1} \cdot (-1) \times h^{\frac{1}{n}+2} + h^{\frac{1}{n}+2} \right\} \quad (\text{B.45})$$

$$\frac{\partial}{\partial x} \int_0^h u(y) dy = \frac{n}{n+1} \times \frac{\partial}{\partial x} \left\{ \left(-g' \frac{2^n}{k} \cdot \frac{dh}{dx} \right)^{\frac{1}{n}} \cdot h^{\frac{1}{n}+2} \left[\frac{-n}{2n+1} + 1 \right] \right\} \quad (\text{B.46})$$

$$\frac{\partial}{\partial x} \int_0^h u(y) dy = \frac{n}{n+1} \times \frac{\partial}{\partial x} \left\{ \left(-g' \frac{2^n}{k} \cdot \frac{dh}{dx} \right)^{\frac{1}{n}} \cdot h^{\frac{1}{n}+2} \left[\frac{-n+2n+1}{2n+1} \right] \right\} \quad (\text{B.47})$$

$$\frac{\partial}{\partial x} \int_0^h u(y) dy = \frac{n}{n+1} \times \frac{\partial}{\partial x} \left\{ \left(-g' \frac{2^n}{k} \cdot \frac{dh}{dx} \right)^{\frac{1}{n}} \cdot h^{\frac{1}{n}+2} \cdot \frac{n+1}{2n+1} \right\} \quad (\text{B.48})$$

$$\frac{\partial}{\partial x} \int_0^h u(y) dy = \frac{n}{2n+1} \times \frac{\partial}{\partial x} \left\{ \left(-g' \frac{2^n}{k} \cdot \frac{dh}{dx} \right)^{\frac{1}{n}} \cdot h^{\frac{2n+1}{n}} \right\} \quad (\text{B.49})$$

Now let us introduce that result of the integral in the equation of continuity (B.31):

$$\therefore \frac{\partial h}{\partial t} + \frac{n}{2n+1} \times \frac{\partial}{\partial x} \left\{ \left(-g' \frac{2^n}{k} \cdot \frac{dh}{dx} \right)^{\frac{1}{n}} \cdot h^{\frac{2n+1}{n}} \right\} = 0 \quad (\text{B.50})$$

This is the final equation we will have to solve for the pseudo plastic fluid (pollutants) as gravity current.

A.5 Equations of motion in an inclined bottom

The projection of the dynamic equation along the y-axis gives the pressure field. As for the horizontal channel, the equation of motion along the y-axis is exactly the same as for the Newtonian fluid. The solution also is the same and we obtain the following expression for the pressure field (Eq. A.67).

$$p(y) = P_{atm} + \rho \cdot g \cdot (h - y) \cos\theta + (\rho - \Delta\rho)(H_o - x \cdot \sin\theta - h \cdot \cos\theta)$$

If we put $\theta=0$ in that expression, we recover the pressure field of the horizontal channel. Projection along the x-axis represented by the general equation of conservation of momentum;

$$\rho \gamma_i = f_i + \sigma_{ij,j}$$

$$(i, j) \in [1, 2, 3] \quad [1 \rightarrow x, 2 \rightarrow y, 3 \rightarrow z]$$

Plane flow $\rightarrow z$ does not appear, only two equations following x and y with;

$$\vec{v} \Big|_0^{u(y)}$$

The equation of conservation of the momentum written as:

$$\rho\gamma_i = f_i + \sigma_{ij,j} \quad (\text{B.51})$$

$$\text{with } \sigma_{11} = -p, \quad \sigma_{22} = -p, \quad \sigma_{12} = \sigma_{21} = k \cdot \frac{1}{2^n} \left(\frac{\partial u}{\partial y} \right)^n$$

Projected on $\overline{\partial x}$, Eq. (B.1) write:

$$\rho \left[\frac{\partial u}{\partial t} + u \frac{\partial u}{\partial x} + v \frac{\partial u}{\partial y} \right] = f_1 + (\sigma_{11,1} + \sigma_{12,2}) \quad (\text{B.52})$$

$$\frac{\partial u}{\partial t} \text{ is stationary, } u \frac{\partial u}{\partial x} = (u = u(y), \text{ and } v \frac{\partial u}{\partial y} = (v = 0)$$

$$0 = -\rho g \sin\theta + \left(-\frac{\partial p}{\partial x} \right) + k \cdot \frac{1}{2^n} \left[\frac{\partial}{\partial y} \left(\frac{\partial u}{\partial y} \right)^n \right] \quad (\text{B.53})$$

$$\text{with; } \frac{\partial p}{\partial x} = g \left[-\rho \sin\theta + \Delta\rho \left(\sin\theta + \cos\theta \frac{\partial h}{\partial x} \right) \right] \quad (\text{B.54})$$

Eq. (B.53) becomes:

$$0 = -\rho g \sin\theta + \rho g \sin\theta - \Delta\rho g \cos\theta \frac{\partial h}{\partial x} + \frac{k}{2^n} \frac{\partial}{\partial y} \left(\frac{\partial u}{\partial y} \right)^n \quad (\text{B.55})$$

$$\text{Put } g \cdot \Delta\rho = g', \quad \therefore \frac{k}{2^n} \cdot \frac{\partial}{\partial y} \left(\frac{\partial u}{\partial y} \right)^n = g' \sin\theta + \Delta\rho \cdot \cos\theta \cdot \frac{\partial h}{\partial x} \quad (\text{B.56})$$

This ordinary differential equation can be solved easily by taking two successive quadratures:

$$\left(\frac{\partial u}{\partial y} \right)^n = g' \cdot \frac{2^n}{k} \left(\sin\theta + \cos\theta \cdot \frac{dh}{dx} \right) y + A \quad (\text{B.57})$$

$$\frac{du}{dy} = \left[g' \cdot \frac{2^n}{k} \left(\sin\theta + \cos\theta \cdot \frac{dh}{dx} \right) y + A \right]^{1/n} \quad (\text{B.58})$$

Taking the second quadrature:

$$u(y) = \frac{1}{\frac{1}{n}+1} \times \frac{1}{g' \frac{2^n dh}{k dx}} \times \left[g' \cdot \frac{2^n}{k} \left(\sin\theta + \cos\theta \cdot \frac{dh}{dx} \right) y + A \right]^{1/n+1+B} \quad (\text{B.59})$$

where A and B are two constants of integration to be determined by the boundary conditions. The boundary conditions are applied to Eq. (B.59) which can be written in the form:

$$u(y) = \frac{n}{n+1} \times \frac{1}{g' \frac{2^n dh}{k dx}} \times \left[g' \cdot \frac{2^n}{k} \left(\sin\theta + \cos\theta \cdot \frac{dh}{dx} \right) y + A \right]^{1/n+1+B} \quad (\text{B.60})$$

The first boundary condition is the no slip condition at the bottom of the basin:

$$y = 0 \rightarrow u = 0 \quad (\text{B.61})$$

$$\text{which leads to: } \frac{n}{n+1} \times \frac{1}{g' \frac{2^n dh}{k dx}} \times A^{\frac{1}{n}+1} + B \quad (\text{B.62})$$

The second boundary condition expresses the continuity of the shear stress at the free surface:

$$\frac{du}{dy} [h(x, t)] = 0 \quad \text{at} \quad y = h \quad (\text{B.63})$$

The expression of $\frac{du}{dy}$ is given by Eq. (B.58) so:

$$\left[g' \frac{2^n}{k} (\sin\theta + \cos\theta \cdot \frac{dh}{dx}) h + A \right]^{1/n} = 0 \quad (\text{B.64})$$

$$g' \frac{2^n}{k} (\sin\theta + \cos\theta \cdot \frac{dh}{dx}) h + A = 0 \quad (\text{B.65})$$

$$\text{So; } A = -g' \frac{2^n}{k} (\sin\theta + \cos\theta \cdot \frac{dh}{dx}) h \quad (\text{B.66})$$

Introducing that expression of A in Eq. (B.11) gives:

$$B = -\frac{n}{n+1} \times \frac{1}{g' \frac{2^n}{k} \frac{dh}{dx}} \times A^{\frac{1}{n}+1} \quad (\text{B.67})$$

$$\therefore B = -\frac{n}{n+1} \times \frac{1}{g' \frac{2^n}{k} \frac{dh}{dx}} \times A^{\frac{1}{n}+1} \times \left[-g' \frac{2^n}{k} (\sin\theta + \cos\theta \cdot \frac{dh}{dx}) h \right]^{1/n+1} \quad (\text{B.68})$$

Substituting these expressions of A and B in $u(y)$ given by Eq. (B.59), we get:

$$u(y) = \frac{n}{n+1} \times \frac{1}{g' \frac{2^n}{k} \frac{dh}{dx}} \times \left[g' \frac{2^n}{k} (\sin\theta + \cos\theta \cdot \frac{dh}{dx}) y - g' \frac{2^n}{k} (\sin\theta + \cos\theta \cdot \frac{dh}{dx}) h \right]^{1/n+1} - \frac{n}{n+1} \times \frac{1}{g' \frac{2^n}{k} \frac{dh}{dx}} \times A^{\frac{1}{n}+1} \times \left[-g' \frac{2^n}{k} (\sin\theta + \cos\theta \cdot \frac{dh}{dx}) h \right]^{1/n+1} \quad (\text{B.69})$$

We arrived at the following expression for the velocity field of a shear-thinning fluid as gravity current over an inclined channel, beneath a quiet volume of water.

$$u(y) = \frac{n}{n+1} \times \frac{1}{g' \frac{2^n}{k} \frac{dh}{dx}} \times \left[g' \frac{2^n}{k} (\sin\theta + \cos\theta \cdot \frac{dh}{dx}) y - g' \frac{2^n}{k} (\sin\theta + \cos\theta \cdot \frac{dh}{dx}) h \right]^{1/n+1} - \frac{n}{n+1} \times \frac{1}{g' \frac{2^n}{k} \frac{dh}{dx}} \times \left[-g' \frac{2^n}{k} (\sin\theta + \cos\theta \cdot \frac{dh}{dx}) h \right]^{1/n+1} \quad (\text{B.70})$$

$$u(y) = \frac{n}{n+1} \times \frac{1}{g' \frac{2^n}{k} \frac{dh}{dx}} \left\{ \left[g' \frac{2^n}{k} (\sin\theta + \cos\theta \cdot \frac{dh}{dx}) (y - h) \right]^{\frac{1}{n}+1} - \left[-g' \frac{2^n}{k} (\sin\theta + \cos\theta \cdot \frac{dh}{dx}) h \right]^{\frac{1}{n}+1} \right\} \quad (\text{B.71})$$

Let us apply the global continuity equation:

$$\frac{\partial h}{\partial t} + \frac{\partial}{\partial x} \left[\int_0^h u(y) dy \right] = 0 \quad (\text{B.72})$$

First of all, let us calculate the integral:

$$\int_0^h u(y) dy = \int_0^h \frac{n}{n+1} \times \frac{1}{g' \frac{2^n}{k} \frac{dh}{dx}} \times \left\{ \left[g' \frac{2^n}{k} (\sin\theta + \cos\theta \cdot \frac{dh}{dx}) (y - h) \right]^{\frac{1}{n}+1} - [(-1)(-1)^{\frac{1}{n}}] \left[g' \frac{2^n}{k} (\sin\theta + \cos\theta \cdot \frac{dh}{dx}) h \right]^{\frac{1}{n}+1} \right\} \quad (\text{B.73})$$

$$\int_0^h u(y)dy = \int_0^h \frac{n}{(n+1)(g' \frac{2^n}{k} \frac{dh}{dx})} \times [g' \frac{2^n}{k}]^{\frac{1}{n}+1} \times \left\{ \left[\left(\sin\theta + \cos\theta \cdot \frac{dh}{dx} \right) (y-h) \right]^{\frac{1}{n}+1} + (-1)^{\frac{1}{n}} \left[\left(\sin\theta + \cos\theta \cdot \frac{dh}{dx} \right) h \right]^{\frac{1}{n}+1} \right\} dy \quad (\text{B.74})$$

$$\int_0^h u(y)dy = \frac{n}{(n+1)(g' \frac{2^n}{k} \frac{dh}{dx})} \times [g' \frac{2^n}{k}]^{\frac{1}{n}+1} \times \int_0^h \left\{ \left[\left(\sin\theta + \cos\theta \cdot \frac{dh}{dx} \right) (y-h) \right]^{\frac{1}{n}+1} + (-1)^n \left[\left(\sin\theta + \cos\theta \cdot \frac{dh}{dx} \right) h \right]^{\frac{1}{n}+1} \right\} dy \quad (\text{B.75})$$

$$\int_0^h u(y)dy = \frac{n}{(n+1) \frac{dh}{dx}} \left(g' \frac{2^n}{k} \right)^{\frac{1}{n}} \times (\sin\theta + \cos\theta \cdot \frac{dh}{dx})^{\frac{1}{n}+1} \left\{ \int_0^h (y-h)^{\frac{1}{n}+1} dy + (-1)^n (\sin\theta + \cos\theta \cdot \frac{dh}{dx})^{\frac{1}{n}+1} \int_0^h h dy \right\} \quad (\text{B.76})$$

$$\int_0^h u(y)dy = \frac{n}{(n+1) \frac{dh}{dx}} \left(g' \frac{2^n}{k} \right)^{\frac{1}{n}} \times (\sin\theta + \cos\theta \cdot \frac{dh}{dx})^{\frac{1}{n}+1} \times \left\{ \frac{1}{\frac{1}{n}+2} [(y-h)^{\frac{1}{n}+2}]_0^h + (-1)^n h^{\frac{1}{n}+1} [y]_0^h \right\} \quad (\text{B.77})$$

$$\int_0^h u(y)dy = \frac{n}{(n+1) \frac{dh}{dx}} \left(g' \frac{2^n}{k} \right)^{\frac{1}{n}} \times (\sin\theta + \cos\theta \cdot \frac{dh}{dx})^{\frac{1}{n}+1} \times \frac{n}{2n+1} \times [-(-h)^{\frac{1}{n}+2}] + (-1)^{\frac{1}{n}} \cdot h^{\frac{1}{n}+2} \quad (\text{B.78})$$

$$\int_0^h u(y)dy = \frac{n}{(n+1) \frac{dh}{dx}} \left(g' \frac{2^n}{k} \right)^{\frac{1}{n}} \times (\sin\theta + \cos\theta \cdot \frac{dh}{dx})^{\frac{1}{n}+1} \times \frac{n}{2n+1} \times [-(-1)^{\frac{1}{n}} \cdot (-1)^2 \cdot h^{\frac{1}{n}+2}] + (-1)^{\frac{1}{n}} \cdot h^{\frac{1}{n}+2} \quad (\text{B.79})$$

$$\int_0^h u(y)dy = \frac{n}{(n+1) \frac{dh}{dx}} \left(g' \frac{2^n}{k} \right)^{\frac{1}{n}} \cdot (\sin\theta + \cos\theta \cdot \frac{dh}{dx})^{\frac{1}{n}+1} (-1)^{\frac{1}{n}} \cdot h^{\frac{1}{n}+2} \left[\frac{n}{2n+1} \times (-1) + 1 \right] \quad (\text{B.80})$$

$$\int_0^h u(y)dy = \frac{n}{(n+1) \frac{dh}{dx}} \left(g' \frac{2^n}{k} \right)^{\frac{1}{n}} (\sin\theta + \cos\theta \cdot \frac{dh}{dx})^{\frac{1}{n}+1} (-1)^{\frac{1}{n}} h^{\frac{1}{n}+2} \left[\frac{-n+2n+1}{2n+1} \right] \quad (\text{B.81})$$

$$\int_0^h u(y)dy = \frac{n}{(n+1) \frac{dh}{dx}} \left(g' \frac{2^n}{k} \right)^{\frac{1}{n}} (\sin\theta + \cos\theta \cdot \frac{dh}{dx})^{\frac{1}{n}+1} \times (-1)^{\frac{1}{n}} h^{\frac{1}{n}+2} \times \frac{n+1}{2n+1} \quad (\text{B.82})$$

$$\int_0^h u(y)dy = \frac{n}{2n+1} \cdot \frac{(-1)^{\frac{1}{n}}}{\frac{dh}{dx}} \times \left(g' \frac{2^n}{k} \right)^{\frac{1}{n}} (\sin\theta + \cos\theta \cdot \frac{dh}{dx})^{\frac{1}{n}+1} \times h^{\frac{1}{n}+2} \quad (\text{B.83})$$

That the expression of the integral, let us introduce it (Eq.B.83) into the global equation of continuity (Eq.B.72):

$$\frac{\partial h}{\partial t} + \frac{n}{2n+1} \left(g' \frac{2^n}{k} \right)^{\frac{1}{n}} \cdot h^{\frac{1}{n}+2} \times \frac{\partial}{\partial x} \left\{ \frac{1}{\frac{dh}{dx}} \left[\sin\theta + \cos\theta \frac{dh}{dx} \right]^{\frac{1}{n}+1} \right\} = 0 \quad (\text{B.84})$$

Bibliography

- Adduce, C., Sciortino, G., and Proietti, S. (2012). Gravity currents produced by lock exchanges: Experiments and simulations with a two-layer shallow-water model with entrainment. *Journal of Hydraulic Engineering*, 138(2), 111–121.
- Allen, J.R.L. (1971). Mixing at turbidity currents heads, and its geological implications. *Sedimentary Petrology*, 41(1), 97 – 113.
- Allen, J.R.L. (1982). *Sedimentary Structures: their Character and Physics Basis*. Elsevier.
- Amy, L. A., Hogg, A. J., Peakall, J., and Talling, P. J., (2005). Abrupt transitions in gravity currents. *Journal of Geophysical Research*, 110, F03001.
- An, S., Julien, P.Y., and Venayagamoorthy, S.K. (2012). Numerical simulation of particle-driven gravity currents. *J. Environ. Fluid Mech.* DOI 10.1007/s10652-012-9251-6.
- Ansong, J.K., Kyba, P.J., Sutherland, B.R., 2008. Fountains impinging on a density interface. *J. Fluid Mech.* 595, 115-139.
- Ashley J. James, Marc K. Smith, and Ari Glezer. (2003) Vibration-induced drop atomization and the numerical simulation of low-frequency single droplet ejection. *J. Fluid Mech.*, 476, 29-62.
- Bagnold, R. A., (1941). *The physics of blown sand and desert dunes*. Methuen.
- Benjamin T. Brooke, (1968). Gravity currents and related phenomena *J. Fluid Mech.*, vol. 31, part 2, pp. 209-248.
- Birman V., Martin J.E., and Meiburg E. 2005. The non-Boussinesq lock-exchange problem. Part 2. High-resolution simulations. *J. Fluid Mech.* 537, 125-44.
- Bleninger T., and Jirka G., H. (2007) Modeling and environmentally sound management of brine discharges from desalination plants. *Desalination* 221:585-597.
- Bonnecaze, R., Hallworth, M., Huppert, H., and Lister, J., (1995). Axisymmetric particle-driven gravity currents. *Journal of Fluid Mechanics*, 294, 93-121.
- Bonnecaze, R., Huppert, H., and Lister, J., (1993). Particle-driven gravity currents. *Journal of Fluid Mechanics*, 250, 339-339.
- Bonometti T. and Balachandar S. (2008). Effect of Schmidt number on the structure and propagation of density currents. *Theor. Comput. Fluid Dyn.* 22, 341-361.
- Breidenthal, R. E., (1992). Entrainment at thin stratified interfaces: The effects of Schmidt, Richardson, and Reynolds numbers. *Physics of Fluids A*, 4 (10), 2141- 2144.
- Britter, R., and Simpson, J., (1978). Experiments on the dynamics of a gravity current head. *Journal of Fluid Mechanics*, 88, 223-240.
- Britter, R.E., 1979. The spread of a negatively buoyant plume in a calm environment. *Atmos. Environ.* 13, 1241-1247.

- BrØrs, B., and Eidsvik, K. L. (1992). Dynamic Reynolds modeling of turbidity currents. *J. Geophys. Res.*, 97(C6), 9645-9652.
- Buckee, C., Kneller, B., and Peakall, J. (2009). Turbulence structure in steady, solute-driven gravity currents. Particulate gravity currents, W. McCaffrey, B. Kneller, and J. Peakall, eds., Blackwell, Oxford, UK, 173-187.
- Cantero, M. I., Balachandar, S., García, M. H., and Bock, D. (2008). Turbulent structures in planar gravity currents and their influence on the flow dynamics. *Journal of Geophysical Research: Oceans* (1978-2012), 113(C8).
- Cantero, M., Balachandar, S., and Garcia, M. (2007b). High-resolution simulations of cylindrical density currents. *J. Fluid Mech.* 590, 437-469.
- Cantero, M., Lee, J. R., Balachandar, S., and Garcia, M. (2007a). On the front velocity of gravity currents. *J. Fluid Mech.* 586, 1-39.
- Cenedese, C. and Dalziel, S.B. (1998) Concentration and depth fields determined by the light transmitted through a dyed solution. In Carlomagno & Grant, editors, *Proceedings of the 8th International Symposium on Flow Visualization*.
- Cenedese, C., and Adduce, C. (2008). Mixing in a density-driven current flowing down a slope in a rotating fluid. *Journal of Fluid Mechanics*, 604, 369-388.
- Cenedese, C., and Adduce, C., (2010). A new parameterization for entrainment in overflows. *Journal of Physical Oceanography*, 40, 1835-1850.
- Cesare, D. G., Boillat, J.L., and Schleiss, A. J. (2006). "Circulation in Stratified Lakes due to Flood-induced Turbidity Currents." *Journal of Environmental Engineering*, 132(11), 1508-1517.
- Chang, Y. S., Xu, X., Özgökmen, T. M., Chassignet, E. P., Peters, H., and Fischer P. F., (2005). Comparison of gravity current mixing parameterizations and calibration using a high-resolution 3D nonhydrostatic spectral element model. *Ocean Modelling*, 10,342-368.
- Chen, J., (1980). Studies on gravitational propagation currents. PhD Dissertation, California Institute of Technology, Pasadena, California.
- Chen, J.C., and List, E.J., (1976). Spreading of buoyant discharges. *Proc., ICHMT Conf., Dubrovnik, Yugoslavia*, pp. 171-182.
- Chowdhury, M. R., and Testik, F. Y., (2014). A review of gravity currents formed by submerged single-port discharges in inland and coastal waters. *Environ Fluid Mech*, 14:265-293.
- Chowdhury, M. R., Testik, F. Y., and Khan, A. A., (2009). Three-dimensional flow structure at the frontal zone of a gravity-driven fluid mud flow. *Journal of Visualization*, 12 (4).
- Christodoulou, G. C., (1986). Interfacial mixing in stratified flows. *J. Hydraul Res.* 24 (2), 77-92.

- Cooper P., and Hunt G.R., (2007). Impinging axisymmetric turbulent fountains. *Phys Fluids* 19:117101.
- Dade, W., and Huppert, H., (1995a). A box model for non-entraining, suspension-driven gravity surges on horizontal surfaces. *Sedimentology*, 42, 453-472.
- Dade, W., and Huppert, H., (1995b). Runout and fine-sediment deposit of axisymmetric turbidity currents. *Journal of Geophysical Research*, 100, 18597-18609.
- Dhafar, I. A., Latrache, N., and Nsom, B. (2015). Applied the Large-Scale Particle Image Velocimetry Technique for Measurement the Velocity of Gravity Currents in the Laboratory. DOI: 10.4236/jwarp.2015.78048, *Journal of Water Resource and Protection* 07(08):597-604.
- Dhafar, I., A., Latrache, N., and Nsom, B. (2015). Image processing applied to characterize the denser gravity current propagates over rigid surface into the lighter fluid. 10th Pacific Symposium on Flow Visualization and Image Processing Conference, Naples, Italy, 15-18 June.
- Dhafar, I. A., Latrache, N., Niang, P., and Nsom, B. (2015). Etallement d'un jet horizontal miscible de flottabilité positive. 22ème Congrès Français de Mécanique, Lyon, France, 24 au 28 Août.
- Dhafar, I. A., Nsom, B. and Latrache, N., (2015). Effect of slope change on the dynamics of pseudoplastic mass movements beneath a static volume of water, ic-rmm2- 2 nd International Conference on Rheology and Modelling of Materials, Miskolc-Lillafüred, Hungary, 5-9, October.
- Dhafar, I. A., Latrache, N., and Nsom, B. (2015). Mesure de vitesse par PIV à grande échelle d'un écoulement de courant gravitaire d'un liquide léger à la surface libre d'un liquide dense. 16ème congrès français du Club FLUVISU (« Visualisation et Traitements d'images en Mécaniques des Fluides pour l'Industrie »), associé au 14ème colloque international francophone du Club CMOI (« Contrôles et Mesures Optiques pour l'Industrie»). Lannion, France, Du 16 au 20 novembre.
- Dhafar, I. A., Latrache, N., and Nsom, B. (2016). Experimental Study of the Effect of the Spreading Buoyant Gravity Current on the Coastal Environment. The 2016 3rd International Conference on Coastal and Ocean Engineering (ICCOE 2016), Tokyo, Japan, 8-9, April.
- Dhafar, I. A., Latrache, N., and Nsom, B. (2017). Experimental Study of the Effect of the Spreading Buoyant Gravity Current on the Coastal Environment. DOI: 10.7763/IJET.2017.V9.957. *International Journal of Engineering and Technology*, 09(02):129-132.
- Dhafar, I. A., Latrache, N., and Nsom, B. (2017b). Mixing of Saline gravity Current Jet into Fresh Water in the Weakly Turbulent Regime (under review).
- Dai, A. (2013). Gravity currents propagating on sloping boundaries. *Journal of Hydraulic Engineering*, 139(6), 593-601.
- Dai, A. (2015). High-resolution simulations of downslope gravity currents in the acceleration phase. *Physics of Fluids*, 27(7), 076602.

- Di Federico, V., Malavasi, S. and Cintoli, S. (2006): Viscous Spreading of Non-Newtonian Gravity Currents on a Plane. *Meccanica*, 41, 207-217.
- Didden, N. and Maxworthy, T. (1982). The viscous propagation of plane and axisymmetric gravity currents. *Journal of Fluid Mechanics*, 121, 27-42.
- Eames, I., Gilberston, M.A., and Landerryou, M. (2005). The effects of an ambient flow on the spreading of a viscous gravity current. *J. Fluid Mech.*, 523, 261-275.
- Ellison, T. H., and Turner, J. S. 1959: Turbulent entrainment in stratified flows. *J. Fluid Mech.*, 6, 423-448.
- Eriksson, J. G., Karlsson, R. I., and Persson, J. (1998). An experimental study of a two-dimensional turbulent wall jet. *Exp. Fluids*, 25, 50-60.
- Etienne, J., Hopfinger, E.J., and Saramito, P. (2005). Numerical simulations of high density ratio lock-exchange flows. *Phys Fluids*. 17 036601.
- Fernando, H. J. S. (1991). Turbulent Mixing in Stratified Fluids. *Annual Review of Fluid Mechanics*, 23, 455-493.
- Fernando, H.J.S. 2000. Aspects of stratified turbulence. In: Kerr, R.M., Kimura, Y. (Eds.), *Development in Geophysical Turbulence*. Kluwer, pp. 81-92.
- Fischer, H. B, List, E. J., Koh, R. C. Y., Imberger, J., and Brooks, N. H. (1979) *Mixing in inland and coastal waters*. Academic Press, Orlando, p 489.
- Fischer, P.F. (1997). An overlapping Schwarz method for spectral element solution of the incompressible Navier-Stokes equations. *J. Comp. Phys.* 133, 84-101.
- Fleischmann, C. M., Pagni, P. J., and Williamson, R. B. (1994). Salt water modeling of fire compartment gravity currents. *Fire Safety Science – Proceedings of the Fourth International Symposium, Ottawa, June 13-17, Internation Association for Fire Safety Science, Gaithersburg* 253-264.
- Fragoso, A. T., Patterson, M. D. and Wettlaufer, J. S. (2013). Mixing in gravity currents. *J. Fluid Mech.*, 734, (R2), 1-10.
- Garcia, M. H. (1993). Hydraulic jumps in sediment-driven bottom currents. *Journal of Hydraulic Engineering*, 119(10), 1049-1117.
- Garcia, M. H. (1994). Depositional turbidity currents laden with poorly sorted sediment. *Journal of Hydraulic Engineering*, 120 (11), 1240-1263.
- Garcia, M. H., and Parker, G. (1993). Experiments on the entrainment of sediment into suspension by a dense bottom current. *J. Geophys. Res.* 98 (C3), 4793-4807.
- Gerber, G., Diedericks, G., and Basson, G., R. (2011). Particle image Velocimetry measurements and numerical modeling of a saline density current. *J. Hyd. Eng.* 137 (3), 333-342.
- Geyer, W. R., and Smith, J. D. (1987). Shear Instability in a Highly Stratified Estuary. *Journal of Physical Oceanography*. 17, 1668-1679.

- Gladstone, C. and Woods, A. (2000). On the application of box models to particle driven gravity currents. *J. Fluid Mech.*, 416, 187-195.
- Gladstone, C., Phillips, J. and Sparks, R. (1998). Experiments on bidisperse, constant volume gravity currents: propagation and sediment deposition. *Sedimentology*, 45, 833-844.
- Guillas, S., Glover, N., and Malki-Epshtein, L. (2014). Bayesian calibration of the constants of the k - ϵ turbulence model for a CFD model of street canyon flow. *Comput. Methods Appl. Mech. Engrg.* 279, 536–553.
- Hacker, J., Linden, P. F. and Dalziel, S. B. (1996) Mixing in lock-release gravity currents. *Dyn. Atmos. Oceans* 24, 183-195.
- Hales, L. (1996). Analysis of dredged material disposed in open water: summary report for technical area 1. TR DRP-96-4, US army engineer waterways experiment station, Vicksburg, Mississippi.
- Hallberg, R. (2000). Time integration of diapycnal diffusion and Richardson number dependent mixing in isopycnal coordinate ocean models. *Mon. Weather Rev.* 128 (5), 1402-1419.
- Hallworth, M. A., and Huppert, H. E. (1998a). Abrupt Transitions in high-concentration, particle-driven gravity currents. *Physics of Fluids*, 10-5, 1083-1087.
- Hallworth, M., Hogg, A., and Huppert, H.E. (1998b). Effects of external flow on compositional and particle gravity currents. *J.Fluid Mech.*359, 109-142.
- Hallworth, M.A., Huppert, H.E. and Ungarish, M. (2001). Axisymmetric gravity currents in a rotating system: Experimental and numerical investigations. *J.Fluid Mech.* 447, 1.
- Hallworth, M.A., Huppert, H.E. and Ungarish, M. (2003). On inwardly propagating high-Reynolds-number axisymmetric gravity currents. *J.Fluid Mech.* 494, 255.
- Hallworth, M.A., Huppert, H.E., Phillips, J.C. and Sparks, R.S.J. (1996). Entrainment into two-dimensional and axisymmetric turbulent gravity currents. *J. Fluid Mech.* 308, 289-311.
- Hallworth, M.A., Phillips, J.C., Huppert, H.E. and Sparks, R.S.J. (1993). Entrainment in turbulent gravity currents. *Nature* 362, 829-831.
- Harris, T.C., Hogg, A.J., and Huppert, H.E. (2001). A mathematical framework for the analysis of particle-driven gravity currents. *Proc. R. Soc. Lond. A* 457, 1241-1272.
- Härtel, C., Carlsson, F. and Thunblom, M., (2000b). Analysis and direct numerical simulation of the flow at a gravity-current head. Part 2. The lobe-and-cleft instability. *J. Fluid Mech.*, 418, 213-229.
- Härtel, C., Kleiser, L., Michaud, M., and Stein, C.F. (1997). A direct numerical simulation approach to the study of intrusion fronts. *J. Eng. Maths*, 32(2-3):103–120.
- Härtel, C., Meiburg, E. and Necker, F. (1999). Vorticity dynamics during the start-up phase. *Il Nuovo Cimento C – Geophy. and Space Phys.*, 22(6):823–833.

- Härtel, C., Meiburg, E. and Necker, F. (2000a). Analysis and direct numerical simulation of the flow at a gravity-current head. Part 1. Flow topology and front speed for slip and no-slip boundaries. *J. Fluid Mech.*, 418, 189-212.
- Hodges, B. R. (2009). Hydrodynamical modeling. *Encyclopedia of Inland Waters*, G. E. Likens, ed., Elsevier, Oxford, U.K.
- Hogg, A., Hallworth, M., and Huppert, H. (2005). On gravity currents driven by constant fluxes of saline and particle-laden fluid in the presence of a uniform flow. *J. Fluid Mech.* 539, 349-385.
- Hogg, A., Huppert, H., and Hallworth, M. (1999). Reversing buoyancy of particle-driven gravity currents. *J. Phys. of Fluids*, 11, 2891-2900.
- Hossain, M. S., and Rodi, W. (1977). Influence of buoyancy on the turbulence intensities in horizontal and vertical jets. *Heat transfer and turbulent buoyant convection*, D. B. Spalding and N. Afgan, eds., McGraw-Hill, New York.
- Hoult, D. P. (1972). Oil spreading on the sea. *Annu. Rev. Fluid Mech.* 4, 341-368.
- Huang, H., Imran, J., and Pirmez, C. (2005). Numerical Model of Turbidity Currents with a Deforming Bottom Boundary. *J. Hydr. Eng. (ASCE)*, 131(4), 283-293.
- Huppert, H. E. and Simpson, J. E. (1980). The slumping of gravity currents. *J. Fluid Mech.*, Vol. 99, 785-799.
- Huppert, H.E. (1982). The propagation of two-dimensional and axisymmetric viscous gravity currents over a rigid horizontal surface, *J. Fluid Mech.*, 121:43-58.
- Huppert, H.E. (2006). Gravity currents: a personal perspective. *J. Fluid Mech.*, 554:299-322.
- Ilicak, M. (2014). Energetics and mixing efficiency of lock-exchange flow. *J. Ocean Modelling*, 83, 1-10.
- Jacobson M.R., and Testik F.Y. (2013). On the concentration structure of high-concentration constant-volume fluid mud gravity currents. *J. Phys. of Fluids*, 25:016602.
- Jacobson, M. R., and Testik, F. Y. (2014). Turbulent entrainment into fluid mud gravity currents. *Environmental Fluid Mechanics*, 14(2), 541-563.
- Jirka G. H. (2008). Improved discharge configurations for brine effluents from desalination plants. *J Hydraul Eng* 134:116-120.
- Johnson, C. G., and Hogg, A. J. (2013). Entraining gravity currents. *J. Fluid Mech.*, 731, 477-508.
- Jones, W. and Launder, B. (1972). The prediction of laminarization with a two-equation model of turbulence. *International Journal of Heat and Mass Transfer*, 15 (2), pp.301-314.
- Karman, T. Von (1940). The engineer grapples with nonlinear problems. *Bull. Am. Math. Soc.*, Vol. 46, 615.

- Kassem, A., and Imran, J. (2001). Simulation of turbid underflows generated by the plunging of a river. *Geology*, 29(7), 655-658.
- Kaye N.B., Hunt G.R. (2007). Overturning in a filling box. *J. Fluid Mech* 576:297-323.
- Klemp, J.B., Rotunno, R., and Skamarock, W.C. (1994). On the dynamics of gravity currents in a channel. *J. Fluid Mech.* 269, 169-198.
- Kneller, B. C., Bennett, S. J., and McCaffrey, W. D. (1999). Velocity structure, turbulence and fluid stresses in experimental gravity currents *J. Geophysical res.* Vol. 104, no. C3, pages 5381-5391.
- Kneller, B., and Buckee, C. (2000). The structure and fluid mechanics of turbidity currents: a review of some recent studies and their geological implications. *Sedimentology*, 47, 62-94.
- Kotsovinos N. (2000). Axisymmetric submerged intrusion in stratified fluid. *J. Hydraul. Eng.* 126(6):446- 456.
- Kranenburg, C. (1993). Gravity current fronts advancing into horizontal ambient flow. *J. Hydraul. Eng.* 119: 369-379.
- Kubat, M., Holte, R. C., and Matwin, S. (1998). Machine learning for the detection of oil spills in satellite radar images. *Machine learning* 30, 195-215.
- La Rocca M., Adduce, C., Sciortino G., Bateman Pinzon A., and Boniforti M.A. (2012). A two-layer shallow water model for 3D gravity currents. *J. Hydr. Res.*, 50(2), 208-217.
- La Rocca, M., Adduce, C., Sciortino, G., and Pinzon, A. (2008). Experimental and numerical simulation of three-dimensional gravity currents on smooth and rough bottom. *Physics of Fluids*, 20, 106603.
- Lawrence G. A., and Maclatchy M. R. (2001). Radially spreading buoyant flows. *J Hydraul Res* 39:583-590.
- Lauder, B.E., Spalding, D.B. (1974). The numerical computation of turbulent flows, *Comput. Methods Appl. Mech. Engrg.*, 3, 269–289.
- Lide, D.R. (1997), eds. *CRC handbook of chemistry and physics*. CRC Press, London.
- Lister, J., and Kerr, R. (1989). The propagation of two-dimensional and axisymmetric viscous gravity currents at a fluid interface. *Journal of Fluid Mechanics*, 203, 215-249.
- Liu, C., and Moncrieff, M.W. (1996). A numerical study of the effects of ambient flow and shear on density current. *Mon. Weather Rev.* 124:2282-2303.
- Lombardi, V., Adduce, C., Sciortino, G., and La Rocca, M. (2015). Gravity currents flowing upslope: Laboratory experimental and shallow water simulations. *Phys. Fluids*, 27(1), 016602.
- Lowe, R. J., Rottman, J. W., and Linden, P. F. (2005). The non-Boussinesq lock-exchange problem. Part 1. Theory and experiments. *J Fluid Mech*, Vol. 537, 101-124.
- Marino, B.M., Thomas, L.P., and Linden, P.F. (2005). The front condition for gravity currents. *J. Fluid Mech.* 536, 49-78.

- Maxworthy, T., (1983). Gravity currents with variable inflow. *J Fluid Mech*, 128, 247-257.
- Meleshko, V.V., and Van Heijst, G.J.F. (1995). Interacting two-dimensional vortex structure: point vortices, contour kinematics and stirring properties. *Chaos Applied to Fluid Mixing*, H. Aref and M.S.El Naschi, Eds., Pergamon, 233-266.
- Middleton, G. (1993). Sediment deposition from turbidity currents. *Annual Review of Earth and Planetary Sciences*, 21, 89-114.
- Miles, J. W. (1961). "On the Stability of Heterogeneous Shear Flows." *Journal of Fluid Mechanics*, 10(04), 496-508.
- Miles, J. W., and Howard, L. N. (2006). "Note on a Heterogeneous Shear Flow." *Journal of Fluid Mechanics*, 20(02), 331.
- Montgomery, P.J., and Moodie, T.B. (1999). Two-layer gravity currents with topography. *stud. Appl. Math.*, 102, pp. 221-266.
- Morris, G. L., and Fan, J. (1998). *Reservoir Sedimentation Handbook*. McGraw-Hill Book Co., New York.
- Morton, B.R. (1959). Forced plumes. *J. Fluid Mech.*, 5:151-163.
- Morton, B.R., Taylor, G.I., and Turner, J.S. (1956). Turbulent gravitational convection from maintained and instantaneous sources. *Proc. R. Soc. Lond. A*, 234:1-23.
- Moursi, A. M., Mccorquodale, J. A., and El-Sebakhy, I. (1995) Experimental studies of heavy radial density currents. *J. Environ Eng* 121:920-929.
- Necker, F., Haertel, C., Kleiser, L. and Meiburg, E. (2002). High-resolution simulations of particle-driven gravity currents. *Intl J. Multiphase Flow* 28, 279-300.
- Nichols, M., and Thompson, G. (1978). A field study of fluid mud dredged material: its physical nature and dispersal. Technical Report D-78-40, US army engineers waterways experiment station, Vicksburg, Mississippi, p. 91.
- Nogueira, H. I. S., Adduce, C., Alves, E., and Franca, M. J. (2013a). Analysis of lock-exchange gravity currents over smooth and rough beds. *Journal of Hydraulic Research*, 51(4), 417-431.
- Nogueira, H. I. S., Adduce, C., Alves, E., and Franca, M. J. (2014). Dynamics of the head of gravity currents. *Environmental Fluid Mechanics*, 14, 519-540.
- Nogueira, H.I.S. (2013c). Experimental characterization of unsteady gravity currents developing over smooth and rough beds. PhD Dissertation, University of Coimbra, Faculty of science and technology, Department of civil engineering.
- Nogueira, H.I.S., Adduce, C., Alves, E., and Franca, M.J. (2013b). Image analysis technique applied to lock-exchange gravity currents. *Meas. Sci. Technol.* 24(047001), 4pp.
- Ooi, S. K., Constantinescu, G., and Weber, L. (2007). A numerical study of intrusive compositional gravity currents. *J. Phys. Fluids*, 29 (076602).

- Ooi, S. K., Constantinescu, G., and Weber, L. (2009). Numerical simulations of lock-exchange compositional gravity current. *J. Fluid Mech.*, 635, 361-388.
- Ottolenghi, L., Adduce, C., Inghilesi, R., Armenio, V., and Roman, F., (2016b). Entrainment and mixing in unsteady gravity currents. *J. Hyd. Res.* 0022-1686 (Print), 1814-2079 (Online). <http://dx.doi.org/10.1080/00221686.2016.1174961>.
- Ottolenghi, L., Adduce, C., Inghilesi, R., Roman, F., and Armenio, V., (2016a). Mixing in lock-release gravity currents propagating up a slope. *J. Phys. Fluids*, 28 (056604). <http://dx.doi.org/10.1063/1.4948760>.
- Ottolenghi, L., Cenedese, C., and Adduce, C. (2017), “Entrainment in a dense current flowing down a rough sloping bottom in a rotating fluid”, *Journal of Physical Oceanography* 47(3), 485-498.
- Özgökmen, T.M., and Chassignet, E.P., (2002). Dynamics of two-dimensional turbulent bottom gravity currents. *J. Phys.Oceanogr.*32/9, 1460-1478.
- Özgökmen, T.M., and Fischer, P.F. (2008). On the role of bottom roughness in overflows. *Ocean Modelling* 20(9), 336-361.
- Özgökmen, T.M., Fischer, P.F., Duan, J., and Iliescu, T., (2004a). Three-dimensional turbulent bottom density currents from a high-order nonhydrostatic spectral element model. *J. Phys.Oceanogr.*34/9, 2006-2026.
- Özgökmen, T.M., Iliescu, T., and Fischer, P.F. (2009). Large eddy simulation of stratified mixing in a three-dimensional lock-exchange system. *Ocean Modelling* 26, 134-155.
- Papakonstantis, I.G. (2009). Turbulent round negatively buoyant jets at an angle in a calm homogeneous ambient. Doctoral Thesis, School of Civil Engineering, National Technical University of Athens, Athens, Greece (in Greek).
- Papakonstantis, I.G., and Christodoulou G.C. (2010). Spreading of round dense jets impinging on a horizontal bottom, *J. Hydro-environment Res.* 4, 289-300.
- Parker, G., Garcia, M., Fukushima, Y. and Yu, W. (1987). Experiments on turbidity currents over an erodible bed. *J. Hydraul Res.* 25 (1), 123-147.
- Patterson, M. D., Caulfield, C. P., McElwaine, J. N., and Dalziel, S. B. (2006). Time-dependent mixing in stratified kelvinhelmholtz billows: Experimental observations. *Geophysical research letters*, 33(15).
- Peng, M., and Lee, C.B. (2010). Frontal Instability of Lock-Exchange Gravity Currents. *Modern Physics Letters B*, 24, 1369-1372.
- Philippe, P., Raufaste, C., Kurowski, P., and Petitjeans, P. (2005). Penetration of a negatively buoyant jet in a miscible liquid, *Phys. Fluid*, 17.
- Pope, S. (2001). *Turbulent flows*. Cambridge University Press.
- Prandtl, L. (1952), *Essential of fluid dynamics*, Blackie and Son, London.
- Princevac, M., Fernando, H. J. S., and Whiteman, C. D., (2005). Turbulent entrainment into natural gravity driven flows. *Journal of Fluid Mechanics*, 533, 259-268.

- Richardson, L. (1920). "The Supply of Energy from and to Atmospheric Eddies." *Proceedings of the Royal Society of London. Series A*, 97(686), 354-373.
- Rodi, W. (1980). *Turbulence models and their application in hydraulics: a state of the art review*. Book publication of International Association for Hydraulic Research, Delft, Netherlands.
- Ross A.N., (2000). *Gravity currents on slope*. PhD Dissertation, University of Cambridge.
- Ross, A. N., Dalziel, S. B. and Linden, P. F. (2006). Axisymmetric gravity currents on a cone. *J. Fluid Mech.* 565, 227-254.
- Rottman, J. W., and Simpson, J. E. (1983). Gravity currents produced by instantaneous releases of a heavy fluid in a rectangular channel. *J Fluid Mech*, Vol. 135, 95-110.
- Sang D.A., (2011). *Interflow dynamics and three-dimensional modeling of turbid density currents in imha reservoir, South Korea*. PhD Dissertation, University of Colorado State.
- Schijf, J.B., and Schönfeld, J.C. (1953). Theoretical considerations on the motion of salt and fresh water. In *Proc. Minn. Intl Hydraulics Conv.* pp. 321-333.
- Sequeiros, O., Naruse, H., Endo, N., Garcia, M. and Parker, G. (2009). Experimental study on self-accelerating turbidity currents. *J. Geophys. Res.* 114, C05025.
- Shao D., and Law A.W., (2010). Mixing and boundary interactions of 30° and 45° inclined dense jets. *Environ Fluid Mech* 10:521-553.
- Sherman, F. S., Imberger, J. and Corcos, G. M. (1978). Turbulence and mixing in stably stratified waters. *Annu. Rev. Fluid Mech.* 10, 267-288.
- Shin, J. O., Dalziel, S. B., and Linden, P. F. (2004). Gravity currents produced by lock exchange. *J. Fluid Mech.*, Vol. 521, 1-34.
- Shringarpure, M., Cantero, M., and Balachandar, S. (2012). Dynamics of complete turbulence suppression in turbidity currents driven by monodisperse suspensions of sediment. *J. Fluid Mech.* 712, 384-417.
- Simpson J. E., (1997). *Gravity Currents in the Environment and the Laboratory* (Cambridge University Press, Cambridge).
- Simpson, J. E. (1982), Gravity currents in the laboratory, atmosphere, and ocean, *Annual Review of Fluid Mechanics*, 14 (1), 213-234.
- Simpson, J. E. and Britter, R. E. (1979). The dynamics of the head of a gravity current advancing over a horizontal surface. *J. Fluid Mech.*, Vol. 94, 477-495.
- Simpson, J. E. and Britter, R. E. (1980). A laboratory model of an atmospheric mesofront. *Q. J. R. Met. Soc.* 106, 485-500.
- Simpson, J.E. (1969). A comparison between laboratory and atmospheric density currents. *Quart. J. R. Met. Soc.* 95, 758-765.
- Simpson, J.E. (1972). Effects of the lower boundary on the head of a gravity current. *J. Fluid Mech.* 53(4), 759-768.

- Slim, A.C., and Huppert, H.E. (2008). Gravity currents from a line source in an ambient flow. *J. Fluid Mech.* 606: 1-26.
- Sorgard, E. (1991). A numerical, three-layered, stationary salt wedge model. *J. Geophys. Res.* 96, 12739-12754.
- Taylor, A. G. I. (1931). Effect of Variation in Density on the Stability of Superposed Streams of Fluid. *Proceedings of the Royal Society of London. Series A.*, 132(820), 499-523.
- Tokyay, T., Constantinescu, G., and Meiburg, E. (2012). Tail structure and bed friction velocity distribution of gravity currents propagating over an array of obstacles. *Journal of Fluid Mechanics*, 694, 252-291.
- Tokyay, T., Constantinescu, G., and Meiburg, E. (2011). Lock exchange gravity currents with a high volume of release propagating over a periodic array of obstacles. *Journal of Fluid Mechanics*, 672, 570-605.
- Turner, J. S. (1973). *Buoyancy effect in fluids*, Cambridge University Press, Cambridge, UK.
- Turner, J.S. (1966). Jets and plumes with negative or reversing buoyancy. *J. Fluid Mech.*, 26 pt 4: 779-792.
- Turner, J.S., (1986). Turbulent entrainment: the development of the entrainment assumption, and its applications to geophysical flows. *J. Fluid Mech.* 173, 431-471.
- Ungarish M., (2007). Axisymmetric gravity currents at high Reynolds number: On the quality of shallow-water modelling of experimental observations. *Phys. Fluid* 19, 036602.
- Ungarish, M. (2009). *An introduction to gravity Currents and intrusions*. Chapman & Hall/CRC press, Boca Raton, London, New York.
- Ungarish, M., and Zemach, T. (2005). On the slumping of high Reynolds number gravity currents in two-dimensional and axisymmetric configurations. *European Journal of Mechanics B/Fluids* 24, 71-90.
- Van Kessel, T., and Kranenburg, C. (1996). Gravity Current of Fluid Mud on Sloping Bed. *Journal of Hydraulic Engineering*, 123, 710-717.
- Versteeg, H. K., and Malalasekera, W. (1995). *An introduction to Computational Fluid Dynamics*. Prentice Hall.
- Winters, K. B., Lombard, P. N., Riley, J. J. and D'asaro, E. A. (1995). Available potential energy and mixing in density-stratified fluids. *J. Fluid Mech.* 289, 115-128.

Etude Expérimentale et Numérique de Courants Gravitaires Modèles en Environnement Côtier: Courant gravitaire dense

Résumé: Le but de ce travail de recherche est de contribuer à une meilleure compréhension de la dynamique de propagation et de la miscibilité de jets gravitaires au-dessous d'un liquide ambiant. Des expériences ont été réalisées en laboratoire à l'aide d'une plateforme expérimentale constituée d'un bassin parallélépipédique contenant de l'eau douce et d'un canal d'injection de section rectangulaire de jets gravitaires de concentration constante initiale fixée. Les calculs mathématiques et numériques sont basés sur les modèles RANS (Reynolds-Averaged Navier Stokes equations), $k-\varepsilon$ (K-epsilon) et DCE (Diffusion-Convective Equation) de la fraction volumique de l'eau salée pour décrire la propagation et le mélange du jet gravitaire. L'évolution du front du jet obtenue expérimentalement est utilisée pour valider le modèle numérique. Par ailleurs, la comparaison des résultats obtenus sur l'écoulement moyen ($z/z_{0.5} = u/u_{max}$) avec ceux des études 2D expérimentales et numériques antérieures ont montré des similarités. La simulation numérique des champs hydrodynamiques montre que la vitesse maximale est atteinte à la position $0.18 z_{0.5}$, où $z_{0.5}$ est la hauteur d'eau pour laquelle la vitesse moyenne u est égale à la moitié de la vitesse maximale u_{max} .

Mots clés: Courant gravitaire dense, Jet flottant, Entraînement, Expériences, Mélange, Simulations Numériques, Modèle RANS.

Experimental and Numerical Study of Model Gravity Currents in Coastal Environment: Bottom Gravity Currents

The aim of this investigation is to contribute to a better understanding of the propagation dynamics and the mixing process of dense gravity currents. The Laboratory experiments proceeded with a fixed initial gravity current concentration in one experimental set-up. The gravity currents are injected using a rectangular injection channel into a rectangular basin containing the ambient lighter liquid. The injection studied is said in unsteady state volume, as the Reynolds number lies in the range 1111 - 3889. The experiments provided the evolution of the boundary interface of the jet, and it is used to validate the numerical model. The numerical model depends on the Reynolds-Averaged Navier Stokes equations (RANS). The $k-\varepsilon$ (K-epsilon) and the Diffusion-Convective Equation (DCE) of the saline water volume fraction were used to model the mixing and the propagation of the gravity current jet. On the other hand, comparison of the mean flow ($z/z_{0.5} = u/u_{max}$) with previous two-dimensional numerical simulations and experimental measurements have shown similarities. The numerical simulations of the hydrodynamic fields indicate that the velocity maximum at $0.18z_{0.5}$, where $z_{0.5}$ is the height at which the mean velocity u is the half of the maximum velocity u_{max} .

Keywords: Bottom Gravity Current, Buoyant jet, Entrainment, Experiments, Mixing, Numerical simulations, RANS model.